Pore Network Modeling and Neutron Imaging-Based Analysis of Transport in Fibrous Porous Transport Layers for PEM Electrolyzers

Dissertation
zur Erlangung des akademischen Grades

Doktoringenieur

(Dr.-Ing.)

von M.Sc. Haashir Altaf

geb. am 01.09.1995 in Pakistan

genehmigt durch die Fakultät für Verfahrens- und Systemtechnik der Otto-von-Guericke-Universität Magdeburg

Gutachter/innen:

Prof. Dr.-Ing. habil. Evangelos Tsotsas

Dr.-Ing. habil. Tanja Vidakovic-Koch

Prof. Dr. Rui Wu

Promotionskolloquium am 05.12.2025

Abstract

Green hydrogen holds great potential as a clean fuel and efficient energy storage solution, enabling the integration of renewable energy sources. Hydrogen produced by polymer electrolyte membrane water electrolyzers (PEMWEs) offers advantages in purity, safety, and dynamic operation. However, issues related to performance, durability, and cost must be addressed for PEMWEs to become a viable and cost-effective alternative. The key advantage of PEMWEs is their ability to operate at high current densities (> 2.0 $A \cdot cm^{-2}$), but mass transport resistances at these densities can reduce performance. This is partly due to the counter-current flow of oxygen and water through the porous transport layer (PTL) at the anode. It is anticipated that, at high current densities, the oxygen produced blocks water pathways to the catalyst layer (CL), hence impeding the reaction rate.

To mitigate this problem, various studies propose strategies based on PTL properties such as pore size, porosity, and thickness, yet a structured overview quantifying the limits of transport regimes as a function of current density and structural properties is still lacking. Moreover, most existing research focuses on low-porosity PTLs (< 50 %), and high-porosity commercial PTLs, which could be suitable for high current density operations, have been rarely investigated. This data scarcity makes it difficult to parametrize continuum models (CMs) for assessing structural impacts of different PTLs on performance as well. Existing models used to study or extract transport parameters are either computationally expensive or lack realistic structural representation.

In this context, pore network models (PNMs) provide a more efficient approach for studying capillary-dominated invasion in PTLs, representing porous structures as networks of pores and throats. PNMs offer insights into the pore-scale behavior and transport parameters, and can be used for parametric studies. However, they rely on high-resolution imaging when extracted pore networks (PNs) are used, with micro-computed X-ray tomography (micro-CT) commonly employed. Without imaging resources, idealized PNs with representative pore size distributions (PSDs) can be used to reduce computational cost. Each approach has its advantages and limitations, making the choice dependent on the specific application. For instance, idealized PNs may be sufficient for comparing the impact of different PSDs, but extracted PNs are more accurate for modeling drainage patterns.

In this work, high-porosity commercial fiber-PTLs (~ 75 %) are investigated using extracted PNs, while idealized PNs are employed to study the impact of different pore/throat size distributions. With the help of extracted PNs, parameters such as permeability and capillary pressure curves are extracted for three PTLs and compared to existing correlations from literature. For absolute permeability, it is shown that the Tomadakis and Sotirchos model (TSM) and the Jackson and James model (JJM) should effectively estimate the permeability of PTLs with larger

fiber diameters. The relative permeability and saturation profiles show that a graded PTL, with smaller fibers at the CL side and larger ones toward the water inlet, is the best candidate for PEMWE, as it provides a good balance between liquid and gas permeability. Additionally, the capillary pressure curves from extracted PNs are compared to the Leverett equation (LE) and Brooks-Corey equation (BCE). It is observed that the literature correlations can only partially represent the PNM-derived curves and are not recommended for high-porosity PTLs. Using Voronoi networks (VNs) and a simplified conduction-based model, the thermal conductivity of the PTLs is also estimated and fitted to Hot Disk experimental data. The resulting values are compared to several structural models from literature as well, none of which agree with the Hot Disk experimental results.

Moreover, with the help of idealized PNs, the impact of microstructure on the drainage through the PTL is highlighted. Various PTLs from literature and arbitrary gradients are analyzed in detail. Consistent with extracted PN results, thicker PTLs show lower relative liquid permeabilities due to enhanced lateral invasion. The permeability values from simulations matched theoretical trends but differed from literature values (non-intrinsic in nature unlike PNM permeability). The simulations with pore/throat size gradients revealed that invasion behavior strongly depends on gradient direction and design. It is shown that a PTL with a gradient, increasing from the CL side towards the water inlet, can enhance oxygen removal while maintaining efficient water transport.

In addition to PNM, neutron imaging experiments using both non-electrochemical and electrochemical cells were conducted to compare different PTLs. The tomographies from the non-electrochemical experiments reveal water scarcity issues even in high-porosity PTLs. The non-electrochemical radiographies show that bubble release patterns are largely governed by PTL structure and/or pressure distribution in the channel and are independent of current density. However, the saturation profiles within the PTL could not be observed. Electrochemical experiments revealed that the PTL saturation is independent of the current density indeed but the inlet water flow rate has an impact on the saturation within a PTL, indicating a shift toward flow-driven behavior. These findings suggest that the PNM assumptions are only valid for certain flow conditions.

The experimental results prompt a reconsideration of certain PNM assumptions, while also highlighting areas for further model refinement. It is perceived that the liquid-gas transport occurs simultaneously around a constant structure-dependent saturation which is unaffected by current density. This is considered in PNM too, where PTL structure controls the drainage pattern alone and the simulations predict residual liquid saturations (maximum possible). However, the electrochemical experiments highlight the impact of increased inlet flow rate. Based on this, it is recommended that the PNM simulations should include imbibition and be coupled with a CM to incorporate the dynamics of fluid transport in PEMWE. In general, comparing different particle-PTLs with fiber-PTLs or PTLs with a micro-porous layer (MPL) will be of great interest in future. Additionally, PTL characterization should encompass the effects of mechanical, topographical, and electrical properties too.

Kurzzusammenfassung

Grüner Wasserstoff besitzt großes Potenzial als sauberer Energieträger und effiziente Energiespeicherlösung und kann die Integration erneuerbarer Energiequellen entscheidend unterstützen. Wasserstoff, der mittels Polymerelektrolytmembran-Wasserelektrolyseuren (engl. polymer electrolyte membrane water electrolyzers, PEMWEs) erzeugt wird, bietet Vorteile hinsichtlich Reinheit, Sicherheit und dynamischer Betriebsfähigkeit. Damit PEMWEs jedoch zu einer wirtschaftlich tragfähigen Alternative werden, müssen Herausforderungen in Bezug auf ihre Leistungsfähigkeit, Langlebigkeit und Kosten überwunden werden. Ein wesentlicher Vorteil von PEMWEs liegt in ihrer Fähigkeit, bei hohen Stromdichten (> 2 $A \cdot cm^{-2}$) zu arbeiten. Allerdings können Massentransport-widerstände bei diesen Stromdichten die Leistung erheblich beeinträchtigen. Ursache hierfür ist unter anderem der Gegenstrom von Sauerstoff und Wasser durch die poröse Transportschicht (engl. porous transport layer, PTL) an der Anode. Es wird angenommen, dass der bei hohen Stromdichten erzeugte Sauerstoff die Wasserwege zur Katalysatorschicht (engl. catalyst layer, CL) blockiert und dadurch die Reaktionsrate reduziert.

Zahlreiche Studien schlagen verschiedene Strategien zur Verbesserung vor, wobei der Fokus auf PTL-Eigenschaften wie Porengröße, Porosität und Dicke liegt. Ein klarer Konsens über den Einfluss der Struktur auf den Stofftransport besteht jedoch bislang nicht. Zudem konzentrieren sich die meisten bisherigen Untersuchungen auf PTLs mit geringer Porosität (< 50 %), während hochporöse, kommerzielle PTLs, die sich möglicherweise besser für den Betrieb bei hoher Stromdichte eignen, bislang kaum erforscht wurden. Diese Datenlücke erschwert die Parametrisierung von Kontinuumsmodellen (engl. continuum models, CM), die zur Bewertung struktureller Auswirkungen auf die Leistung dienen. Bestehende Modelle sind entweder sehr rechenintensiv oder vereinfachen die Struktur stark.

In diesem Kontext bieten Porennetzwerkmodelle (engl. pore network models, PNM) einen effizienteren Ansatz zur Untersuchung kapillardominierter Strömungen in PTLs, indem sie poröse Strukturen als Netzwerke aus Poren und Halsverbindungen abbilden. Sie liefern Einblicke in das Verhalten auf Porenebene und die Transportparameter und ermöglichen parametrische Studien. Dabei werden entweder aus hochaufgelösten Bilddaten (z. B. Röntgentomographie) extrahierte Porennetze (engl. pore networks, PN) verwendet oder idealisierte Netzwerke mit repräsentativen Porengrößenverteilungen zur Reduktion des Rechenaufwands eingesetzt. Beide Ansätze haben spezifische Vor- und Nachteile, deren Eignung vom jeweiligen Anwendungsfall abhängt: ein idealisiertes PNM genügt etwa für den Vergleich von Porengrößenverteilungen, während extrahierte Netzwerke eine präzisere Modellierung von Entwässerungsmustern (engl. drainage) ermöglichen.

In der vorliegenden Arbeit werden kommerzielle Faser-PTLs mit hoher Porosität (~ 75 %) mithilfe extrahierter PN untersucht. Parallel dazu werden idealisierte PN verwendet, um den Einfluss verschiedener Poren- und Halsgrößenverteilungen zu analysieren. Auf Basis der extrahierten Netzwerke werden Permeabilität und Kapillardruckkurven für drei PTLs ermittelt und mit Literaturkorrelationen verglichen. Dabei zeigt sich, dass die Modelle von Tomadakis und Sotirchos sowie Jackson und James nur bei PTLs mit größeren Faserdurchmessern zuverlässig die absolute Permeabilität vorhersagen. Die relativen Permeabilitäts- und Sättigungsprofile deuten darauf hin, dass eine abgestufte PTL (mit kleineren Fasern auf der CL-Seite und größeren in Richtung Wassereinlass) die beste Option für PEMWEs darstellt, da sie ein ausgewogenes Verhältnis zwischen Flüssigkeits- und Gaspermeabilität bietet. Darüber hinaus zeigen Vergleiche der Kapillardruckkurven mit der Leverett-Gleichung und der Brooks-Corey-Gleichung, dass diese Korrelationen die mit PNM berechneten Kurven nur unzureichend abbilden und für hochporöse PTLs nicht empfohlen werden. Unter Verwendung von Voronoi-Netzwerken (engl. Voronoi networks, VN) und eines vereinfachten, leitungsbasierten Modells wird der Einfluss der Flüssigkeitssättigung auf die Wärmeleitfähigkeit der PTL eingeschätzt und an experimentelle Daten der Hot-Disk-Methode angepasst. Die daraus resultierenden Werte werden mit diversen Strukturmodellen aus der Literatur verglichen, von denen keins mit den Ergebnissen der Hot Disk Experimente übereinstimmt.

Darüber hinaus veranschaulichen idealisierte PN den Einfluss der Mikrostruktur auf die Entwässerung. Verschiedene in der Literatur beschriebene PTLs sowie frei definierte Gradienten wurden im Detail analysiert. Im Einklang mit den Ergebnissen aus PNM-Simulationen zeigen dickere PTLs aufgrund verstärkter lateraler Invasion eine geringere relative Flüssigkeitspermeabilität. Die aus den Simulationen abgeleiteten Permeabilitätswerte folgen zwar den theoretisch erwarteten Trends, weichen jedoch von Literaturwerten ab, da letztere im Gegensatz zur PNM-basierten Permeabilität nicht intrinsischer Natur sind. Simulationen mit Poren-/Halsgrößengradienten zeigen, dass das Invasionsverhalten stark von Richtung und Gestaltung des Gradienten abhängt. Es wird gezeigt, dass ein PTL-Gradient, der von der Katalysatorschicht (CL) in Richtung Wassereinlass zunimmt, den Sauerstoffabtransport verbessern kann, während der Wassertransport weiterhin effizient bleibt.

Neben den PNM-Simulationen wurden auch Neutronenbildgebungs-Experimente mit elektrochemischen und nicht-elektrochemischen Zellen durchgeführt, um verschiedene PTLs zu vergleichen. Die Tomographien der nicht-elektrochemischen Experimente verdeutlichen, dass selbst in hochporösen PTLs Wassermangel auftreten kann. Die Radiographien zeigen, dass die Phasenverteilung innerhalb der PTLs weitgehend von der PTL-Struktur und/oder Druckverteilung im Kanal abhängt und unabhängig von den Stromdichten ist. Die Sättigungsprofile innerhalb der PTL konnten jedoch nicht beobachtet werden. Die elektrochemischen Experimente zeigten, dass die Sättigung der PTL tatsächlich unabhängig von der Stromdichte ist, jedoch beeinflusst die Wasserdurchflussrate

am Einlass die Sättigung innerhalb der PTL, was auf ein strömungsgetriebenes Verhalten hinweist. Diese Ergebnisse legen nahe, dass die Annahmen des PNM nur unter bestimmten Strömungsbedingungen gültig sind.

Die experimentellen Ergebnisse weisen auf die Notwendigkeit hin, zentrale Annahmen der PNM-Modelle zu überprüfen und liefern Impulse für deren Weiterentwicklung. So wird angenommen, dass Flüssigkeits- und Gastransport gleichzeitig um eine konstante, strukturabhängige Sättigung erfolgen, unabhängig von der Stromdichte. In den PNMs zeigt sich auch, dass die PTL-Struktur allein das Entwässerungsmuster bestimmt und die Simulationen (maximal mögliche) Restflüssigkeitssättigungen vorhersagen. Die elektrochemischen Experimente heben den Einfluss von erhöhten Einflussraten hervor. Daraus ergibt sich die Empfehlung, zukünftige PNM-Simulationen um Imbibition zu erweitern und sie mit Kontinuumsmodellen zu koppeln, um die Dynamik des Flüssigkeitstransports in PEMWEs umfassend abzubilden. Generell erscheint der Vergleich von Partikel-PTLs mit Faser-PTLs oder PTLs mit mikroporöser Schicht (engl. micro-porous layer, MPL) vielversprechend. Zukünftige PTL-Charakterisierungen sollten über den Stofftransport hinaus auch mechanische, topografische und elektrische Eigenschaften berücksichtigen.

Nomenclature

a	chemical activity	-
A	area	m^2
C	percentage compression	%
d	diameter	m
E	electrode potential	V
f	weighting parameter	-
F	Faraday's constant	$C \cdot mol^{-1}$
G	Gibb's free energy	$J \cdot mol^{-1}$
h	heat transfer coefficient	$W \cdot m^{-2} \cdot K^{-1}$
i	current density	$A \cdot m^{-2}$
k	relative permeability	-
K	absolute permeability	m^2
L	length	m
$\dot{M}$	mass flow rate	$kg \cdot s^{-1}$
$\tilde{M}$	molar mass	$kg \cdot mol^{-1}$
n	number of electrons	-
P	pressure	Pa
$\dot{Q}$	heat flow rate	$J \cdot s^{-1}$
r	radius	m
R	universal gas constant	$J \cdot K^{-1} \cdot mol^{-1}$
s	saturation	-
T	temperature	K
v	volume	m^3
$\dot{v}$	volumetric flow rate	$m^3 \cdot s^{-1}$
V	potential	V
W	water thickness	m
x	width	m

Greek symbols

α	fitting parameter *(Tomadakis and Sotirchos model)*	-
β	pore size distribution index	-
γ	surface tension	$N \cdot m^{-1}$
ε	porosity	-
η	overpotential	V
θ	contact angle	°
λ	thermal conductivity	$W \cdot m^{-1} \cdot K^{-1}$
μ	dynamic viscosity	$Pa \cdot s$
ρ	density	$kg \cdot m^{-3}$
σ	standard deviation (radii)	m
ψ	attenuation coefficient	m^{-1}
ω	stoichiometry	-

Subscripts and superscripts

ac	activation
an	anode
atm	atmospheric
c	capillary
ca	cathode
ch	channel
exp	experiment
f	fluid
F	Faraday
g	gas
l	liquid
lit	literature
mem	membrane
mt	mass transport
p	pore
r	residual
rel	relative
rev	reversible
t	throat
tn	thermo-neutral

Abbreviations

ACL	anode catalyst layer
BPP	bipolar plate
CC	counter current
CCL	cathode catalyst layer
CCM	catalyst coated membrane
CL	catalyst layer
CM	continuum model
micro-CT	micro-computed X-ray tomography
DC	dry cell
DF	dark field
DP	dual-porosity
EDT	Euclidean distance transform
GDL	gas diffusion layer
HER	hydrogen evolution reaction
HTL	high to low
JJM	Jackson and James model
LTH	low to high
LP	larger pores
MEA	membrane electrode assembly
OER	oxygen evolution reaction
PEM	polymer electrolyte membrane
PEMWE	polymer electrolyte membrane water electrolyzer
PN	pore network
PNM	pore network model
PSD	pore size distribution
PTL	porous transport layer
SI	sample image
SOE	solid oxide electrolyzer
SP	smaller pores
TSD	throat size distribution
TSM	Tomadakis and Sotirchos model
TT	thin and tunable
VPS	vacuum plasma spraying

Contents

Abstract i
Kurzzusammenfassung iii
Nomenclature vi
Contents ix
Chapter 1 Introduction 1
1.1 Motivation 2
1.2 State of the art in PEMWE 5
1.2.1 Design and principles 5
1.2.2 Operating conditions 6
1.2.3 Losses in PEMWE 8
1.2.4 Role of PTL and the impact of its structure 8
1.2.5 Modeling transport in PTLs 13
1.2.6 Experimental characterization methods 19
1.3 Scope and outline 23
Chapter 2 Pore Network Modeling and Experimental Methods 26
2.1 Pore network modeling 27
2.1.1 General model assumptions 27
2.1.2 Pore network geometry and reconstruction 28
2.1.3 Drainage model for capillary controlled invasion 34
2.1.4 Computation of permeability 35
2.1.5 Computation of thermal conductivity 38
2.2 Hot Disk experiments 43
2.3 Neutron imaging experiments 43
2.3.1 Non-electrochemical cells 44
2.3.2 Electrochemical cells 50
Chapter 3 Extracted Pore Networks 52
3.1 Validation of pore network model 53
3.2 Commercial PTLs 58
3.2.1 Micro-CT scans 58
3.2.2 Determination of structure-related mass transport parameters 61
3.3. Comparison of idealized and extracted PNs 80
Chapter 4 Idealized Pore Networks 82
4.1 Study of the impact of structure based on PTLs from literature 83
4.1.1 Thickness 84

4.1.2 Standard deviation in throat sizes 86
4.1.3 Permeability 88
4.2 Impact of pore size gradients 92
4.2.1 Pore network setup 93
4.2.2 Invasion and permeability profiles 94
4.2.3 Variations in throat size gradients 100
4.2.4 Comparison of dual-porosity pore networks 103
Chapter 5 Neutron Imaging Experiments 105
5.1 Non-electrochemical cells 106
5.1.1 Tomography of water imbibition into empty cells 106
5.1.2 Radiography of counter-current flow through cells 107
5.1.3 Determination of break-through points 113
5.1.4 Transparent cell and influence of stoichiometry 115
5.2 Electrochemical cells 117
Chapter 6 Conclusion 123
6.1 Summary 124
6.2 Key highlights and findings 132
6.3 Outlook 133
Bibliography 135
Appendix 146
Declaration 158
Journal publications and conferences 159

Chapter 1
Introduction

1.1 Motivation

Climate change is one of the most critical and difficult challenges of our time. There has been overwhelming evidence provided by the Intergovernmental Panel on Climate Change (IPCC), that human activities, particularly the burning of fossil fuels and deforestation, are propelling significant changes in the Earth's climate[1]. The devastating impacts of climate change are already being observed across the globe. For instance, the forest fires in Australia in 2020, driven by record-breaking temperatures and lengthy drought, burned over 18 million hectares, destroyed thousands of homes, and led to the loss or displacement of nearly three billion animals[2]. Unfortunately, climate change disproportionately affects vulnerable populations, worsening existing inequalities. Several communities in sub-Saharan Africa, which are already coping with food and water insecurity, are dealing with much more droughts. These droughts are not just becoming more frequent but also more severe, further endangering their livelihoods[3]. These examples highlight the human and ecological toll of climate change worldwide and emphasize the need for action, including the transition to sustainable and efficient energy production and storage systems.

The primary energy mix of the world is entirely dominated by fossil fuels[4] (Figure 1-1). However, the primary source of greenhouse gas emissions is also a result of fossil fuel combustion. The substantial dependence on fossil fuels has profound environmental and health implications. Combustion of fossil fuels releases not only CO_2 but also other harmful pollutants.

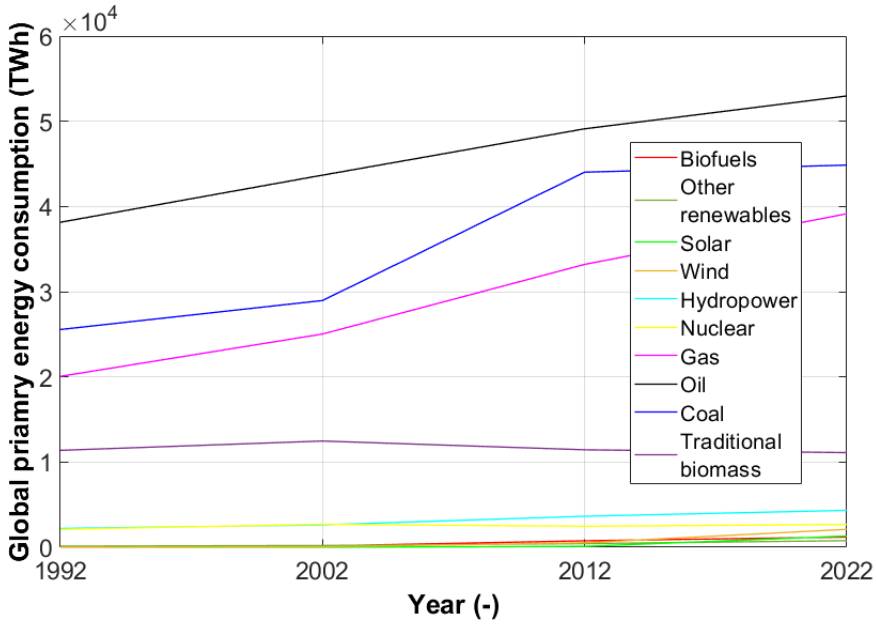

Figure 1-1: The primary energy consumption of the world over the last two decades. The data highlights a consistent domination of fossils fuels[4].

To mitigate climate change and reduce the adverse influences of fossil fuels, a transition to renewable energy sources is vital. In the recent years, wind and solar power have been among the most promising and rapidly growing renewable energy technologies. Despite the rapid expansion of wind and solar energy, these

technologies face significant challenges that must be addressed to fully realize their potential. One of the primary issues is their intermittent nature. This means that wind and solar power generation depend on weather conditions and the time of day, leading to inconsistencies in energy supply. This intermittency issue needs the development of efficient and scalable energy storage systems to ensure a stable and reliable energy supply. Currently, lithium-ion batteries are the most widely used technology for energy storage. This is attributed to their high energy density, efficiency, and decreasing costs. However, these batteries face several limitations that hinder their scalability and, as well as, sustainability[5].

Green hydrogen, produced through water electrolysis using renewable energy sources, offers a compelling solution to the limitations of lithium-ion batteries and the intermittency issues associated with wind and solar power. The production of hydrogen through electrolysis involves splitting water (H_2O) into hydrogen (H_2) and oxygen (O_2) using an electric current. When the electricity supplied to this process is obtained from renewable sources, such as wind or solar energy, the hydrogen produced is known as "green hydrogen".

Hydrogen, as an energy carrier, can be stored in various forms. This includes compressed gas, liquid state, and even in the form of chemical compounds such as ammonia. This versatility allows hydrogen to be used in a wide range of applications, including power generation, transportation, and industrial processes. Heavy industries, which are difficult to electrify, can be decarbonized by the potential of green hydrogen.

Moreover, green hydrogen can be integrated into existing energy infrastructure with a few modifications. For example, existing natural gas pipelines can be repurposed to transport hydrogen, and, additionally, hydrogen can also be mixed with natural gas in the existing gas networks to reduce the carbon footprint of heating and power generation[6]. This facilitates a smoother transition from fossil fuels to renewable energy systems.

For green hydrogen production, various technologies are available, each offering distinct advantages and facing specific challenges. The three main technologies include alkaline electrolysis, solid oxide electrolysis (SOE), and proton exchange membrane (PEM) electrolysis.

- **Alkaline electrolysis**: Alkaline electrolysis is the most mature out of the three technologies and widely used method for hydrogen production. It operates using an alkaline electrolyte, typically potassium hydroxide (KOH) or sodium hydroxide (NaOH), and two electrodes which are usually made of nickel. Alkaline electrolysis is known for its relatively low cost, maturity, and durability. However, alkaline electrolysis has limitations in terms of efficiency and response time to fluctuating power inputs. The response time limitation is significantly important because it makes it less suitable for integration with intermittent renewable energy sources, like wind and solar energy[7].

- **SOE**: Solid oxide electrolysis uses a solid, dense ceramic oxide electrolyte to conduct oxygen ions from the cathode to the anode. This technology operates at elevated temperatures (around 700 °C to 1000 °C), which improves the efficiency of the system. SOE can also produce syngas (a mixture of hydrogen and carbon monoxide) by co-electrolyzing water and carbon dioxide, which can be used to produce synthetic fuels and chemicals. However, the high temperatures can cause significant thermal stress and accelerate the degradation of materials, posing durability challenges and requiring advanced engineering solutions to ensure long-term stability and performance[8].
- **PEM electrolysis**: PEM electrolysis uses a solid polymer electrolyte to conduct protons from the anode to the cathode while separating the gases produced during electrolysis. This technology operates at lower temperatures (~ 80 °C) compared to SOE[9] and offers several advantages over alkaline electrolysis[10]. PEM electrolysis has the ability to operate at higher current densities and the capability to operate at fluctuating loads, which is crucial for integrating with intermittent renewable energy sources. The use of a solid polymer electrolyte instead of a liquid electrolyte, reduces the corrosion and maintenance issues significantly. Additionally, PEM water electrolyzers (PEMWEs) produce high-purity hydrogen (99.99 %), which is essential for applications in sensitive processes, such as fuel cells[11].

PEM water electrolysis stands out as a promising technology due to its higher efficiency, faster response times, and greater compatibility with renewable energy sources, compared to other technologies. The compact design and operational flexibility of PEMWEs make them well-suited for distributed hydrogen production, where hydrogen can be generated on-site at renewable energy facilities or end-use locations, reducing the need for extensive transportation infrastructure. This decentralization of hydrogen production can, not just enhance energy security, but also reduce costs associated with transportation and storage.

However, PEM electrolysis faces several challenges too, that need to be addressed for widespread adoption. One of the primary challenges is the high cost of the materials used, such as platinum and iridium, which are used as catalysts. These materials are expensive and have limited availability, posing supply chain risks. Research is ongoing to develop alternative catalysts that are less expensive and more abundant while maintaining high performance and durability. Another challenge is the need for improvements in overall electrolyzer efficiency and durability of the large-scale electrolyzer stacks. While PEMWEs offer high efficiency, further advancements in membrane technology, electrode design, and system integration are needed to enhance long-term performance at scale and reduce costs. The development of advanced materials and manufacturing processes can contribute to these improvements.

1.2 State of the art in PEMWE

1.2.1 Design and principles

In PEMWE, the inlet water at the anode is split into protons, electrons and oxygen. The protons travel through the proton conducting membrane to the cathode, where they recombine with electrons to form hydrogen gas. Due to the electro-osmotic drag, some of the water is also transported through the membrane to the cathode side. In principle, the membrane allows only protons to pass through while blocking electrons and gases. At the anode side, the membrane is typically coated with a catalyst like iridium oxide (IrO_2) or ruthenium oxide (RuO_2) to facilitate the oxygen evolution reaction (OER). At the cathode side, the membrane is usually coated with platinum or platinum-based catalysts to facilitate the hydrogen evolution reaction (HER). This catalyst coated membrane (CCM) is sandwiched between a porous transport layer (PTL) at the anode side and a gas diffusion layer (GDL) at the cathode side (Figure 1-2). The membrane, two catalyst layers (CLs), PTL, and the GDL are often referred to as membrane electrode assembly (MEA). On each side of the MEA, bipolar plates (BPPs) are present, engraved with flow channels to distribute and collect fluids at the anode and cathode.

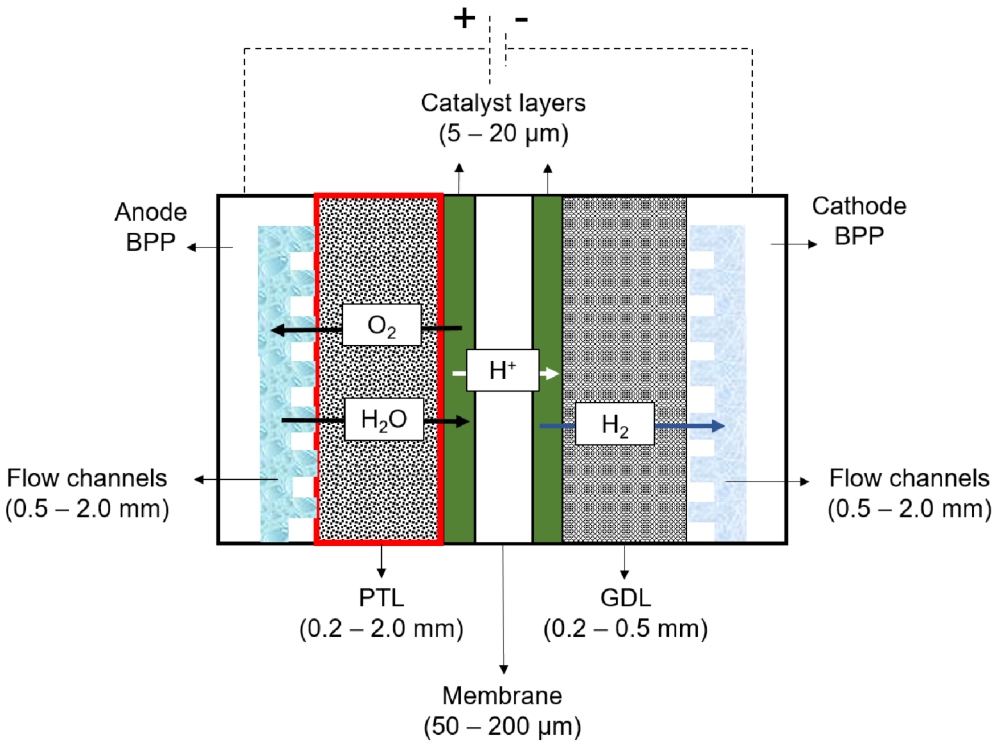

Figure 1-2: A schematic of a PEMWE, along with the typical thicknesses of its components[12–22].

At the anode, water is oxidized to produce oxygen gas, protons, and electrons:

$$H_2O\,(l) \rightarrow 0.5O_2\,(g) + 2H^+ + 2e^-. \qquad (1\text{-}1)$$

The protons conducted by the membrane to the cathode combine with the electrons traveling through the external circuit to form hydrogen gas:

$$2H^{+} + 2e^{-} \rightarrow H_2\,(g). \tag{1-2}$$

And hence, the overall reaction for water splitting is:

$$H_2O\,(l) \rightarrow 0.5O_2\,(g) + H_2\,(g). \tag{1-3}$$

At standard conditions (25 °C and 1 bar), the minimum free energy required for water splitting is ΔG° = 237 kJ·mol^{-1}. This corresponds to a reversible cell potential,

$$\left|V_{rev}^{\circ}\right| = \frac{\Delta G^{\circ}}{nF} = 1.23\ \text{V}, \tag{1-4}$$

which is the electrical work needed to split water. However, some entropy is also generated during the water splitting so the electrical work required, denoted by thermo-neutral potential is,

$$V_{tn}^{\circ} = \frac{\Delta H^{\circ}}{nF} = \frac{\Delta G^{\circ}}{nF} + \frac{T\Delta S^{\circ}}{nF} = 1.48\ \text{V}. \tag{1-5}$$

This corresponds to a reaction enthalpy of 286 kJ·mol^{-1}. The reversible limit (1.23 V) corresponds to no ohmic/kinetic losses; between 1.23 V and 1.48 V the reaction absorbs heat from the surroundings; at 1.48 V the cell operates adiabatically; and above 1.48 V excess electrical energy is dissipated as heat. In practice, the overall cell potential (generally > 1.5 V due to overpotentials/resistance) is the difference between the electrode potentials which are calculated using the Nernst equation. The Nernst equation accounts for the deviations from the standard state using the activities and temperature. The electrode potential at the anode can be written as,

$$E_{an} = E_{an}^{\circ} + \frac{RT}{2F}\ln\left(\frac{a(H^{+})^2\, a(O_2)^{0.5}}{a(H_2O)}\right), \tag{1-6}$$

and at the cathode,

$$E_{ca} = E_{ca}^{\circ} + \frac{RT}{2F}\ln\left(\frac{a(H^{+})^2}{a(H_2)}\right). \tag{1-7}$$

The overall cell potential then becomes:

$$V_{cell} = E_{ca} - E_{an}. \tag{1-8}$$

1.2.2 Operating conditions

In terms of operating temperature, a range between 70 °C to 90 °C is usually preferred. Generally, the performance of an electrolyzer improves at elevated temperatures due to the reduction in the ohmic losses[23]. This is due to higher proton

conductivity through the membrane. Consequently, at higher temperatures (> 90 °C), the amount of electrical energy required is reduced. On the other hand, the deterioration of the PEM at high temperatures limits the possibility to operate at elevated temperatures[23]. Moreover, there is also a safety risk associated with increased hydrogen crossover across the membrane, from cathode to anode, at higher temperatures. This is because the membrane is not 100 % efficient in controlling the hydrogen crossover to the anode side, especially at high operating temperatures. At elevated temperatures, the diffusivity of hydrogen through the membrane increases due to enhanced molecular motion and thermal energy, thereby reducing the membrane's effectiveness in limiting gas crossover.

In terms of pressure, typically commercial electrolyzers operate with a differential pressure operation. In differential pressure PEMWE, the anode (oxygen side) operates at near-atmospheric pressure, while the cathode (hydrogen side) is pressurized, with membrane separating the two compartments. This means that the hydrogen produced at the cathode is directly collected at a higher pressure, usually between 30 bar and 50 bar[23]. The PEM maintains a pressure differential between the two sides, enabling the collection of hydrogen at high pressure. This is one of the main reasons why PEMWEs have an advantage over the alkaline water electrolysis. However, the actual cell potential and operational efficiency can also be influenced by these pressure conditions. The activities in the Nernst equation (Eq. 1-6 and Eq. 1-7), which can be defined as the ratio of effective to standard concentrations, show the effect of pressure on the cell potential. At the cathode, when the hydrogen is collected at high pressure, the activity increases, which can slightly increase the cell potential required to sustain the reaction. However, commercial systems are designed to handle these conditions. Some commercial prototypes have been even reported to reach a value of 350 bar[24].

Hydrogen produced at high pressures is attractive to businesses or customers as it saves the compression energy to transport or store hydrogen. Nevertheless, elevated hydrogen pressures also pose a safety risk associated to hydrogen crossover. The permeation of hydrogen is a function of current density, pressure at the cathode and, as well as, membrane thickness. It is clear that the current density applied is directly proportional to the amount of gases produced during electrolysis which could lead to higher hydrogen crossover and hence, the associated risks of hydrogen crossover to the anode side[25]. For this reason, the typical operating current density for PEMWE is between 1.0 $A \cdot cm^{-2}$ and 3.0 $A \cdot cm^{-2}$. Generally, membranes are 50 µm to 175 µm thick but with a thinner membrane (50 µm), a current density of 19.0 $A \cdot cm^{-2}$ has also been reported by Lewinski et al.[26]. However, for such cases, the excess heat and degradation would decrease the life of the cell in the long term. Technically, there is not one fixed operating current density at which PEMWE could be operated. The minimum and maximum limit of current density is actually determined by the amount of gas crossover permitted and the overpotentials associated with higher current densities, respectively. There has to be a trade off between various variables, which calls for a continuous innovation in engineering solutions and design strategies.

1.2.3 Losses in PEMWE

In an operating PEMWE, overpotentials caused by kinetic barriers at the electrodes, ohmic resistance in the membrane and other components, and mass transport losses must be considered. These factors typically increase the actual operating voltage needed above the reversible potential, often to values around 1.80 to 2.20 V, depending on the current density and the efficiency of the system[18]. The total operating voltage,

$$V_{cell} = V_{rev} + \eta_{kinetic} + \eta_{ohmic} + \eta_{mt}\,, \tag{1-9}$$

is then defined as the sum of the reversible cell potential (V_{rev}), the kinetic overpotential ($\eta_{kinetic}$), ohmic overpotential (η_{ohmic}), and the mass transport overpotential (η_{mt})[27].

At low current densities (< 0.1 A·cm^{-2}), the kinetic losses (or overpotentials) of the oxygen and hydrogen evolution reactions dominate the cell performance, while other losses are not significant[27]. At medium current densities (between 0.1 A·cm^{-2} and 2.0 A·cm^{-2}), ohmic losses dominate cell performance[27]. The ohmic overpotential usually includes the membrane resistance, the PTL resistance, the resistance of the BPPs and the associated interfacial contact resistance.

At high current densities (> 2.0 A·cm^{-2}), mass transport losses become significantly more pronounced[27–29], The main reason for these losses at high current densities is attributed to the accumulation of oxygen gas at the anode. Gaseous oxygen that is generated at the CL is collected in the pore spaces of the PTL, hindering water transport. The results of the experimental work of Suerman et al.[28] show that the mass transport losses contribute between 20 % to 25 % to the total overpotential, and that these losses are mainly due to poor oxygen removal from the anode at higher current densities.

1.2.4 Role of PTL and the impact of its structure

On the cathode side, the produced hydrogen flows through the GDL to exit the system along with the water that is pushed to the cathode through the membrane due to the electro-osmotic drag. This results in a parallel flow configuration, which does not complicate the transport at the cathode. At the anode, where the OER occurs, the produced oxygen must leave the system against the flow of water through the PTL. Therefore, PTL plays a significant role in the overall efficiency of the system by transporting fluids to and from the CL.

In this context, a reduction in mass transport overpotential (η_{mt} in Eq. 1-9) serves as a measurable indicator of improved gas and liquid transport, especially at high current densities where limitations in oxygen removal and water supply become significant. PTL's ability to transport fluids strongly influences mass transport

overpotential[28], which is governed by fundamental principles e.g., Darcy's law for pressure-driven flow. In two-phase flow conditions, where both oxygen and water are present, the effective permeability of the PTL becomes dependent on the phase saturation, described by the relative permeability. As the gas saturation increases (e.g., due to oxygen accumulation), the relative permeability for liquid water decreases, limiting its transport and leading to mass transport losses and contributing towards η_{mt}. Additionally, the capillary pressure curves dictate how easily one phase displaces the other within the PTL. If the PTL has a steep capillary pressure curve, gas can become trapped near the CL interface, increasing local saturation and creating blockages. This affects both oxygen removal and water access, resulting in localized concentration gradients and, ultimately, increased η_{mt}. This means, changes in PTL transport properties such as permeability, saturation behavior, or pore structure can either alleviate or exacerbate mass transport overpotential. Therefore, electrochemical measurements of mass transport overpotential, typically extracted using Tafel slopes[28] or electrochemical impedance spectroscopy (EIS)[30], can be quantitatively correlated with PTL's design and transport parameters.

Beyond mass transport, PTLs also influence other sources of overpotential. For example, thermal conductivity is a key transport parameter that affects how efficiently the heat generated during operation is dissipated through the cell. Inadequate heat removal can cause local temperature increases, which may degrade CCM, indirectly affecting kinetic and ohmic losses. A PTL with good thermal conductivity can help maintain uniform temperature profiles, which supports stable membrane resistance and consistent reaction kinetics. Therefore, thermal conductivity, alongside permeability, should be considered a critical property when optimizing PTL materials for improved performance.

Moreover, the acidic environment provided by the sulfonic acid groups in PEM and the presence of oxygen, requires PTL to be corrosion resistant. In fuel cells, carbon materials are commonly used as PTLs but they cannot be applied for PEMWEs, as the conditions at the anode can lead to the oxidation of carbon and rapid corrosion of the material. The PTL should also have high electrical conductivity in order to transport electrons efficiently. Under differential pressure operations, PTLs play a big role in providing mechanical stability to the relatively fragile membrane as well. Material such as carbon felts would not withstand high differential pressures. Therefore, titanium PTLs are most commonly used in PEMWEs, which offer high specific strength, electrical conductivity and corrosion resistance in acidic environments[31]. In this work, whenever the term "PTL" is used, it refers exclusively to a PTL made of titanium.

To further enhance the electrical conductivity and, consequently, performance through reduction in ohmic losses, surface of the PTLs can even be coated with platinum, iridium or gold. This would ensure that the contact resistance between the PTL and CL does not increase with time, preventing a decrease in cell

performance[32]. Liu et al.[33] suggested that iridium, although rare and expensive, may be the most suitable material to coat PTLs with.

i) Material choices for PTLs

Sintered fiber and sintered particle PTLs are most commonly found in PEMWE literature[18,34]. Both types are manufactured via a sintering process, but the base materials and resulting structures differ, leading to variations in performance, durability, and application. Fiber-PTLs can offer a wide range of porosities (even up to 80 %) and higher permeability due to their larger and more open porous structure[35]. This allows for better water and oxygen transport through the PTLs. This can be advantageous at high current densities when mass transport issues dominate. Particle-PTLs, on the other hand, have lower porosities (25 % to 50 %) and smaller pore sizes (< 35 µm) leading to restricted flow paths[35–37]. In terms of mechanical strength, particle-PTLs have an advantage due to more rigid and compact structure[38], whereas fibers can be compressed and lose structural integrity with time. The compact and uniform structure of particle-PTLs also provide better contact resistance by offering a higher specific surface area[35]. This higher interfacial contact results in better utilization of CL and, consequently, better overall performance[36,39]. There are even a few studies[40,41] that have used titanium mesh as a PTL. However, it was shown by Steen et al.[41] that mesh PTLs are outperformed by fiber-PTLs due to poor contact with the CL.

ii) PTLs with a micro-porous layer

To enhance the contact and performance, an addition of micro-porous layer (MPL) on the PTL side facing the CL is suggested in literature[42,43]. The goal is to keep the contact resistances low without compromising the permeability of fluids significantly. MPLs can be introduced on both, particle and fiber-PTLs, in the form of small particles. In case of fiber-PTLs, a small-pore region, made of thinner fibers, at the CL side of the PTL can also be used as an MPL to improve the contact[44,45] (Figure 1-3).

Schuler et al.[42] prepared MPLs using titanium powder with different average particle sizes (5 µm, 17 µm, and 18 µm) on a particle-PTL, with a mean pore size of 33 µm, to improve contact area. They operated their cells at 2.0 $A \cdot cm^{-2}$ and showed a decrease in mass transport losses up to 50 % when compared to a PTL without MPL. Ernst et al.[43], used a particle-PTL substrate too, and fabricated an MPL on it using powder sintering. They operated their cells up to a current density of 6.0 $A \cdot cm^{-2}$. Their electrochemical impedance spectroscopy (EIS) results showed a 15 % reduction in high frequency resistance (HFR) value, which indicates improved contact and better conductivity.

Lettenmeier et al.[46,47] developed MPLs using vacuum plasma spraying (VPS). They showed that an MPL on a particle-PTL can increase the contact area with the CL,

which was depicted by the polarization curves (obtained for current densities up to 2.0 A·cm^{-2}. They also found that the optimal pore diameter in contact with the electrode should be between 6 µm and 11 µm and the porosity must be more than 22 %.

Figure 1-3: A PTL with two different fiber diameters (25 µm and 40 µm) manufactured by Sylatech GmbH, Germany. This PTL has thinner fibers (also smaller pore sizes) towards the CL intended for a better contact with CCM and larger pores towards the water inlet.

Other than PTLs with MPLs, the PTLs can be manufactured with graded porosity too. Lee et al.[48] investigated particle-PTLs with graded porosity, fabricated via VPS using two different titanium powder sizes (45 µm and 125 µm). They compared two configurations: One had low-porosity region towards CL and high-porosity region towards water channel, and the other with the opposite arrangement. Their results showed that with a low-porosity region at the CL side, the cell potential can be reduced by up to 29 %, the mass transport overpotential by 38 % and the gas saturation by up to 50 %, leading to better water uptake. They operated their cells at a current density of up to 4.5 A·cm^{-2}.

iii) <u>Impact of PTL thickness</u>

The direct influence of PTL thickness on performance is shown by a few studies using mesh and fiber-PTLs[40,41,49]. Li et al.[40] analyzed the impact of PTL thickness by using two titanium meshes with different thicknesses (0.2 mm and 0.3 mm) at a current density of 2.0 A·cm^{-2}. The results showed that the thinner PTL (0.2 mm) performed better than the thicker one (0.3 mm) with a minimum electrolysis voltage of 1.69 V obtained using the thinner mesh PTL.

Steen et al.[41] examined seven mesh and fiber-PTLs with different thicknesses up to a current density of 2.0 A·cm^{-2} and showed that PTL thickness plays an important role in the performance of the cell. The results showed that the use of thinner PTLs leads to the reduction of ohmic resistances (from 0.78 Ω·cm^{-2} to 0.47 Ω·cm^{-2}) and transport resistances (from 0.47 Ω·cm^{-2} to 0.38 Ω·cm^{-2}) and, consequently, improves performance (operating voltage reduced from 2.62 V to 2.14 V).

In a study by Mo et al.[49], focused only on fiber-PTLs, three different thicknesses (0.3 mm, 0.5 mm, and 1.0 mm) were investigated. Polarization curves and EIS

results suggest that a PTL with a thickness of 0.3 mm achieved the best performance compared to the thicker ones. At a current density of 2.0 $A \cdot cm^{-2}$, the cell voltage decreased from 2.41 V (obtained using a PTL with thickness of 1.0 mm) to 1.90 V, with a thinner PTL (0.3 mm thick).

iv) Impact of pore size and porosity

Schuler at al.[39] investigated fiber-PTLs with two different porosities (56 % and 76 %) and different fiber sizes (14 µm, 20 µm, and 50 µm) using GeoDict software and electrochemical experiments. They compared these PTLs to each other and to a particle-PTL with a porosity of 35 %. For the same fiber diameter, the permeability of 76 % PTLs was significantly higher (even up to 10 times). Their comparison with a particle-PTL, which had even lower porosity, showed that fiber-PTLs resulted in better transport properties, with permeability two orders of magnitude higher and diffusivity four times greater. They also argued that low-porosity PTLs have higher effective heat conductivity. They made these arguments by measuring the temperature difference across the PTL and CCM while operating electrochemical cells up to 4.0 $A \cdot cm^{-2}$. Temperature differences of up to 5 K and 22 K were reported for low-porosity and high-porosity PTLs, respectively. This can be crucial for heat management, particularly when thicker membranes are used, which generate more heat due to higher resistance. The greater temperature difference for high-porosity PTLs was explained by their low thermal conductivities. The low-porosity PTLs had an average conductivity of 5.4 $W \cdot m^{-1} \cdot K^{-1}$ and high-porosity PTLs had an average value of 2.1 $W \cdot m^{-1} \cdot K^{-1}$. At a current density of 1.0 $A \cdot cm^{-2}$, identical temperature increases of 5 K were reported.

Ito et al.[50] experimentally investigated the effects of changes in the pore structure of the PTL on PEMWE performance with different fiber-PTLs. They examined two PTLs with same fiber diameter (20 µm), and different porosities (50 % and 75 %), and showed that PTL with 50 % porosity provides better results, attributing it to a better contact between PTL and CL. Grigoriev et al.[37] compared various particle-PTLs with different porosities (between 28 % and 40 %) and pore sizes (between 8 µm and 100 µm). They reported that the porosity has no significant influence on PEMWE performance for operations at current densities up to 2.0 $A \cdot cm^{-2}$. In another study, Steen et al.[41] investigated the effect of porosity of mesh and fiber-PTLs. The results showed that at the same thickness, a reduction in the porosity of PTL leads to an improvement in performance due to the increase in the contact area between the PTL and the CL. They also showed that a small pore size towards the CL side is important to have an improved contact with CCM.

Majason et al.[51] investigated the influence of the microstructure of two particle-PTLs with different parameters on the performance of PEMWE by combining ex-situ and in-situ methods. The PTLs with a smaller pore diameter (16 µm) and a porosity of 34.3 % were designated as SP-PTL and those with larger pore diameter (60 µm) and a porosity of 32.7 % as LP-PTL. It was concluded from the polarization curves

that the SP-PTL has better performance (200 mV difference) than the LP-PTL at current densities between 0.1 A·cm^{-2} and 3.0 A·cm^{-2}). However, at a current density greater than 3.0 A·cm^{-2}, the mass transport resistance was slightly greater in SP-PTL. In addition, the ohmic resistance of the SP-PTL was significantly lower at all current densities. They argue that larger pore diameter of LP-PTL can improve fluid transport and permeability, but other properties such as tortuosity, contact resistance and pore size distribution (PSD) can still be counteractive.

1.2.5 Modeling transport in PTLs

The transient behavior of a real PEMWE cell can be best described by a continuum model (CM) and, for this reason, such models are of significant interest. However, fluid transport through PTLs is not well addressed in such models and is often simplified. Either the geometry of the PTLs is simplified, or correlations such as Leverett equation (LE) or Brooks-Corey equation (BCE) are used, none of which is specifically derived for fiber- or particle-PTLs. For instance, combining Fick's law with the Nernst equation can be used to predict the mass transport losses due to the blockage of reaction sites at the CL, as done by Marangio et al.[52]. While such models are easy to implement, they assume homogeneity throughout the PTL and, therefore, fail to capture the microscopic heterogeneity of the PTL. As a result, they do not provide detailed insights into the impact of local fluid transport in PTLs on a PEMWE. In another study, by Oliviera et al.[53], a PTL structure was simplified to three cylinders to reduce the modeling effort of a CM. Such simplifications do not by far represent the microscopic heterogeneity of PTLs. Similarly, in the cases of LE and BCE, homogeneity across the porous media is assumed, and these equations do not explicitly consider pore-scale interactions and connectivity. These correlations are mainly derived from drainage and imbibition in soils and rock formations, and as such, they may not be easily applicable to other materials. For instance, according to Brooks et al.[54], a system under consideration (e.g. PTL in this case) needs to be similar to the ones studied by them, for the correlations to be scalable. The similarity, as stated in their work, lies in the macroscopic boundary conditions as well as the PSD index, which is measured using the capillary pressure curve. A higher PSD index indicates a narrower PSD, resulting in a flatter capillary pressure curve, and vice versa. According to them, naturally occurring sands usually have a high PSD index compared to engineering prototypes, and the boundary conditions across a PTL in PEMWE and sands studied in their work are of great difference.

Various imaging techniques can also be used as a starting point to model transport in PTLs and extract transport parameters[55]. Usually, micro-computed X-ray tomography (micro-CT) imaging is able to clearly capture the skeleton structure and voids within the porous material[56]. Once a 3D image stack is obtained, it goes through an image processing work flow, after which it can be used to run simulations directly within the structure[55]. This gives a very clear insight on the transport and flow properties of a material. The challenge in such techniques is the

availability of computational power because this puts a limit on the domain size to be investigated. For example, solving the Navier-Stokes equation using any computational fluid dynamics (CFD)[56] platform within just a few hundred pores can be very computationally intensive and time consuming. Although the achievable accuracy through such simulations can be quite high, the domain size must be compromised based on the available computational effort. Similarly, the lattice Boltzmann method (LBM) can be used for modeling multiphase flows in complex porous geometries such as PTLs too[57], but the requirement of computational resources is quite high for LBM simulations as well.

Pore network models (PNMs) offer a discrete approach to model transport within PTLs at a relatively low computational cost. PNM is a powerful computational technique used to simulate and study the behavior of fluids in porous media. It has been widely applied in fields like geosciences[58], process engineering[59–61], and materials science[62–64], due to its ability to provide insights into the transport properties of complex porous materials e.g. rocks, soils, membranes, etc. In principle, PNM represents the pore space of a material as a network of interconnected pores and throats. It offers numerous advantages that make it an effective tool for various applications:

- *Simplification of complex systems:* One of the main benefits of PNM is that it simplifies the complexity of real porous media by reducing the complex geometry into a simple network model[55]. Though the actual pore space may consist of irregular shapes and connectivity, PNM helps to represent this complexity in a structured, computationally feasible way.

- *Microscopic insight into macroscopic behavior:* PNM provides a direct connection between the microscopic porous structure and the macroscopic behavior of the porous material[59]. By modeling fluid flow and transport at the pore scale, PNM is able to predict large-scale phenomena, such as permeability of the material. This makes it an effective tool for understanding how changes in microstructure can affect material properties.

- *Computational efficiency:* Compared to literature approaches or direct numerical simulations (DNS) that solve complex partial differential equations on finely discretized space, PNM offers significant computational efficiency[65]. It requires less processing power, allowing for the simulation of larger domains or longer time scales without compromising accuracy as much, compared to generalized correlations.

- *Ease of parametric studies:* Once a PNM is constructed (or reconstructed), it is relatively simple to conduct parametric studies. Factors such as PSD, pore sizes, and thickness can be varied to observe how these changes impact the overall behavior of the system. This is particularly useful for optimizing materials for practical applications.

- *Integration with experimental data:* PNM can be combined with experimental data (such as porosity or wettability measurements) to calibrate and validate

the models[66]. This allows for more accurate predictions and a much better understanding of the materials being analyzed. Conversely, PNM can also complement experimental data by providing insights that are difficult to gain experimentally, such as microscopic flow distributions.

On the other hand, despite its advantages, PNM has certain limitations too:

- *Simplifications and assumptions:* The simplified representation of a complex porous structure using e.g., spherical pores, may overlook certain complexities of the material. For instance, pores may have highly irregular shapes, or interfaces, which are difficult to capture in a simplified PNM[67].
- *Dependence on high-quality imaging:* In some cases, e.g., for extracted PNs, PNM relies on accurate data, often obtained through high-resolution imaging techniques like micro-CT or even scanning electron microscopy (SEM)[67]. Limitations in resolution or image processing can lead to inaccuracies in PNM as well.
- *Difficulty in capturing dynamic effects:* Although PNM is quite suitable for simulating steady-state or quasi-static processes, it may be challenging to simulate dynamic phenomena, such as rapid fluctuations in pressure, phase transitions, or chemical reactions over very short time scales, in a computationally efficient way.

Generally, the development of a PNM involves, primarily, three main steps:

1) *Network extraction:* The first step involves obtaining a network that represents the structure of the porous medium to be analyzed. This can be done using image-based extractions[55], stochastic PN generation[68] or idealized PN lattice constructions[67].
2) *Geometric representation:* Pores and throats are assigned geometric parameters such as radius, volume, length, etc. These parameters are then used for modeling flow and transport processes.
3) *Modeling of flow and transport:* The governing physics for fluid dynamics (e.g., Hagen-Poiseuille equation) are applied to simulate flow through a PN[60]. Parameters, such as permeability, capillary pressure curve[66] and gas-liquid saturations[69] are then extracted.

To generate PNs, various methods can be employed depending on the type of porous material, the required level of detail, and the availability of data/resources. The primary methods used in PN generation are as follows:

- *Image-based PN extraction:* This method involves extracting a PN directly from high-resolution 3D images of a porous material. These images show the internal structure of a material, including the distribution and connectivity of voids. Thresholding of grayscale image is then used to differentiate between solid and void spaces, followed by segmentation techniques to identify different regions and their connectivity. From the segmented image,

pores and throats are identified and assigned geometrical properties (e.g. radius, length, shape, etc.). The result is a PN that represents the porous structure within a material referred to as an extracted PN. The advantage of extracted PNs is that they capture the actual microstructure and connectivity, providing a more accurate representation of the material's properties. On the other hand, high-resolution imaging can be quite expensive and time-consuming, and there may be limitations in capturing fine details of smaller voids.

- *Stochastic PN generation:* In this method, the PN is generated based on statistical descriptions of the PSD, throat size distribution (TSD), and pore connectivity. Rather than using direct imaging data, the network is created using probabilistic rules and distributions that represent the overall characteristics of the porous medium. The main advantage is that it allows for generating PNs for materials where direct imaging is not available or feasible. But, since these are not extracted from an actual structure, the generated network may not capture complex features of the real material. The statistical generation can sometimes oversimplify the geometry and connectivity of the pore space, which can affect the accuracy of simulations.

- *Idealized lattice networks:* In idealized lattice networks (or idealized PNs), the porous medium is represented by a network of pores arranged in a structured grid (e.g., cubic lattice). This approach is based on idealized assumptions and does not aim to capture the exact structure of a real porous medium but rather provides a simplified framework for understanding flow and transport properties. It is less demanding computationally and easy to implement, making it useful for understanding basic principles of flow and transport in porous media. Even though the idealized PNs oversimplify the structure of porous media, which can lead to inaccurate predictions of transport properties, they can be adjusted to represent the extracted PNs and used to predict transport parameters.

- *Voronoi tessellation-based networks:* Voronoi tessellation is a mathematical technique used to discretize space into regions based on a set of seed points (pore centers). In the context of PN generation, Voronoi tessellation can be used to create a VN of pores by placing seed points (nodes) in a 2D or 3D space. Each Voronoi cell represents the region closer to its corresponding seed than to any other seed. The centers of the Voronoi cells represent pores, and the edges between adjacent cells define the connections (throats), thorough which fluid can flow between pores. Voronoi tessellation can generate irregular, realistic PNs that represent the randomness of natural porous materials. The method allows for control over the number of seed points and their arrangement, leading to customizable network structures too.

With respect to PTLs, PNMs can provide valuable insights into the behavior of oxygen drainage profiles through the PTL by simulating simplified two-phase

capillary flow through a PN representing a PTL. However, no PNM of fiber-PTLs exists in literature. Although there are a few studies available on extracted PNs for fiber-GDLs[55,70,71]. In addition to these, a study about a novel PTL design with fine titanium powder layered on to a titanium mesh exists by Stiber et al.[72], which also used extracted PNs from micro-CT images. They used a PNM to obtain the drainage curves and permeabilities of the PTL. Additionally, in two studies by Lee at al.[68,73], extracted PNs were used for PTLs, but they were derived from stochastically generated particle-PTL structures and not for fiber-PTLs.

All in all, among the various modeling approaches, PNMs hold significant promise for advancing the understanding of transport in PTLs. The key advantage of PNMs lies in their ability to capture the detailed structure of the PTL, including PSD, pore connectivity, and heterogeneity. PNMs are also relatively efficient in terms of computational resources compared to LBM or CFD simulations. The experiment-based literature correlations (e.g., BCE) are computationally efficient too, but they lack the granularity required to model local phenomena such as the role of pore connectivity in transport. An overview of various methods used to predict/model transport in PTLs is provided in Table 1-1. By contrast, PNMs strike a good balance between computational efficiency and accuracy. Another important feature of PNMs is their ability to be combined with large-scale CMs. This hybrid approach using PNMs to inform CMs can provide a powerful tool for modeling PEMWEs.

Table 1-1: Overview and comparison of different methods used to model/predict transport in PTLs. Key advantages and limitations of each method are summarized to highlight trade-offs between accuracy, computational cost, and structural representation[74–80].

	PTL parameters	Pros	Cons
PNM	Capillary pressure curve; saturation profile; absolute and relative permeability; thermal conductivity.	Captures pore-scale heterogeneity and connectivity; low computational costs.	Simplified pore/throat geometry; requires microstructural data; not suitable for fine-scale physics.
CFD	Capillary pressure curve; saturation profile; absolute and relative permeability; thermal conductivity.	High accuracy; detailed flow/thermal field information; can model complex geometries and multi-physics.	High computational cost; requires detailed geometry; less suited for large-scale systems.
LBM	Capillary pressure curve; saturation profile; absolute and relative permeability; thermal conductivity.	Efficient for complex boundaries/shapes; inherently parallelizable; can handle multiphase and transient flows in detail	High computational cost; requires fine grids for accuracy; less mature than CFD for some applications.
LE	Capillary pressure curve.	Simple, easy to apply; requires few parameters; good for average behaviour estimation.	Empirical nature; assumes homogeneous media; limited accuracy for heterogeneous materials or complex structures.
BCE	Capillary pressure curve.	Simple yet flexible; accounts for PSD; widely validated for several applications.	Empirical nature; requires fitting to experimental data; assumes uniform pore geometry.

1.2.6 Experimental characterization methods

Several experimental techniques have been employed to study the impact of mass transport in PTLs on electrochemical performance. Electrochemical techniques such as EIS, limiting current density analysis, and Tafel plots are commonly used to quantify mass transport overpotential in PEMWEs. These methods provide valuable quantitative data on transport limitations by analyzing cell polarization, diffusion resistance, and reaction kinetics under different operating conditions.

For example, EIS can separate ohmic, kinetic, and mass transport resistances by analyzing the frequency-dependent response. By fitting equivalent circuit models, transport-related impedance components can be isolated and linked to PTL properties like porosity and permeability[30]. In addition to EIS, limiting current density analysis has been widely employed to assess mass transport constraints. This method determines the maximum current density at which reactant (water) can be transported through the PTL before concentration polarization limits performance[81]. However, electrochemical methods infer the impact of PTLs on mass transport indirectly, often assuming that observed limitations stem primarily from the PTL structure without spatially resolving the gas-liquid distribution or water pathways. This indirect approach can lead to ambiguous interpretations, as mass transport losses may also originate from CL flooding, membrane dehydration, etc.

In contrast, in-operando imaging techniques (e.g., neutron imaging) enable direct visualization of gas-liquid distribution within PTLs under realistic conditions. Such spatially resolved data allows to observe exactly how PTL microstructure influences transport, revealing preferential flow paths, stagnant zones, and local gas entrapment that cannot be captured by electrochemical data alone. This direct insight is critical for linking PTL design to mass transport within, reducing reliance on assumptions.

Most imaging approaches are based on 2D in-plane imaging of the whole PEMWE or of microfluidic cells that capture only the mass transfer at the anode side[82–84]. In-plane means that the cross-section of the PTL between water flow channel and CL is visualized (Figure 1-4). From this, the accumulated information about the distribution of gas along the depth of the PTL is obtained (y-axis in Figure 1-4).

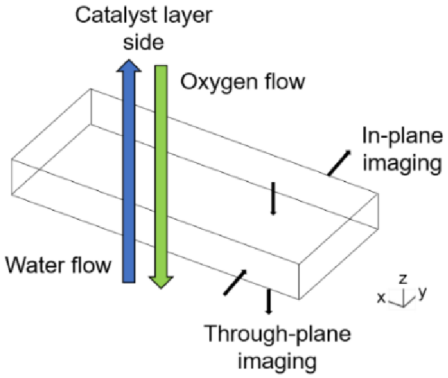

Figure 1-4: In-plane and through-plane orientations used for visualizing PTLs in PEMWEs using different imaging techniques.

With through-plane imaging[85,86], the PTL is visualized through the xy-plane, thus accumulating the gas and liquid distribution across the z-axis (Figure 1-4). In contrast to in-plane studies, this visualization allows to investigate the spatially distributed break-through of oxygen along the water flow channel.

In several imaging-based studies, gas-liquid distributions are observed to be independent of the operating parameters. For example, Satjaritanun et al.[56] used micro-CT to study the oxygen pathways through the PTL in a PEMWE that was operated at 1.0 A·cm^{-2} and 4.0 A·cm^{-2}. Although, they used two carbon paper GDLs as a PTL. The porosity profile showed an average porosity of the PTL between 30 % and 40 %. They observed that oxygen takes certain preferential pathways through the PTL regardless of the water flow rate and current density. Similarly, using a PEMWE with an active area of 1 cm^2 and in-plane configuration (operating temperature 50 °C and pressure 2 bar), Seweryn et al.[83] found that the distribution of oxygen and water is unaffected by the flow variations and current densities from 0.1 A·cm^{-2} to 2.5 A·cm^{-2}. They used a particle-PTL with a porosity of 30 % and thickness 1.2 mm. Additionally, no water scarcity in the PTLs was reported. Selamet et al.[86] investigated two-phase transport using through-plane neutron imaging in PEMWEs. They performed experiments at lower current densities (0.1 A·cm^{-2} and 0.4 A·cm^{-2}) and at two different temperatures (25 °C and 40 °C). They used a 1.0 mm thick fiber-PTL with a porosity of 44 %. They showed that the water distribution was impacted by the proximity to the inlet and outlet channels as well as gravity and buoyancy forces. Furthermore, they observed the periodic release of gas bubbles from the same spots during the operation. At the same time, they also showed that various stagnant regions exist in the PTL, which do not contribute to the imbibition of water.

Zlobinski et al.[87] explored the impact of various current densities (0.1 A·cm^{-2} to 2.0 A·cm^{-2}) and pressure conditions (1 bar to 8 bar) in a PEMWE at a constant temperature of 50 °C. They used a particle-PTL with 35 % porosity and 1.0 mm thickness. They showed that the flow within the PTL is completely capillary-driven and that the increased mass transport losses might possibly be due to the interface between the PTL and CL. This outcome was explained with independence of saturation profiles inside the PTL on current density and pressure variations. They concluded that hydrophobic regions in the PTL actually prevent the complete wetting of the PTL and hence promote the gas pathways, while also leading to local gas entrapments. This was confirmed in Panchenko et al.[84], where various stoichiometries (ω), between 95 and 1037 were realized in a non-electrochemical cell using a particle-PTL to investigate the gas-liquid distribution. They defined stoichiometry as the ratio of the volume of inlet water supplied to the volume consumed by the water-splitting reaction. It was found that gas bubbles always exit from the same location, independent of the flow conditions, and that 37 % of the pore volume could not be wetted by water.

In contrast to these examples, other works found PTL invasion and gas-liquid distribution to depend on flow conditions. For example, Maier et al.[85] demonstrated that increasing current density can decrease the water thickness in the PTLs. They

combined micro-CT and neutron radiography to investigate the structural dependence of mass transport in PTLs. They used a PEMWE with a through-plane configuration to compare three different PTLs. They used one particle-PTL with 30 % porosity and 2.0 mm thickness, and two fiber-PTLs: one with 47 % porosity and 1.0 mm thickness, and one with 77 % porosity and 0.1 mm thickness. The PEMWE was operated up to 1.5 $A \cdot cm^{-2}$ and with an inlet water temperature of 50 °C. Moreover, their study showed significant inhomogeneity in water thickness across the active area of the PTL i.e., water thickness was higher where the flow velocity was higher in the flow channels and vice versa. This showed a connection between the flow channel geometry and the two-phase flow in the PTL. They reported that a major volume of pores remained unused during operation due to the poor water intake of the PTLs and suggested that much more work should go into the design of novel PTLs which can increase the pore utilization.

Panchenko et al.[88] reported that at higher current densities the oxygen produced is not drained properly and blocks the pathway of water to the CL. They operated their PEMWE between 0.1 $A \cdot cm^{-2}$ and 1.0 $A \cdot cm^{-2}$ and used particle-PTL at the anode. This was confirmed by Lee et al.[82,89], who applied current densities between 2.0 $A \cdot cm^{-2}$ and 9.0 $A \cdot cm^{-2}$ and used a particle-PTL with 35 % porosity, 0.25 mm thickness, and an active area of 0.8 cm^2. They reported that especially at high current densities, the gas accumulates at the CL and blocks water pathways. They found that gas accumulation led to a 6 % increase in the overpotential of the PEMWE[89]. To mitigate the water starvation issue, Panchenko et al.[88] suggested to use a stoichiometry value greater than 100.

A comprehensive overview of neutron imaging experiments, highlighting the lack of a clear understanding regarding the influence of different operating conditions and PTL materials, is provided in Table 1-2. It also reveals a notable scarcity of studies focusing on fiber-based PTLs in the current literature.

Table 1-2: Summary of neutron imaging experiments used to visualize mass transport in PTLs, highlighting PTLs used, operating conditions, and key findings.

Source	Cell and orientation	PTL specifications	Operating conditions	Key findings
Lee et al.[82]	Electro-chemical; in-plane.	Particle-PTL; 35 % porosity; 0.25 mm thick.	2.0 – 9.0 $A \cdot cm^{-2}$.	Gas accumulation at CL blocks water pathways at high current densities.
Seweryn et al.[83]	Electro-chemical; in-plane.	Particle-PTL; 30 % porosity; 1.2 mm thick.	0.1 – 2.5 $A \cdot cm^{-2}$; 50 °C; 2 bar.	Oxygen and water distribution unaffected by flow and current variations; no water scarcity.
Panchenko et al.[84]	Non-electro-chemical; in-plane.	Particle-PTL; 49 % porosity; 0.8 mm thick.	-	Gas bubbles exit from same locations; water starvation in PTL; recommend high stoichiometries.
Maier et al.[85]	Electro-chemical; through-plane.	Particle- and fiber-PTLs; 30 – 77 % porosity; 0.1 – 2.0 mm thick.	0.1 – 1.5 $A \cdot cm^{-2}$; 50 °C.	Under utilization of pore volume for both PTL types; decreasing water thickness with increasing current density
Selamet et al.[86]	Electro-chemical; through-plane.	Fiber-PTL; 44 % porosity; 1.0 mm thick.	0.1 – 0.4 $A \cdot cm^{-2}$; 25 – 40 °C.	Stagnant regions in PTLs exist; periodic release of bubbles in the channel; water distribution in PTL impacted by channel geometry.
Zlobinski et al.[87]	Electro-chemical; in-plane.	Particle-PTL; 35 % porosity; 1.0 mm thick.	0.1 – 2.0 $A \cdot cm^{-2}$; 50 °C; 1 – 8 bar.	Fluid distributions unaffected by current density and operating pressure; capillary-dominated flow in PTLs.
Pancehnko et al.[88]	Electro-chemical; through-plane.	Particle- and fiber-PTL; 54 and 55 % porosity; 0.5 and 1.0 mm thick.	0.1 – 2.0 $A \cdot cm^{-2}$; 80 °C;	Higher stoichiometries can aid gas removal in both PTL types; membrane dehydration due to hindered transport through PTLs.

1.3 Scope and outline

Although various modeling approaches and imagine techniques (like micro-CT and neutron imaging) have made it easier to study mass transfer through PTLs, several questions about the influence of PTL structure on the mass transfer within remain unresolved. The available literature on the topic leaves the current understanding unclear, particularly because various studies often contradict with each other and cannot be directly compared. This is mainly because the studies differ significantly in experimental conditions, materials used or cell designs. Specifically, it remains uncertain how PTL structural properties should be optimized to enhance water/oxygen transport through the PTL. So far, no definitive recommendations exist for tailoring PTL structures to enhance mass transport. In fact, many studies overlook the influence of structure completely. A few studies that do compare different PTLs focus mostly on PTLs with different porosities and rarely on PTLs with different PSDs, gradients and thicknesses.

Moreover, it is observed that most of the PTL literature is fuel cell oriented. The materials inspected are not specific to PEMWE applications and there is no consistent pattern observed in the thickness, porosity and type of the PTLs used. Most of the studies cited in Section 1.2 are also based on low-porosity particle-PTLs rather than fiber-PTLs. In author's knowledge, for industrial applications, fiber-PTLs are most commonly used. However, the fiber-PTLs mentioned in literature are never directly compared with PTLs with the same porosity and different porous structure – to study the impact of PTL structure. Especially in the case of high-porosity PTLs (> 60 %), different thickness and porous structures have not been studied at all. This is not only true for ex-situ/in-situ imaging studies or electrochemical experimental studies but also for model-based studies. Even the data available to parameterize the CMs with high-porosity fiber-PTL characteristics is quite scarce. On the other hand, it is quite abundant for low-porosity PTLs and particle-PTLs. Additionally, approaches such as PNM have never been used specifically for fiber-PTLs to extract their transport parameters using extracted or idealized PNs. The existing models use correlations, such as LE, to parameterize the CMs.

The lack of available data on fiber-PTLs (especially high-porosity ones) becomes a motivation to study them experimentally and by PNM. PNM can be used to extract the capillary pressure curves, saturation profiles and transport parameters such as permeability. The alternate to acquiring these parameters are computationally expensive CFD or LBM based approaches or experimental correlations mostly derived using geological porous media. This leaves a gap that could be covered with extracted PNMs which provide a good balance between computational efficiency and accuracy. In this work, for the first time, a pore scale study of structure-transport correlation based on various commercial fiber-PTLs with different structures is shown. Primarily, three PTLs are chosen with approximately 70 % to 80 % porosity with two of them having a pristine thickness of 1.0 mm and one of them 0.5 mm. One of the two thicker PTLs has a graded structure with two different fiber diameters. Such a PTL is used to study the influence of microstructure

and not just the bulk porosity of the PTL. This is the first time that extracted PNs are used to retrieve the transport coefficients of high-porosity PTLs, which can be used in CMs. The same PTLs are then also used in neutron imaging experiments of flow cells to visualize the structural dependence of flow patterns through PTL using different flow conditions. In addition, neutron imaging experiments using electrochemical cells with PTLs of different porosities (77 % and 42 %) are conducted to further observe the impact of operating conditions on fluid distributions within the PTLs.

First of all, in Chapter 2, PNM is explained. This includes the drainage algorithm and model assumptions used for idealized and extracted PNMs. For the extracted PNs, reconstruction of PNs from micro-CT scans with the help of an image processing workflow is explained. Computation of permeability through the PN is shown in this chapter along with the computation of thermal conductivity using a Voronoi network (VN). In this chapter, neutron imaging experiments are explained too. The experiments were performed in non-electrochemical cells, in a setup similar to a Hele-Shaw flow cell, and in electrochemical cells. The cell design, materials used, experimental setup, and image processing steps to obtain information about the water thickness in the PTLs from the raw images are explained in detail.

In Chapter 3, first, the PNM is validated using a microfluidic network that represents flow through PTLs, along with LBM and CFD simulations. Secondly, the results of drainage simulations on extracted PNs from commercial PTLs are presented. Parameters such as permeability, capillary pressure curves, and thermal conductivity are extracted and compared with experiments and correlations from literature. In the end, a comparison between regular and extracted PNs is drawn.

In Chapter 4, idealized PNs are used to perform simulations using data from the literature. Various PTLs from the literature are simulated and comparisons are made between the invasion patterns of different PTL structures. The results of these simulations highlight the impact of structure on the gas-liquid distribution through the PNs. PTLs with a graded structure, most commonly a low-to-high pore/throat size gradient, are analysed with the help of idealized PNs and, other arbitrary gradients and pore/throat size gradients are analyzed too.

In Chapter 5, the results of in-situ neutron imaging experiments are discussed to gain further insights on the role that PTL structure could play on PEMWE performance. This is done using the through-plane images obtained from non-electrochemical flow cells. The usage of a non-electrochemical cell reduces the number of components, and hence the quality of images. The size of the region of interest (ROI) and the image quality is also compromised when using electrochemical cells. The break-through points of each PTL are observed and the time needed for the gas to build up pressure and break-through different PTLs is compared. Additionally, tomography data obtained from neutron imaging are used to visualize different states of the PTL during invasion processes and to compare the water uptake and retention of different PTLs. Moreover, the experiments help

in validating some assumptions made for PNM and, as well as, provide insights for improvements. With the help of neutron imaging of electrochemical cells, the saturation and water-thickness profiles of PTLs with different porosities are shown too. This is obtained for current densities up to 9.0 $A \cdot cm^{-2}$ and its influence on PTL saturation is observed. The discussion also presents a comparison of both experiments, examining which aspects of real-cell behavior can be captured by a non-electrochemical setup, and outlining the limitations of each method.

Lastly, in Chapter 6, the conclusion of the thesis is presented. This includes a summary of the research carried out and the key findings derived from it. Additionally, an outlook is provided, outlining possible improvements and potential directions for future research based on the insights gained throughout the thesis.

Chapter 2
Pore Network Modeling and Experimental Methods

Parts of this chapter have been published in:

i) Vorhauer, N.; Altaf, H.; Tsotsas, E.; Vidakovic-Koch, T. Pore network simulation of gas-liquid distribution in porous transport layers. *Processes* 2019, *7* (9), 558. DOI: 10.3390/pr7090558.

ii) Altaf, H.; Vorhauer, N.; Tsotsas, E.; Vidaković-Koch, T. Steady-state water drainage by oxygen in anodic porous transport layer of electrolyzers: A 2D pore network study. *Processes* 2020, *8* (3), 362. DOI: 10.3390/pr8030362.

iii) Vorhauer-Huget, N.; Altaf, H.; Dürr, R.; Tsotsas, E.; Vidaković-Koch, T. Computational optimization of porous structures for electrochemical processes. *Processes* 2020, *8* (10), 1205. DOI: 10.3390/pr8101205.

iv) Altaf, H.; Miličić, T.; Vidakovic-Koch, T.; Tsotsas, E.; Arlt, T.; Kardjilov, N.; Manke, I.; Vorhauer-Huget, N. Neutron imaging experiments to study mass transport in commercial titanium felt porous transport layers. *Journal of Electrochemical Society* 2023. DOI: 10.1149/1945-7111/acd7a8.

v) Altaf, H.; Miličić, T.; Faber, F.; Vidaković-Koch, T.; Tsotsas, E.; Vorhauer-Huget, N., Use of reconstructed pore networks for determination of effective transport parameters of commercial Ti-felt PTLs, *Processes* 2025, *13*(4), 943. DOI: 10.3390/pr13040943.

In this chapter, PNM is introduced, covering the model assumptions, drainage algorithm and micro-CT-based reconstruction of extracted PNs. The extraction of parameters such as permeability, thermal conductivity, etc., is explained. This is followed by a detailed description of neutron imaging experiments, including the cell design, materials used and experimental setup. Non-electrochemical experiments, using a flow cell, visualize through-plane water distribution in three different PTLs with similar porosities, whereas electrochemical experiments explore PTLs with different porosities, capturing in-plane images to study gas-liquid distributions. The chapter also describes how raw images undergo a series of image processing steps to extract information about water thickness in the PTLs.

2.1 Pore network modeling

2.1.1 General model assumptions

PNMs are generally distinguished between quasi-static and dynamic models[90]. For the simulation of the steady-states in capillary dominated applications[91,92], quasi-static models are used. Zlobinski et al.[87] reported that viscous forces are negligible in the two-phase flow in PTLs. They calculated the capillary numbers ($10^{-8} < Ca < 10^{-6}$) and viscosity ratios ($10^{-2} < Vi < 10^{-1}$). According to the flow regimes defined by Lenormand[93] and Zhang et al.[94], such low Ca and Vi values occur in the capillary dominated regimes, instead of viscous fingering or compact displacement dominated regimes. From this, it is deduced that the transport in PTLs occurs by capillary fingering. A transition to another invasion regime depends on the fluid properties, flow rates and the heterogeneity of the porous material[92]. For example, a homogenously-structured material could promote a transition to other flows regimes. Such effects are observed in the research of drying of PNs, where sufficiently narrow PSDs can result in stable, i.e., viscosity-dominated invasion[60]. When viscosity comes into play, the width of the invasion front scales with the capillary number. For PTLs, generally heterogenous, it is then assumed that the entry capillary pressure of voids controls the displacement of liquid (drainage) or gas (imbibition) in PTLs[95]. For this reason, viscous forces are neglected. This means that any type of displacement in the PTL is considered to be dependent on the radius distribution of the voids and is influenced by the structure of the PTL alone. Additionally, the gravitational forces are assumed to be negligible too.

Based on experimental findings reported in literature[86–88], it is assumed that liquid and gas transport occurs simultaneously around constant average gas-liquid saturations in PTL. These saturations are between the break-through saturation and the water-disconnection or residual liquid saturation. This means, drainage-based invasions are computed until the first gas break-through, and break-through saturations are reported. In addition to that, invasion is continued until complete disconnection of water across the height of the PN, at which point no further invasion can occur. This represents the minimum possible liquid saturation corresponding to limiting current densities.

In terms of void space, spherical pores and cylindrical throats are assumed. This is based on the studies focusing on fibrous media. Wang et al.[96] studied fibrous materials and the effect of geometric properties on the extraction of PNs. Their results showed that, despite the geometric approximation to spheres and cylinders, PNM provides a very good estimation of surface area and void space volume. In another study of fibrous porous media, Huang et al.[97] validated the PNMs using LBM simulations. They extracted the pore sizes from the images using inscribed maximal ball, area-equivalent radius, and a shape factor. They used all three methods and LBM to plot a relative permeability curve with non-wetting phase saturation. The results showed a good agreement in magnitude and trend between all three methods and LBM for predicted curves.

Moreover, the pores at the bottom side of the network are interpreted as water sources as they represent the connection links to the water inlet channel. Conversely, all pores at the top side of the PN (Figure 2-1) are assumed to be connected to the oxygen sources inside the CL at the anode side of the electrolyzer and directly supplied with gaseous oxygen. All of the pores, except the ones supposed to be connected to the oxygen source, are assumed to be saturated with water before the drainage starts.

2.1.2 Pore network geometry and reconstruction

In this work, 3D extracted and 3D idealized PNs are primarily used, while 2D idealized PNs are occasionally employed for simpler visualization. (Figure 2-1).

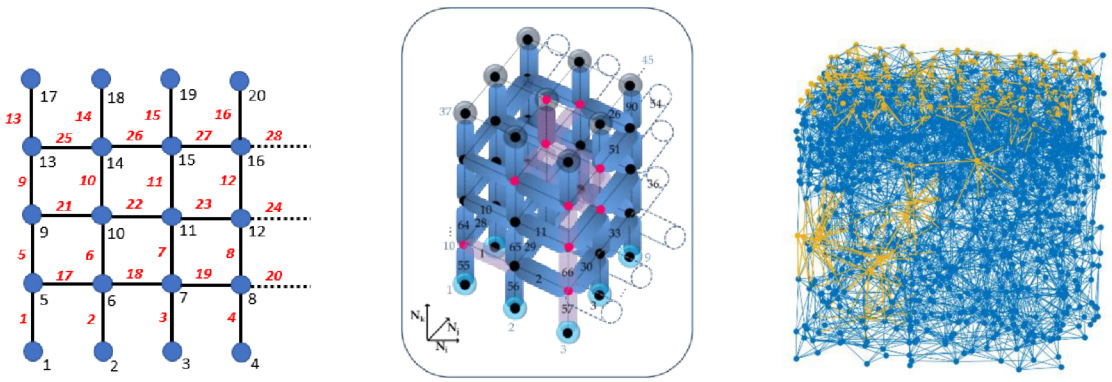

a) b) c)

Figure 2-1: a) Labeling of pore and throats in a 2D idealized PN, reproduced from Altaf et al.[98], under the Creative Commons Attribution 4.0 International License (CC BY 4.0); b) labeling in a 3D idealized PN, reproduced from Vorhauer et al.[99], under the Creative Commons Attribution 4.0 International License (CC BY 4.0); c) an extracted PN, highlighting the irregular distribution of pores and throats.

The information about the connections between the pores and throats in the network are stored in matrices. This means that the geometric arrangement of pores and throats and the neighbor relations are specified by the different matrices, e.g., *pnp* contains pores' information regarding neighboring pores, *tnt* contains throats' information regarding neighboring throats, and similarly for *tnp* and *pnt* also.

Exemplarily, the following equation matrices are based on the idealized 3D PN shown in Figure 2-1b.

$$pnp(\text{pore } 10) = \begin{bmatrix} \vdots & \vdots & \vdots & \vdots & \vdots & \vdots \\ 1 & 11 & 12 & 13 & 16 & 19 \\ \vdots & \vdots & \vdots & \vdots & \vdots & \vdots \end{bmatrix}, \tag{2-1}$$

$$tnp(\text{throat } 1) = \begin{bmatrix} 10 & 11 \\ \vdots & \vdots \end{bmatrix}, \tag{2-2}$$

$$pnt(\text{pore } 10) = \begin{bmatrix} \vdots & \vdots & \vdots & \vdots & \vdots & \vdots \\ 1 & 3 & 28 & 34 & 55 & 64 \\ \vdots & \vdots & \vdots & \vdots & \vdots & \vdots \end{bmatrix}, \tag{2-3}$$

$$tnt(\text{throat } 1) = \begin{bmatrix} 2 & 3 & 28 & 29 & 34 & 35 & 55 & 56 & 64 & 65 \\ \vdots & \vdots & \vdots & \vdots & \vdots & \vdots & \vdots & \vdots & \vdots & \vdots \end{bmatrix}. \tag{2-4}$$

The coordination number of the PN is 6 as can be seen from the pore connections shown in Eq. 2-1 and 2-3. From Figure 2-1a, it can also be seen that for a 2D PN the coordination number is 4 i.e., each pore has 4 connections. The geometrical parameters, such as distance between pore centers (L) and the neighbor relations, are kept constant for the idealized PNs, while the radius distribution of the throats and the pores stochastically varies in these networks. The throat lengths are calculated using the pore radii of corresponding pores. The radii of pores and, radii and length of throats are then used to obtain volumes of these (Figure 2-2). The pore and throat sizes, as well as porosities, indicate the input parameters (e.g., obtained from imaging data or literature) in the PNM, whereas wetting angle (θ = 60°) and temperature (T = 80 °C) are kept constant.

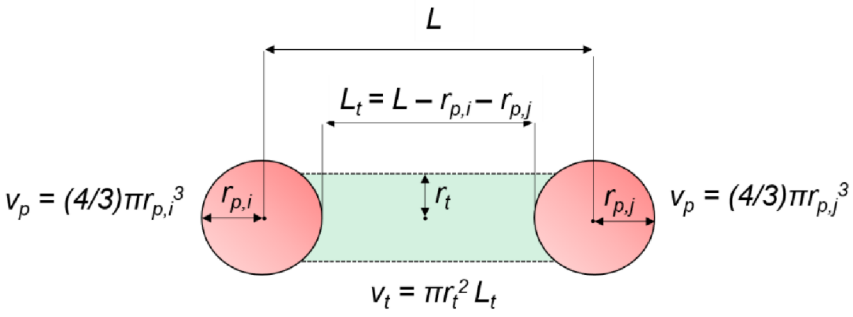

Figure 2-2: Geometric information about pores and throats in an idealized PN, where L is the constant length between two pore centers, v is the volume, A is the area and r is the radius. The subscript p represents pores and t is for throats. Image reproduced from Altaf et al.[98], under the Creative Commons Attribution 4.0 International License (CC BY 4.0).

For the extracted PNs, the geometric parameters such as throat length and neighbor relations are not constant. In such networks, the microstructure is extracted from micro-CT images. In this work, the tomography scans are obtained for commercially available high-porosity fiber-PTLs (Table 2-1) using CT-Alpha by ProCon X-ray GmbH, Germany. PTL samples of size 5.4 mm × 5.1 mm are scanned

(Figure 2-3) with a resolution of 3.9 µm per voxel. Notably, the PTL provided by Sylatech (PTL-1) has a graded structure (see Figure 1-3), featuring smaller pores and thinner fibers on one side and larger pores and fibers on the other side. It is important to mention that PTL-1 had been previously used in PEMWE prior to the micro-CT scans, resulting in a compression-induced reduction of 0.15 mm in thickness. This means that the actual thickness of PTL-1 used in this study was 0.85 mm.

After the scan, the image has to be binarized to make a clear distinction between the solid and void space. Micro-CT scans produce gray images where the intensity of each voxel represents the attenuation of X-rays. To obtain meaningful information about the structure, the 3D image must be simplified to a binary representation. Since the attenuation coefficients of titanium and air are much different from each other[100], Otsu thresholding is able to separate the solid and the pore space in terms of gray-values explicitly. As a result, the scan is converted to a black and white image stack.

Table 2-1: Commercial PTLs used in this study and the parameters provided by the suppliers. For PTL-1, the two average fiber diameters represent the average of each region in the graded structure. Top refers to the CL side of the PTL and bottom refers to the water inlet or water channel side of the PTL.

Supplier data for pristine PTLs			
Supplier	**Thickness, z** (mm)	**Porosity, ε** (%)	**Average fiber diameter, $\bar{d}_f$** (µm)
Sylatech (PTL-1)	1.0	80	25 (top) and 40 (bottom)
Bekaert (PTL-2)	0.5	77	20
Bekaert (PTL-3)	1.0	77	20

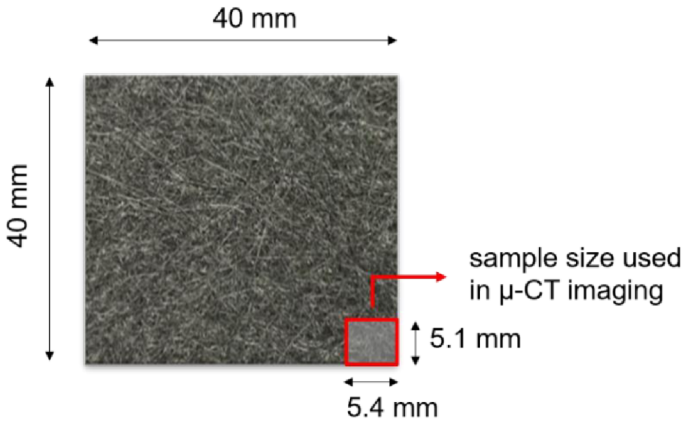

Figure 2-3: PTL-2 from Bekaert used in this work. Image reproduced from Altaf et al.[101], under the Creative Commons Attribution 4.0 International License (CC BY 4.0).

A small section of the PTL-1 sample is shown in Figure 2-4 to demonstrate the image processing steps. Once the image is binarized (Figure 2-4a), it needs to be segmented into discrete pore and throat bodies. For this purpose, at first, an in-

house image processing workflow developed in Python is used[102], based on OpenPNM by Gostick et al.[78]. The starting point is the application of Euclidean distance transform (EDT). This transformation works out the distance between the voxels in the solid and the void (Figure 2-4b). The resulting distance map yields the local minima, which are then used as markers by the watershed algorithm[103]. As explained by Gostick[55], the plateaus created by solid faces running next to each other can lead to many misidentified peaks. This could lead to extra number of markers for watershed, and the image could be oversegmented. To avoid this issue, a Gaussian blur filter is applied with a value of 0.4[55]. The markers are later on used as the pore centers in the network.

The smoothened image is then segmented using watershed algorithm (Figure 2-4c). The Euclidean distance map is utilized as a topographical relief. The algorithm regards the minima from EDT as the basins which are then flooded. Dams are erected where the water meets to separate different (void) regions. A unique integer value (label) is assigned to each region which would then assist in converting the scan into a PN. Masking the watershed image with the original binary image (Figure 2-4a) results in the final segmented image (Figure 2-4c).

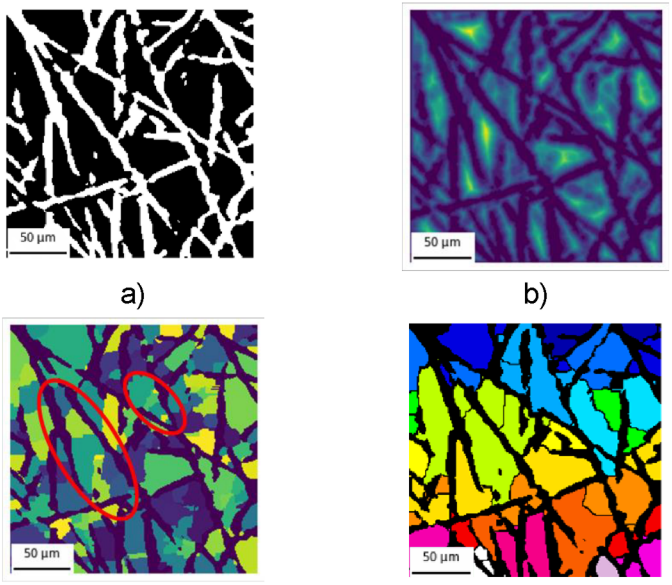

Figure 2-4: Image processing workflow shown on a small section of PTL-1: a) Binarization of raw image; b) Euclidean Distance Transform (EDT); c) watershed algorithm applied in Python to identify the voids (over-segmentation highlighted in red); d) watershed image obtained from MorphoLibJ Plugin in ImageJ (Version 2.1051). Image reproduced from Altaf et al.[101], under the Creative Commons Attribution 4.0 International License (CC BY 4.0).

As it can be seen from Figure 2-4c, the image is clearly over-segmented (marked by red circles). As an alternative, the MorphoLibJ plugin in ImageJ (Version 2.1051) developed by Legland et al.[104] is used to process these images using the same workflow. The watershed image resulting from their method is shown in Figure 2-4d alongside the other watershed image for comparison. It can be evidently seen that the pore space is relatively adequately segmented (Figure 2-4d), in comparison to the segmented image (Figure 2-4c) from OpenPNM-based method[102].

The entire process of image processing to characterize pore spaces depends strongly on the imaging technique applied and the quality of the images[67]. The image resolution acts as the main limiting factor which could result in uncertainties. In the case of PTLs, the rough fibers may not be reproduced as accurately as they should, which could lead to poor network reconstruction. Also, due to fiber overlaps, narrow constrictions may not be reproduced in the best possible way. Improvements can still be made to the segmentation process by utilizing high-resolution images; however, this would require compromising the domain size. For the PTLs in this work, the used resolution of 3.9 µm is much smaller than the void sizes, generally observed in the PTLs. Therefore, any potential loss of information is minimal compared to the average void size. As a result, the impact of such artifacts is considered negligible on the bulk properties.

Once the image stack is segmented, the information about the pores can be exported from ImageJ to a spreadsheet. This information includes pore numbers, positions, volumes, radii, as well as the information about neighbors of each pore. The radii obtained are calculated using the inscribed ball method[104] i.e., the radius of the largest sphere that can fit into a void. Normally, the two common options to obtain the PSD are: identifying the pore sizes using inscribed ball method or equivalent volume method. The equivalent volume method computes the pore radius of a spherical volume equal to the void volume. Thus, all the void volume is consumed by the pores and there is none left for the throats. Contrary to the equivalent volume method, the inscribed ball method allows construction of a pore and throat network, where each of the spherical pore and cylindrical throat has its own volume. This suits well to the ellipsoidal nature of the voids in the fiber-PTL because the inscribed spheres do not occupy the void volume completely and the leftover volume is compensated by the throats (Figure 2-5). Thus, it is presumed that the amount of volume assigned to the throats makes up for the leftover volume by the inscribed pores. This assumption is supported by findings in the literature[55,105] but is also be verified by comparing the resulting porosities with the binarized porosities.

For the throat radii, the intersection areas between two adjacent watershed regions are measured. When the watershed algorithm is applied, the segmented regions are labelled with a unique number. The solid parts of the image are labelled with number "1" (Figure 2-6a). This segmented image can be represented as a 3D array of labels in MATLAB. This array can then be used to find the interfaces between two segmented regions adjacent to each other (Figure 2-6a). From these interfacial areas, the radii of the equivalent circles are calculated and used as the throat radii (Figure 2-6b). In this case, unlike inscribed ball for pores, the equivalent circles account for the actual cross-sectional area of the constrictions, which are important in governing the invasion pathways[79]. Using extracted PNs, Gostick et al.[55] also showed that the capillary pressures agreed well with the experiments when equivalent circles were used to obtain throat radii instead of inscribed balls.

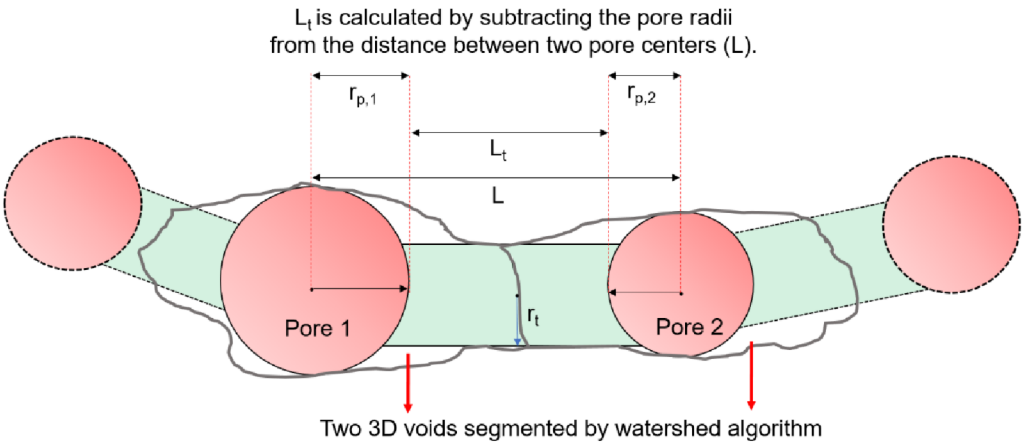

Figure 2-5: A simplified 2D schematic showing the segmentation of void space into pores and throats. Image reproduced from Altaf et al.[101], under the Creative Commons Attribution 4.0 International License (CC BY 4.0).

After the void space has been reconstructed into a PN, all the information is stored in the form of matrices, as also done for the idealized PNs (Eq. 2-1 to Eq. 2-4).

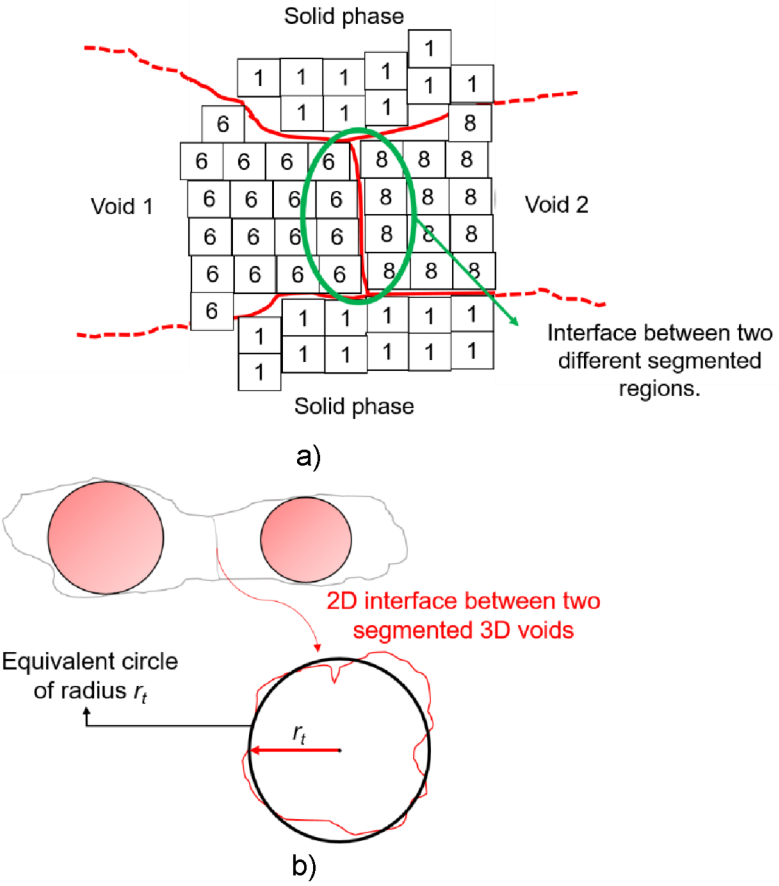

Figure 2-6: a) The segmented image, after watershed algorithm is applied, can be exported as a 3D array of slices in the stack with each segmented region labelled by a unique number. Using these labels, the exact area of the interface can be measured (green circle in the image); b) the 2D interface can then be used to find the radius of an equivalent circle, which is used as the throat radius.

2.1.3 Drainage model for capillary controlled invasion

Invasion percolation rules for quasi-static capillary invasion are employed to simulate the displacement of water by oxygen. The invasion of the PN is then based on the Young-Laplace equation[79],

$$P_l = P_{atm} - \frac{2\gamma cos\theta}{r}, \tag{2-5}$$

where P_l is the liquid pressure, P_{atm} is the atmospheric pressure, γ is the surface tension, θ is the wetting angle, and r is the radius of the pore or throat.

After the geometric parameters are specified, active clusters i.e., clusters being invaded with their menisci are identified and the maximum liquid pressure is computed within them using Eq. 2-5. The algorithm then selects the largest accessible void for gas invasion. Invasions or displacements occur when they are energetically more favorable. This means, the pressure difference between the wetting fluid (water) and the non-wetting fluid (oxygen) leads to the formation of a curvature with a radius depending on the pressure difference. In the case of drainage inside a hydrophilic PN, the non-wetting phase is the one with higher pressure to be forced through the porous structure. This results in the invasion of the liquid-filled pores and throats, with liquid pressures depending on their radius and wettability (Eq. 2-5). The order of invasion thus follows the radius distribution of the pores and throats in a PN. This means, pores and throats are invaded independently of each other according to their individual invasion pressure threshold. The stepwise invasion of the interconnected void space results in the formation of distinct invasion patterns that depend on the pore and throat size distributions and their connectivity.

During this process, labeling of liquid clusters is very important to identify the pores and throats which are connected to each other and form a pathway for liquid and gas transport. At the start of the invasion process, the network is completely occupied by liquid (except surface pores) and there is only one cluster spanning the whole network and conducting the liquid phase. With initiation of invasion, numerous liquid clusters can form that are distinguished into liquid conducting clusters (connected to bottom and top side of the PN) and isolated clusters, which do not contribute to liquid transport. The Hoshen-Kopelman algorithm[106] is used for the labeling of these clusters. Clusters are reviewed and relabeled after each invasion step to update the connections between the pores and throats.

Similarly, the empty and filled pores and throats are assigned unique labels. This information is then used to calculate the liquid saturation using,

$$s_l = \frac{\sum v_{t,l} + \sum v_{p,l}}{\sum v_t + \sum v_p}. \tag{2-6}$$

The gas saturation s_g is then,

$$s_g = 1 - s_l. \tag{2-7}$$

To compute the saturation profile in idealized PNs, the domain is discretized into uniform slices, where each slice includes one layer of pores, horizontal throats, and vertical throats. This layered structure allows direct attribution of pore and throat volumes to specific slices, enabling straightforward calculation of local saturation in each layer. The resulting saturation profile reflects the distribution of gas or liquid phase across the network height.

In the case of extracted PNs, the calculation is adapted due to the non-uniform geometry. The PTL is divided into thin horizontal slices of 8 µm in height. Saturation is computed based on the position of pore centers and throat centers within each slice. If a throat spans two adjacent slices, its entire volume is attributed to the slice containing its center, since it cannot be physically split. This approach enables a consistent estimation of the saturation profile despite the geometrical complexity.

2.1.4 Computation of permeability

The computation of permeability is adapted from the work of Vorhauer[107]. It is to be clearly stated here that PNM yields the capillary-invasion based gas-liquid distributions and the viscosity is only considered for the calculation of permeability. Once the invasion profiles are obtained, gas and liquid flow rates through the partially drained PNs are computed. Firstly, the Hagen-Poiseuille equation is used to compute the laminar viscous flow through each throat:

$$\dot{M}_{l,g} = \frac{\rho_{l,g} \pi r_t^4}{8 \mu_{l,g} L_t} \left(P_1 - P_2 \right). \tag{2-8}$$

The subscripts 1 and 2 in Eq. 2-8 are the two neighboring pores of a throat between which the pressure gradient is considered for the computation of flow. The conductance of the throats[60] is defined as,

$$g_{l,g} = \frac{\rho_{l,g} \pi r_t^4}{8 \mu_{l,g} L_t}. \tag{2-9}$$

Conductance is computed only for the throats, as flow through the pores themselves is neglected. This simplification is supported by studies showing that omitting pressure drop within pores still yields permeability values in good agreement with experimental results[108]. As a simplified example to understand permeability calculation, consider four pores and three throats in Figure 2-7.

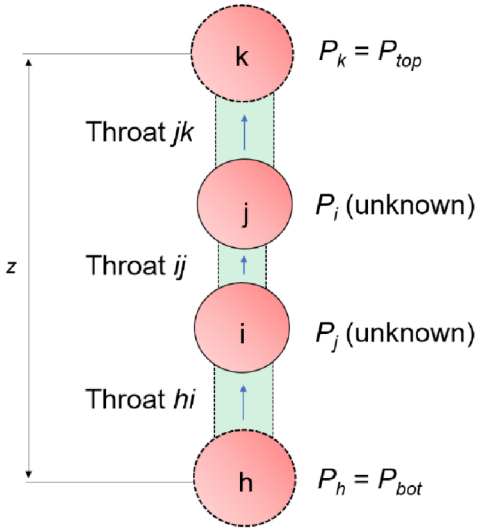

Figure 2-7: A simplified sketch of four pores and three connecting throats to show how the linear equations (Eq. 2-12 and Eq. 2-13) are transferred into the matrix notation (Eq. 2-14).

Without any accumulation, condensation, or evaporation in pores, the mass flow across pore *i* can be defined using corresponding throats as,

$$\dot{M}_{ij} = \dot{M}_{hi}\,. \tag{2-10}$$

Using Eq. 2-8, Eq. 2-10 can be written as,

$$\frac{\rho_{l,g}\pi r_{ij}^{\,4}}{8\mu_{l,g} L_{t,ij}}\left(P_i - P_j\right) = \frac{\rho_{l,g}\pi r_{hi}^{\,4}}{8\mu_{l,g} L_{t,hi}}\left(P_h - P_i\right). \tag{2-11}$$

Substituting Eq. 2-9 in Eq. 2-11 results in,

$$-g_{ij}P_j + (g_{ij} + g_{hi})P_i = g_{hi}P_h\,. \tag{2-12}$$

Similarly, for pore *j*, the equation would be,

$$-g_{ij}P_i + (g_{jk} + g_{ij})P_j = g_{jk}P_k\,. \tag{2-13}$$

It must be emphasized here that this is an extremely simplified example for better understanding of the calculations. These equations become much more complicated when actual coordination numbers are considered and several throats are contributing to mass transport.

The two equations (Eq. 2-12 and Eq. 2-13) can now be transferred to a matrix notation,

$$\begin{bmatrix} g_{ij} + g_{hi} & -g_{ij} \\ -g_{ij} & g_{jk} + g_{ij} \end{bmatrix}\begin{bmatrix} P_i \\ P_j \end{bmatrix} = \begin{bmatrix} g_{hi}P_h \\ g_{jk}P_k \end{bmatrix}. \tag{2-14}$$

With P_h = P_{top} and P_k = P_{bot}, the matrix notation shows two equations and two unknowns that can compute the unknown pressures. In a PN, the number of unknown pressure values is the difference between the total number of pores and the top and bottom pores. The set of linear equations, derived for each pore, is then transferred into a matrix notation, represented by,

$$\boldsymbol{A}P = b, \tag{2-15}$$

where $\boldsymbol{A}$ is a symmetrical square matrix that represents the full matrix of all the conductances in the PN, with $\boldsymbol{A}^T = \boldsymbol{A}$. P represents the unknown pressure field through the PN, which needs to be calculated for the calculation of the overall mass transport through the PN. The known boundary conditions associated to each pore are given in b. More generally, when a PN with arbitrary pores u, v and w would have higher coordination numbers, $\boldsymbol{A}$ can be written as[107],

$$\boldsymbol{A} = \begin{bmatrix} & \vdots & & \vdots & \\ \cdots & \sum g_{uv} & \cdots & -g_{vw} & \cdots \\ & \vdots & & \vdots & \\ \cdots & -g_{vw} & \cdots & \sum g_{wv} & \cdots \\ & \vdots & & \vdots & \end{bmatrix}, \tag{2-16}$$

and,

$$b = \sum g_{uv} P_u. \tag{2-17}$$

To facilitate the flow through PTLs, the boundary conditions of the PN are set to P_{top} = 1 bar and P_{bot} = 2 bar. Equation 2-15 yields the pressure fields in the PNs, and the mass flow through ($\dot{M}_{l,g}^{PN}$) the PN is then calculated. For this calculation, the conductance between the bottom layer of the PTL (represented by pore h in Figure 2-7) and the bulk phase (represented by pore i and pore j in Figure 2-7). The pressures at the bulk phase boundary are known from Eq. 2-15, while the pressure at the bottom layer (P_{bot}) is defined as 2 bar. A product of the conductances of throats between these two regions and the pressure differences between them provides $\dot{M}_{l,g}^{PN}$. In simpler terms, and referring to the PN in Figure 2-7, the mass flow can be described as,

$$\dot{M}_{l,g}^{PN} = g_{hi}(P_h - P_i). \tag{2-18}$$

Finally, the absolute permeability through the PN at a given pressure gradient can be calculated using,

$$K = \frac{\mu_{l,g}}{\rho_{l,g}} \frac{\dot{M}_{l,g}^{PN}}{A^{PN}} \frac{z}{\Delta P}, \tag{2-19}$$

with A_{PN} being the cross-sectional area and *z* the thickness of the PN (Figure 2-7). The boundary conditions for the PN simulations are P_{bot} at the bottom side of the PN and P_{top} at the top side with,

$$\Delta P = P_{bot} - P_{top}. \tag{2-20}$$

The relative permeability (k_{rel}) for a partially saturated PN is simply the ratio of mass flow through the partially saturated PN to that of the corresponding completely saturated PN. In particular, relative liquid permeability ($k_{rel,l}$) of a partially saturated PN would be,

$$k_{rel,l} = \frac{\dot{M}_l^{PN}(0 < s_l < 1)}{\dot{M}_l^{PN}(s_l = 1)}. \tag{2-21}$$

2.1.5 Computation of thermal conductivity

For the estimation of thermal conductivity, the heat pipe effect[109–111], an enhanced heat transfer mechanism driven by phase change and capillary action, is omitted to simplify the calculations. While the heat pipe effect can significantly increase heat transport efficiency[112], especially under conditions of sufficient liquid saturation, high temperature and high temperature gradients, incorporating it into the model would require modeling liquid-vapor phase change[113] and vapor diffusion. This would significantly increase the computational complexity and detract from the primary goal of this study, i.e., understanding the impact of structure on transport in PTLs with simple models. Additionally, the temperature gradients for high-porosity PTLs can be assumed to be low due to uniform water flow and high permeabilities, reducing the driving force for evaporation and condensation cycles critical for heat pipe effects[114].

To estimate thermal conductivity of heterogeneous materials, a wide range of structural and semi-empirical models have been proposed. Some of these models are tuned for specific applications by modifying a parent equation and adjusting it to the variations in the material being studied[115,116]. On the other hand, some models make use of an empirical or weighting parameter to account for the structural differences. More accurate but computationally inefficient method would be to determine the effective thermal conductivity of porous materials with known structure using numerical simulations, e.g., those based on finite element methods. Nevertheless, in many applications, analytical models are favored over numerical models due to their foundation in physical principles, less computation times, lower costs, and the ability to deliver reasonable accuracy even when the microstructure is not fully known.

Most effective thermal conductivity models in the literature are generally derived from five basic structural models: Maxwell-Eucken (ME) in two forms ME-1 and

ME-2, Effective Medium Theory (EMT), Series and Parallel models (Table 2-2). These models offer advantages over other generic models, such as the semi-empirical Krischer model, because each is based on a distinct physical principle and does not rely on any empirical parameters. The ME model assumes that small spheres of one component are dispersed within a continuous matrix of another component[117,118]. Two variations of the ME model are therefore depending on which component constitutes the continuous phase. The EMT model assumes a completely random distribution of two-phases[119]. The Series and Parallel models assume the components are arranged in layers, either perpendicular or parallel to the direction of heat flow, respectively. Generally, Series and Parallel models, provide the lower and upper limits of the thermal conductivity values, respectively. In volume-averaged-Krischer[120], the Series and Parallel models, along with a weighting factor (*f*), allow for accounting how these models contribute to the overall effective conductivity of the material. This approach helps handle the complexity of materials like PTLs, which have heterogeneous properties, and simplifies the calculation by considering averages over a volume rather than specific local porosities or saturations.

Table 2-2: Five basic effective thermal conductivity structural models, and semi-empirical Krischer model used to calculate effective conductivity using Series and Parallel models.

Model	**Equation**
ME-1	$\lambda_{ME1} = \dfrac{\lambda_f \varepsilon + \lambda_s (1-\varepsilon)\dfrac{3\lambda_f}{2\lambda_f + \lambda_s}}{\varepsilon + (1-\varepsilon)\dfrac{3\lambda_f}{2\lambda_f + \lambda_s}}$
ME-2	$\lambda_{ME2} = \dfrac{\lambda_s (1-\varepsilon) + \lambda_f \varepsilon \dfrac{3\lambda_s}{2\lambda_s + \lambda_f}}{(1-\varepsilon) + \varepsilon \dfrac{3\lambda_s}{2\lambda_s + \lambda_f}}$
EMT	$\varepsilon \dfrac{\lambda_f - \lambda_{EMT}}{\lambda_f + 2\lambda} + (1-\varepsilon)\dfrac{\lambda_s - \lambda_{EMT}}{\lambda_s + 2\lambda} = 0$
Series	$\lambda_{ser} = \dfrac{1}{\dfrac{\varepsilon}{\lambda_f} + \dfrac{1-\varepsilon}{\lambda_s}}$
Parallel	$\lambda_{par} = \varepsilon\lambda_f + (1-\varepsilon)\lambda_s$
Krischer (effective)	$\lambda_{eff} = \dfrac{1}{\dfrac{f}{\lambda_{ser}} + \dfrac{1-f}{\lambda_{par}}}$

In this work, a Fourier's law based VN model coupled with extracted PNs is employed. This offers significant advantages in terms of simplicity and computational efficiency, enabling a clear focus on conduction-driven heat transfer with variations in local porosity and even saturations. A Krischer-based approach, using the Series and Parallel models, is applied basically, but the equations are solved locally to calculate the heat transfer between adjacent Voronoi cells based on the interfacial contact area (local porosity) between each cell. This way, model treats heat transfer in PTLs as a function of PTL geometry and local conductivity values, effectively capturing the role of solid and fluid phases.

Generally, in Krischer-based approaches, the drawback is that the value of weighting parameter, *f*, is either to be determined by experiments or intuitive estimates. In this work, *f* is fitted using the experimental results. Although both Krischer-based methods require fitting, volume-averaged and VN-based, the one based on specific void connectivity and interfacial porosities could arguably generalize better across different PTLs. This means, a VN-based Krischer model, after fitting, could more effectively predict conductivity across a broader range of PTLs. In contrast, the volume-averaged Krischer model, which assumes a highly anisotropic physical structure[119], may only provide reliable predictions for the specific PTLs to which it is fitted, and could fail to capture trends in PTLs with different structures, making it less versatile. Furthermore, the localized approach with VNs and extracted PNs can account for local saturations and estimate conductivity for partially saturated PTLs, whereas the volume-averaged method can only provide conductivity values for completely wet or completely dry conditions. This highlights why a VN-based Krischer model can be superior to its volume-averaged counterpart, as it better captures the intrinsic variability in a PTL and could account for partially saturated PTLs as well.

Certainly, the simplified VN-based method has its limitations as well. Similar to other models mentioned, it does not account for non-conductive heat transfer mechanisms such as convection or phase changes, leading to potential underestimation of thermal conductivity in systems where such effects are significant. Furthermore, idealizations such as spherical pores clearly deviate from the complex heterogeneities in voids observed in real PTLs.

To estimate the thermal conductivity from micro-CT images and the extracted data, the solid part must not be ignored anymore. For this reason, a VN is used (Figure 2-8). To generate the VN, "3D_voronoi_cuboid_bounded" plugin in MATLAB is used. The pore centers obtained using the watershed segmentation are used as seeds for the VN. Similar to the permeability calculations, these pores represent discrete points that form the temperature field, with throats serving as the connecting pathways between them. The coordinates of the interface between the cells are obtained, through which the throats are passing (Figure 2-9), from the "3D_voronoi_cuboid_bounded" plugin. These are then used to calculate the area of the interface between adjacent VN cells.

The interfacial area (Figure 2-9) between two Voronoi cells is important for the calculation of heat transfer between those cells. For this reason, it must also be identified how much area is occupied by the voids (oxygen or water) and how much by the solid (titanium), as the local conductivity would vary based on this. This can be simply understood as the superimposition of the PN onto the VN (Figure 2-9).

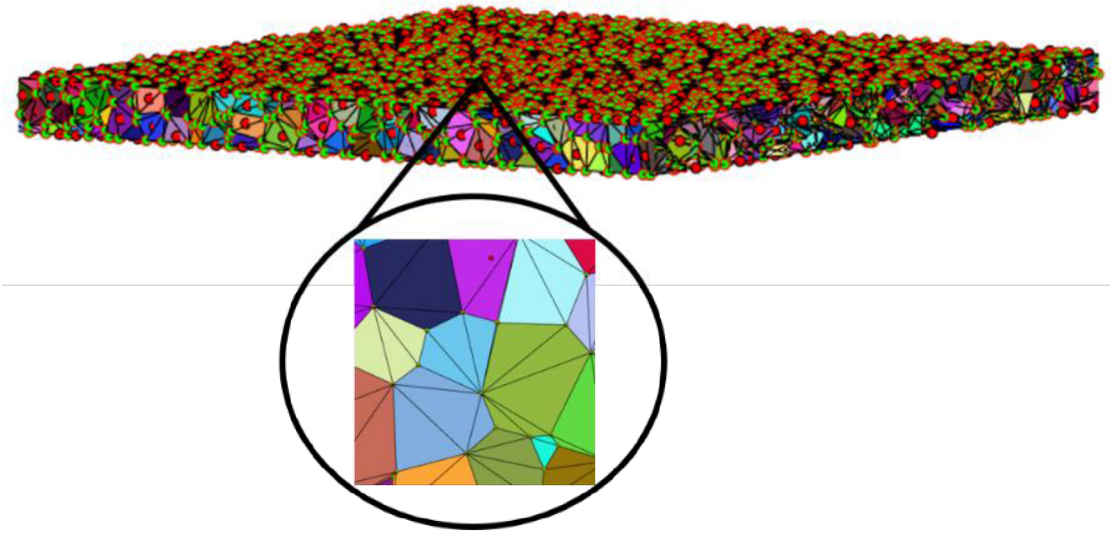

Figure 2-8: A Voronoi network generated from the extracted micro-CT scan data using MATLAB's "3D_voronoi_cuboid_bounded" plugin.

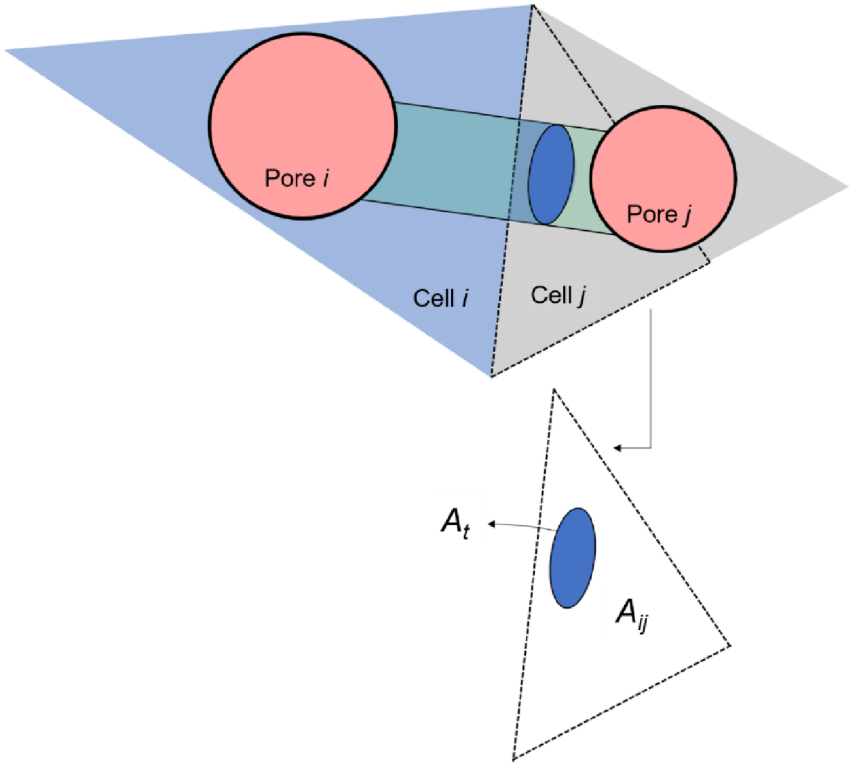

Figure 2-9: A geometric representation of how a VN is used to estimate the interfacial areas between adjacent cells. a) Two adjacent Voronoi cells superimposed by two pores and one throat from the extracted PN; b) the interfacial area used to calculate the heat transfer between two cells (not drawn to scale).

Analogous to the mass transport calculations, first of all, the heat transfer through each Voronoi interface is calculated using Fourier's equation,

$$\dot{Q}_{ij} = \frac{A_{ij}\lambda_{ij}}{L_t}\left(T_i - T_j\right). \tag{2-22}$$

To calculate the local conductivity (λ_{ij}), interfacial porosity (ε_{int}) is required for each Voronoi interface as shown in Figure 2-9. This is calculated as

$$\varepsilon_{\text{int}} = \frac{A_{ij} - A_t}{A_{ij}}. \tag{2-23}$$

This aids in calculating the series (λ_{ser}) and parallel (λ_{par}) conductivities and then the effective conductivity (λ_{ij}) between two pores (pores *i* and *j*):

$$\lambda_{ser} = \frac{1}{\frac{\varepsilon_{\text{int}}}{\lambda_f} + \frac{1-\varepsilon_{\text{int}}}{\lambda_s}}, \tag{2-24}$$

$$\lambda_{par} = \varepsilon_{\text{int}}\lambda_f + (1-\varepsilon_{\text{int}})\lambda_s, \tag{2-25}$$

$$\lambda_{ij} = \frac{1}{\frac{f}{\lambda_{ser}} + \frac{1-f}{\lambda_{par}}}. \tag{2-26}$$

λ_f is either the conductivity of water or oxygen, depending on the PTL condition (dry or wet) and f is the weighting parameter for parallel and series conductivities. A value of f is fitted based on the dry conductivity value from Hot Disk experiments (shown in Section 2.2).

Similar to the permeability calculations (Eq. 2-14 to Eq. 2-17), the linear equations are solved together for all Voronoi cells and the temperature distribution is obtained. The total heat flow through the network is then calculated, which is used to determine the overall thermal conductivity of the PTL with,

$$\lambda_{PTL} = \dot{Q}^{VN}\frac{z}{A^{VN}\Delta T}. \tag{2-27}$$

The boundary conditions used are T_{bot} = 25 °C at the bottom (water channel side) and T_{top} = 80 °C at the top (CL side) of the PN, which are applied to calculate ΔT across the network of thickness z (as depicted in Figure 2-7).

2.2 Hot Disk experiments

The thermal conductivity of the three PTLs used in this work were also measured using Hot Disk Transient Plane Source System TPS2500s by Hot Disk AB, Göteborg, Sweden, in collaboration with Anhalt University of Applied Sciences, Köthen, Germany. The experimental values obtained from these experiments are used to fit the weighting parameter *f* in the VN model for thermal conductivity calculations and to compare the results with structural models from the literature.

To measure thin sheets, such as PTLs, a specific module (thin film add-on) was used, which uses the transient plane source technique[121,122]. In this technique, a sensor composed of a thin metallic (nickel) probe[123] is placed between two pieces of the sample (4 cm × 4 cm) to be measured, which is also the heat source. A constant electric power is supplied through this hot disk heating element. The time duration of the applied power is kept short enough for the thickness of the surrounding samples to be considered infinite during the transient measurement. The generated heat is then dissipated in the surrounding samples and, at the same time, the sensor heating element measures temperature increase as a function of time. This collected data is then used to estimate the thermal conductivity of the sample[122].

The measurements for PTLs were done using a so-called Kapton insulated sensor with 1 kg of applied weight to maintain a good contact between the sensor and samples. The measuring time was 10 s and a power of 1 W was applied.

2.3 Neutron imaging experiments

Neutron imaging is a highly effective, non-destructive technique for studying porous media. Its unique interaction with materials makes it well-suited for investigating fluid transport and structural characteristics. Neutron imaging relies on the interaction between neutrons and atomic nuclei, providing distinct advantages compared to X-ray imaging.

Neutrons, being highly sensitive to light elements like hydrogen, enable the visualization of liquid water distribution and dynamics within materials such as PTLs. Unlike X-rays, neutrons can penetrate thick metal layers, such as titanium, making them particularly suitable for imaging experiments. While neutron imaging facilities are costly and less widely available, they are preferred over X-ray imaging for studying dynamic processes.

In this section, the neutron imaging experiments for the observation of two-phase flow within the PTLs are explained. The purpose is to study water-gas distributions in commercial fiber-PTLs with different structural parameters at different flow conditions. Such PTLs have never been studied before in imaging experiments or mathematical models. The results of these experiments provide an insight on how the structure and the flow settings influence the mass transport through the PTL.

The experiments were performed in collaboration with Helmholtz-Zentrum Berlin (HZB) and were conducted at the NeXT[124] beam line at Institut Laue-Langevin (ILL) in Grenoble, France. A high flux of $1.4 \cdot 10^{10}$ $n \cdot cm^{-2} \cdot s^{-1}$ is at disposal at their location. A high-resolution detector was utilized, consisting of a 20 µm thick Gadox scintillator, a 50 mm f./1.2 Canon imaging lens, a 55 mm f./1.0 objective lens, and a Hamamatsu ORCA-Flash V3 sCOMS camera.

2.3.1 Non-electrochemical cells

i) Cell design

The cell design is based on the work of Panchenko et al.[84] with certain modifications. A photograph of the prototype based exactly on their design in shown in Figure 2-10. Figure 2-11 depicts the schematic representation of the non-electrochemical cells used in this study, also referred to as flow cells, for neutron imaging experiments.

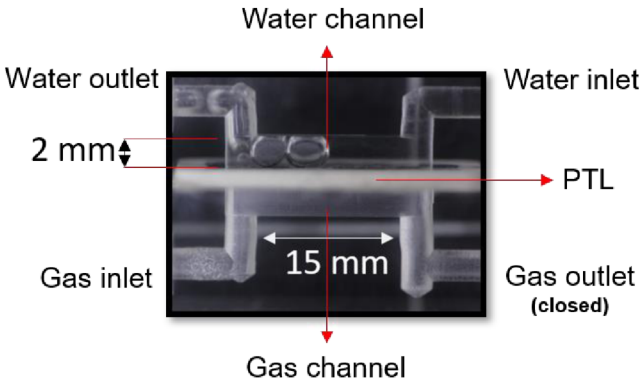

Figure 2-10: A transparent acrylic glass non-electrochemical cell, inspired by Panchenko et al.[84] built as a prototype before development of actual cells (Figure 2-11) to be used for neutron imaging experiments.

These cells were specifically designed for through-plane imaging, with the face of the PTL facing towards the neutron source (Figure 2-11). Consequently, the shape of the cells was elongated, and the flow inlets and outlets were positioned at the top (Figure 2-11) rather than on the sides of the cell (Figure 2-10). This design choice offered several advantages for tomography measurements, as it facilitated rotation of the cell without causing entanglement of the pipes during the rotation process.

To construct the cells, aluminum was used for the cell body, screws, and connectors. Teflon was employed for sealing the water channel and the PTL. As illustrated in Figure 2-11, the cells consisted of two channels, each measuring 0.5 mm in thickness, 4 mm in width, and 13.5 mm in length. The PTL was positioned between these channels, occupying an active area of 13.5 mm by 4 mm. Each channel was connected to an inlet and outlet, designated for water or air, respectively.

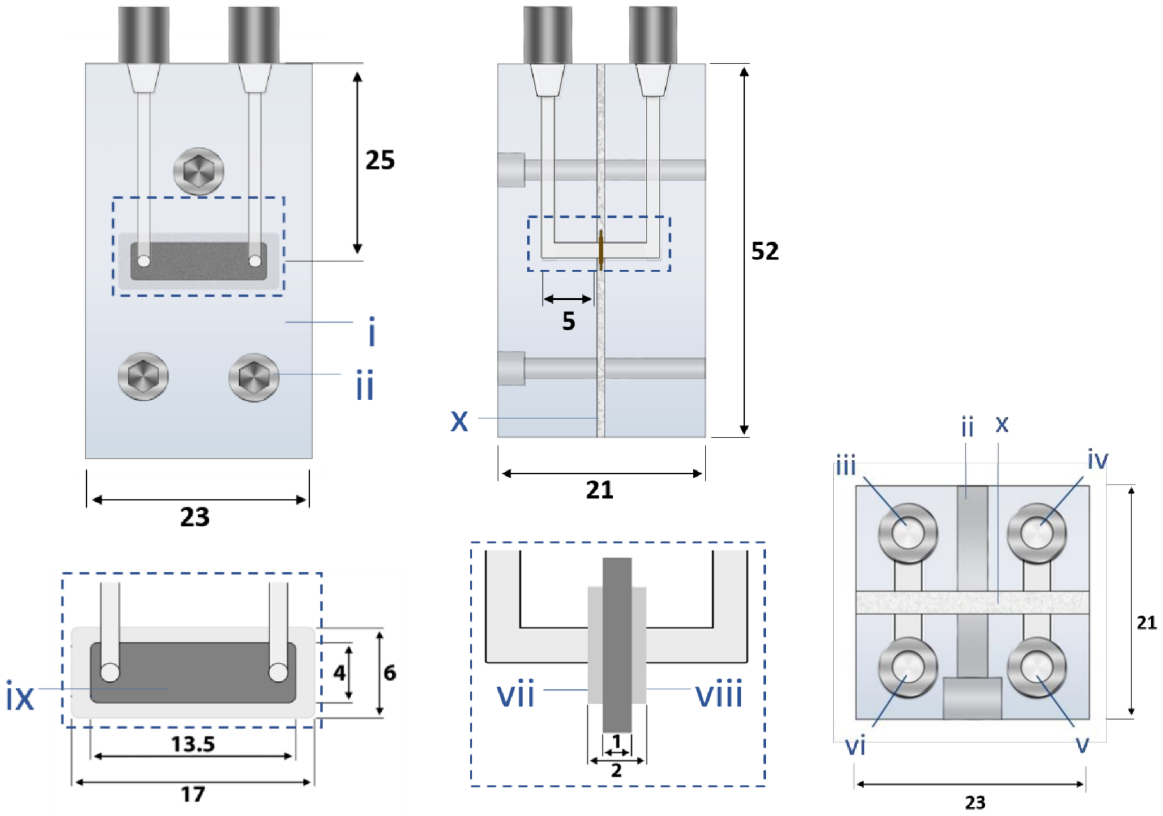

a) Cross-section (through-plane)

b) Cross-section (in-plane)

c) Top view

Figure 2-11: Design of the flow cell, dimensions in mm and labelled parts: i - cell housing; ii - connection screws; iii - water inlet; iv - water outlet; v - air inlet; vi - air outlet; vii - air supply channel; viii - water supply channel; ix - PTL; x - Teflon sealing. a) Cross-section of through-plane view; b) cross-section of in-plane view; c) top view. Image reproduced from Altaf et al.[125], under the Creative Commons Attribution 4.0 International License (CC BY 4.0).

ii) Experimental setup

To achieve high local resolution, the cell was positioned in close proximity to the detector. During radiography imaging, the distance between the cell and detector was set at 12 mm, resulting in a spatial resolution of 6.5 µm. The visualized ROI had a smaller cross section (9.5 mm × 4 mm) compared to the actual PTL, as indicated in Figure 2-12. For tomography, the gas-liquid distribution was stabilized by tightening screw clamps at all inlet and outlet ports of the cell. Tomographic scans were performed with an exposure time of 1.5 s, acquiring 800 projections per 360° rotation, and at a distance of 15 mm from the detector. A resolution of 22 µm is achieved for all tomographies.

A trade-off had to be made between contrast, domain size, and resolution. The spatial resolution employed was not sufficient to visualize individual pore invasions, but it allowed for the identification of distinct break-through regions on a relatively

larger domain. Regarding time resolution, 10 images per second was considered suitable for observing the release of air through the PTL into the channel. However, the time scales associated with pore-scale drainage (or Haines jumps) are much shorter[126] and could not be observed with a resolution of 0.1 s.

For the supply of water and air, two syringe pumps from World Precision Instruments Germany GmbH were employed (details in Appendix A.2). These pumps provided non-oscillating fluid supply with a dispensing accuracy of ±1 %. To ensure the avoidance of radioactive activation during measurements, the pumps were located approximately 80 cm away from the cell. Polyethylene pipes with an inner diameter of 2 mm were used for connections, and screw clamps made of stainless steel were utilized to seal the pipes during different operations.

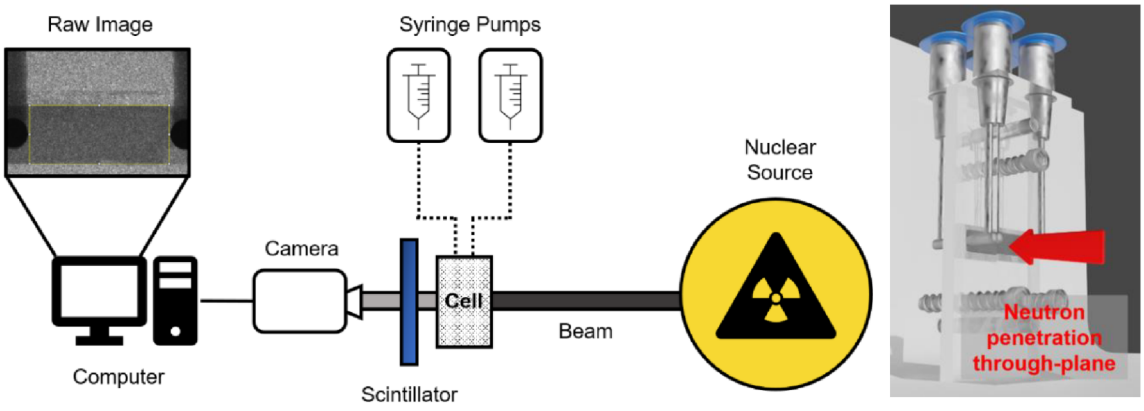

Figure 2-12: a) Schematic diagram of the experimental setup; b) cell orientation in the through-plane view setup. Images reproduced from Altaf et al.[125], under the Creative Commons Attribution 4.0 International License (CC BY 4.0).

iii) Flow settings

Air and deionized water were used for these experiments. The air mass flow rates and the water mass flow rates given in Table 2-3 were calculated using Faraday's law,

$$\dot{M}_i^F = \frac{\tilde{M}_i \cdot I}{c_i \cdot F}, \tag{2-28}$$

for i = H_2O, O_2 and with Faraday constant F = 96485 A·s·mol^{-1}, charge number c = 4 for the gas phase and c = 2 for water, molecular weight $\tilde{M}_{O_2}$ = 32 g·mol^{-1} or $\tilde{M}_{H_2O}$ = 18 g·mol^{-1}, and current I in A,

$$I = j \cdot A, \tag{2-29}$$

with the corresponding current density j provided in Table 2-3 and surface area A = 54 mm^2. Stoichiometry (ω) used for each setting is also provided in Table 2-3. This is the ratio of the volume flow rate of water supplied to the experiment, $\dot{v}_{H_2O}^{exp}$,

to the required amount of water consumed in the reaction, $\dot{v}^F_{H_2O} = \rho^F_{H_2O} \big/ \dot{M}^F_{H_2O}$, calculated by:

$$\omega = \frac{\dot{v}^{\exp} \cdot \rho^F_{H_2O}}{\dot{M}^F_{H_2O}}. \tag{2-30}$$

For each cell, various operational scenarios were conducted, including filling (water imbibition into an empty PTL), counter-current (CC) flow of air and water, as well as drainage, as indicated in Table 2-3 and Figure 2-13. During the filling process, the gas channels on both sides (inlet and outlet) were sealed using screw clamps, and water was supplied at a constant flow rate specified in Table 2-3.

Table 2-3: Flow settings used for each cell; CC: Counter-current flow of liquid and gas.

Flow setting	**H_2O flow rate** ($ml \cdot min^{-1}$)	**Air flow rate** ($ml \cdot min^{-1}$)	**Stoichiometry** (-)	**Corresponding current density** ($A \cdot cm^{-2}$)
Filling	1.00	-	-	-
CC-setting 1	0.58	3.95	100	2.0
CC-setting 2	2.18	9.87	150	5.0
CC-setting 3	3.06	13.82	150	7.0
CC-setting 4	3.93	17.77	150	9.0
Drainage	-	7.90	-	-

In the case of CC flows, four different settings were chosen, corresponding to varying overall flow rates. Only the gas exit valve was closed during CC operation to allow for pressure build-up on the gas side. So that the gas only exits from the PTL as in an actual electrolyzer cell. During drainage, both the water inlet and the gas outlet were closed, enabling higher pressure build-up to drain out water.

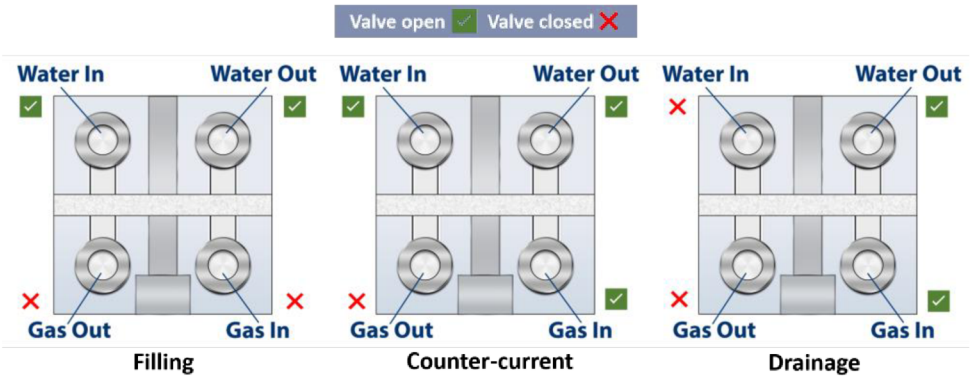

Figure 2-13: Three operating scenarios used in the experiments. The green checks identify the open valves; red crosses identify closed valves. Image reproduced from Altaf et al.[125], under the Creative Commons Attribution 4.0 International License (CC BY 4.0).

iv) Image processing

The imaging experiment results are used for analysis, which involves converting raw image data into neutron transmittance and water thickness values. All image processing steps are performed using ImageJ (Version 2.1051).

At first, dark-field (*DF*) and dry-cell images (*DC*) are used to normalize the sample images (*SI*). For this purpose, *DF* median images are subtracted from the *SI* and also from the median of *DC* images. By that, the grayscale deviations, which are caused by sensitivity of the CCD camera and the detector, are accounted for and, thus, the transmittance image is obtained using,

$$Tr = \frac{SI - DF}{DC - DF}. \tag{2-31}$$

This resulting image (Tr) contains just the information about water distribution i.e., without the titanium fibers.

As the images are taken with a frame rate of 10 images per second, the change of the Tr could be investigated with high temporal resolution. The change of water saturation inside the cell could then be correlated with a change of the transmittance signal. Higher transmission values are correlated with more air in the image and lower transmission means more water. Using Tr, the water thickness, W, is obtained with the help of Beer-Lambert law (BLL),

$$W = \frac{\ln Tr}{-\psi}, \tag{2-32}$$

with ψ being the attenuation coefficient of water (approx. 0.5 mm^{-1})[100]. In the through-plane view, the thickness comprises of the water inside the water channel, with a thickness of 0.5 mm, as well as the water contained in the PTLs, with thicknesses varying between 0.5 mm and 1.0 mm and porosities specified in Table 2-1. Gas bubbles, both inside the PTL and the water channel, and titanium fibers reduce the overall water thickness in through-plane view direction.

The average water thickness, $\overline{W}$, is computed for all images taken during steady-state operating conditions of each experiment as a function of the horizontal distance across the PTL width, x. This means, $\overline{W}$ contains the data from all pixels along the vertical height of the image at a horizontal point across x. The global minimum water thickness across an image indicates the break-through location of the gas phase of each experiment. For better visualization, look-up tables (LUTs) are applied, which are basically used to convert grayscale images into different color maps (Figure 2-14).

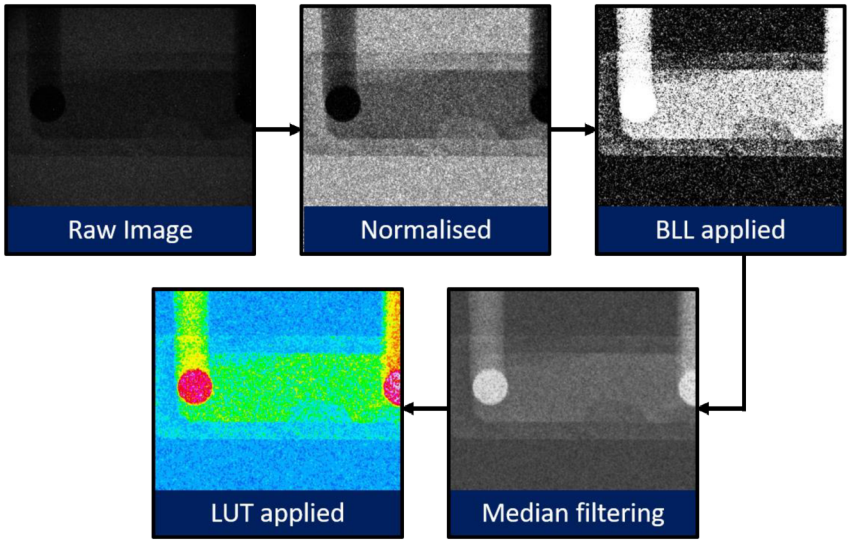

Figure 2-14: Image processing workflow shown as an example using the raw images of the cell containing PTL-2. The through-plane images show a rectangular PTL sample in the center.

v) Acrylic glass cell

In addition to the cells used in neutron imaging experiments, the acrylic glass cell (Figure 2-10), initially built as a prototype, was used to visualize the bubble release into the water channel through the PTL. The results of these experiments are used in this work to analyze the impact of stoichiometry on the bubble release patterns and break-through locations into the water channel.

The experiments were performed using the counter-current setting (corresponding to a current density of 4.0 A·cm^{-2}) as explained in Section 2.3.1 (iii), at different stoichiometries (Table 2-4). The images/videos were captured with a Canon EOS 550D camera. The difference here from the work of Panchenko et al.[84] primarily is that they used flow rates corresponding to 2.0 A·cm^{-2}, but here a higher gas flow rate was used, which corresponds to a higher current density (4.0 A·cm^{-2}). Secondly, the PTL in this case has much higher porosity (PTL-1 in Table 2-1) with a graded structure compared to the one used in their study (a particle PTL with 49 % porosity).

Table 2-4: Different stoichiometries (ω) and corresponding flow rates in the transparent cell experiments used for the visualization of bubble release through the PTL into the channel.

	ω-1	**ω-2**	**ω-3**
Air flow rate (ml·min^{-1})	4.2	4.2	4.2
Water flow rate (ml·min^{-1})	0.48	1.06	3.48
ω	142	315	1037

2.3.2 Electrochemical cells

In addition to the non-electrochemical cells explained in Section 2.3.1, electrochemical cells were also employed for the neutron imaging experiments. These experiments were the result of a collaborative effort and were conceptualized, planned, and supervised by M.Sc. Tamara Miličić (a Ph.D. candidate at the Max Planck Institute, Magdeburg). Details about the cell design, components used, and experimental conditions can be found in the master's thesis[127] by B.Sc. Ece Cakmak (OVGU, Magdeburg), primarily supervised by M.Sc. Tamara Miličić and co-supervised by the author of this work. A detailed description of the experimental setup, electrochemical characterization methods, and the impact of water distribution on cell performance will be presented in the Ph.D. thesis of M.Sc. Tamara Miličić and remains unpublished at this time. The main goal of these experiments was to measure the electrochemical performance using different PTLs and, at the same time, visualize the water distribution in the cells. Within the scope of this thesis, only in-plane images of different PTLs are used to analyze the impact of operating conditions and PTL structure on liquid saturation. The through-plane imaging was also employed during these experiments but, due to the presence of several components and accumulation of imaged information, the resulting images do not to provide any valuable information.

The electrochemical cell was divided into three segments: top, middle, and bottom, with a total height of 120 mm (Figure 2-15). The middle segment had a thinner rectangular cross-section of 15 mm × 15 mm and a height of 40 mm. This middle section contained the active cell area of 20 mm height and 5 mm width containing PTL, CCM, GDL and flow channels. This design minimized neutron attenuation and enhanced image contrast. In contrast, the top and bottom segments, which were not intended for imaging, were made larger to accommodate connections for reactant supply and product removal. The two aluminum endplates (with a total thickness of 10 mm) were not regarded as a part of active cell area.

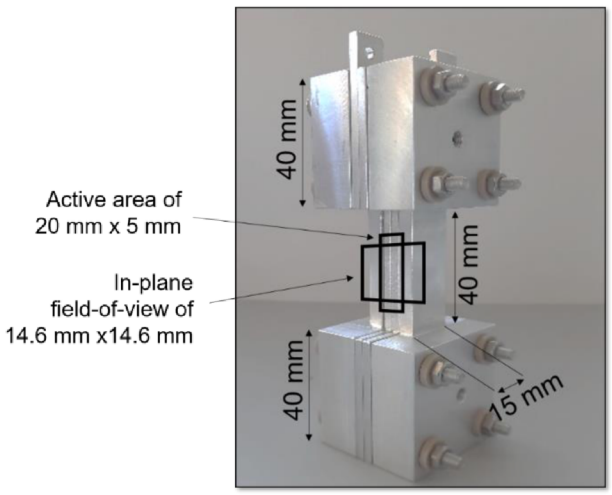

Figure 2-15: A photograph of one of the electrochemical cells, conceptualized by M.Sc. Tamara Miličić. A thinner middle section was used to reduce the absorption of neutrons around the active area. Image adapted from the work of Cakmak[127], a master's thesis supervised by M.Sc. Tamara Miličić and co-supervised by the author of this work.

Two different cells each containing a unique PTL (Table 2-5) were used. One of the two cells was built using PTL-3 from Table 2-1, and referred to as PEMWE-1 in electrochemical experiments. The second cell (PEMWE-2) also had a fiber-PTL with 42 % porosity but same thickness (1.0 mm) and manufacturer (Bekaert) as PTL-3. At the cathode, a carbon GDL (0.27 mm thick) manufactured by Freudenberg SE, Germany was used. As a CCM, a commercially available Nafion® 117 membrane (270 µm thick) by Chemours, USA coated with IrO_x and Pt as catalysts on anode and cathode side, respectively, was used. To ensure contact and avoid leakage through the different components in the cells, the cells were compressed during assembly (PEMWE-1: 20 % and PEMWE-2: 8 %). Due to this compression, the porosity reduction was theoretically calculated using the percentage compression (*C*) using,

$$\varepsilon_{th} = \frac{\varepsilon - C}{100 - C} \cdot 100\% . \tag{2-33}$$

The resulting values are provided in Table 2-5. For the image acquisition, the same equipment used for the non-electrochemical cells was used for these experiments too. With a field of view of 14.6 mm × 14.6 mm, a pixel size of 14.3 µm was realized, with a temporal resolution of 0.1 s. 1200 images were captured for different current densities once the steady-state was achieved (Table 2-5).

For processing the raw data, the same steps outlined in Section 2.3.1 (iv) are followed. In this case, the water thickness values obtained are used to calculate saturation of PTLs, assuming a uniform porosity of PTLs, using

$$s_l = \frac{W}{x_{PTL} \cdot \varepsilon_{th}} , \tag{2-34}$$

with water thickness W from Eq. 2-32, x_{PTL}, the width of PTL, and ε_{th}, theoretical porosity (Table 2-5).

Table 2-5: Porosities of PTLs used in the PEMWE cells. PEMWE-1 used PTL-3 used in this work for PNM simulations and non-electrochemical experiments.

	ε (supplier) (%)	**ε_{th} (compressed)** (%)	**Anode inlet flow rate** ($ml \cdot min^{-1}$)	**Current density applied** ($A \cdot cm^{-2}$)
PEMWE-1	77	71	3.25	1.0, 3.0, 6.0 and 9.0
PEMWE-2	42	37	3.25 and 10.00	0.1, 1.0, 3.0, 6.0 and 9.0

Chapter 3
Extracted Pore Networks

Parts of this chapter have been published in:

i) Altaf, H.; Vorhauer, N.; Tsotsas, E.; Vidaković-Koch, T. Steady-state water drainage by oxygen in anodic porous transport layer of electrolyzers: A 2D pore network study. *Processes* 2020**,** *8* (3), 362. DOI: 10.3390/pr8030362.

ii) Altaf, H.; Miličić, T.; Faber, F.; Vidaković-Koch, T.; Tsotsas, E.; Vorhauer-Huget, N., Use of reconstructed pore networks for determination of effective transport parameters of commercial Ti-felt PTLs*, Processes* 2025**,** *13*(4), 943*.* DOI: 10.3390/pr13040943.

The micro-CT scans used this chapter have been archived in an online repository:

DOI: 10.5281/zenodo.17315443.

In this chapter, Section 3.1 first compares invasion patterns from 2D PN drainage simulations with a microfluidic image and 3D PN simulations with LBM and CFD simulations. Section 3.2 applies the PN extraction method from Section 2.1 to extract PNs from micro-CT images. The extracted PNs for each PTL are compared, and transport parameters are calculated. These parameters are then evaluated against various literature approaches for all PTLs. In general, the influence of structure on transport parameters is discussed.

3.1 Validation of pore network model

In this section, a 2D microfluidic network is qualitatively compared to a 2D extracted PN, followed by a comparison of 3D extracted PN to an LBM simulation on the same domain using invasion pattern and saturation profile. Due to the absence of experimental data, that helps in visualizing pore-scale invasion, for PTLs used in this study, the results of microfluidic experiments from literature are used to draw a qualitative comparison with PNM-derived invasion profile. The neutron imaging experiments provided in this work cannot be used for this purpose because tomography images could not be obtained under dynamic conditions to observe the fluid pathways. The main goal here is to validate the drainage aspect of the PNM simulations, i.e., whether the path of least resistance is dependent on the radius of the invading menisci or not.

For this reason, a pore and throat network is constructed using the break-through image of a microfluidic experiment from Arbabi et al.[128]. The images captured during these experiments provide the gas (air) drainage pattern through a microfluidic network, designed to depict the PTLs. Basically, a PN is constructed onto the image (Figure 3-1) and then the pores and throats are ranked based on their sizes. These rankings are enough for the qualitative analysis, as the main goal is to observe if the drainage rule is followed i.e., the largest meniscus is always invaded or not. The absolute values are not important for the observation of drainage pattern in this case. Due to the simplicity of the image and the presence of a few pores and throats, no complicated image processing tools are applied. Additionally, the invasion pattern and the solid parts of the network have the same color (dark gray in Figure 3-1) and Otsu thresholding would not have been able to segment the image, as it does for extracted PNs which are used on dry PTL images (3D micro-CT scans). Unlike extracted networks explained in Section 2.1.2, and only in this case, the sizes are measured using the length measuring tool in ImageJ. The network of pores and throats is shown in Figure 3-1. The gas pores and throats are shown in blue (pores) and yellow (throats) while liquid pores are in red and liquid throats in black. As explained in Section 2.1.3, that pores and throats were invaded independently of each other.

The ranked pore and throat sizes are implemented in the PNM to compute the successive invasion of the PN. The result of the simulation is shown in Figure 3-2. It is observed that the invasion pattern simulated with the PNM is identical with the

experimental image (Figure 3-2). A good agreement shows the suitability of the drainage model to predict the invasion patterns based on the pore and throat size distributions.

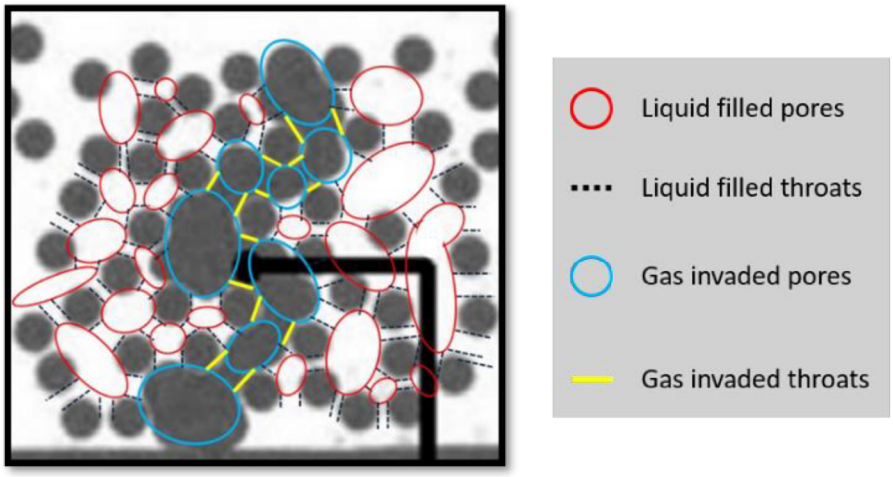

Figure 3-1: Microfluidic drainage experiment from Arbabi et al.[128] superimposed by a 2D PN. The image shows the steady-state invasion pattern at break-through of the gas phase into the water channel (at the top side of the image). Image reproduced from Altaf et al.[98], under the Creative Commons Attribution 4.0 International License (CC BY 4.0).

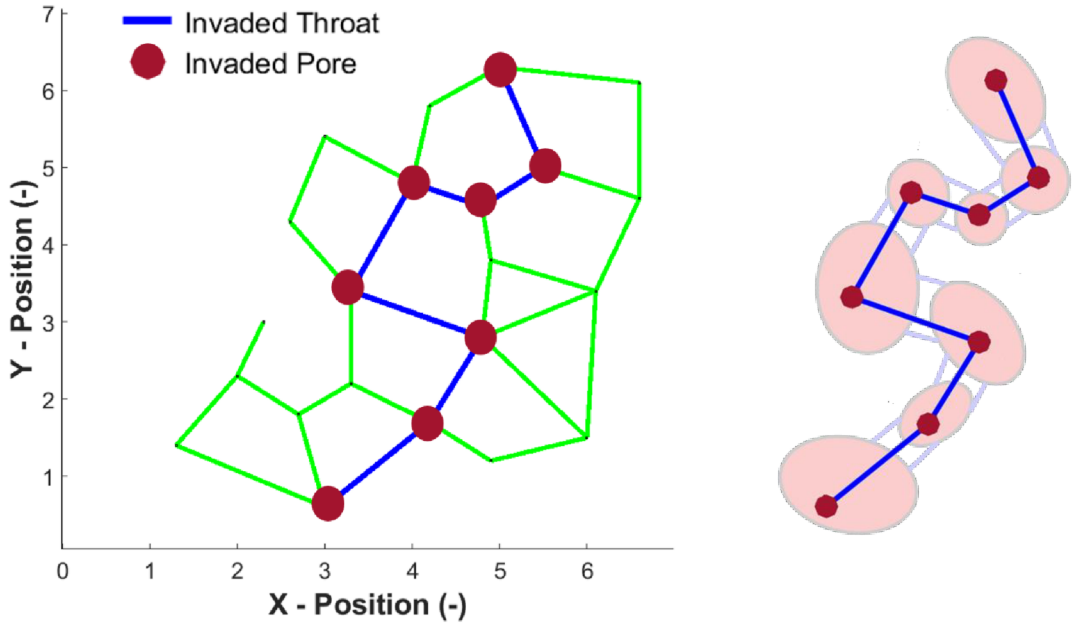

a) b)

Figure 3-2: a) Invasion pattern obtained from PNM simulation; b) comparison of invasion patterns from PNM simulation and experiment result: The blurred background shows the drainage pattern from the experimental image. The blue lines and red dots depict the pathway obtained through PNM simulations. Images adapted from Altaf et al.[98], under the Creative Commons Attribution 4.0 International License (CC BY 4.0).

To compare the invasion profile from a 3D PN, LBM simulation results from Bhaskaran et al.[57] are used. They computed the saturation profiles for PTL-1 (Table 2-1) along with the phase distribution using a domain size of

400 µm × 400 µm × 800 µm. The results from this study are compared to an extracted PN simulated using PNM on the exact same structure (Figure 3-3).

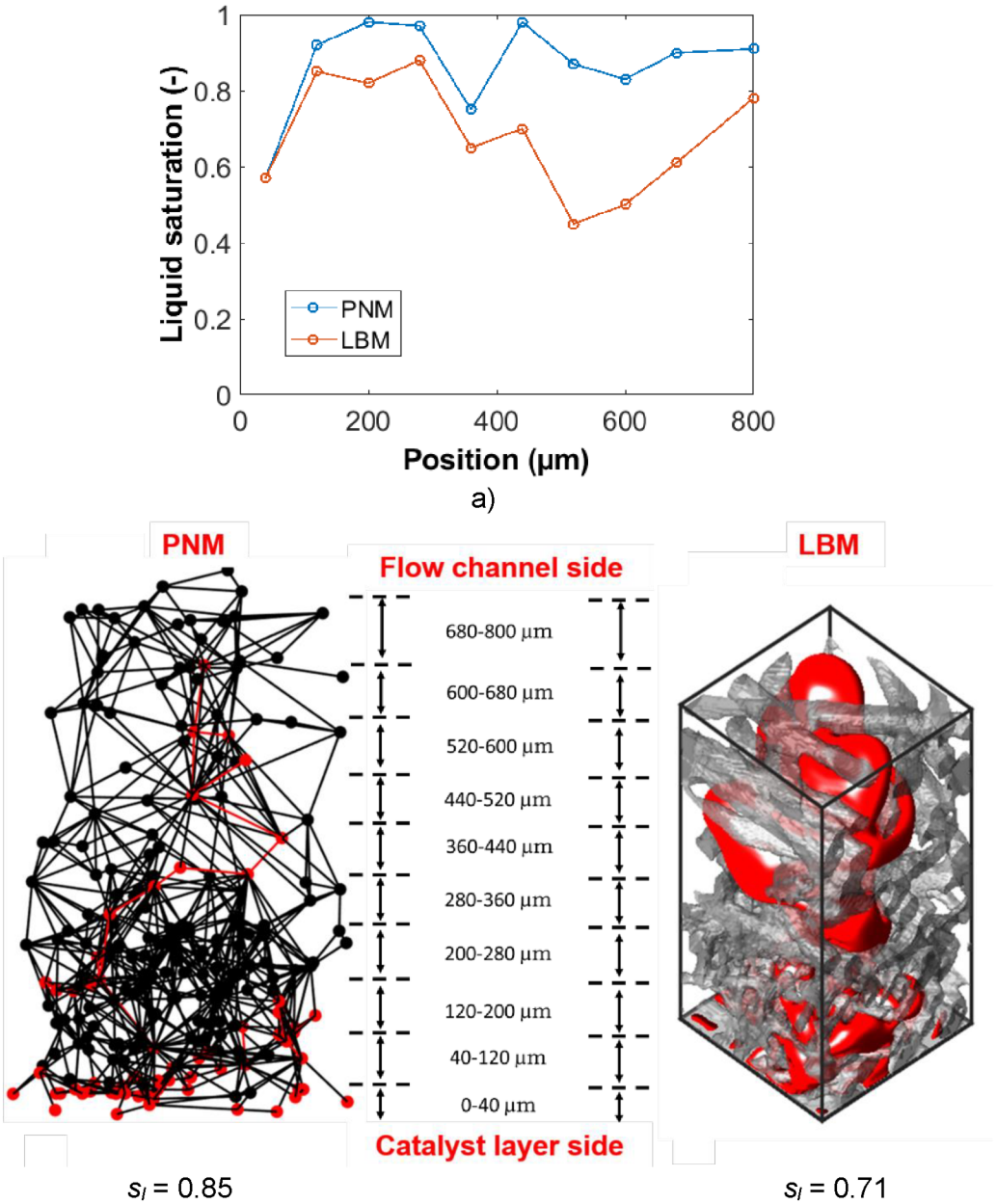

Figure 3-3: a) Comparison of saturation profiles for PNM and LBM; b) visualization of gas invasion pattern (in red) obtained through PNM and LBM. The phase distribution and saturation data presented here are taken from the work of Bhaskaran et al.[57], which also provides the details of the LBM simulation.

The invasion pattern obtained by the PNM is found out to be fairly similar to the one predicted by the LBM (Figure 3-3a). It can be seen that the invasion follows a similar trend i.e., the shape of the two graphs, with respect to position, is quite similar. These profiles are obtained by dividing the domains into several slices and the saturation in each slice is plotted against its position.

In Figure 3-3a, it can be clearly seen that the exact values of saturation with respect to position differ from each other. This difference in the saturation profiles is mainly due to the core difference in the geometry of both domains (PN: spheres and cylinders; LBM: actual domain from micro-CT) and the difference between the nature of invasion: PNM employs a quasi-steady, stepwise invasion, whereas LBM captures a fully transient invasion process. In addition to that, in the case of PNM, the saturation profiles are obtained based on the position of pore and the position of throat centers. If a throat is present in between two slices (Figure 3-3b), it cannot be split up to attribute its volume to both slices for the calculation of saturation. The saturation profiles only consider the position of the center and assign it to the corresponding slice. Moreover, in PNM, the pores and throats are either completely filled or empty. This is why the exact amount of liquid or gas present in each slice cannot be obtained. On the other hand, in LBM plot, the liquid and gas pixels at each location can be used to plot saturation profile, which depicts exactly the liquid and gas regions in the geometry.

Beyond these differences, in PNM all pores on the gas inlet side are assumed to be gas-saturated at the start of the simulation, whereas Bhaskaran et al.[57] randomly distributed 13 gas injection points, each 4 µm thick, at the gas inlet of the geometry. This also explains the difference of 14 % between the overall break-through saturation of PNM and LBM (Figure 3-3b). Regardless of these differences, a good agreement between the invasion trend and a fair agreement between the overall saturations underscores the applicability of the PNM, even with structural approximations.

Arguably, it can be said that LBM is suitable for exact solutions when the physics of pore-scale invasions need to be studied. For studying larger domains and estimating transport parameters from a porous structure, PNMs, although simplified, offer a computationally efficient option. Generally, a compromise between domain size, accuracy, and computational time has to be made when choosing a suitable simulation method. This depends on the required target of the simulations.

In a similar manner, a smaller domain of 200 µm × 300 µm × 300 µm from PTL-1 (Figure 3-4a) is also used to compare the invasion patterns, overall saturation, and simulation time of PNM with LBM and CFD using the Volume of Fluid (VoF) approach in StarCCM+. For this collaborative work, the LBM simulations were performed by M.Sc. Supriya Bhaskaran at OVGU, Magdeburg using the LBM provided in their published work[57]. The CFD simulations were performed by M.Sc. Adarsha Kumara Adagalale Jinadath as part of their Master's thesis[129], supervised by Dr. Nicole Vorhauer-Huget at OVGU, Magdeburg.

A small domain size was chosen due to high computational power requirements for LBM and CFD simulations. The invasion pattern obtained from PNM is found to be in good agreement with both of the approaches i.e., a drainage path at the right side of the outer most plane (Figure 3-4b). 2D images with a perspective from xy-plane are used to highlight this plane, where the invaded pores in red for all

simulation approaches can be seen. In this region, larger sized pores (~ 100 µm) are present compared to the average pore size (~ 60 µm) of this network.

Similar to the 14 % difference in overall breakthrough saturation between PNM and LBM observed in Figure 3-3b, the overall break-through saturation values differed by 12 % in these simulations too (Figure 3-4b). When compared to CFD, the PNM-predicted saturation differed by 18 %. These discrepancies can be attributed to fundamental differences in the simulation methods and the geometries used. However, a significant difference in computational time was also observed (Figure 3-4b), with PNM being considerably faster than both LBM and CFD. This highlights the practical applicability of PNM. Despite its inherent approximations and simplifications, PNM successfully captured invasion patterns that showed good agreement with LBM and CFD, while also predicting saturation values that are reasonably consistent with those obtained from these more computationally intensive methods.

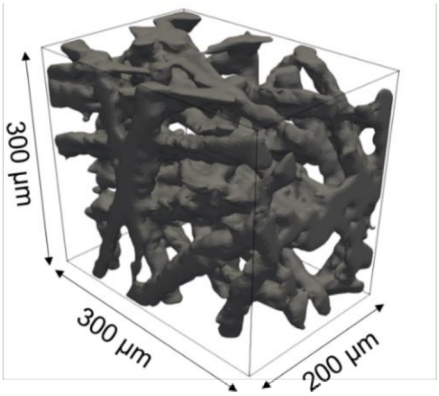

a)

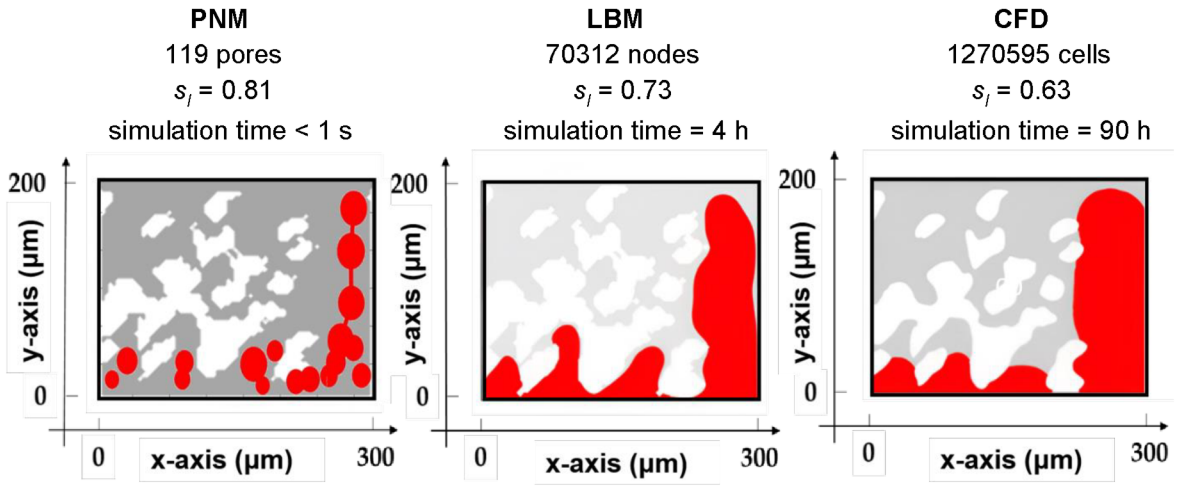

b)

Figure 3-4: a) 3D domain used for the comparative analysis of different simulation methods; b) comparison of gas invasion patterns (shown in red) obtained from each method. For this collaborative study at OVGU Magdeburg, LBM simulations[57] were performed by M.Sc. Supriya Bhaskaran and CFD simulations[129] by M.Sc. Adarsha Kumara Adagalale Jinadath as part of their Master's thesis, supervised by Dr. Nicole Vorhauer-Huget.

3.2 Commercial PTLs

3.2.1 Micro-CT scans

The structural information is extracted by X-ray micro-CT using CT-Alpha by ProCon X-ray GmbH, Sarstedt, Germany with a resolution of 3.9 µm per voxel. The image reconstruction is done using Volex (Fraunhofer ISS, Fürth, Germany) and image processing is performed in ImageJ (2.1051). In Table 3-1, it can be seen that the porosity values are slightly smaller than the producer values. This is most probably explained with small uncertainties in both, binarization[130] and the local variation in porosities (ε) and fiber diameters (d_f) in the PTLs. The porosity values reported by suppliers are typically based on bulk weight measurements of large PTL sheets, and thus represent averaged properties over a large area. However, porosity can vary locally within the structure, especially over smaller domains like those used in image-based analyses. Additionally, the suppliers generally do not provide any indication of the measurement uncertainty or variability in porosity across the produced PTLs, which can further contribute to the observed differences. To verify, the porosity is also calculated using GeoDict simulation software by Math2Market GmbH, Germany and Pulverpyknometer/GeoPyc 1360 (Micromeritics Instruments Corporation) for compressed PTL-1, and both resulted in a porosity value of 74 %, which is exactly the same as obtained from the binarization of the micro-CT image (Table 3-1).

Table 3-1: PTL data extracted from micro-CT scans. Only PTL-1 was compressed as it has been used in electrochemical experiments. The other two PTLs were used in pristine state.

PTL	Producer data			Micro-CT measurements		
	z (mm)	$\bar{d}_f$ (µm)	ε (%)	z, (mm)	ε (%)	$\bar{r}_p$ (µm)
						$\bar{r}_t$ (µm)
						$\bar{d}_f$ (µm)
Sylatech **(PTL-1)**	1.0	25 (top) 40 (bottom)	80	0.85 *(compressed)*	74	42.8 ± 14
						31.8 ± 20
						29.7 ± 10.9
Bekaert **(PTL-2)**	0.5	20	77	*(not compressed)*	73	50.9 ± 13
						32.4 ± 19
						23.4 ± 8.2
Bekaert **(PTL-3)**	1.0	20	77	*(not compressed)*	72	36.7 ± 9
						26.1 ± 17
						22.2 ± 5.9

The average pore radius ($\bar{r}_p$) and average throat radius ($\bar{r}_t$) for each PTL are provided in Table 3-1. Moreover, the fiber diameter (d_f) is analyzed using BoneJ[131] plugin in ImageJ. The average values obtained are: 29.7 ± 10.9 µm for PTL-1, 23.4 ± 8.2 µm for PTL-2 and 22.2 ± 5.9 µm for PTL-3. These measured fiber diameters, in contrast to the uniform values provided by the suppliers (Table 3-1), exhibit noticeable variations. These discrepancies likely contribute to the differences in porosity compared to the supplier's reported values. Highlighting these size variations here serves as a foundation for the subsequent discussion of results, particularly regarding permeability. The supplier-provided values represent bulk-averaged properties for a given product PTL and do not account for local variations within the inhomogeneous structure.

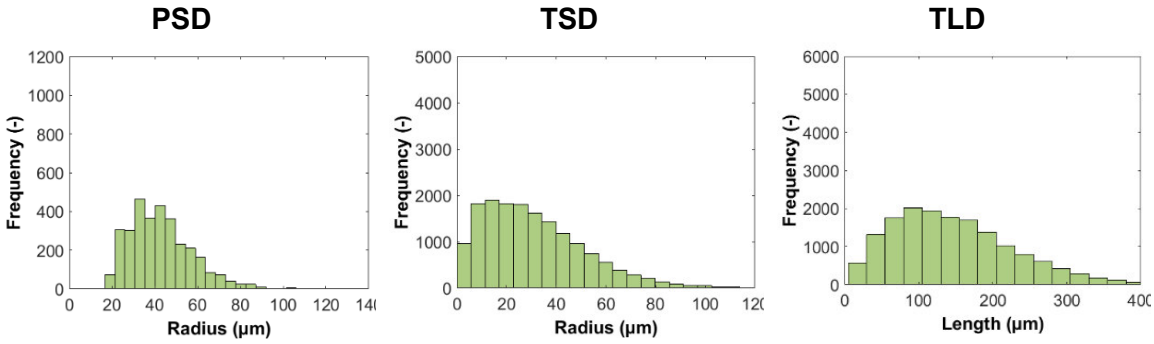

a) PTL-1

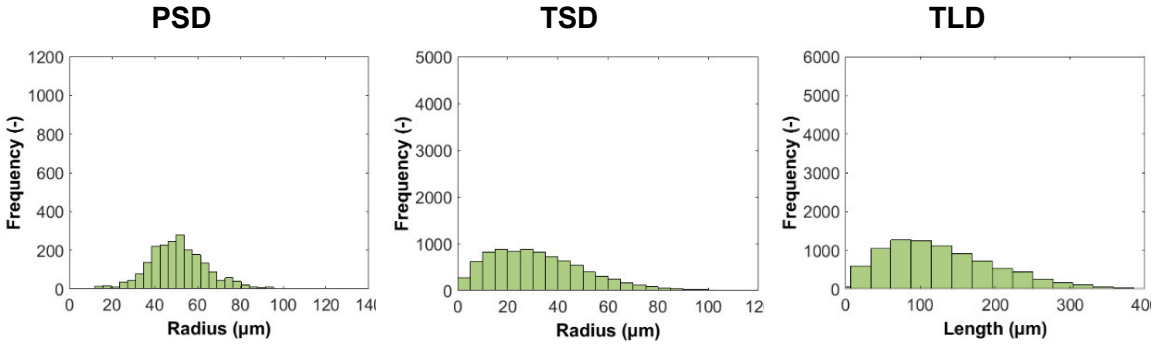

b) PTL-2

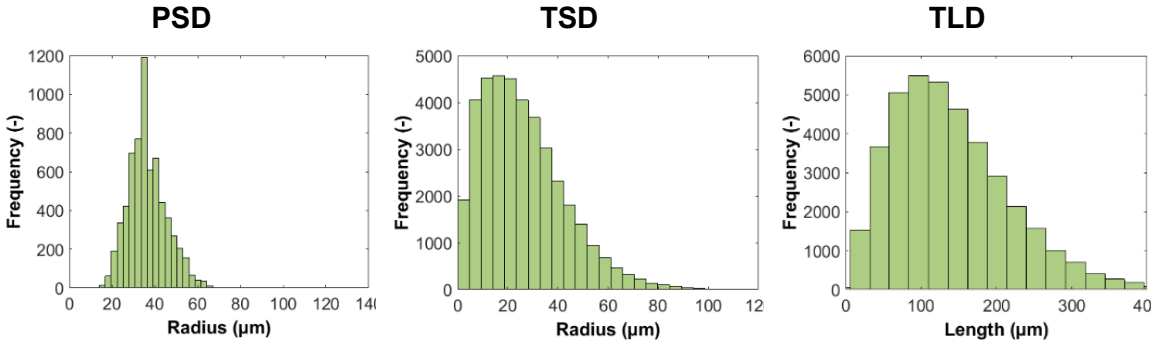

c) PTL-3

Figure 3-5: PTLs used in this work and their PSDs, TSDs and TLDs: a) PTL-1 from Sylatech, b) PTL-2 from Bekaert and c) PTL-3 from Bekaert. Scanned surface area for each PTL is 5.4 mm × 5.1 mm. Image reproduced from Altaf et al.[101], under the Creative Commons Attribution 4.0 International License (CC BY 4.0).

The PSDs/TSDs for the three PTLs obtained from watershed segmentation are shown in Figure 3-5. In addition to PSDs and TSDs, throat length distributions (TLDs) are also shown in Figure 3-5, with mean throat length *($\bar{L}$)* 148 µm, 128 µm and 140 µm for PTL-1, PTL-2 and PTL-2, respectively. The variations in the size distributions for PTL-2 and PTL-3, despite their similar thickness, structure, and imaging conditions, likely stem from local differences in fiber arrangement/sizes and diameter, sensitivity of binarization to subtle contrast variations, resolution limits affecting thin features, and potential reconstruction artifacts during image processing.

Information about the reconstructed PNs is summarized in Table 3-2. The overall volume of pores and throats in the network is used to calculate the porosity in order to make sure that the residual volume of inscribed pores is well distributed among the throats. The resulting porosities for PTL-1, PTL-2 and PTL-3 were found to be 73.7 %, 67.4 % and 71.6 %, respectively. This shows a very good agreement for PTL-1 and PTL-3 with a binarized porosity of 74 % and 72 % (Table 3-2), and highlights the applicability of the spherical pores and cylindrical throats. The difference of 5.6 % in the porosity of PTL-2 is possibly due to the lower coordination number (~ 8) compared to the other two PTLs (Table 3-2) and hence, resulting in less possibilities to allocate the residual pore volume to throats by a pore with an inscribed ball. In such cases, other concepts e.g., the work of Faber et al.[132], could yield a better accuracy.

Table 3-2: PN parameters of the studied PTLs. Note that the domain thickness is less than the sample thickness provided in Table 3-1 due to the cropping of some layers from the micro-CT image stacks, which is required for image processing. Reproduced from Altaf et al.[101], under the Creative Commons Attribution 4.0 International License (CC BY 4.0).

	PTL-1	**PTL-2**	**PTL-3**
Computational domain (mm^3)	5.40 × 5.10 × 0.53	5.40 × 5.10 × 0.34	5.40 × 5.10 × 0.78
No. of pores (-)	3134	2065	6547
No. of throats (-)	16063	8513	38873
Mean coordination number (-)	10.3	8.3	11.9
Reconstructed PN porosity (%)	73.7	67.4	71.6
Binarized micro-CT image porosity (%)	74	73	72

3.2.2 Determination of structure-related mass transport parameters

Utilizing the reconstructed domains and the PNM explained in Section 2.1, capillary pressure curves along with absolute and relative permeabilities, and residual PN liquid saturations are derived from PNM simulations. The simulations are performed using T = 353.15 K, γ = 0.0627 N/m and θ = 60°. The selected wettability is based on the wettability of Ti with water[133]. Additionally, the capillary pressure curves and absolute permeabilities are determined using correlations from literature relevant to PEMWE.

i) Saturation

In PNM simulations, residual liquid saturation (s_r) represents the final saturation level, occurring when the liquid phase is completely fragmented into isolated clusters, preventing any continuous connection between the top and bottom of the PTL[134]. At this stage, liquid transport ceases, and the remaining liquid cannot be drained by the invading gas phase. The PN liquid saturation (using Eq. 2-6) at this point, is referred to as the residual liquid saturation. For PTL-1, the liquid phase is entirely fragmented at a liquid saturation of 64 %, halting transport across the domain. Similarly, residual saturations are observed for PTL-2 (65 %) and PTL-3 (19 %) too. The significantly lower liquid saturation in PTL-3 suggests that it allows more lateral gas pathways, which could hinder water transport if these pores are not imbibed efficiently again by water. In contrast, PTL-1, with its graded structure, exhibits gas fingering, where the gas phase preferentially follows the vertical pore size gradient rather than spreading laterally[135]. Larimi et al.[136] also showed that, in thicker PTLs, the probability of lateral invasion pathways being formed increases. They argued that the increased number of lateral pathways would then hinder the water imbibition in such PTLs.

The comparison between PTL-1/PTL-2 and PTL-3 emphasizes the balance between gas removal and liquid retention, which is vital for optimal performance. Although PTL-3, with its slightly narrower PSD, appears to enhance gas removal, the graded structure of PTL-1 and relatively thin PTL-2 supports more effective liquid retention while still providing adequate pathways for gas removal. This suggests that if the drained pores in PTL-3 do not become repeatedly saturated with water during actual operation, the lower residual liquid saturation could lead to water starvation in PEMWE. The repeated imbibition is highly unlikely at steady-state operations and dry regions tend to persist, as reported in literature[87,88]. Such water starvation would not only reduce system efficiency but also accelerate component degradation, particularly CCM, due to reduced heat transfer across the PTL. This is especially critical during high current density operations, where maintaining effective heat removal through sufficient liquid transport is essential. Considering only the saturation, PTL-1 and PTL-2 seem to offer better water retention in comparison to PTL-3.

Along with the residual saturation, the liquid saturation profiles for each PTL are presented in Figure 3-6. The dotted lines in Figure 3-6 indicate the top of the PTL. In Figure 3-6a, the profiles are shown at the beginning of the simulation, when only the surface pores are empty, while all other pores and throats are saturated with liquid. Figure 3-6b illustrates the profiles at the moment of initial gas break-through at the bottom of the pore network. This break-through occurs shortly after gas begins to invade the system in all cases. At this stage, only a minor change in overall saturation is observed compared to Figure 3-6a, as the PNs are relatively thin, with only a few pores (< 5) across the thickness, and the break-through happens after just a few invasion events in all cases (fewer than 10).

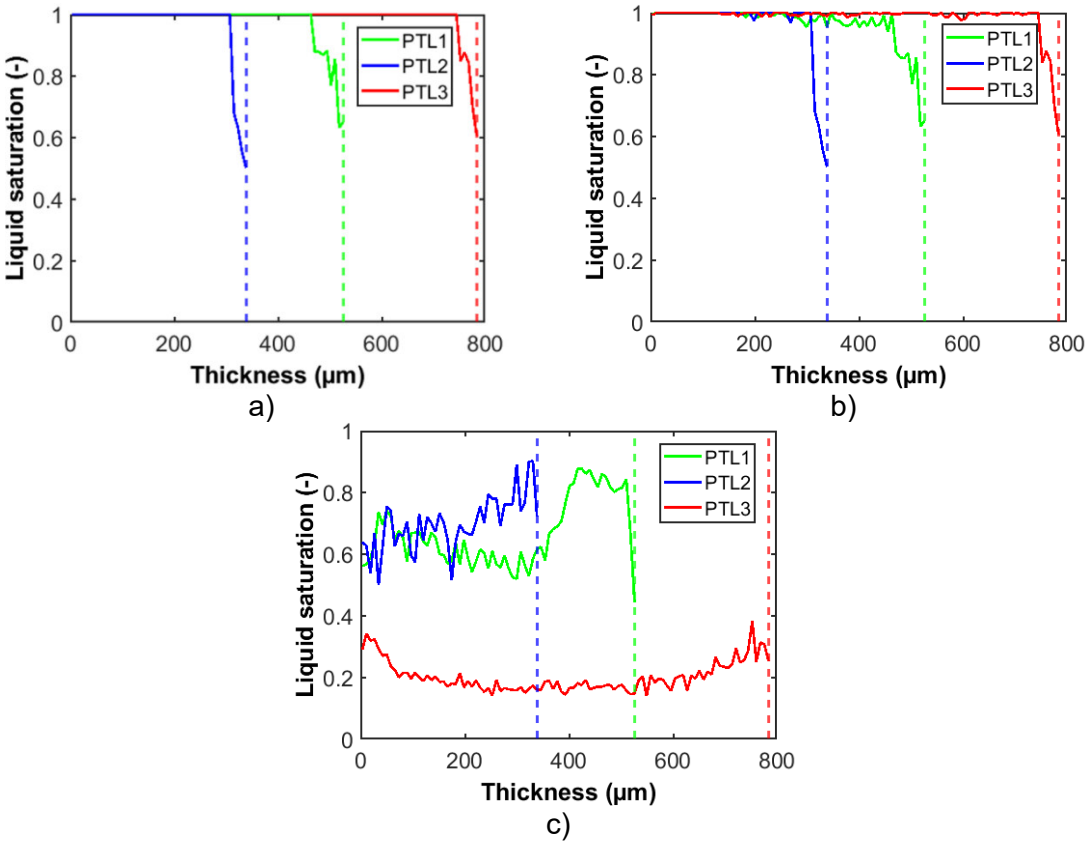

Figure 3-6: Saturation profiles as a function of PTL thickness: a) At the beginning of the simulation, where all surface pores are saturated with gas (initial saturations are s_l = 0.98, 0.97, and 0.99 for PTL-1, PTL-2 and PTL-3, respectively; b) the point of initial gas break-through (s_l = 0.97, 0.96, and 0.99); c) the moment of complete water-disconnection ($s_l = s_r$ = 0.64, 0.65, and 0.19). The bottom of a PTL is represented by the zero of x-axis, and the dotted lines represent the top side (CL side). Image reproduced from Altaf et al.[101], under the Creative Commons Attribution 4.0 International License (CC BY 4.0).

In Figure 3-6c, the saturation profiles are shown for the scenario where the water transport pathways between the top and bottom are completely interrupted (also reflecting the residual liquid saturation in the PN). The results indicate that the top of PTL-1 (~ 150 µm) has a higher liquid saturation (> 0.8) compared to its bottom (~ 0.6). This is attributed to the favorable invasion of larger pores at the bottom side. Such a saturation profile may be advantageous for high current density operations, where efficient liquid management is critical to maintain performance and prevent

membrane dehydration. A similar behavior is observed in PTL-2, which lacks a graded structure.

In contrast, PTL-3 shows a more uniform distribution of the remaining isolated liquid clusters (as seen in Figure 3-6c), which is notably different from the other two PTLs. Interestingly, in PTL-3, break-through occurs at a high liquid saturation similar to the other two cases. However, following the break-through, the gas phase spreads significantly and rather evenly before complete disconnection of liquid clusters is achieved. This is due to the greater thickness of the material (Table 3-1), which offers more invasion pathways before complete water-disconnection occurs.

ii) Absolute permeability

The PTLs' permeabilities are determined using the extracted PNM. The computed values are summarized in Table 3-3. Additionally, PTL-1 was analyzed using the commercial flow simulation software GeoDict (see Appendix A.5) to calculate the intrinsic permeability. A permeability of $1.1 \cdot 10^{-10}\,m^2$, which is similar to permeability of $1.5 \cdot 10^{-10}\,m^2$ for PTL-1 in Table 3-3, was found for a domain size of 1.95 mm × 1.95 mm × 0.80 mm. In general, the absolute permeability values from PNM are fairly similar, likely due to the comparable pore sizes and nearly identical porosities of these PTLs. A slightly higher value for PTL-1 can be attributed to the PSD in PTL-1 with less smaller pores below 20 µm. Notably, the maximum pore size for PTL-1 (128 µm) is also higher than for other PTLs (PTL-2: 106 µm and PTL-3: 88 µm). For comparison, intrinsic permeabilities are computed with the Jackson and James model (JJM)[55,137], usually applied to high-porosity fiber materials,

$$K = \frac{3d_f^2}{80(1-\varepsilon)}[-\ln(1-\varepsilon) - 0.931]\,. \tag{3-1}$$

In addition to JJM, the Tomadakis and Sotirchos model (TSM)[138,139],

$$K = \frac{\varepsilon(\varepsilon-\varepsilon_p)^{(\alpha+2)}d_f^2}{32(\ln\varepsilon)^2(1-\varepsilon_p)^{\alpha}[(\alpha+1)\varepsilon-\varepsilon_p]^2}, \tag{3-2}$$

used for random fiber structures is employed as well. In the given equations, d_f is the fiber diameter and ε is the porosity (Table 3-1). In Eq. 3-2, α = 0.785 (fitting parameter) and ε_p = 0.11 (percolation threshold) are the Archie's law parameters for a fibrous structure like PTL when fibers are arranged in a 2D plane and the flow is perpendicular to the plane of fibers[138]. The computed absolute permeabilities using Eq. 3-1 and 3-2 are summarized in Table 3-3 along with the PNM results. Note that the results for PTL-2 and PTL-3 are identical when using Eq. 3-1 and Eq. 3-2 because they have the same values of porosity and fiber diameter provided by the supplier (Table 3-1).

The differences between the PNM-permeability values and the intrinsic permeability values derived from TSM and JJM are essentially due to the underlying assumptions and limitations of each approach. These specifically developed intrinsic correlations for porous media with fibrous structures make several key idealizations to simplify the complex nature of real porous materials. For example, TSM assumes a porous medium with homogenous and isotropic structure in terms of porosity and fiber size, whereas PNM accounts for the local changes in porosity, as it is based on the extracted structure. In porous materials, such as PTLs, local variations can have a large impact on permeability. Although, these assumptions are necessary to create analytical expressions for permeability, they can introduce discrepancies when comparing their results to PNM extracted permeability. Clearly, PNM simplifies the pore geometry by a large extent too, but accounts for the pore connectivity and local transport. The errors due to thresholding, image resolution, neglection of varying contact angles and finite size effects also play a role in the permeability predictions of PNM. The advantage simply lies in the computationally efficient approach of PNMs while taking the microstructure into account.

Table 3-3: Absolute permeabilities determined by PNM simulations and literature correlations. Reproduced from Altaf et al.[101], under the Creative Commons Attribution 4.0 International License (CC BY 4.0).

K (m^2)	PTL-1		PTL-2	PTL-3
PNM	$1.5 \cdot 10^{-10}$		$1.4 \cdot 10^{-10}$	$1.1 \cdot 10^{-10}$
TSM	$0.7 \cdot 10^{-10}$	(d_f = 25 µm)	$0.3 \cdot 10^{-10}$	$0.3 \cdot 10^{-10}$
	$1.8 \cdot 10^{-10}$	(d_f = 40 µm)		
	$1.3 \cdot 10^{-10}$	(Mean)		
JJM	$0.8 \cdot 10^{-10}$	(d_f = 25 µm)	$0.4 \cdot 10^{-10}$	$0.4 \cdot 10^{-10}$
	$2.0 \cdot 10^{-10}$	(d_f = 40 µm)		
	$1.4 \cdot 10^{-10}$	(Mean)		

Figure 3-7 illustrates the variation in permeability as predicted by two literature-based approaches, highlighting its dependence on key parameters. Both methods yield comparable permeability values across the range of porosities and fiber diameters outlined in Table 3-1 and Table 3-3, particularly when the TSM is adjusted using $\varepsilon_p = 0.11$ and $\alpha = 0.785$. However, the JJM model consistently predicts slightly higher permeability values than the TSM. Within the studied range, permeability exhibits a linear relationship with porosity. Furthermore, a change in porosity of about 8 % results in a 2.5 times higher permeability (i.e., an increase from $K = 0.2 \cdot 10^{-10}$ m² to $K = 0.5 \cdot 10^{-10}$ m², assuming a fiber diameter of 20 µm and applying the JJM model).

Fiber diameter, however, has a more pronounced impact, leading to permeability variations spanning more than an order of magnitude, from approximately $K = 2.0 \cdot 10^{-11}$ m² to $K = 2.0 \cdot 10^{-10}$ m², for both approaches within the studied range.

This suggests that accurately determining fiber diameter is more critical for permeability estimation than other parameters. This is why it is argued that the PNM values are much more accurate than the empirical models, because PNM considers the variations in fiber diameter, whereas the literature models consider a constant value for fiber diameter. Additionally, Figure 3-7 indicates that parameters α and ε_p can influence permeability in a manner comparable to porosity and fiber diameter.

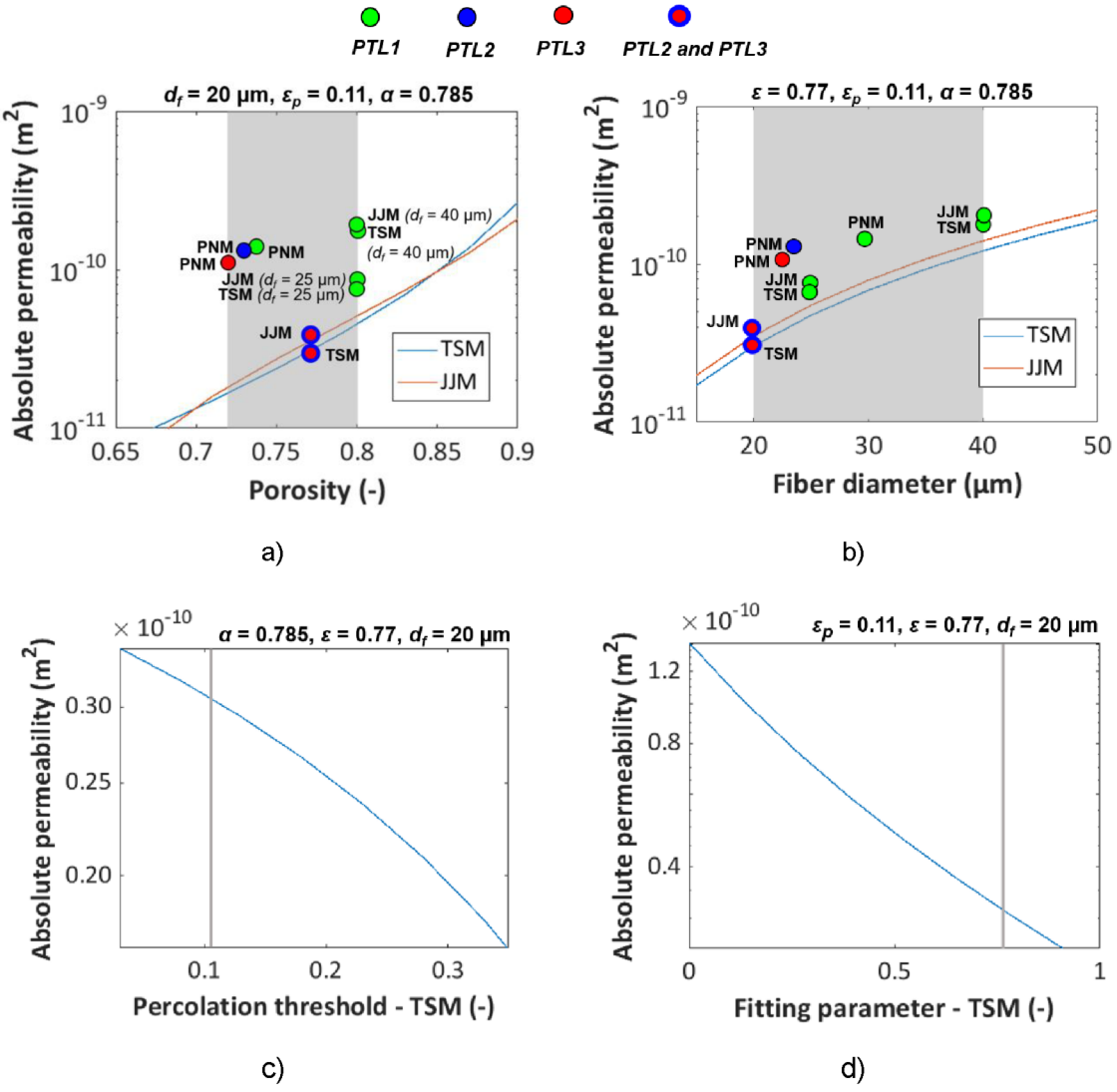

Figure 3-7: Dependence of TSM and JJM on: a) porosity (ε) with a fiber diameter of 20 µm; b) fiber diameter (d_f) with a porosity of 0.77; c) percolation threshold (ε_p); d) the fitting parameter (α), applicable only to TSM, within the ranges relevant to the studied cases (ε = 0.77 and d_f = 20 µm). In (c) and (d), the gray lines indicate the reference setting of the TSM, while the shaded areas in a) and b) represent the range of values observed in the studied PTLs. Permeability values derived from PNM are plotted against the corresponding average porosity and fiber diameter for each case. Image reproduced from Altaf et al.[101], under the Creative Commons Attribution 4.0 International License (CC BY 4.0).

Given these findings, it is not surprising that the best agreement between PNM simulations and theoretical models is observed for PTL-1, which features a graded structure. Since permeability is more sensitive to fiber diameter than other

parameters, the thicker fibers (d_f = 40 µm) in PTL-1 make up for the underpredicted values observed for other PTLs when a single fiber diameter (d_f = 20 µm) is used. A good agreement of JJM and TSM with PNM is found for a fiber diameter of 40 µm or a porosity of 80 % for PTL-1 (Table 3-3; Figure 3-7).

iii) Relative permeability

The relative permeabilities of gas (oxygen) and liquid (water) are computed on the basis of saturation profiles ($s_{l,g}$) obtained by PNM simulations resulting in partially saturated PNs. The results are summarized in Figure 3-8 for liquid saturations varying between s_l = 1 (starting point of invasion) and s_r (residual saturation). Figure 3-8 illustrates that liquid permeability remains relatively high in both PTL-1 and PTL-2.

Notably, PTL-1 exhibits 1.75 times greater liquid permeability than PTL-2, despite their similar structural properties and residual liquid saturation levels. This suggests that the liquid distribution in PTL-1 is more conducive to liquid transport, likely due to differences in invasion patterns, specifically the more pronounced gas fingering observed in the graded structure of PTL-1 with larger pores on one side. In contrast, PTL-3, which has a significantly lower residual liquid saturation (0.19) than the other two PTLs (0.65), experiences a sharp decline in relative liquid permeability, dropping below 0.1.

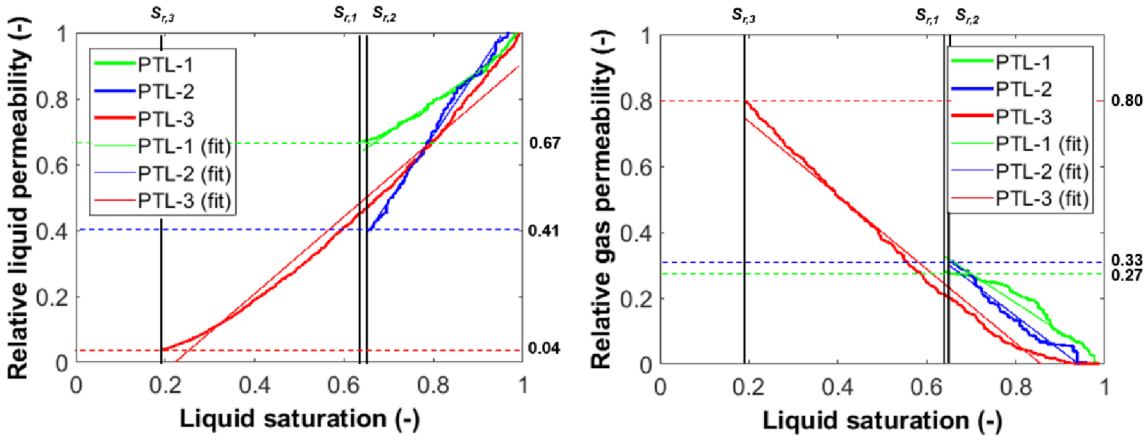

a) b)

Figure 3-8: Relative permeability of a) liquid and b) gas as a function of overall liquid saturation. The residual liquid saturation s_r is specified by the black vertical lines. The thin colored lines are linear approximations of the relationships. Image reproduced from Altaf et al.[101], under the Creative Commons Attribution 4.0 International License (CC BY 4.0).

As expected, maximum relative gas permeability occurs when high gas pressures displace the maximum amount of water just as liquid clusters disconnect (Figure 3-8b). This indicates that gas transport would improve under high gas pressures, as more gas pathways open, but that could be at the cost of lower liquid saturation or dehydration of PTL. Due to the higher residual liquid saturations in PTL-1 and PTL-2, their relative gas permeabilities remain lower than in PTL-3, where gas is

able to drain more pores and throats containing water. Consequently, PTL-3 exhibits the highest relative gas permeability, as it retains the least amount of liquid.

As shown in Figure 3-8, PTL-1 exhibits additional advantageous characteristics. Its high liquid saturation along with the larger pores in its graded structure results in high relative liquid permeability (0.67). At the same time, the relative gas permeability of PTL-1 (0.27) is almost the same as that of PTL-2 (0.33), leading to a significantly better overall liquid and gas transport. Since the absolute permeability of PTL-3 is only slightly lower than that of PTL-1 and PTL-2, it can be inferred that PTL-3 can offer better gas transport properties because of high saturations. This would only be beneficial if drainage and imbibition cycles occur repeatedly i.e., after each drainage cycle the PTL is wetted again up to the maximum possible value. However, this is yet to be proven with the help of high resolution (pore-scale) and in-operando PEMWE experiments. The evidence, so far is nonexistent.

In literature, only one study[140] mentions periodic imbibition and drainage cycles with the help of microfluidic experiments. In these microfluidic experiments, a few linear channels represent a PTL which can be simply drained and imbibed with the same pattern after each cycle. In reality, if a PTL such as PTL-3, drains a lot of water out of the PTL, it is not guaranteed that the water imbibition will results in reoccupying of the gas pores. The pressure fluctuations in the PEMWE or in inlet water channels cannot be easily predicted. It is more likely that this does not happen and, in such cases, the PTL will be left with few water saturated pores leading to a decline in cell performance due to poor water permeability and increased degradation due to poor heat transport.

According to Maier et al.[85], no new pathways are created in a PTL during operation and the ratio of water to gas transport pores stays the same. Therefore, maintaining a balanced distribution of liquid and gas pathways is crucial for optimal performance. Other works have also mentioned unchanging gas/liquid distributions in the PTL regardless of the operating current densities instead of cyclic drainage and imbibition[39,83,87]. Considering this, it is more advantageous to have a PTL, such as PTL-1, with graded structure leading to a quick release of gas due to favored vertical invasions and providing a balance between liquid and gas transport. This not just prevents gas accumulation in the PTL but, as well as, provides sufficient water supply at the CL for the reaction and membrane hydration.

The relative permeabilities in Figure 3-8 can be approximated by linear relationships,

$$k_{rel,l}(s_l) = c_l \cdot s_l + n_l\,, \tag{3-3}$$

and

$$k_{rel,g}(s_l) = c_g \cdot s_l + n_g\,, \tag{3-4}$$

where,

$$s_l = 1 - s_g . \tag{3-5}$$

The fitting parameters are provided in Table 3-4 which can be used for the parameterization of CMs. These linear relationships are significantly different than the usually assumed cubic dependence[141–143],

$$k_{rel,l} = s_l^3 , \tag{3-6}$$

derived from empirical observations, especially for the non-wetting phase.

Table 3-4: Fitting parameters of relative permeability plots approximated by linear relationships using Eq. 3-3 and Eq. 3-4. Adapted from Altaf et al.[101], under the Creative Commons Attribution 4.0 International License (CC BY 4.0).

	PTL-1	**PTL-2**	**PTL-3**
c_l	0.94	2.00	1.17
n_l	0.04	-0.91	-0.26
c_g	-0.87	-1.03	-1.12
n_g	0.89	0.97	0.97

iv) Capillary pressure

The capillary pressure curves for all PTLs are shown in Figure 3-9. The dotted lines in Figure 3-9 represent the incremental steps in pressure, leading to the simultaneous invasion of multiple pores and throats at a specific pressure level. This results in a corresponding stepwise decrease in liquid saturation. With this approach, it is assumed that all pores with an entry pressure lower than the current invasion pressure will be invaded automatically once the invasion front reaches them. This ensures a fair comparison with literature approaches shown in this section. If the P_c values of invaded pores or throats are plotted against s_l, the result would be a scattered point cloud, similar to what was reported by Vorhauer et al.[61].

The highest capillary pressures during the invasion process occurred at the moment when liquid clusters disconnected, corresponding to the residual PTL liquid saturation levels (PTL-1: 0.64; PTL-2: 0.65; PTL-3: 0.19). This marks the point at which the continuous liquid pathway between the open PTL invasion interface and the opposite side was lost. Beyond this stage, the capillary pressure curves are extended by fully invading the domains with gas. As illustrated in Figure 3-9, both the critical saturations and the capillary pressure curves obtained from PNM simulations are highly dependent on the PTL structure.

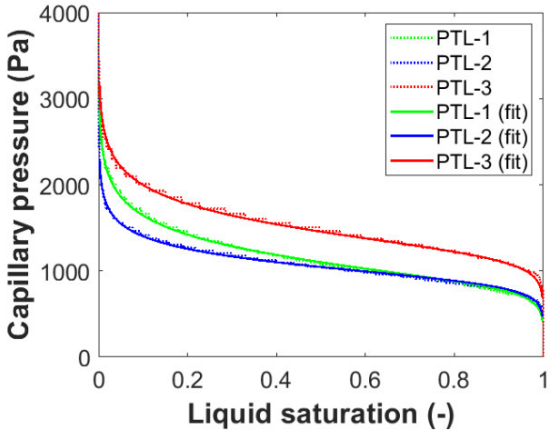

Figure 3-9: Comparison of capillary pressure curves obtained by PNM simulation for PTL-1, PTL-2 and PTL-3. The dotted lines are obtained from the PNM simulation and the solid lines represent the curve fit. Image reproduced from Altaf et al.[101], under the Creative Commons Attribution 4.0 International License (CC BY 4.0).

Figure 3-9 highlights two key observations. First, PTL-2 and PTL-3 exhibit nearly parallel trends. PTL-3, which consists of smaller pores, generally reaches higher capillary pressures compared to PTL-2, which has larger pores. This indicates that greater gas pressures are necessary to penetrate the smaller pores in PTL-3. The resulting rise in gas pressure at the CL interface could enhance gas transport by promoting higher gas pressure gradients across the PTL (i.e., between the CL and the flow channel), along with increased relative gas permeability and comparable absolute permeability to PTL-1 and PTL-2. Second, the capillary pressure curve of the graded PTL-1 transitions between the behaviors of PTL-2 (larger pores) and PTL-3 (smaller pores). At higher liquid saturations (above approximately s_l = 0.5), PTL-1 and PTL-2 exhibit significant overlap. This strong agreement suggests that PTL-1 and PTL-2 undergo similar invasion processes and require comparable gas invasion pressures, regardless of the graded structure.

The curves representing the PNM simulations results in Figure 3-9 could also be fitted using the correlation,

$$P_c = b \cdot \tanh^{-1}\left(2 \cdot s_l - 1\right) + e + m \cdot s_l^u \ , \tag{3-7}$$

with parameters b, e, and m (all in Pa) and u (unitless), summarized in Table 3-5.

In order to allow comparison with the correlations from literature[141–143], the capillary pressure curves are even computed for saturations lower than the residual saturations shown in Figure 3-9, realized by invading also the isolated liquid clusters in the PNM. The capillary pressure curves derived using the Leverett equation (LE)[142] are given by,

$$P_{c,LE} = \gamma \cdot \cos\theta \cdot \left(\frac{\varepsilon}{K}\right)^{0.5} \cdot J(s_l) \ . \tag{3-8}$$

In Eq 3-8, $J(s_l)$ is the Leverette function,

$$J(s_l) = 1.417 \cdot (1 - s_l) - 2.120 \cdot (1 - s_l)^2 + 1.263 \cdot (1 - s_l)^3, \quad (3\text{-}9)$$

that introduces the capillary pressure dependence on saturation for 0° < θ < 90°. ε and K represent porosity and absolute permeability respectively.

Along with LE, the Brooks-Corey equation[54] (BCE) is also commonly used for determination of capillary pressure curves of PTLs for PEMWE modeling[80,141]. The BCE is mathematically expressed as,

$$P_{c,BCE} = 2\gamma \cdot \frac{\cos\theta}{r_{max}} \cdot s_l^{-\frac{1}{\beta}}, \quad (3\text{-}10)$$

where r_{max} is the maximum pore radius in the porous medium and β is the PSD index. A higher value of β refers to a narrower PSD and vice versa. Unless stated otherwise, the BCE-plots in this section are plotted using β = 4, based on the work of Rajora et al.[141] for PEMWE and Brooks et al.[54]. Normally, at the place of s_l in Eq. 3-10, a normalised saturation s_l^n is used which depends on the residual saturation,

$$s_l^n = \frac{s_l - s_r}{1 - s_r}, \quad (3\text{-}11)$$

to account for the incomplete emptying of porous materials up to a certain saturation as illustrated in Figure 3-10. But for sake of comparison with PNM and LE, BCE is also plotted for an overall saturation between 0 and 1 i.e., $s_l^n = s_l$ in Eq. 3-10. Same values for surface tension and contact angle in Eq. 3-8 and Eq. 3-10 are used as for the PNM simulations (γ = 0.0627 N/m and θ = 60°). All other parameters used are taken from Table 3-2 and Table 3-3.

Table 3-5: Parameters of the capillary pressure curve correlation Eq. 3-7. Adapted from Altaf et al.[101], under the Creative Commons Attribution 4.0 International License (CC BY 4.0).

	b (Pa)	***e*** (Pa)	***m*** (Pa)	***u*** (-)
PTL-1	$-1.7 \cdot 10^2$	$-3.1 \cdot 10^4$	$3.2 \cdot 10^4$	$-6.8 \cdot 10^{-3}$
PTL-2	$-1.6 \cdot 10^2$	$7.1 \cdot 10^1$	$9.1 \cdot 10^2$	$-1.0 \cdot 10^{-1}$
PTL-3	$-2.1 \cdot 10^2$	$-3.2 \cdot 10^4$	$3.3 \cdot 10^4$	$5.9 \cdot 10^{-3}$

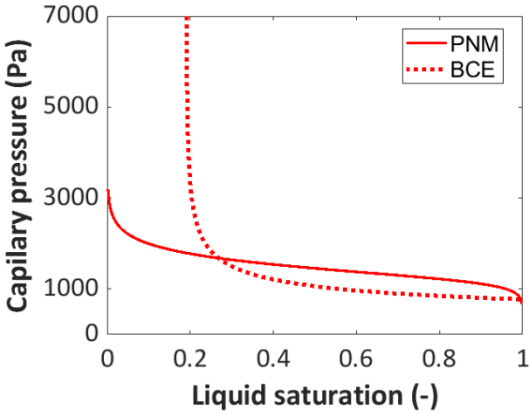

Figure 3-10: Capillary pressure curves for PTL-3 with parameters from Table 3-6 are plotted as an example to illustrate how BCE curve cannot be compared to LE and PNM when employing s_l^n instead of s_l. Image reproduced from Altaf et al.[101], under the Creative Commons Attribution 4.0 International License (CC BY 4.0).

Figure 3-11 illustrates that variations in the parameters used in both approaches allow for some flexibility in adjustments. Overall, both empirical correlations capture trends similar to those observed in the PNM. The best matches are highlighted in Figure 3-12 and Table 3-6.

Notably, Figure 3-11 suggests that porosity variations and maximum pore sizes are not the dominant factors. Instead, achieving accurate permeability values and an appropriate wetting angle appears to be crucial for aligning with PNM results. However, the plots indicate that good agreement between the literature correlations and PNM is primarily observed at intermediate liquid saturation levels. The values provided in Table 3-6 align well only with the assumed wetting angle of 60° (associated with LE); however, both the permeability and the maximum pore radius are notably lower in the fitted curves compared to those obtained from the PNM analysis.

Significant deviations are particularly noticeable for BCE at low saturations and for LE at both low and high saturations. The PNM simulation results show an offset in P_c at $s_l = 1$, meaning the curves do not start at P_c ($s_l = 0$) = 0. This is expected, as invasion begins at the first (top) interface pore at a discrete P_c value greater than zero, which is influenced by the size of the largest interface pore, as described by Young-Laplace equation (Eq. 2-5). While BCE partially captures this behavior, LE does not reflect it at all. BCE also aligns well at low saturations; however, considering the residual saturation for liquid cluster isolation, this aspect has minimal relevance for drainage invasion simulations. If the residual saturation were used in BCE instead, this would significantly overestimate capillary pressures, as illustrated in Figure 3-10. In conclusion, based on the findings of this study, neither LE nor BCE can be recommended for the studied high-porosity PTLs.

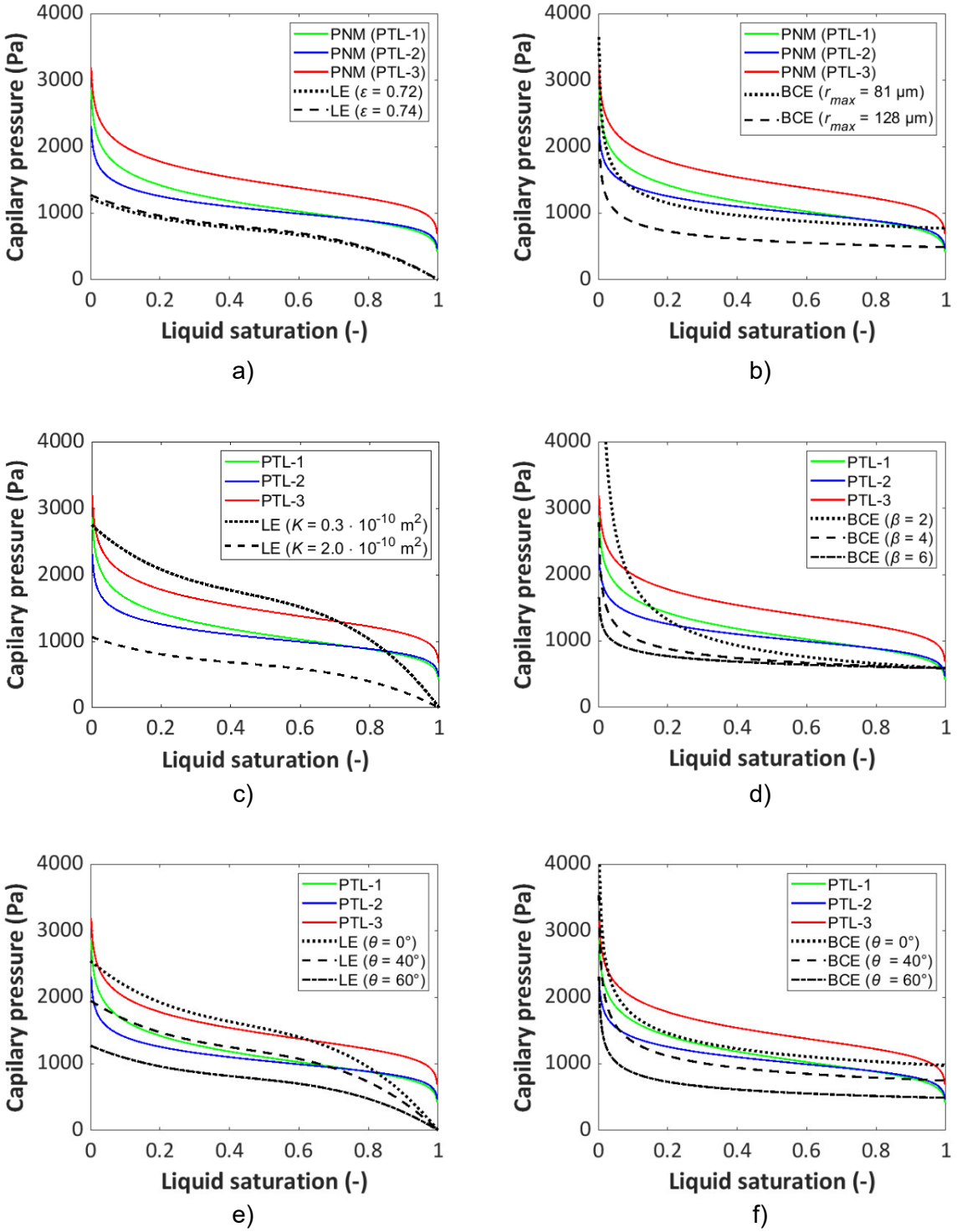

Figure 3-11: Comparison of LE and PNM capillary pressure curves at minimum and maximum values of a) porosity, ε (with θ = 60° and K = 1.4 · 10^{-10} m^2) and c) permeability, K (with θ = 60° and ε = 0.74). In e) LE curves are shown for θ = 0°, 40° and 60° (with ε = 0.74 and K = 1.4 · 10^{-10} m^2). Comparison of BCE and PNM capillary pressure curves: b) using minimum and maximum values of maximum pore radius, r_{max} (with θ = 60° and β = 4); d) using pore size index, β = 2, 4 and 6 (with θ = 60° and r_{max} = 106 μm); f) using θ = 0°, 40° and 60° (with β = 4 and r_{max} = 106 μm). Image reproduced from Altaf et al.[101], under the Creative Commons Attribution 4.0 International License (CC BY 4.0).

Table 3-6: Parameters of LE and BCE capillary pressure curves in Figure 3-12. Reproduced from Altaf et al.[101], under the Creative Commons Attribution 4.0 International License (CC BY 4.0).

	PTL-1	PTL-2	PTL-3
LE parameters			
ε	0.74	0.73	0.72
K	$0.60 \cdot 10^{-10}$ m^2	$0.84 \cdot 10^{-10}$ m^2	$0.39 \cdot 10^{-10}$ m^2
θ	60°	60°	60°
BCE parameters			
r_{max}	100 µm	90 µm	80 µm
β	4.3	5.2	5.2
θ	40°	50°	35°

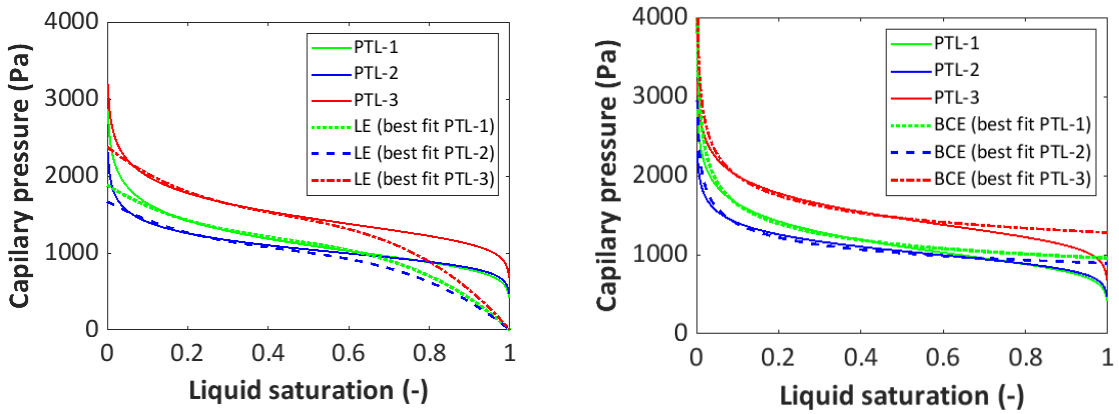

Figure 3-12: Best-fits for PTL-1, PTL-2 and PTL-3 using LE, BCE in comparison with PNM capillary pressure curves. Image reproduced from Altaf et al.[101], under the Creative Commons Attribution 4.0 International License (CC BY 4.0).

v) Thermal conductivity

In this section, the thermal conductivities of PTLs, obtained using a simplified model based on Fourier's law and Krischer's model are presented. This approach relies solely on conduction, while neglecting more complex heat transfer mechanisms such as heat pipe effect[109,110] or convection[144]. These additional mechanisms could play an important role under certain conditions, but are assumed to be secondary in the porous structure of PTLs under standard operating conditions. Certainly, incorporating more advanced models that include the heat pipe effects or convective contributions would yield more accurate results. However, the computational expense and complexity of such models must be carefully weighted against their added value for specific applications. Incorporating convective heat

transfer within the pores/throats or phase-change effects would require significantly more complex modeling approaches which are computationally expensive and require additional assumptions regarding fluid movement and phase interactions. This would be counterproductive to the goal of the methods presented in this work.

An advantage of using PNs and VNs is that they naturally account for the local geometry and connectivity of the porous structure. Unlike structural and semi-empirical models that rely on effective medium approximations, this method explicitly considers the spatial distribution of pores/throats and their thermal pathways, allowing for a more detailed representation of heat transfer within the structure. This makes the approach computationally efficient while relying on simple pore/throat geometries, yet still capable of capturing structural effects that influence heat transport, providing a valuable tool for analyzing the role of PTLs in heat transfer within a PEMWE.

The VN, along with the micro-CT extracted information from PNM, is used to calculate the thermal conductivity for the PTLs as explained in Section 2.1.5. The conductivity values for the completely dry ($s_l = 0$) and wet ($s_l = 1$) PTLs are shown in Table 3-7. The conductivities were also measured experimentally for dry PTLs using Hot Disk experiments. The mean value, for each PTL, from 15 single measurements is shown in Table 3-7. The value for PTL-1 is used to fit the weighting parameter, f (Eq. 2-25). An agreement was found between the dry conductivity value and VN-based value at $f = 0.81$ for PTL-1. On the other hand, the lower bound for thermal conductivity at $f = 1$ (λ_{ser}), for PTL-2 and PTL-3, was higher than the experimentally found value of 0.21 $W \cdot m^{-1} \cdot K^{-1}$ for PTL-2 and 0.20 $W \cdot m^{-1} \cdot K^{-1}$ for PTL-3 (Table 3-7). This can be attributed to the simplified nature of the model and, hence, loss of precision (difference of 0.05 and 0.08 $W \cdot m^{-1} \cdot K^{-1}$ from the minimum possible value i.e., λ_{ser}, for PTL-2 and PTL-3, respectively). The difference is not very significant. However, this means, the experimental values could not be used to fit the weighting parameter exactly for PTL-2 and PTL-3. For this reason, $f = 1$ is assumed for PTL-2 and PTL-3, so that the values can be as close as possible to the experimental values. Using a value of $f = 1$ yields conductivity values of 0.26 $W \cdot m^{-1} \cdot K^{-1}$ and 0.28 $W \cdot m^{-1} \cdot K^{-1}$, for PTL-2 and PTL-3, respectively i.e., a difference of 0.05 $W \cdot m^{-1} \cdot K^{-1}$ for PTL-2 and 0.08 $W \cdot m^{-1} \cdot K^{-1}$ for PTL-3 from the experimentally measured value.

High values of f mean that the series conductivity dominates. The series thermal conductivity model dominates when heat flows perpendicular to the layers of different materials – this occurs in laminated or layered structures, where materials with different thermal conductivities are stacked one on top of another. Arguably, high-porosity fiber-PTLs also exhibit such a structure where fibers are not perfectly connected in the direction of heat flow but rather stacked upon each other with layers of large pores between them. This means that heat must travel through the less conductive voids (air) between fibers. This increases thermal resistance, making the material behave more like a series model. Secondly, the overall material

porosities being ~ 75 % indicates that the heat transfer is limited by the insulating gas phase (air), similar to the conduction pathways in series model.

Table 3-7: Thermal conductivities: Estimated and measured values for all three PTLs using λ_s = 32.70 W·m^{-1}·K^{-1} for titanium, λ_f = 0.68 W·m^{-1}·K^{-1} for water, and 0.03 W·m^{-1}·K^{-1} for air. All the values used are for T = 80 °C.

Thermal conductivity (W·m^{-1}·K^{-1})		**PTL-1**	**PTL-2**	**PTL-3**
Dry	VN	0.34 (f = 0.81)	0.26 (f = 1)	0.28 (f = 1)
Dry	Hot Disk experiment	0.34	0.21	0.20
Dry	VN; λ_{ser} (f = 1)	0.27	0.26	0.28
Dry	VN; λ_{par} (f = 0)	26.05	26.28	27.20
Partially wet	VN; (s_r from PNM)	4.71 (f = 0.81) (s_r = 0.64)	2.58 (f = 1) (s_r = 0.65)	1.28 (f = 1) (s_r = 0.19)
Wet	VN	5.43 (f = 0.81)	4.39 (f = 1)	4.81 (f = 1)

The thermal conductivity values are also calculated for all PTLs, using the phase distribution from PNM of partially saturated PTLs at the water disconnect point (Section 3.2.2). As expected, PTL-3 has the lowest value of 1.28 W·m^{-1}·K^{-1} due to the lowest residual liquid saturation of 0.19. PTL-1 and PTL-2 had similar residual saturation (0.64 and 0.65, respectively) but their conductivity values have a difference of almost 2 W·m^{-1}·K^{-1}. This could be due to the large liquid pores present in PTL-1 at the water channel side due to the graded structure. These large liquid-filled pores can significantly impact the overall liquid conductivity. Another possible explanation could be the slightly lower reconstructed porosity of PTL-2 compared to PTL-1 (Table 3-2).

For the wet PTLs, only one study, by Schuler et al.[39], has been conducted for a PTL (thickness 1.0 mm and porosity 76 %) similar to the one in this work (PTL-3: thickness 1.0 mm and porosity 77 %), which can be used for comparison. With the help of measured temperature differences within an operating electrolyzer cell, they estimated the effective thermal conductivity of 3.0 W·m^{-1}·K^{-1} at 50 °C. Other than the difference in measuring methods, the difference of 30 °C between this study (λ at 80 °C) and their study (λ at 50 °C) could explain the slight difference in the thermal conductivity values of the wet PTLs. Additionally, various studies[84,87] have shown that the PTL cannot be completely wetted, whereas the VN-estimated value of 4.81 W·m^{-1}·K^{-1} assumes a fully wet PTL. Regardless, considering the model assumptions and the fact that the estimated value is not for a completely wet PTL (saturation not provided in the cited study), the difference between the two values is not substantial.

Additionally, the structural models mentioned in Section 2.1.5 (ME, EMT, etc.) are used to calculate the dry conductivity values. The results are shown in Table 3-8. Interestingly, none of these values come close to the values obtained using the Hot Disk experiments, except for EMT predicted values for PTL-2 and PTL-3 and the non-linear exponential relation for PTL-1. Similarly, in a study by Wang et al.[119] based on GDLs it was also shown that these correlations are not able to predict values closer to the experimental results unless they are modified for specific applications. It can be deduced that while the VN-based model requires fitting, it offers a better tool than these correlations and accounts for local pore connectivity effects and localized conduction bottlenecks. In contrast, the ME models[117,118] and EMT model[119] assume homogeneity, leading to over- or under-predicted values.

In Table 3-8, the Series and Parallel models provide upper and lower bounds for thermal conductivity, respectively. These vary significantly from the series and parallel conductivity values provided in Table 3-7 using VNs. This is certainly because in the volume-averaged approach bulk porosity is used and in the VN, local interfacial porosities are used. Figure 3-13 shows the distribution of interfacial porosities for each PTL, as determined from their respective VNs. The average values of 0.47, 0.45 and 0.46 are found for PTL-1, PTL-2 and PTL-3, respectively. These values are lower in comparison to the bulk porosities of reconstructed PNs (Table 3-2).

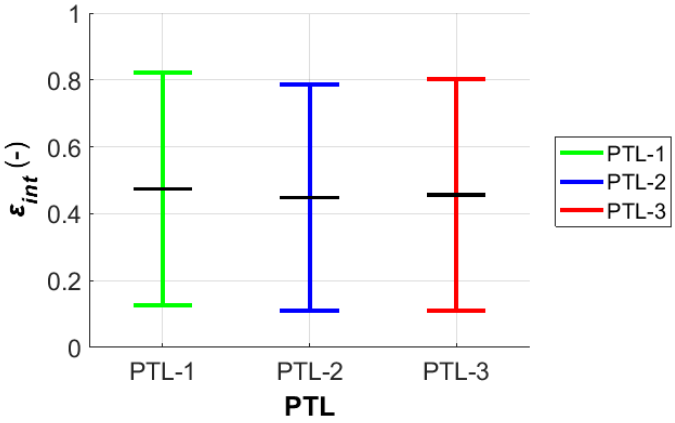

Figure 3-13: Distribution of interfacial porosities, which are used to calculate the heat transfer through conduction between neighboring Voronoi cells. The black line in the middle shows the mean value and the edges of each error bar represent the standard deviation.

The key to understanding this difference lies in recognizing that overall (bulk) porosity and local interfacial porosity capture two distinct aspects of the material's microstructure. Overall porosity measures the total fraction of void volume within the entire structure. Whereas, local interfacial porosities reflect the void fraction at the specific interfaces or cross-sectional areas that are relevant to thermal conduction between regions. It measures the effective area available for conduction at the boundary between two regions, where the arrangement of voids and solid may differ from the bulk average. In many fibrous materials, pores are not distributed uniformly[77,145]. It is common to have larger or more interconnected voids

in certain regions while the regions that dominate the conduction paths (i.e., the interfaces) have a higher fraction of solid material.

Table 3-8: Thermal conductivity models from literature with their equations and resulting values for each PTL at dry conditions (s_l = 0).

Model	Equation	Thermal conductivity (W·m^{-1}·K^{-1})		
		PTL-1 (ε = 74 %)	PTL-2 (ε = 73 %)	PTL-3 (ε = 72 %)
ME-1[117,118]	$\lambda_{ME1} = \dfrac{\lambda_f \varepsilon + \lambda_s (1-\varepsilon) \dfrac{3\lambda_f}{2\lambda_f + \lambda_s}}{\varepsilon + (1-\varepsilon) \dfrac{3\lambda_f}{2\lambda_f + \lambda_s}}$	6.23	6.49	6.75
ME-2[117,118]	$\lambda_{ME2} = \dfrac{\lambda_s (1-\varepsilon) + \lambda_f \varepsilon \dfrac{3\lambda_s}{2\lambda_s + \lambda_f}}{(1-\varepsilon) + \varepsilon \dfrac{3\lambda_s}{2\lambda_s + \lambda_f}}$	0.06	0.06	0.06
EMT[119]	$\varepsilon \dfrac{\lambda_f - \lambda_{EMT}}{\lambda_f + 2\lambda} + (1-\varepsilon) \dfrac{\lambda_s - \lambda_{EMT}}{\lambda_s + 2\lambda} = 0$	0.13	0.15	0.17
Exponential relation[119]	$\lambda_{eff} = \exp(\dfrac{-\frac{3}{2}\varepsilon}{1-\varepsilon})\lambda_s$	0.46	0.56	0.69
Series[120]	$\lambda_{ser} = \dfrac{1}{\dfrac{\varepsilon}{\lambda_f} + \dfrac{1-\varepsilon}{\lambda_s}}$	0.04	0.04	0.04
Parallel[120]	$\lambda_{par} = \varepsilon\lambda_f + (1-\varepsilon)\lambda_s$	8.52	8.85	9.17
Volume-averaged-Krischer (effective)[120]	$\lambda_{eff} = \dfrac{1}{\dfrac{f}{\lambda_{ser}} + \dfrac{1-f}{\lambda_{par}}}$	0.34 (fitted; f = 0.11)	0.21 (fitted; f = 0.19)	0.20 (fitted; f = 0.19)

The volume-averaged-Krischer effective thermal conductivities (Table 3-8) are then fitted using the experimental values. An agreement with the experimental value was found at f = 0.11 for PTL-1 and f = 0.19 for PTL-2 and PTL-3. Even though both methods require fitting, VN-based-Krischer and volume-averaged-Krischer, it can be argued that the VN-based variant may generalize better across a wider range of porosities of fiber-PTLs. The volume-averaged-Krischer model, assuming high anisotropy, is less versatile and may not capture trends in slightly different PTL structures. Moreover, estimating conductivity for partially saturated PTLs using volume-averaged-Krischer requires an additional empirical parameter (the wetted

surface ratio which depends on the liquid content)[146]. While a generalized expression for this parameter exists, it is primarily developed for particulate media[147]. An alternative would be to obtain material-specific empirical coefficients through experiments, but this adds further complexity.

Additionally, a relationship between the saturation and conductivity for high-porosity fiber-PTLs is derived (Figure 3-14). Since the interfacial porosities (Figure 3-13) and the bulk properties are quite similar across all PTLs, only a single correlation is shown in Figure 3-14 using the extracted data of PTL-1. For the other two PTLs, a similar trend is expected.

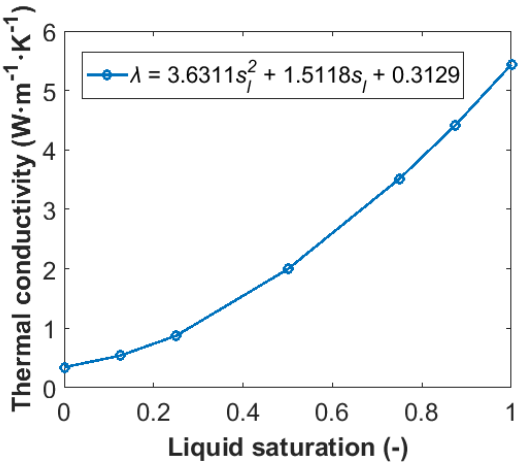

Figure 3-14: A correlation of thermal conductivity with respect to the liquid saturation calculated using the VN.

While the ideal approach to establishing a relationship between saturation and thermal conductivity would involve using PNM-derived saturation profiles at each step, such a method is not straightforward in the context of PNM of fiber-based PTLs. In the PNM employed in this work, saturation is not dynamically updated with changing operating conditions (e.g., current density). Instead, two meaningful saturation states are typically extracted: break-through saturation, where the first continuous gas path forms through the PTL, and residual saturation, where water becomes completely disconnected. The thermal conductivity at residual saturation has already been provided in Table 3-7, and since the break-through saturations of all three PTLs are approximately 0.98, the conductivities listed for the wet PTLs offer a reasonable estimate.

Extending the correlation beyond these discrete saturation points using simulation results poses two main challenges. First, drainage simulations in PNM rarely capture the full saturation range from zero to one, as clustering occurs, and the saturation never reaches zero. Second, the water distribution resulting from a drainage simulation is highly specific to the geometry, PSD, and connectivity of a particular PTL. As such, any saturation versus conductivity correlation derived from it would reflect a single structural case, limiting its broader applicability.

To overcome these limitations, a randomized assignment of pores and throats as gas or liquid is used to generate a wide range of saturation levels from zero to one

(completely dry to completely wet). This method enables a more generalized trend of how thermal conductivity varies with saturation in fiber-based PTLs, independent of any specific invasion pathway or geometry. While this approach is less physically rigorous, it provides a practical and versatile approximation of saturation effects, which would otherwise require a significantly larger and more diverse dataset of PTL structures and residual saturations to develop a correlation.

In summary, the use of randomized saturation states offers a balanced and justifiable compromise that captures the qualitative impact of saturation on thermal conductivity without over-interpreting structure-specific invasion patterns. This method thus serves as a useful tool for understanding trends and guiding future model development, even if it lacks the microscopic precision of simulation-derived saturation profiles.

3.3. Comparison of idealized and extracted PNs

In this section, a smaller part of PTL-1 (854 µm × 854 µm × 854 µm) is used to extract a PN and compared with an idealized PN using the PNM explained in Section 2.1. The extracted PN results in 1110 pores and an idealized PN is created with the same number of pores for comparison. The extracted PN has an average pore radius of 34.1 ± 8 µm and 50.1 ± 15 µm in the smaller and larger fiber diameter regions, respectively. The average throat radius of 35.7 ± 10 µm is used. The same average values are used in the idealized PN. The phase distribution results are shown in Figure 3-15.

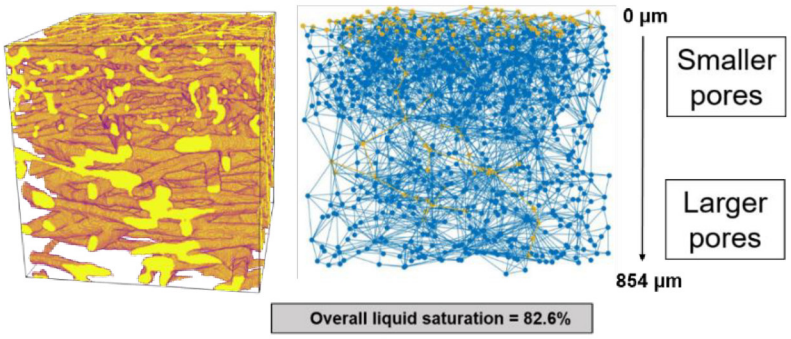

N_p = 1110; N_t = 4500; Average coordination number = 8.3

a)

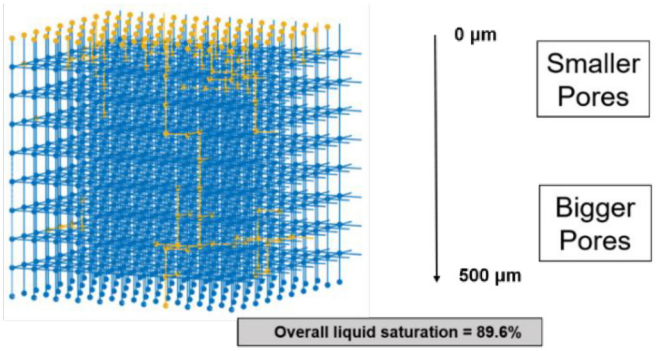

N_p = 1110; N_t = 2750; Coordination number = 6

b)

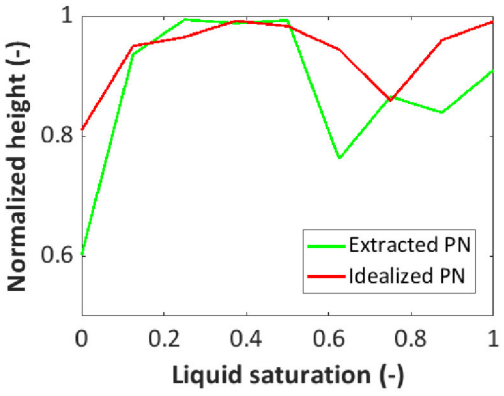

c)

Figure 3-15: Phase distributions in a) extracted and b) idealized PNs, with gas phase in yellow; c) comparison of saturation profiles plotted against normalized network height.

The overall liquid saturation in both PNs is comparably high, though not in perfect agreement. This discrepancy arises from inherent differences in coordination number and pore-throat arrangement, leading to variations in the total number of invasion events. It is important to emphasize that the purpose of idealized PNM is not to provide the most precise solutions, as achieved in direct numerical simulations. Instead, their strength lies in capturing the representative invasion patterns of a fluid phase enabling efficient flow simulations based on percolation theory, which can effectively estimate key transport properties with computational efficiency.

In terms of drainage (invasion) pattern, both PNs can be compared because they have the same graded-structured PSDs. In the saturation profiles provided in Figure 3-15, the change in saturation values can be observed with respect to normalized height, from top (0) to bottom (1) of the PNs. It can be seen that, in both cases, the slice saturation increases towards the middle of the network (extracted: 0.62 to approximately 1.0; idealized: 0.81 to approximately 1.0) and then decreases again for both networks before it finally increases again to a value of approximately 1.0. The difference in these slice saturation values is due to the pore/throat arrangement and the way both PNs are discretized into slices to calculate the slice saturations. In the case of extracted PNM, the saturation profiles are obtained based on the position of pores and the position of middle points of throats. If a throat is present in between two slices, it cannot be split up to attribute its volume to both slices for the calculation of saturation. This is why, the exact amount of liquid or gas present in each slice cannot be calculated, but rather an estimated pattern is calculated. On the other hand, in the idealized PNs, the discretization is quite simple and straightforward with each pore and throat associated to a slice.

Additionally, such PNs provide a simplistic way for parameter extraction. It can be seen in Table 3-9 that the idealized PNs provide a reasonably good agreement with the extracted PNs in terms of permeability values. The values are also compared to the ones calculated using the TSM in Table 3-9. It is seen that the idealized PN permeability is in much better agreement with the extracted PN, much more than the TSM (Eq. 3-2). The value calculated from the TSM is same as shown previously in Table 3-3, because they are dependent only on the fiber diameter and bulk porosity.

Table 3-9: Comparison of permeability values for extracted and idealized PNs and, empirical model (TSM).

Model	$\boldsymbol{K}$ (m^2)
Idealized PN	$2.3 \cdot 10^{-10}$
Extracted PN	$3.2 \cdot 10^{-10}$
TSM	$0.3 \cdot 10^{-10}$

The applicability of simplified and idealized PNs is further highlighted in Chapter 4, where idealized PNs are used to study the impact of PTL structure, using several PTLs from literature and arbitrary graded-structures.

Chapter 4
Idealized Pore Networks

Parts of this chapter have been published in:

Vorhauer-Huget, N.; Altaf, H.; Dürr, R.; Tsotsas, E.; Vidaković-Koch, T. Computational optimization of porous structures for electrochemical processes. *Processes* 2020, *8* (10), 1205. DOI: 10.3390/pr8101205.

In Chapter 3, it is demonstrated how micro-CT imaging can be used to extract PNs, enabling the estimation of transport parameters. While this approach provides a representative interconnectivity of voids, it is often constrained by its dependency on high-resolution imaging. In Section 3.3, it has been shown that idealized PNs can also suffice the need for the extraction of permeability and saturation profiles, and can be used to study and compare PTLs. For this reason, the focus in this chapter shifts towards idealized PNs. By reducing the complexity of the structure, idealized PNs allow for even more computationally efficient simulations. This helps in predicting the permeability and saturations for various PTLs from literature, with the help of the structural data available (e.g. pore sizes, porosity, etc.). Moreover, idealized PNs enable the incorporation of various types of pore size gradients and distributions, that may be challenging to study in extracted PNs. In this chapter, at first in Section 4.1, simulation results of the PTLs from literature are shown. In this section, some of the simulation results, figures and tables are reproduced/adapted from the Master's thesis[148] of M.Sc. Marjan Ghafourian (completed at OVGU Magdeburg), supervised by Dr. Nicole Vorhauer-Huget, in which a parametric study was conducted using the PNM developed by the author of this work. This is followed by an analysis of different gradients in PTL structure in Section 4.2.

4.1 Study of the impact of structure based on PTLs from literature

In this section, the PTL literature data used to generate PNs for simulations is shown. Table 4-1 shows the list of PTLs used. These PTLs are chosen to cover a wide range of porosities and thicknesses. The porosities (ε) vary between 21.8 % and 62.0 % and, thickness (z) between 0.3 mm and 1.4 mm. All simulation results shown in this section are averaged values from three repetitions.

Table 4-1: Properties of the PTLs used from literature to perform PNM simulations. Table adapted from the work of Ghafourian[148], a master's thesis that used the PNM presented in this work for a parametric study, supervised by Dr. Nicole Vorhauer-Huget at OVGU.

PTL	$\bar{r}_p$ (µm)	z (mm)	ε (%)	K (m^2)	Ref.
i	8.0	1.0	21.8	-	Majasan et al.[149]
ii	11.5	0.3	26.5	$1.0 \cdot 10^{-12}$	Lee et al.[68]
iii	8.0	1.0	30.0	$1.4 \cdot 10^{-12}$	Suermann et al.[36]
iv	8.1	1.3	38.0	$4.9 \cdot 10^{-12}$	Grigoriev et al.[37]
v	10.5	1.4	40.0	$6.3 \cdot 10^{-12}$	Grigoriev et al.[37]
vi	12.9	0.3	40.5	$2.5 \cdot 10^{-12}$	Lee et al.[68]
vii	11.7	0.3	50.0	-	Hwang et al.[150]
viii	9.5	1.0	52.0	$2.3 \cdot 10^{-12}$	Lickert et al.[27]
ix	13.0	1.0	52.0	$0.5 \cdot 10^{-11}$	Zielke et al.[151]
x	17.5	0.3	62.0	$1.2 \cdot 10^{-11}$	Zielke et al.[151]

To achieve the PTL properties provided in Table 4-1, each of the parameters such as the mean distance between pores ($\bar{L}$), the standard deviation of pores/throats (σ), the mean pore and throat size ($\bar{r}_p$, $\bar{r}_t$), and the height of the PTLs (N_k) is adjusted during each simulation. The values of σ and $\bar{L}$ are adjusted to match the desired porosity provided in the literature. The surface area of the network ($N_i \times N_j$) is chosen to be 25 × 25, for a network thickness of 0.3 mm, and 30 × 30, for thickness ≥ 1mm. N_i, N_j and N_k actually are number of pores/nodes in each direction of the PN, with their product resulting in the total number of pores in the PN. The simulation parameters are shown in Table 4-2 for each PTL. The mean pore and throat sizes are assumed to be same for these simulations, which are the average pore radii provided in Table 4-1 from the literature. The reason for this is that little or no information on the throat size is available in the literature and, secondly, this makes it easier to match the overall porosity and invasion thresholds as close as possible to the PTL.

Table 4-2: Parameters used in simulations of PTLs from the literature. N_i, N_j, N_k denote the columns, rows, and thickness of the PNs. Table adapted from the work of Ghafourian[148], a master's thesis that used the PNM presented in this work for a parametric study, supervised by Dr. Nicole Vorhauer-Huget at OVGU.

PTL	PN size ($N_i \times N_j \times N_k$)	$\bar{r}_p$ (µm)	$\bar{r}_t$ (µm)	σ (µm)	$\bar{L}$ (µm)	z (mm)	ε (%)
i	25 × 25 × 23	8.0	8.0	1.0	45	1.0	21.5
ii	30 × 30 × 6	11.5	11.5	0.5	53	0.3	26.8
iii	25 × 25 × 28	8.0	8.0	0.5	36	1.0	30.1
iv	25 × 25 × 42	8.1	8.1	0.5	31	1.3	38.1
v	25 × 25 × 37	10.5	10.5	0.5	38	1.4	40.0
vi	30 × 30 × 7	12.9	12.9	0.4	45	0.3	40.7
vii	30 × 30 × 9	11.7	11.7	0.6	35	0.3	50.0
viii	25 × 25 × 37	9.5	9.5	0.5	27	1.0	52.8
ix	25 × 25 × 27	13.0	13.0	1.0	38	1.0	52.0
x	30 × 30 × 8	17.5	17.5	0.5	38	0.3	61.2

4.1.1 Thickness

To observe the impact of thickness on gas saturation, break-through gas saturations are obtained for all PTLs. Table 4-3 lists the break-through gas saturation values obtained for the PTLs. In Figure 4-1, PTLs with same thickness are grouped together and the line of best-fit is plotted.

In PTLs, lower gas saturation value (with quick gas-break-throughs) is favored, so that the wet PTL can efficiently deliver water to the reaction site[48]. As expected, in

Figure 4-1, gas saturation generally increases with increasing thickness. This is because the gas has to go through a longer path to reach the water channel side. Branching of the oxygen pathways in the PTL arises and, as a result, gas saturation increases with increasing thickness. This was also observed for PTL-3 in Chapter 3. As the thickest PTL studied, PTL-3 showed higher gas saturation due to increased lateral invasions, consistent with Larimi et al.[136]. These additional lateral pathways may hinder water transport to the CL, especially at high current densities (> 3.0 A·cm^{-2}), as reported by Han et al.[142] using a mathematical model.

Table 4-3: Summary of gas saturations at break-through for all the PTLs. Each gas saturation value is obtained using three PNM simulations. Table adapted from the work of Ghafourian[148], a master's thesis that used the PNM presented in this work for a parametric study, supervised by Dr. Nicole Vorhauer-Huget at OVGU.

PTL	ε (%)	z (mm)	s_g (-)
i	21.5	1.0	0.190 ± 0.057
ii	26.8	0.3	0.142 ± 0.026
iii	30.1	1.0	0.188 ± 0.044
iv	38.1	1.3	0.232 ± 0.026
v	40.0	1.4	0.327 ± 0.065
vi	40.7	0.3	0.184 ± 0.013
vii	50.0	0.3	0.190 ± 0.018
viii	52.8	1.0	0.228 ± 0.089
ix	52.0	1.0	0.147 ± 0.035
x	61.2	0.3	0.226 ± 0.009

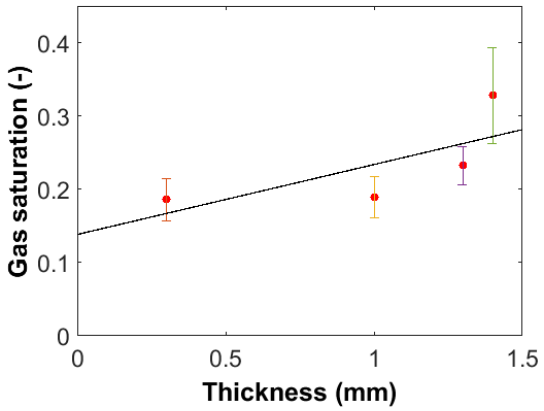

Figure 4-1: Gas saturation (s_g) as a function of PTL thickness (z), highlighting increased lateral invasions in thicker PTLs. The linear fit is represented by the equation: $s_g = 0.09z + 0.14$. Figure adapted from the work of Ghafourian[148], a master's thesis that used the PNM presented in this work for a parametric study, supervised by Dr. Nicole Vorhauer-Huget at OVGU.

The saturation values are also plotted against the porosity in Figure 4-2. This plot is used only to exhibit that the gas saturation values are independent of bulk porosity but rather depend on the PSDs and TSDs. As the standard deviations are adjusted to match the porosity of the PN, it can be argued that the porosities are a function of standard deviations and can therefore influence gas saturation. However, this is only partially true, as porosity depends much more on the distance between pore centers (L in Table 4-2), which is also adjusted to match the porosity along with the standard deviation. For this reason, it is not possible to directly observe any trend between the gas saturation values and porosity.

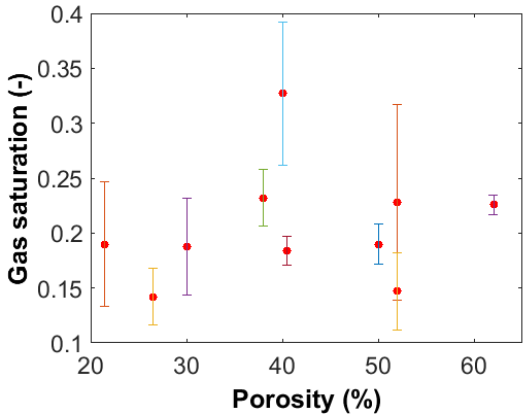

Figure 4-2: Gas saturation values for all the simulated PTLs from literature plotted against porosity showing no clear trend due to its dependency on PSDs/TSDs instead of absolute porosity.

4.1.2 Standard deviation in throat sizes

To observe the impact of the width of void size distributions on gas saturation, a PTL from the work of Lee et al.[73] is chosen as an example (Table 4-4). Simulations are carried out using the same parameters, with only the standard deviations of throat sizes varying between 0.5 µm to 3 µm (Figure 4-3). Varying only the standard deviation of throat sizes is sufficient to illustrate the effect of wider distributions. The pore sizes had a constant standard deviation value of σ = 0.5 µm.

Table 4-4: Simulation parameters used in the PN used to study the impact of standard deviation in throat sizes on the break-through gas saturation.

PN size ($N_i \times N_j \times N_k$)	30 × 30 × 7
$\bar{r}_p$ (µm)	16.8
$\bar{r}_t$ (µm)	12.5
$\bar{L}$ (µm)	37

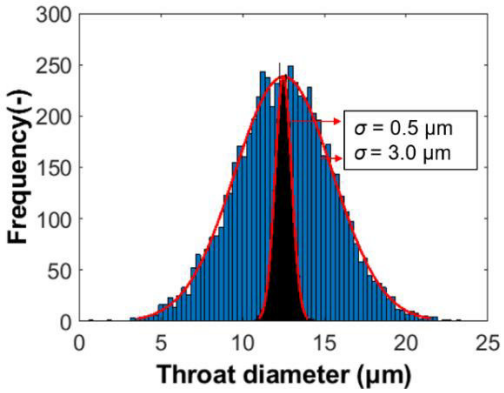

Figure 4-3: Variations in throat sizes with respect to different standard deviations.

The simulation results are summarized in Table 4-5 and Figure 4-4. In general, it is observed that the final gas saturation increases at break-through with widening of the radius distribution, although the increase in the porosity of the network is negligible (Table 4-5). This is because at higher values of standard deviation the numbers of throats with relatively large and small radii are also more. These larger throats are more prone to gas invasions based on the invasion rules described in Section 2.1.3, i.e., the larger the radius, the more favorable is the invasion. For this reason, the gas saturation values increase from a mean of 0.2 to 0.3 as the throats with larger volumes are occupied more abundantly. This increase of 50 %, from approximately 0.2 to 0.3, is significant when compared to the increase in porosity (< 1 %) in Table 4-5.

Table 4-5: Summary of the simulation results for different values of standard deviations in throat sizes. Each gas saturation value is obtained using three PNM simulations. Table adapted from the work of Ghafourian[148], a master's thesis that used the PNM presented in this work for a parametric study, supervised by Dr. Nicole Vorhauer-Huget at OVGU.

σ (μm)	s_g (-)	ε (%)
0.5	0.185 ± 0.012	54.51
1.0	0.216 ± 0.009	54.57
1.5	0.261 ± 0.021	54.63
2.0	0.262 ± 0.005	54.73
2.5	0.263 ± 0.028	54.85
3.0	0.307 ± 0.031	55.07

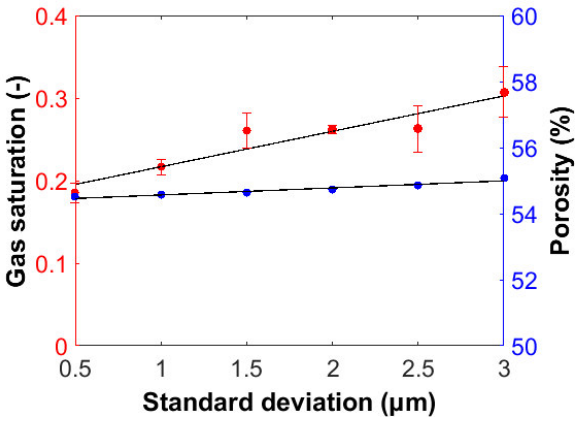

Figure 4-4: Gas saturation at break-through and porosity variations resulting from different standard deviation values between 0.5 µm to 3.0 µm.

4.1.3 Permeability

The permeability values obtained from PNM for the PTLs from literature are summarized in Table 4-6. On the one hand, the comparison between these values and the values taken from literature is not valid even though a fair agreement can be observed in some cases. This is because the literature values are mostly non-intrinsic (except for PTL-iii), either obtained from GeoDict or capillary flow porometry (CFP). When compared to intrinsic permeability values from PNM, these methodologies differ fundamentally in their assumptions and boundary conditions. On the other hand, some degree of comparison can still be meaningful. These values taken from literature represent practical estimates under realistic conditions, though influenced by specific fluid properties or experimental setups.

For example, GeoDict incorporates the resolution of images and may simulate fluid properties explicitly, resulting in values that are often slightly higher or lower than the intrinsic permeability of PNM. It is to be clearly stated here that GeoDict can provide both intrinsic and non-intrinsic permeabilities. The value provided in Section 3.2.2 from GeoDict is intrinsic in nature. CFP, while experimental in nature, approximates permeability based on fluid flow through the largest connected voids, which could correlate with the preferential flow pathways in PNM. Thus, while not directly equivalent, such comparisons may still highlight trends or relative differences in permeability that are reflective of the underlying pore structures.

In general, as expected, the results show that the higher the porosity, the higher the permeability value, and a good agreement with literature values is found for PTLs with a porosity between 30 % and 40 % (Figure 4-5). An increase in permeability by approximately two orders of magnitude is observed as porosity rises from 21.5 % to 61.2 % in both PNM and literature values. Moreover, the least value of ΔK is found for PTL-iii (Table 4-6), where both values (K_{PNM} and K_{lit}) are intrinsic in nature, showing a good agreement between the values obtained from PNM and GeoDict (as also observed in Section 3.2.2 for extracted PNs).

Table 4-6: Summary of absolute permeabilities in comparison to the values found in the literature. It should be noted that the literature permeabilities are not intrinsic, so direct comparisons should be interpreted with caution. Table adapted from the work of Ghafourian[148], a master's thesis that used the PNM presented in this work for a parametric study, supervised by Dr. Nicole Vorhauer-Huget at OVGU.

PTL	ε (%)	K_{PNM} (m^2)	K_{lit} (m^2)	$\Delta K = \lvert K_{PNM} - K_{lit} \rvert$ (m^2)	Ref.
i	21.5	$1.3 \cdot 10^{-12}$	-	-	Majasan et al.[149]
ii	26.8	$2.3 \cdot 10^{-12}$	$1.0 \cdot 10^{-12}$	$1.3 \cdot 10^{-12}$	Lee et al.[68]
iii	30.1	$2.2 \cdot 10^{-12}$	$1.4 \cdot 10^{-12}$	$0.8 \cdot 10^{-12}$	Suermann et al.[36]
iv	38.1	$3.9 \cdot 10^{-12}$	$4.9 \cdot 10^{-12}$	$1.0 \cdot 10^{-12}$	Grigoriev et al.[37]
v	40.0	$7.8 \cdot 10^{-12}$	$6.3 \cdot 10^{-12}$	$1.5 \cdot 10^{-12}$	Grigoriev et al.[37]
vi	40.7	$7.9 \cdot 10^{-12}$	$2.5 \cdot 10^{-12}$	$5.4 \cdot 10^{-12}$	Lee et al.[68]
vii	50.0	$1.4 \cdot 10^{-11}$	-	-	Hwang et al.[150]
viii	52.8	$1.5 \cdot 10^{-11}$	$0.2 \cdot 10^{-11}$	$1.3 \cdot 10^{-11}$	Lickert et al.[27]
ix	52.0	$2.2 \cdot 10^{-11}$	$0.5 \cdot 10^{-11}$	$1.7 \cdot 10^{-11}$	Zielke et al.[151]
x	61.2	$2.4 \cdot 10^{-10}$	$0.1 \cdot 10^{-10}$	$2.3 \cdot 10^{-10}$	Zielke et al.[151]

It is also important to understand that regardless of which method is used, some limitations exist almost always. Intrinsic permeability, as derived from the PNM, is inherently fluid-independent, while non-intrinsic permeabilities are influenced by the properties of the working fluid or the conditions under which they were measured or simulated. For instance, non-intrinsic permeability from GeoDict simulations may incorporate fluid slip effects or compressibility which are not accounted for in intrinsic permeability calculations. Similarly, experimental techniques like CFP may overestimate or underestimate permeability due to the interactions between the fluid and porous material. However, it is important to explicitly state the assumptions and limitations of each method, ensuring that any observed discrepancies are understood in the context of the different frameworks used to calculate permeability.

Table 4-7 summarizes the relative liquid permeabilities obtained from these simulations. Additionally, the values are also plotted against porosity in Figure 4-6. As expected, no clear pattern can be observed for relative permeability with respect to porosity. This is because the relative permeability is a function of invasion profiles, which depend on the thickness of the network and strongly on PSDs/TSDs.

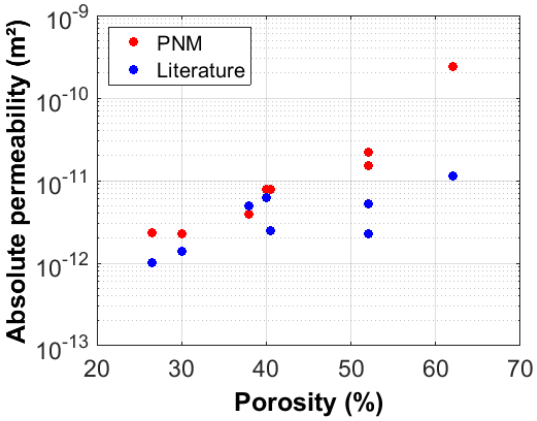

Figure 4-5: Absolute permeability values calculate using PNM and the values from literature with respect to porosity. The PNM permeabilities can be fitted with a logarithmic function of the form, $K = a \cdot e^{b \cdot \varepsilon}$, with $a = 5.8 \cdot 10^{-14}$ m^2 and $b = 0.12$.

In Figure 4-6, the two outliers with comparatively low relative permeability values can be seen for PTL-iv (corresponding to ε = 38.1 %) and PTL-v (corresponding to ε = 40.0 %). This is because these are relatively thick PTLs (1.3 mm and 1.4 mm) which resulted in more lateral invasion and higher gas saturation values and, hence, fewer water pathways leading to lower relative liquid permeability values. This is similar to what is observed for PTL-3 in Section 3.2.2. In the following Section 4.2, the impact of pore/throat size gradients is analyzed. The influence of various invasion patterns, driven by differences in size distributions, on permeability is then shown in detail.

Table 4-7: Relative liquid permeabilities obtained from PNM simulations for all the PTLs. Each permeability saturation value is obtained using three PNM simulations. Table adapted from the work of Ghafourian[148], a master's thesis that used the PNM presented in this work for a parametric study, supervised by Dr. Nicole Vorhauer-Huget at OVGU.

PTL	ε (%)	$k_{rel,l}$ (-)
i	21.5	0.672 ± 0.138
ii	26.8	0.790 ± 0.062
iii	30.1	0.583 ± 0.071
iv	38.1	0.425 ± 0.038
v	40.0	0.368 ± 0.042
vi	40.7	0.686 ± 0.100
vii	50.0	0.675 ± 0.047
viii	52.8	0.491 ± 0.165
ix	52.0	0.656 ± 0.086
x	61.2	0.657 ± 0.027

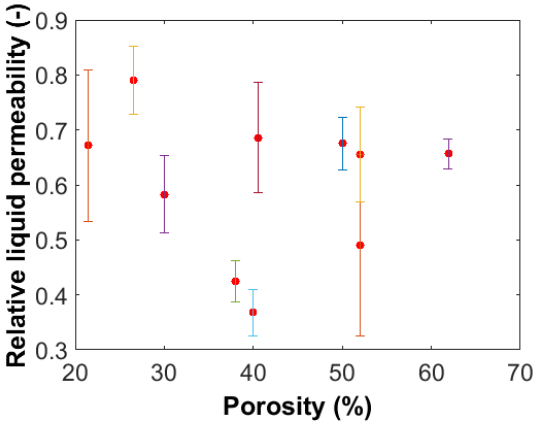

Figure 4-6: Relative liquid permeability for all the simulated PTLs from literature plotted against porosity showing no clear trend as it is argued that they are a function of PSDs/TSDs and not of bulk properties in capillary dominated regimes.

4.2 Impact of pore size gradients

The impact of bulk parameters on the PTL permeability and saturations has been discussed in the first half of this chapter. In this section, the focus shifts towards the defined gradients of the porous structure. Graded structures in PTLs can arise unintentionally during operation or intentionally through controlled manufacturing steps to enhance the material properties.

Unintentional grading could occur as a result of harsh and/or non-uniform conditions that change the structure of the PTL over time. For example, prolonged exposure to uneven thermal, mechanical, or chemical stresses can lead to localized compression and deformation of the PTL. These changes can result in uneven pore size distributions or gradients in porosity across the PTL. Such changes can create regions with reduced permeability or obstructed pathways for efficient fluid transport.

In contrast, intentional grading is introduced to modify the PTL properties for specific functional advantages. By employing a controlled gradient in porosity or pore sizes manufacturers can enhance fluid transport. These focused modifications aim to balance competing requirements, such as maximizing reactant access and removal of by-products while keeping the mechanical properties. In a wide range of production methods, the structure modifications occur rather through sintering of fibers/powders and the interplay of different fiber/powder sizes to control the pore sizes to a certain extent[152,153]. Therefore, it is important to better understand the correlation between graded structures and transport properties.

Exemplarily, Figure 4-7 shows the top and bottom view of a graded PTL (PTL-1 from Section 3.2). As can be seen, the pore structure differs between the top and the bottom side. Small-sized pores are present at the CL side (applied at the top side) and larger pores towards the water channel side (connected to the bottom side). The variation is mainly induced by the manufacturer using fibers of different diameters (25 and 40 µm). The top side of the PTL is designed to enhance the contact between the PTL and CL, while the bottom side facilitates water transport. The PTL-1 shown here is compressed (by 15 %) during operation, but this is not the reason for the graded structure in this case. The extracted parameters from this PTL are shown in Figure 3-5.

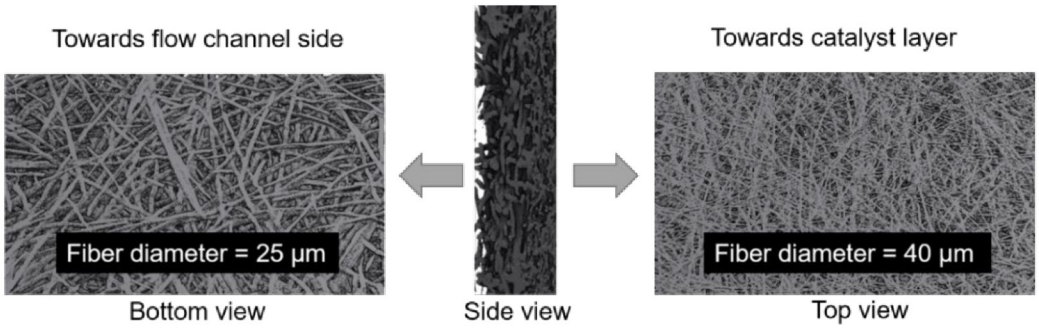

Figure 4-7: Compressed fiber-PTL from SylaTech Germany; d_f = 25 µm and 40 µm. The images were obtained from micro-CT of PTL-1 (Figure 3-5).

4.2.1 Pore network setup

Basically, five different cases are studied at first (Table 4-8). Two of them using 2D PNs and three of them using 3D PNs:

1) 2D PN without gradient for reference.
2) 2D PN with a continuous low-to-high (LTH) gradient.
3) 3D PN with a continuous LTH gradient.
4) 3D PN with a continuous high-to-low (HTL) gradient i.e., opposite of LTH.
5) 3D PN with two different porosity regions denoted as dual-porosity (DP) PN.

A deliberate variation in pore/throat sizes can be applied to the layers in a PN, as depicted in Figure 4-8a. The slices in the five simulated cases are graded with a fixed change in mean throat radius value between each two layers i.e., 0.5 µm (referred to as ΔR). For the intended observations, altering the throat sizes alone is sufficient; however, for consistency, pore sizes are also graded across the layers, with a change of 0.25 µm in pore radius between each two layers.

Even if the primary variations are inflicted on to the pore and throat sizes in each layer of the PN, they have a direct impact on the layer porosity too. This is explained with the constant lattice spacing i.e., the distance between pores, as well as the constant overall network size and/or height.

Table 4-8: Overview of the simulation parameters used in this section. The standard deviation in pore and throat sizes is 4 µm and 6 µm, respectively.

	Case 1 (No gradient)	**Case 2** (2D LTH)	**Case 3** (3D LTH)	**Case 4** (3D HTL)	**Case 5** (2D LTH)
PN size ($N_i \times N_j \times N_k$)	80 × 10	80 × 10	10 × 10 × 7	10 × 10 × 7	10 × 10 × 7
$\boldsymbol{N_p}$	800	800	700	700	700
$\boldsymbol{N_t}$	1360	1360	1600	1600	1600
$\boldsymbol{d_p}$ (µm)	33	30 to 34.5	30 to 33	30 to 33	28 and 38
$\boldsymbol{d_t}$ (µm)	28	22 to 30	22 to 27	22 to 27	20 and 30
$\boldsymbol{L}$ (µm)	50	50	50	50	50
$\boldsymbol{z}$ (µm)	450	450	300	300	300
$\boldsymbol{\varepsilon}$ (%)	60	48 to 66	36 to 50	36 to 50	22 and 52

As the pore and throat sizes are increased or decreased, with no change in the size of the PN, a gradient in porosity is also observed across the thickness of the PTL. For this reason, only in this study, gradient in pore sizes also refers to a gradient in porosity. However, this is not always true for real porous materials. This gradient in porosity through the PNs is shown in Figure 4-8a by dividing each PN into slices and plotting the slice porosity against the corresponding slice number. The bottom

slice in a PN is referred to as Slice 1 and the top slice, towards the CL side, is Slice 8 in 2D PNs and Slice 5 in 3D PNs (Figure 4-8a). The surface and bottom pores are not considered in any slice. Additionally, in Figure 4-8b, TSDs for the two regions in 3D DP (Case 5) are shown as an example (PSDs not shown).

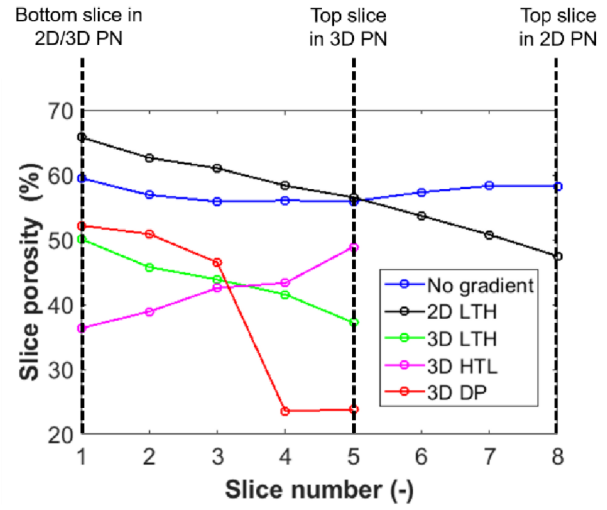

a)

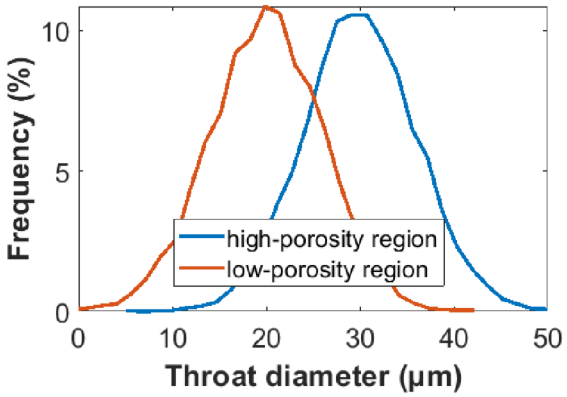

b)

Figure 4-8: a) Spatial variation of porosity in the five cases studied in this section. These porosity variations resulted from a variation in pore and throat sizes in Table 4-8; b) the TSDs of the low and high porosity regions in DP PN (Case 5), similar to the structure shown in Figure 4-7.

4.2.2 Invasion and permeability profiles

i) Case 1 and Case 2

At first, a 2D PN without gradient (Case 1) is compared to a 2D PN with LTH gradient (Case 2) to show the impact of the gradient on the final distribution of gas and liquid and the resulting transport properties. Besides the phase distributions in Figure 4-9, the saturation profiles and the relative gas and liquid permeabilities are compared in Figure 4-10 and Figure 4-11, respectively.

The main differences between the two cases are the final saturations at break-through and until water-disconnection point. The phase distributions in Figure 4-9 indicate that the liquid saturation can be increased from around 83 % to around 93 % until break-through and from 35 % to 41 % until water disconnect point, by application of a pore/throat size gradient. A similar finding is reported by Lee et al.[154] with the application of a micro-porous layer on the PTL. They observed an increase from 30 % to 50 % in liquid saturation using microfluidic networks.

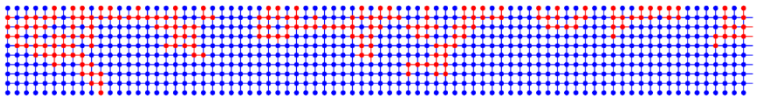

a) Case 1 until break-through Overall liquid saturation = 83 %

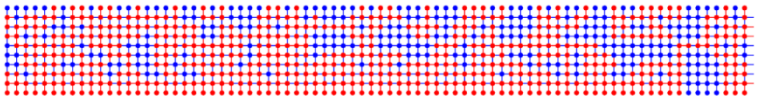

b) Case 1 until water-disconnection Overall liquid saturation = 35 %

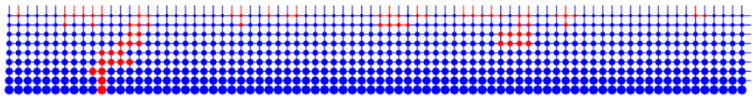

c) Case 2 until break-through Overall liquid saturation = 93 %

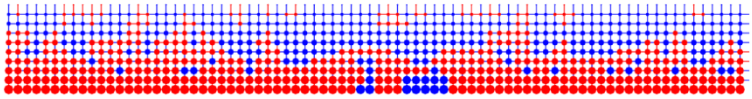

d) Case 2 until water-disconnection Overall liquid saturation = 41 %

Figure 4-9: Comparison of invasion patterns of 2D PNs without gradient (Case 1) and with LTH gradient (Case 2) with gas phase in red and liquid in blue: a) Phase distribution until break-through point for Case 1; b) phase distribution until water-disconnect point for Case 1; c) phase distribution until break-through point for Case 2; d) phase distribution until water-disconnect point for Case 2. Images reproduced from Vorhauer et al.[69], under the Creative Commons Attribution 4.0 International License (CC BY 4.0).

The saturation profiles in Figure 4-10 highlight a similar behavior across different layers of the PN until the break-through point, i.e., higher liquid saturations for LTH gradients. At the water-disconnect point, in the PN without gradient (Case 1), the liquid saturation is almost uniform across the height of the network, approximately 40 % (Figure 4-10a). The PN with LTH gradient (Case 2) in Figure 4-10b has a steep liquid saturation plot, about 65 % at the top of the PN (Slice 8) to less than 20 % at the bottom (Slice 1). This means that for PN with LTH gradient more gas accumulates at the bottom (away from the CL in PEMWE) due to the presence of large sized pores/throats, whereas for PN with no gradient, a constant spread is found throughout the network.

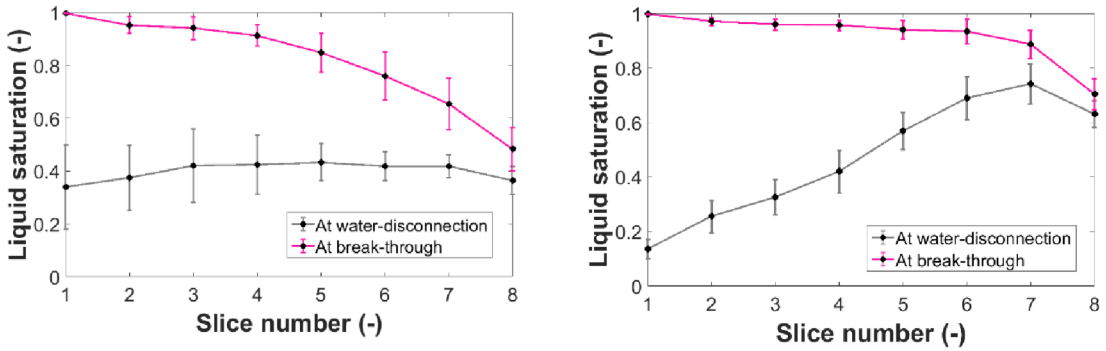

a) No gradient b) LTH

Figure 4-10: Saturation profiles for a) Case 1 and b) Case 2. The plots are obtained from 15 simulations using parameters summarized in Table 4-8. Slice 1 represents the bottom of the PN, and Slice 8 the top. Images adapted from Vorhauer et al.[69], under the Creative Commons Attribution 4.0 International License (CC BY 4.0).

In Figure 4-11a, it is shown that the higher liquid connectivity results in an overall higher relative liquid permeability in the PN with LTH gradient (between liquid saturation 0.8 to 0.5). The two counter-current effects of liquid and gas transport induce an optimization problem in the structure in order to satisfy the optimal transport properties for both phases.

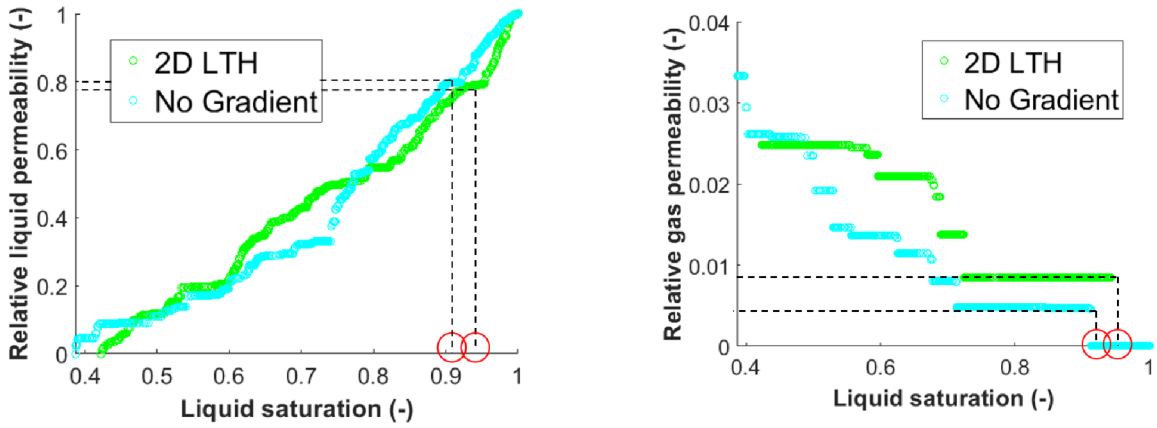

a) b)

Figure 4-11: a) Relative liquid permeability and b) relative gas permeability of the 2D PN simulations (Case 1 and Case 2). The red circles highlight the break-through point. Images adapted from Vorhauer et al.[69], under the Creative Commons Attribution 4.0 International License (CC BY 4.0).

From Figure 4-11, it can be concluded that the optimum gas-liquid configuration to obtain high liquid permeability is between the break-through point (highlighted using red circles in Figure 4-11) and liquid saturation of 0.5, in case of the LTH gradient. In this range the computed gas permeability (Figure 4-11b) is also comparably high for the LTH gradient. This is explained by the saturation profiles in Figure 4-10. Whether this issue depends on the gradient only or also on the geometry of the PN (and thus pore connectivity) will be analyzed further using the 3D simulation results in the next section.

ii) Case 3 and Case 4

In Figure 4-12, the invasion patterns for 3D PNs with LTH (Case 3) and HTL (Case 4) gradients are shown. The higher overall gas saturations are obtained for PN with HTL gradient at break-through, whereas in case of the LTH gradient distinct gas fingers penetrating through the PN are seen. This obviously results from the position of larger pores, which are also more favorable for invasion based on the Young Laplace equation. In HTL network (Figure 4-12c), such pores are present at the top, resulting in more lateral invasions and lower overall liquid saturation at break-through and vice versa for LTH network (Figure 4-12a). At the water-disconnect point, networks with both gradients have almost the same overall liquid saturation but the important thing here is the regions where the water filled pores are present in majority i.e., close to the top (CL side) or towards the bottom of the network (water channel side). This distribution is critical as it ensures that the membrane remains adequately hydrated, facilitates efficient heat transfer from the CCM, and supports effective transport of water to the CL.

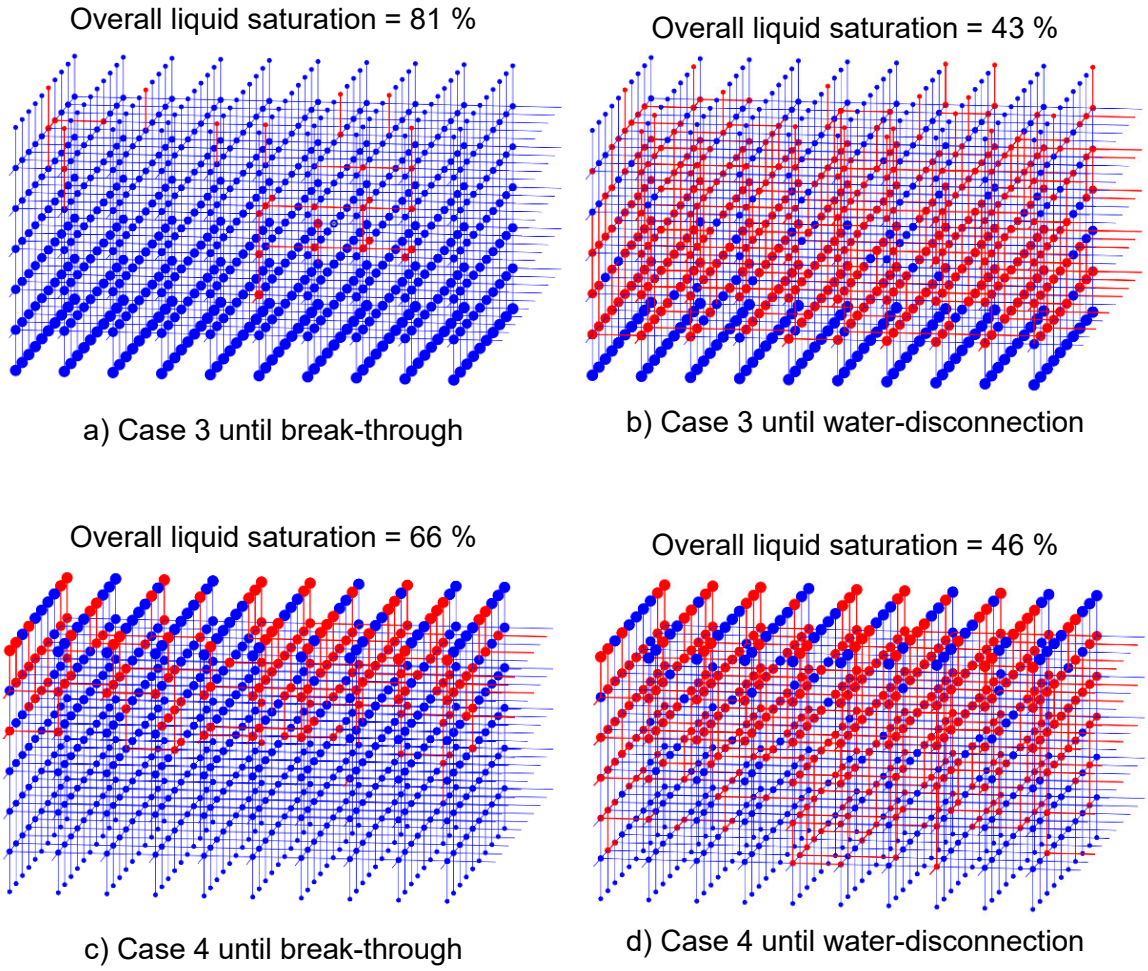

Figure 4-12: Phase distributions with gas phase in red and liquid in blue, and overall liquid saturations of a) Case 3 at break-through, b) Case 3 at water-disconnection, c) Case 4 at break-through, and d) Case 4 at water-disconnection. Images reproduced from Vorhauer et al.[69], under the Creative Commons Attribution 4.0 International License (CC BY 4.0).

Repetition of the simulations reveals the recurring patterns with the help of liquid saturation profiles with respect to the height of the network. The results are summarized in Figure 4-13. As can be seen, the liquid saturation is almost uniform in the LTH case (Figure 4-13a). The highest liquid saturation is around 80 % at the top of the network at break-through. This is much lower than in the 2D Case 1 (Figure 4-10a), where it was around 50 %. Even when the simulation is continued to invade further until the water-disconnection point, the liquid saturation at the top side remains low (at around 40 % in Figure 4-13a) while gas invasion occurs mainly at the bottom side (where the liquid saturation is lower). The behavior is inversed in case of the HTL, in which the top side has always a lower liquid saturation (Figure 4-13b) than the bottom side, where the pores and throats are smaller and the resulting invasion pressures are higher. But, interestingly, the invasion profiles of LTH and HTL are not inversed. Instead, significant differences occur especially when regarding the break-through point, while after break-through the saturation profiles tend to become almost opposed (water-disconnect curves in Figure 4-13).

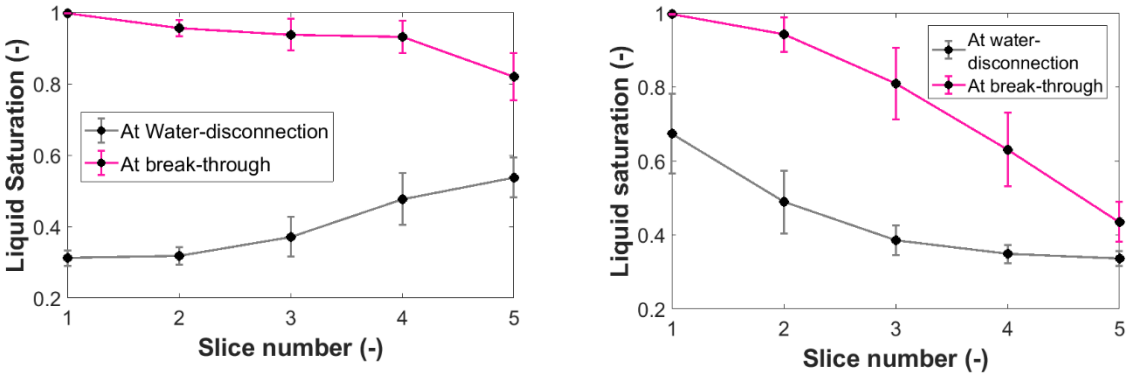

a) LTH b) HTL

Figure 4-13: Saturation profiles summarized for a) LTH (Case 3) and b) HTL (Case 4) 3D simulations. The plots are obtained from 15 simulations using parameters summarized in Table 4-8. Slice 1 represents the bottom of the PN, and Slice 5 the top. Images adapted from Vorhauer et al.[69], under the Creative Commons Attribution 4.0 International License (CC BY 4.0).

In Figure 4-14, it can be seen that the overall higher relative liquid permeabilities are found in the LTH network, also after break-through. At the same time, the relative gas permeability is also higher at higher liquid saturation. This indicates that the LTH network (Case 3) has generally better transport properties for both, gas and liquid phase, than the HTL network (Case 4).

In summary, in the LTH cases, the larger voids are located at the bottom side and the invasion is favored towards the bottom of the network because of the lower invasion pressure thresholds. Compared to the HTL case, the LTH cases are characterized by an invasion pattern like capillary fingering[93], both in 2D and 3D PNs. Break-through of the gas phase occurs with a significantly lower number of invasions steps. This means, that the final gas saturation at the break-through point is lower compared to the HTL case, where the larger voids are located at the top side. In contrast to LTH, in HTL case the voids at the top side are favorably invaded. Thus, in the case of HTL the invasion results in the formation of a gas-liquid

distribution similarly as in stable displacement with a wider invasion front[93]. This could be observed in 2D and in 3D PNs. However, the stabilization is more significant in 2D due to the lower pore connectivity.

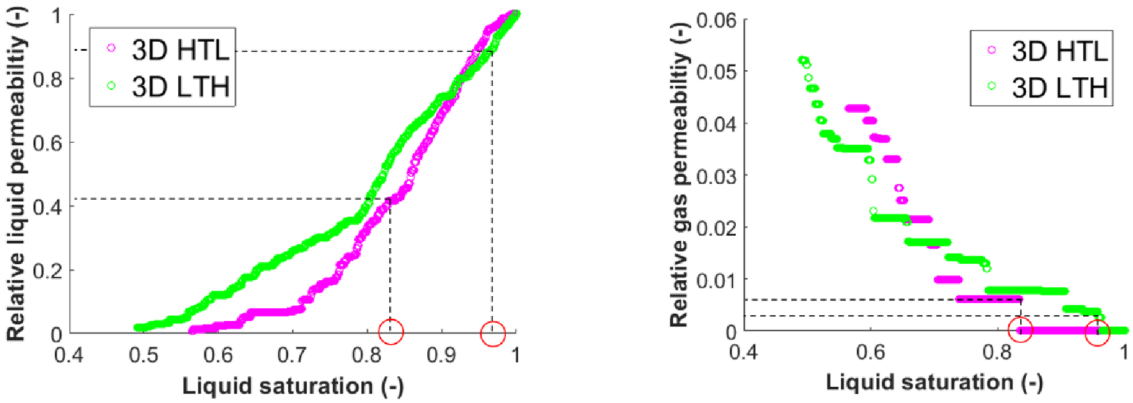

a) b)

Figure 4-14: Comparison of relative a) liquid and b) gas permeabilities of Case 3 and Case 4. The red circles highlight the break-through point. Images adapted from Vorhauer et al.[69], under the Creative Commons Attribution 4.0 International License (CC BY 4.0).

iii) Case 5

In Figure 4-15 and Figure 4-16 the invasion of a dual-porosity PN, depicting the PTL shown in Figure 4-7, is studied. The key difference between the idealized PN discussed in Section 3.3 and Case 5 lies in the thickness of the network. In this section, a uniform thickness of N_k = 7 is used for all 3D idealized PNs to ensure a fair comparison. In contrast, the idealized PN in Section 3.3 uses N_k = 10, chosen specifically to match the total number of pores in the corresponding extracted PN.

It is seen in Figure 4-15a that distinct gas fingers form inside the low-porosity region, whereas more pore invasions occur inside the high-porosity region compared to the LTH cases. The liquid saturation inside the top layer (Figure 4-15b) is almost similar to the PNs with LTH gradient (Figure 4-13a). The region adjacent to the top (CL side) stays more wet. But in the high-porosity region significantly more gas is contained, as observed in the case of PTL-1 in Section 3.2.2 for extracted PN and Section 3.3 for idealized and extracted PNs. This results in a higher overall gas saturation and the formation of more isolated single liquid clusters at break-through and at water-disconnection as well.

As can be found in Figure 4-16, the relative liquid permeabilities of the DP network are lower when compared to the PNs with LTH gradient. The gas permeabilities are significantly lower and remain on a constant low level because the low-porosity region is not further invaded even if the gas pressure is increased after break-through. If one would deduce a grading strategy from this comparison, a PN with LTH gradient would rather be recommended than DP network, if low gas saturations and high liquid and gas permeabilities should be realized.

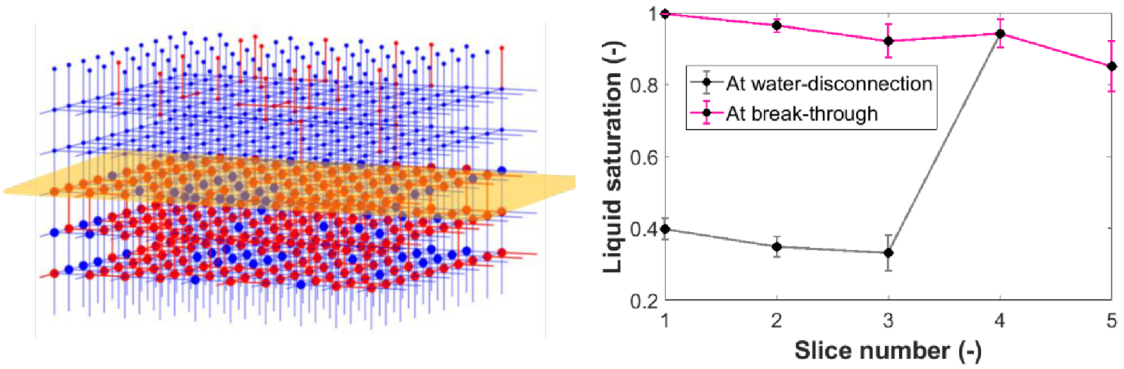

a) b)

Figure 4-15: a) Phase distribution, with gas phase in red and liquid in blue, and liquid-gas barrier represented by yellow plane; b) saturation profiles of a 3D pore network with dual porosity, Case 5 (similar as in Figure 3-13). Slice 1 represents the bottom of the PN, and Slice 5 the top. Images adapted from Vorhauer et al.[69], under the Creative Commons Attribution 4.0 International License (CC BY 4.0).

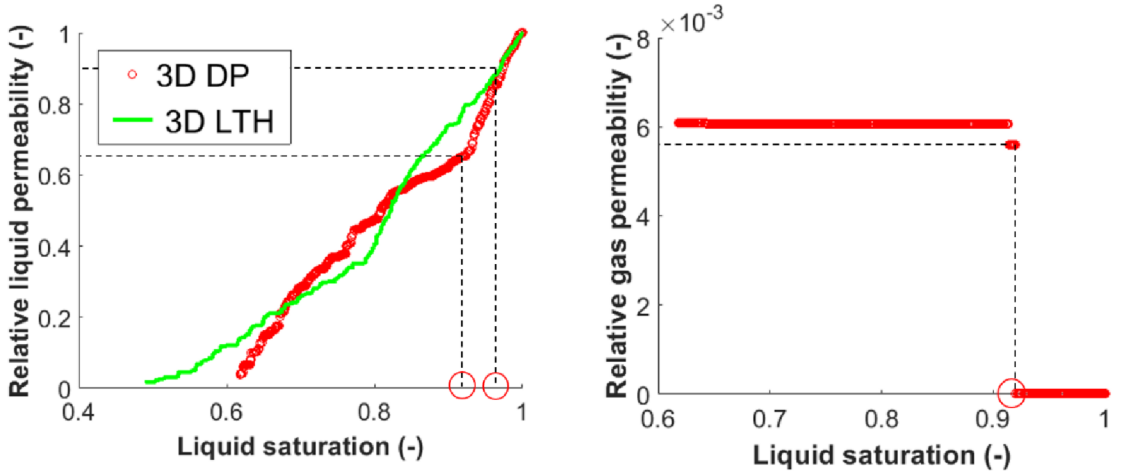

a) b)

Figure 4-16: Relative permeability of a) liquid and b) gas phase in the dual porosity PN (Case 5). The green line in a) represents the LTH case (Case 3). The red circles highlight the break-through point. Images adapted from Vorhauer et al.[69], under the Creative Commons Attribution 4.0 International License (CC BY 4.0).

4.2.3 Variations in throat size gradients

In the previous section, the slices in the network were graded with a fixed change in mean throat radius value between each layer i.e., ΔR = 0.5 μm. In this section, different values of ΔR are used to study the impact of different gradients using a relatively large 3D network (N_i = 25; N_j =25; N_k = 10). All other simulation parameters are kept the same.

This expands the scope of the study as each gradient (LTH and HTL) will be examined within a range of ΔR = 0.1 to 0.7 μm. This means that the range of mean throat diameter for each layer will be different. In Section 4.2.1, the 22 to 27 μm range was chosen for throat diameter variations in 3D LTH (Case 3) and 3D HTL (Case 4) corresponding to ΔR = 0.5 μm (Table 4-8). Now, at ΔR = 0.1 μm and

ΔR = 0.7 µm, the mean throat diameters will be from 22 µm to 23 µm, and from 22 µm to 29 µm, respectively.

The range of ΔR between 0.1 µm and 0.7 µm is chosen. This is because, at ΔR < 0.1 µm, the PN behaves as if no gradient was inflicted; at ΔR ≥ 0.7 µm, the HTL network is mostly occupied by the non-wetting phase (gas phase), which blocks the wetting phase (water) flow paths entirely (Figure 4-17). Exemplarily, in Figure 4-17, 2D PN phase distributions are used to show the differences between different values of ΔR and their impact on HTL PNs.

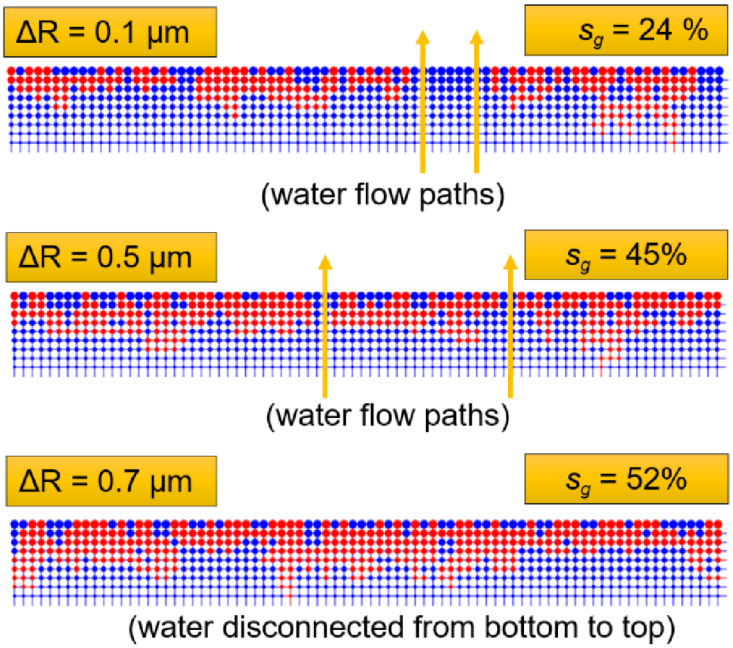

Figure 4-17: An example showing the effect of ΔR on overall gas saturation (s_g) at break-through and phase distributions in HTL, with gas phase in red and liquid in blue. It can be seen that the water-disconnection occurs as the value of ΔR approaches 0.7 µm.

For the sake of reference, a 3D PN with the same network size (25 × 25 × 10) with no gradient in pore or throat sizes is also simulated ($\bar{d}_t$ = 27 ± 6 µm), referred to as ΔR = 0 in Figure 4-18. Figure 4-18 shows the relative liquid permeability plots with variations in ΔR for LTH and HTL PNs.

Compared to the base case with no gradient, all of the simulations show higher relative liquid permeabilities in the LTH PNs (Figure 4-18a) and vice versa for HTL PNs (Figure 4-18b). The relative liquid permeabilities decrease in the HTL case as the ΔR increases because of the flattening of the gas invasion front which blocks more and more liquid supplying voids. The relative liquid permeability values approach zero at ΔR = 0.4 µm for HTL PNs, as the water-disconnect point is reached. It can be said that the LTH gradient favors the drainage of non-wetting phase more than the HTL gradient. The invasion potential increases in the LTH gradient, with lower threshold pressure pores present in the subsequent layers, which makes it convenient for the oxygen to invade.

Generally, the gas saturation of 3D HTL increases with an increasing ΔR due to more lateral invasions (Figure 4-19). This increase in overall gas saturation goes from 38 % at ΔR = 0.1 µm to around 63 % at ΔR = 0.7 µm. On the other hand, in case of LTH gradients, the overall gas saturation drops from 17 % to 10 % when ΔR changes from ΔR = 0.1 µm to 0.5 µm and then it stays in the same range as the ΔR approaches to 0.7 µm. The unchanged gas saturation value from ΔR = 0.5 µm onwards shows that after these points the emergence of new gas fingers is not favored because the probability of larger pores being available is much higher.

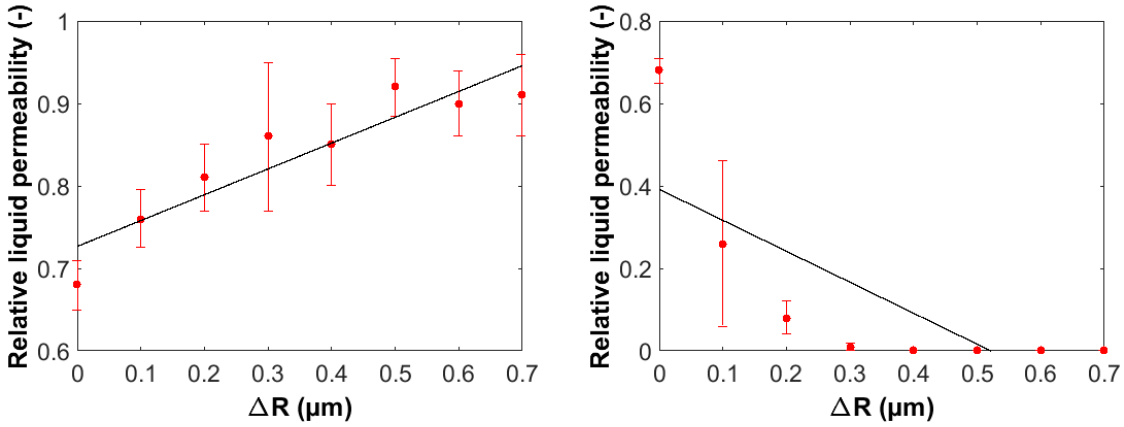

Figure 4-18: Relative liquid permeability in 3D PN at break-through points for a) LTH and b) HTL gradients. Simulations with 15 repetitions at each value of ΔR are shown in these plots. ΔR = 0 shows data points for PN simulations without any gradient.

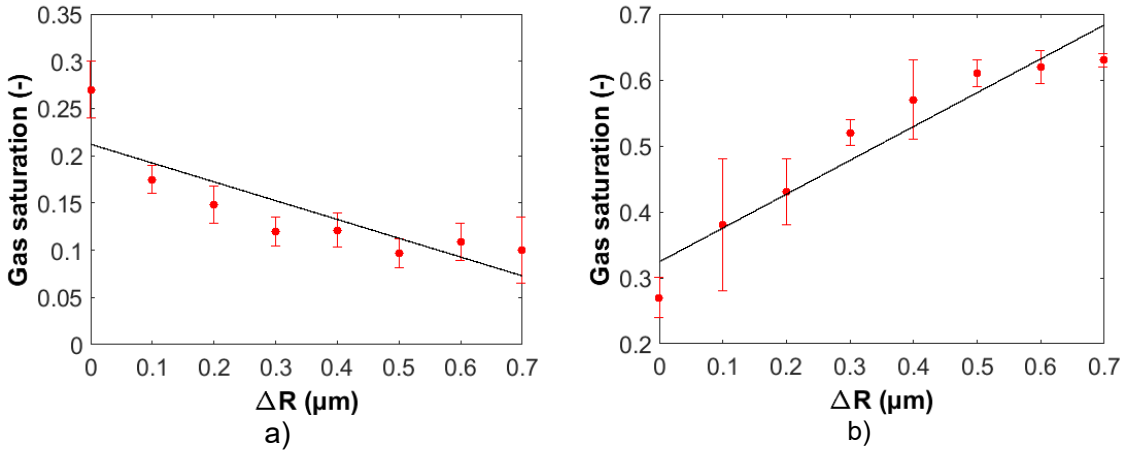

Figure 4-19: Final gas saturation at break-through in 3D a) LTH and b) HTL gradients. Each data point represents the mean of 15 simulations.

4.2.4 Comparison of dual-porosity pore networks

Additionally, two variations of the 3D DP network (Case 5 from Table 4-9) are simulated and compared with each other, as well as with a reference PN with no gradient, referred to as ΔR = 0 in Figure 4-18.

Table 4-9: Variations of Case 5: DP-1 with a difference of 20 % between the two different porosity regions in the PN, and DP-2 with a difference of 34 % between the two regions.

Case 5 variations	CL-side	Water channel side
DP-1	ε = 24 % $\bar{d}_p$ = 26 ± 4 µm $\bar{d}_t$ = 23 ± 6 µm	ε = 58 % $\bar{d}_p$ = 34 ± 4 µm $\bar{d}_t$ = 30 ± 6 µm
DP-2	ε = 30 % $\bar{d}_p$ = 28 ± 4 µm $\bar{d}_t$ = 25 ± 6 µm	ε = 50 % $\bar{d}_p$ = 32 ± 4 µm $\bar{d}_t$ = 28 ± 6 µm

The liquid permeabilities and gas saturations obtained are shown in Figure 4-20. DP-1 and DP-2 gradients tend to be better than HTL gradients with smaller pores at the top and bigger ones at the bottom but are quite similar to PNs with no gradient. Moreover, due to the sudden shift between the two different regions, a liquid-gas barrier could exist as shown in 4.2.2 for Case 5 (Figure 4-15a). However, regardless of the liquid-gas barrier, results of Case 5 suggest that, like LTH (Case 3), DP networks also have the majority of water-filled pores close to the top (CL side) which is critical for membrane hydration, and are still better than HTL networks (Case 4). Based on these findings, it can be concluded that the most suitable way for the gas phase to exit the PTL is provided by a constant LTH gradient in pore/throat sizes throughout the PTL, which can favor the movement of oxygen out of the system layer by layer, followed by DP networks.

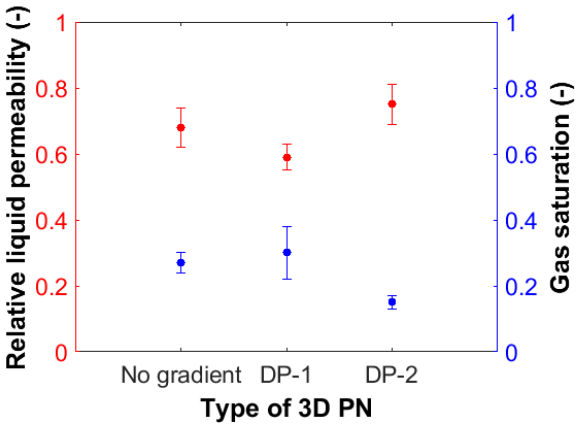

Figure 4-20: Relative liquid permeability at break-through points of 3D PNs: DP-1, DP-2, and reference without gradient. Results from 15 repetitions are shown in these plots.

To conclude, it is to be stated here as in other works[47,150], that the phase distributions depend much more on the distribution of the pore/throat sizes rather than on the average size itself in the absence of viscous forces. In contrast to HTL, LTH gradient showed a more linear profile with vertical break-through point being achieved much more easily than horizontal i.e., less tortuous gas fingers which lead to better transport properties. Moreover, a gradient of at least $\Delta R = 0.4$ for PTLs with LTH gradient i.e., from the CL to the water channel side, is most favorable based on these PNM simulations. The decision to make would be about the upper limit of this gradient. Up to this point, based on these findings, it is established that an LTH gradient could improve the oxygen drainage. Even a choice of $\Delta R > 0.7$ would not change the invasion pattern; on the other hand, much larger volumes of pore can have the capacity to drain more amount of oxygen which, of course, depends on the operating current density of the cell also. For large production rates at high current densities it would be favorable to have graded pores with largest possible sizes. Such a value cannot be provided without mechanically testing the PTLs with different structures. If the difference in porosity over the entire PTL is very large, this could also impact the mechanical properties of the material.

Based on the impact of saturation on thermal conductivity discussed in Section 3.2.2, it must also be reiterated here that higher water saturations in the PTL are favorable for better heat transport, especially for thicker membranes at high current densities. The higher water saturation values resulted in higher thermal conductivity values which play a crucial role in heat management[39]. Higher conductivity values mean that the temperature difference between the CCM and the water inlet can be reduced. This is because a higher conductivity PTL can transport more heat away from the CCM and prevent degradation within a PEMWE. The LTH graded PTLs have clearly shown an increased water permeability and saturation in the PNM simulations. This could mean that the PTLs manufactured with LTH gradient would also tend to retain more water and hence improve thermal conductivity and reduce degradation with respect to time.

Chapter 5
Neutron Imaging Experiments

Parts of this chapter have been published in:

Altaf, H.; Miličić, T.; Vidakovic-Koch, T.; Tsotsas, E.; Arlt, T.; Kardjilov, N.; Manke, I.; Vorhauer-Huget, N. Neutron imaging experiments to study mass transport in commercial titanium felt porous transport layers. *Journal of Electrochemical Society* 2023. DOI: 10.1149/1945-7111/acd7a8.

The experimental data used in Section 5.1 have been archived in an online repository:

DOI: 10.5281/zenodo.17672899.

This chapter discusses the results of neutron imaging experiments explained in Section 2.3. The chapter is split into two parts: Section 5.1 discusses the experiments performed using PTL-1, PTL-2 and PTL-3 (Table 2-1) in a non-electrochemical cell (Figure 2-11); Section 5.2 discusses the results obtained from the experiments performed with electrochemical cells namely, PEMWE-1 and PEMWE-2.

5.1 Non-electrochemical cells

5.1.1 Tomography of water imbibition into empty cells

In these experiments, at first, the empty PTLs were fed with water at a flow rate of 1.0 ml·min^{-1}. This was done for a duration of 3 to 4 minutes before the tomography was performed, with an intention to wet the PTLs as much as possible. After this, the water inside the cells was stabilized by closing the screw clamps on the inlets and outlets. Figure 5-1 shows the center slice of the obtained 3D image stacks in through-plane view for PTL-2 (thickness 0.5 mm) and PTL-3 (thickness 1.0 mm). The tomography for PTL-1 could not be performed due to the limited beam time allocation at the neutron imaging facility in ILL, Grenoble.

In Figure 5-1, it can be clearly seen that PTLs were only partially wet even after being subjected to high flow rates. Anticipating that the dark spots refer to empty pores/regions, one can conclude that PTL-3 shows much more non-uniform water uptake in comparison to PTL-2. In Figure 5-1a, for the thinner PTL (PTL-2) only a few dark regions are observed, whereas for the thicker PTL (PTL-3) much more dark regions can be seen. These regions identify structures in the PTL where water was scarce. This indicates local water scarcity in both PTLs (much more in PTL-3), similarly as already reported in literature[85,87]. In both cases, the formation of gas islands throughout the PTLs is observed. This phenomenon is also expected to occur during the dynamic operation of a PEMWE. Therefore, understanding the dependence of these gas islands on PTL structure and operating conditions should be of great interest.

To investigate the behavior of gas islands, the tomography scans were repeated after purging the cells with air at a flow rate of 7.9 ml·min^{-1} for approximately 5 minutes. Surprisingly, the gas islands persisted even after the purging process. They only slightly increased in size and number. This observation highlights that water scarcity can indeed pose challenges for mass transport, even under dynamic conditions involving repeated release of gas through the PTL. Although, the impact of gas islands on the relative permeabilities of liquid and gas within the PTL has not been analyzed so far with the help of experiments. It has been anticipated that these non-wetted islands aid in oxygen transport and become the preferential pathways for oxygen release through the PTL.

According to Maier et al.[85], no new pathways are created in a PTL during operation and the ratio of water to gas transport pores stays the same. They based their findings on neutron imaging experiments performed at current densities up to

1.5 A·cm^{-2}, using both a fiber and a particle PTL. In addition to that, Zlobinski et al.[87] also reported that the PTL cannot be completely imbibed with water and gas-liquid distributions in the PTL are independent of the current density. Based on these studies, if the gas-liquid distributions remain unchanged, it becomes even more relevant to analyze the wetting capability of PTLs with different properties and design strategies to enhance them. From these observations alone, PTL-2 would offer more benefits than PTL-3 with more uniform water distribution.

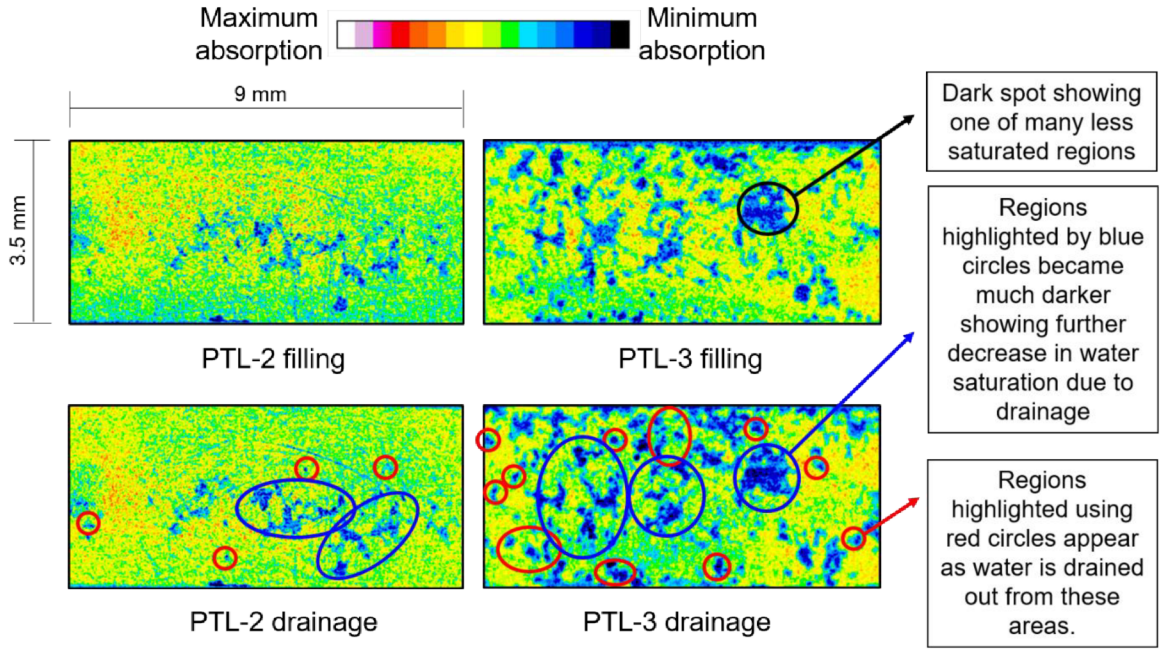

Figure 5-1: Images from the middle of 3D image stacks obtained by tomography of PTL-2 and PTL-3 after filling and drainage (through-plane view). The spatial resolution is 22 µm. Image adapted from Altaf et al.[125], under the Creative Commons Attribution 4.0 International License (CC BY 4.0).

5.1.2 Radiography of counter-current flow through cells

The dynamic change of water and air saturation during the CC settings is studied based on radiographies which were captured at a frame rate of 10 images per second. Based on the image data and equations in Section 2.3.4, the temporal change of the average transmittance can be illustrated. High values of the average transmission correspond to lower water content and vice versa. The change of the average transmittance corresponds to the change of the water or air saturation in the through-plane view i.e., inside the PTL and the channels. This means that the transmittance values used in the analysis are cumulative and include information about both the PTL and channel saturations. This can potentially obscure the specific transmittance information related to the PTLs. Figure 5-2 illustrates, using an in-plane image, how the presence of gas bubbles within the water channel can influence the through-plane data.

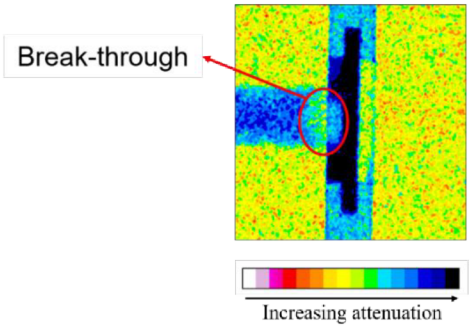

Figure 5-2: In-plane image taken during counter-current flow in the moment when air breaks through the PTL (red circle) from the gas channel side (on the right) to the water channel side (on the left). PTL and water represented by light to dark blue colors; air and aluminum housing in yellow to green colors. Image reproduced from Altaf et al.[125], under the Creative Commons Attribution 4.0 International License (CC BY 4.0).

As an example, the change in average transmittance through PTL-2 with time at Setting 4 (Table 2-3) is illustrated in Figure 5-3. It can be seen that the average transmittance changes periodically, which indicates a periodic change of the through-plane water distribution. Based on the neutron imaging literature[84–88] and Figure 5-2, such strong fluctuations are unlikely to result solely from changes in water content within the PTL. Instead, a more plausible explanation is that these variations arise from changes in the water and bubble distribution in the adjacent gas/liquid channels (each 0.5 mm wide), which are also in the field of view. Similar through-plane fluctuations linked to bubble transport in the channels have been reported reported by Selamet et al.[86] for PTLs and by Mularyzyk et al.[155] for GDLs.

This implies that the saturation state within the PTL likely remains stable during operation, even though the measured transmission fluctuates due to the contribution from the channels. As the through-plane setup cannot isolate the transmittance of the PTL and the surrounding channel, the exact saturation levels within the PTL were not directly resolved. However, coupling a dynamic electrochemical model with a PTL could provide saturation profiles under various operating conditions. In this regard, the PNM simulations in Chapters 3 and Chapter 4 provide useful bounds: they yield a range of liquid saturation values from $s_l = 1$ to $s_l = s_r$, where s_r represents the saturation at which continuous water pathways across the PTL become fully disconnected. These PNM-derived saturation values correspond to invasion thresholds under quasi-steady drainage and can serve as realistic estimates of the upper and lower saturation limits in the PTL during operation. When combined with information about inlet flowrates, current density and oxygen production rates, such PNM-informed saturation bounds can help interpret the average saturation states that would realistically exist in the PTL, even when direct experimental observation is limited.

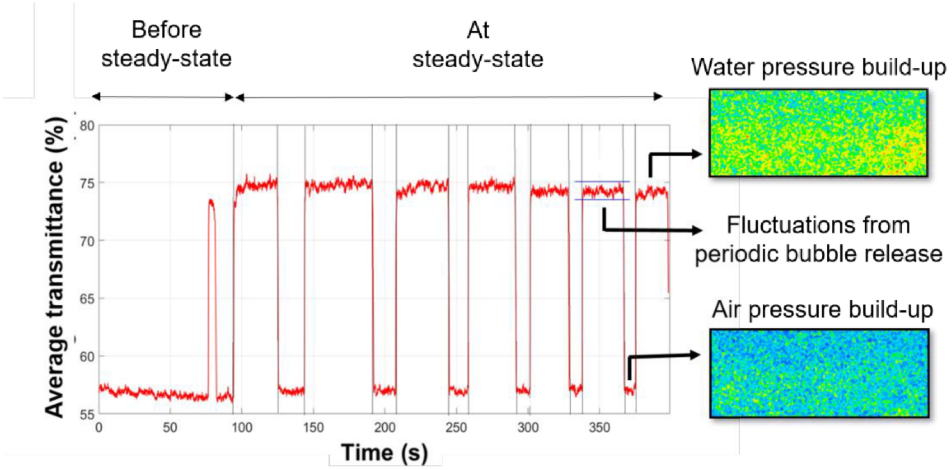

Figure 5-3: Illustration of periodic change of the average transmittance of neutron radiation following the air and water pressure build-up cycles. Here the example of PTL-2 at Setting 4 is shown. Image adapted from Altaf et al.[125], under the Creative Commons Attribution 4.0 International License (CC BY 4.0).

In addition to that, the filling and drainage tomographic images for PTL-2 and PTL-3 in Figure 5-1 also suggest that there is no significant change in the empty or gas saturated PTL regions. Periodic drainage and imbibition cycles have only been reported with microfluidic PEMWE cell by Bhaskaran et al.[140]. The PTL in these experiments was depicted by a few rectangle channels, arranged like throats in an idealized PN, which poorly represents a PTL to be used for flow characterization experiments. Considering this, it appears to be that most of the gas is transported through the existing preferential pathways (comprised of unsaturated regions and invaded regions that could not be imbibed again).

In Figure 5-3, when no air is being pushed through the PTL into the channel, a lower average transmittance value is observed (~ 57 %) and both channels are filled with water. This represents the period during which the air pressure is being built up to push back from the air channel, through the PTL, and is referred to as air pressure build-up time. At approximately 90 s (Figure 5-3), the change in transmission indicates the moment when the air pressure reaches the critical threshold needed to form a continuous air pathway from the air channel, across the PTL through the existing preferential pathways, and into the water channel. At this point, air bubbles were seen exiting into the channel, flowing across the PTL. The average transmission level changed from 57% to around 75 %. At this level of transmittance, the air bubbles kept getting released into the water channel. This phenomenon is more likely a representation of the two-phase flow in the PTLs, where the gas bubbles are released constantly through the path of least resistance and water transport happens simultaneously through the already available wet clusters.

During this periodic bubble release, the saturation remained constant (~ 75 %) for an interval of approximately 30 s, while air was continuously removed through the PTL and water channel. This was the time when water pressure was building up in the water inlet to counteract against the air flow. The noise during these peaks (at values around 75 % in Figure 5-3) corresponds to the periodic bubble release in

the channel. The released air bubbles displaced the water in the liquid channel in the flow direction, resulting in small fluctuations in the average transmittance of the 2D through-plane image. The major change in the average transmittance between air pressure build-up time and air release time is due to the emptying of the channel at the air side which was filled with water during the air pressure build-up time.

The periods during which the water pressure was building up and air bubbles were being released are portrayed in Figure 5-3 with the help of images along with the plot. The yellow regions show air rich regions in this case and blue color shows water rich regions. In the water pressure build-up phase more yellow is seen as air bubbles would also sometimes move around in the water channel or even coalesce. Once the pressure from the air was overcome by inlet water flow, this process ceased, and water refilled both channels again. After this, air pressure started to build-up again until air bubbles start to get released again. This was repeated with an almost constant duration (approx. 10 to 20 s) and amplitude of the interval (approx. between 57 % and 75 %). In the example presented in Figure 5-3, the average frequency of this cycle is 0.0214 s^{-1} and the amplitude change is 17.4 %. The average transmission plots for the three PTLs (Table 3-1) and different settings (Table 2-3) are shown in Figure 5-4.

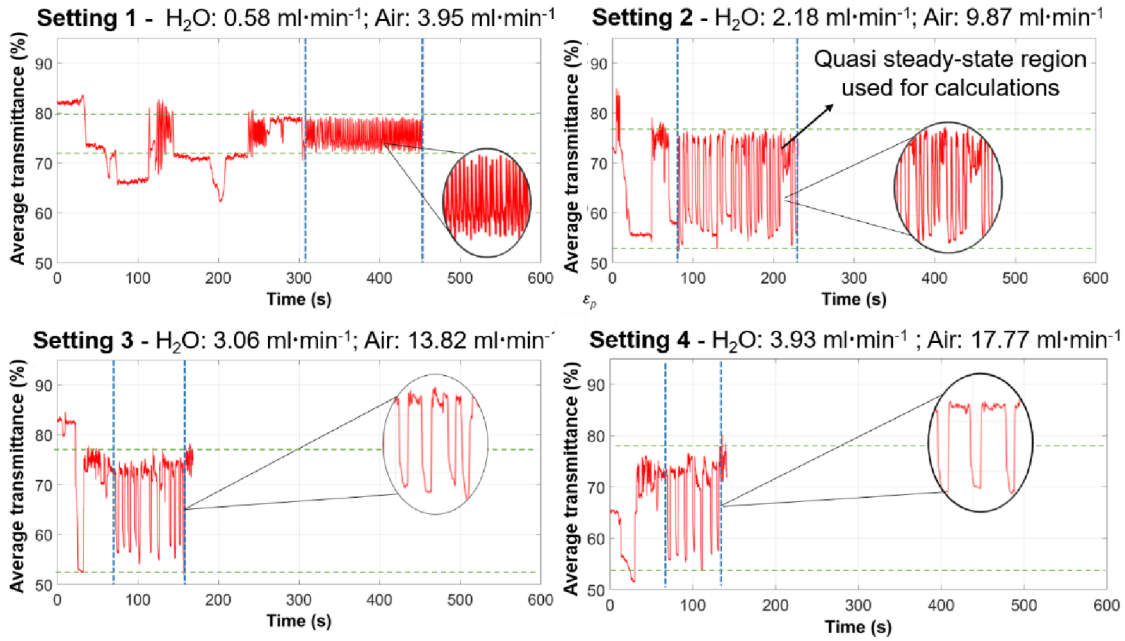

a) PTL-1

(Figure continued on next page)

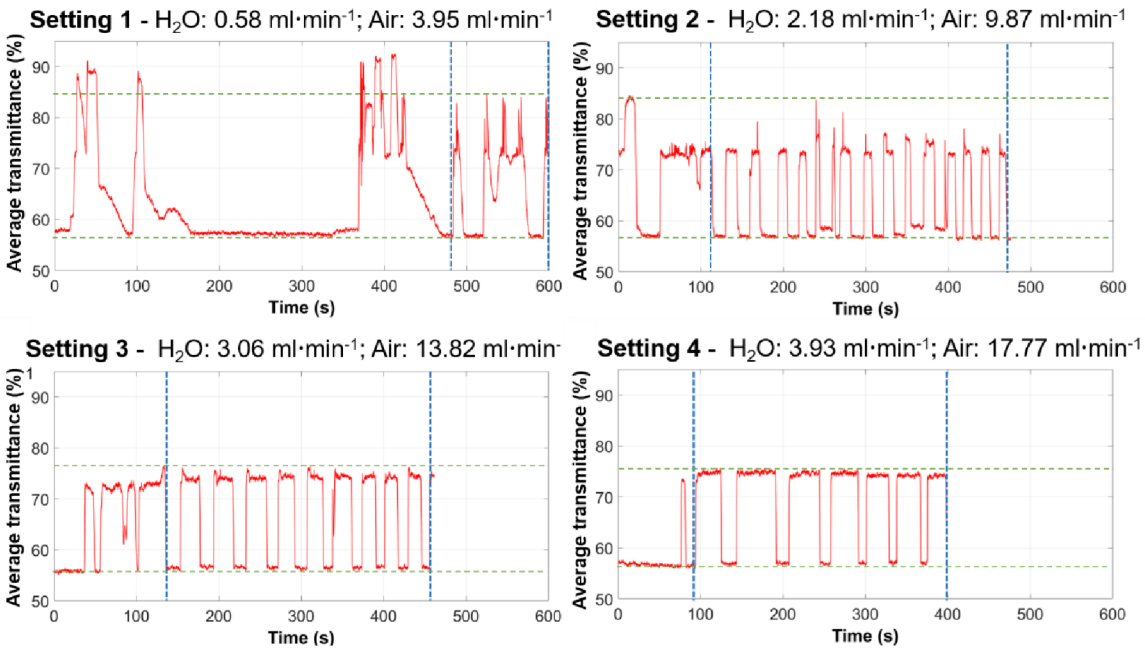

b) PTL-2

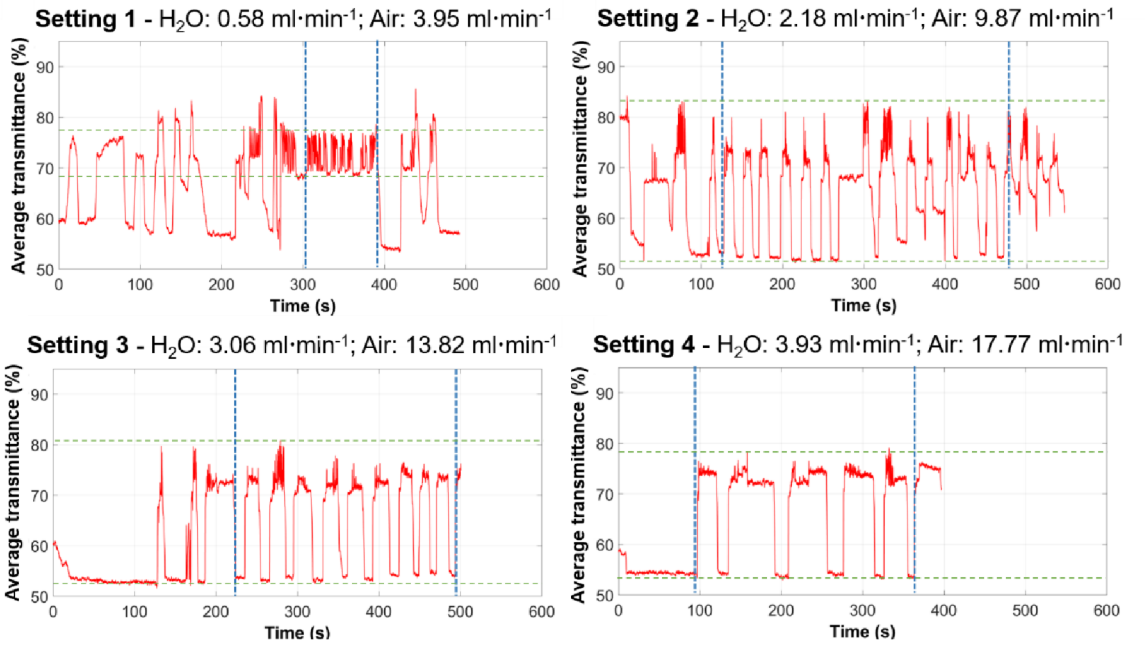

c) PTL-3

Figure 5-4: Time-dependent average transmission plots for a) PTL-1, b) PTL-2, and c) PTL-3 at different flow settings. The vertical blue lines define the steady-state periods that used for calculations. Image reproduced from Altaf et al.[125], under the Creative Commons Attribution 4.0 International License (CC BY 4.0).

The images in Figure 5-4 suggest that the initial neutron transmission was obtained again after each cycle for all measurements, indicating that a similar water saturation level in the cells (channels and PTL) was achieved following every cycle of air release. The water flow rates were increased along with the air flow rates, resulting in higher invasion pressure thresholds for air release through the PTLs. Consequently, longer air release times periods are anticipated for higher gas flow rates, as more air needs to be released. The frequencies of these cycles are

presented in Figure 5-5 and Table 5-1. The pressure build-up times and frequencies can be used to compare the impact of PTL structure. Interestingly, PTL-1 exhibits shorter pressure build-up periods compared to the other two PTLs, overall and particularly at low gas and liquid flow rates. This behavior might be attributed to the graded structure and presence of larger pores on the water-channel side in PTL-1, thus indicating a possible influence of the specific PTL structure.

Based on the observations from Figure 5-4, Figure 5-5 and Table 5-1, the following conclusions can be drawn. The frequency of the pressure build-up cycles appears to be influenced by both the PTL structure and the process conditions, including fluid flow rates and resulting pressure differences. Notably, for PTL-1, which is a graded PTL, the impact of flow conditions is more pronounced compared to the other two PTLs. However, even for the thin PTL-2, the influence of flow conditions is still higher than for the thicker PTL-3, where the flow conditions have minimal impact on the frequency of cycles. In Section 3.2.2, with the help of saturation and permeability profiles, a unique behavior for PTL-1 was also seen. It was observed that graded PTL provided a good balance between liquid and gas permeability at a constant saturation obtained. PTL-1 also offered a high liquid saturation region adjacent to the CL. Considering all of this, PTL-1 has an advantage over other PTLs due to its graded structure and it can be the best candidate for PEMWE, especially at high current density operations.

Table 5-1: Analysis of the plots in Figure 5-4. Average air and water pressure build-up times and frequency of the pressure build-up cycles. Table adapted from Altaf et al.[125], under the Creative Commons Attribution 4.0 International License (CC BY 4.0).

PTL	Setting	Time of air pressure build-up (s)	Time of water pressure build-up (s)	Average frequency (s^{-1})
PTL-1	1	0.9 ± 0.2	0.9 ± 0.1	0.612
	2	3.4 ± 1.8	3.1 ± 1.5	0.181
	3	2.3 ± 0.4	5.2 ± 2.9	0.137
	4	2.5 ± 0.3	7.2 ± 1.2	0.104
PTL-2	1	16.5 ± 6.8	9.8 ± 1.6	0.049
	2	13.1 ± 3.5	10.9 ± 2.3	0.045
	3	13.0 ± 2.4	20.4 ± 3.5	0.030
	4	12.6 ± 4.1	32.7 ± 7.6	0.021
PTL-3	1	4.3 ± 2.6	6.4 ± 4.8	0.112
	2	10.6 ± 2.5	10.2 ± 2.5	0.052
	3	10.3 ± 1.9	18.3 ± 2.9	0.037
	4	14.1 ± 4.6	39.1 ± 13.4	0.019

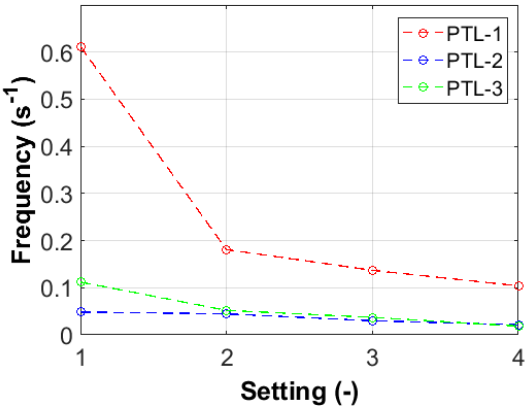

Figure 5-5: Dependence of frequency of pressure build-up cycles on PTL structure and flow settings. Image reproduced from Altaf et al.[125], under the Creative Commons Attribution 4.0 International License (CC BY 4.0).

In literature, the dependency of invasion on PTL-structure and flow conditions is studied independently of each other[82,85]. This separation may contribute to discrepancies in reported outcomes, as discussed in Section 1.2.6. Some studies indicate water scarcity in PTLs under certain flow conditions/current densities, while others suggest that water saturation remains unchanged regardless of operating conditions. A more comprehensive analysis of the correlations between structure, flow conditions, and PTL invasion, similar to this study but covering a broader range of parameters, is needed to improve the understanding of transport limitations. In addition to investigating various flow rates and PTLs with different structures, pressure conditions and variations within PEMWE cells and their flow channels should also be studied to gain deeper insights into invasion patterns and fluid distributions within the PTL.

5.1.3 Determination of break-through points

To better understand air break-through into the water channel through the PTL, the positions of break-through points are analyzed using water thickness plots (Figure 5-6). The periods with steady-state pressure build-up cycles, as indicated by the blue vertical lines in Figure 5-4, are selected for analysis. The break-through region, denoting the minimum water thickness observed across all images, is identified and examined.

As can be seen, the break-through region is unique for each PTL i.e., independent of the flow conditions. A unique break-through location, as seen in Figure 5-6, can be explained by two main factors. One is the spatially distributed ΔP between water and air channel (see Appendix A.7). This means that the pressure distributions in the channels and across the channels could favor the invasion and release of air through the PTL at certain locations at the channel/PTL interfaces; second is the PSD of the PTLs. These findings align with those of Seweryn et al.[83], Zlobinski et al.[87], and Panchenko et al.[84], who also identified constant gas break-through regions, indicating a structural dependency of transport in PTLs.

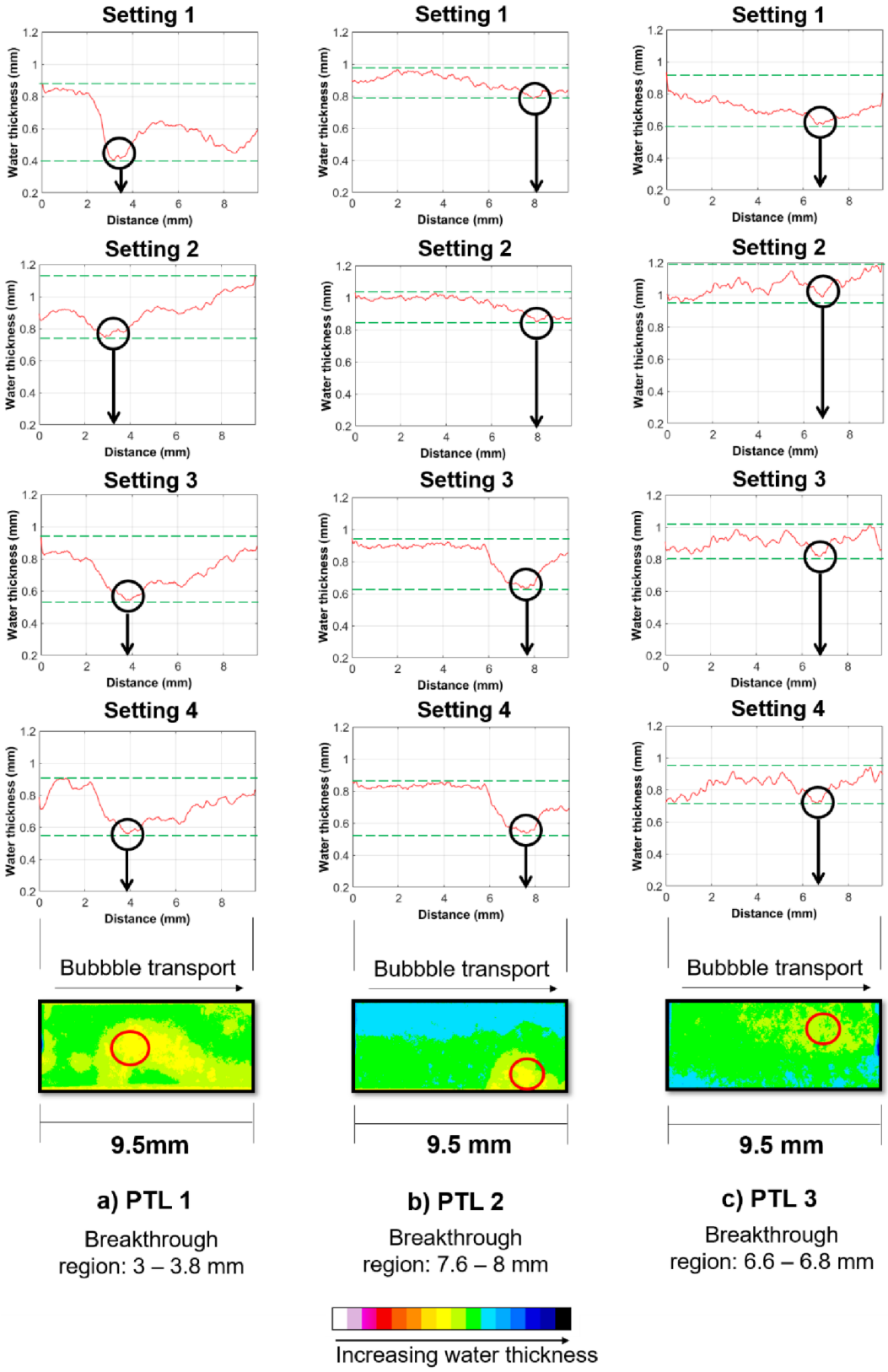

Figure 5-6: Break-through locations for each cell and setting using water thickness plots. The data is averaged over the time periods highlighted in Figure 5-4. Image reproduced from Altaf et al.[125], under the Creative Commons Attribution 4.0 International License (CC BY 4.0).

5.1.4 Transparent cell and influence of stoichiometry

The transparent cell (Figure 2-10), built as a prototype for non-electrochemical operation, was used to visualize the impact of stoichiometry. Specifically, bubble growth and release patterns were observed at different stoichiometries, an aspect not captured in the neutron imaging experiments. The results of these experiments are analyzed in this section. The water flows in the upper channel of the cell shown in Figure 2-10 and permeates through the PTL. Gas channel outlet is closed so the pressure builds up and the eventually pushes itself through the PTL. The air break-through from the PTL is seen in the form of bubbles in the water channel. The flow rates used correspond to a current density of 4.0 A·cm^{-2} (Table 2-4).

In Figure 5-7, it is seen that for each case (*ω*-1, *ω*-2 and *ω*-3), the bubble always exits the PTL at the same spot. More clearly, it is pointed out by red arrows in Figure 5-7b. This was also observed in the neutron imaging experiments, agrees with the literature[84,87,88] and hints towards the existence of preferential pathways. On the other hand, this could be due to the pressure distribution across the channel as well.

For each stoichiometry four images are shown. The time interval between image-a and image-d is 1 s in Figure 5-7. For *ω*-1, it is seen that the bubble exits the PTL (highlighted using white circle in image-a for *ω*-1) and then gradually grows in size (image-b). It then occupies almost the entire length in the channel in the direction of water flow (highlighted by a green oval in image-c) and then exits the channel while a new bubble starts to form at the same spot (blue arrow in image-d).

A similar trend is observed in *ω*-2 as can be seen from image-a to image-d. The only difference is that due to a higher water flow rate the bubble transport is faster. This can be visualized by comparing image-b for *ω*-1 and *ω*-2. Instead of a bubble growing in size at the same spot, it is carried further away by the water flow, and a new bubble starts to emerge at the break-through location (image-b for *ω*-2 in Figure 5-7). They all then agglomerate to form a big bubble (8.5 mm) that is carried away by the water (green circle in image-c for *ω*-2). Between the detachment of the previous bubble and the formation of a new one, the interface probably briefly retreats into the pore or throat region before reappearing at the break-through site, where a new bubble begins to emerge. The faster the water flow is, the faster the bubbles are removed from the channel, which was also suggested by various studies in the literature[50,82]. This is much more evident from *ω*-3. As seen for *ω*-3, image-a to image-d, the bubbles are much smaller in size (3.0 mm) as they have not enough time to agglomerate (yellow circles in Figure 5-7). In these experiments, it is seen that as the stoichiometry increases, the bubble size decreases. This is also in agreement with the work of Panchenko et al.[84]. In case of PEMWE cells, it means that, close to the water outlet, there could be large slugs of oxygen present. This is because all the oxygen produced will have to exit from one outlet and, hence, if the water flow rate is low the oxygen bubbles could agglomerate at the channel outlet. This could affect PTL wetting and water transport near the channel outlet[85,86], by temporarily blocking water access to the PTL surface, especially if long slugs

form and persist. As seen in case of ω-3, a higher flow rate aids in an efficient transport of bubbles from the PTL surface to the outlet without any slug formation. This could prevent the formation of gas slugs and support the establishment of bubbly flow through the channels so that water can uniformly be distributed throughout the surface area of the PTL.

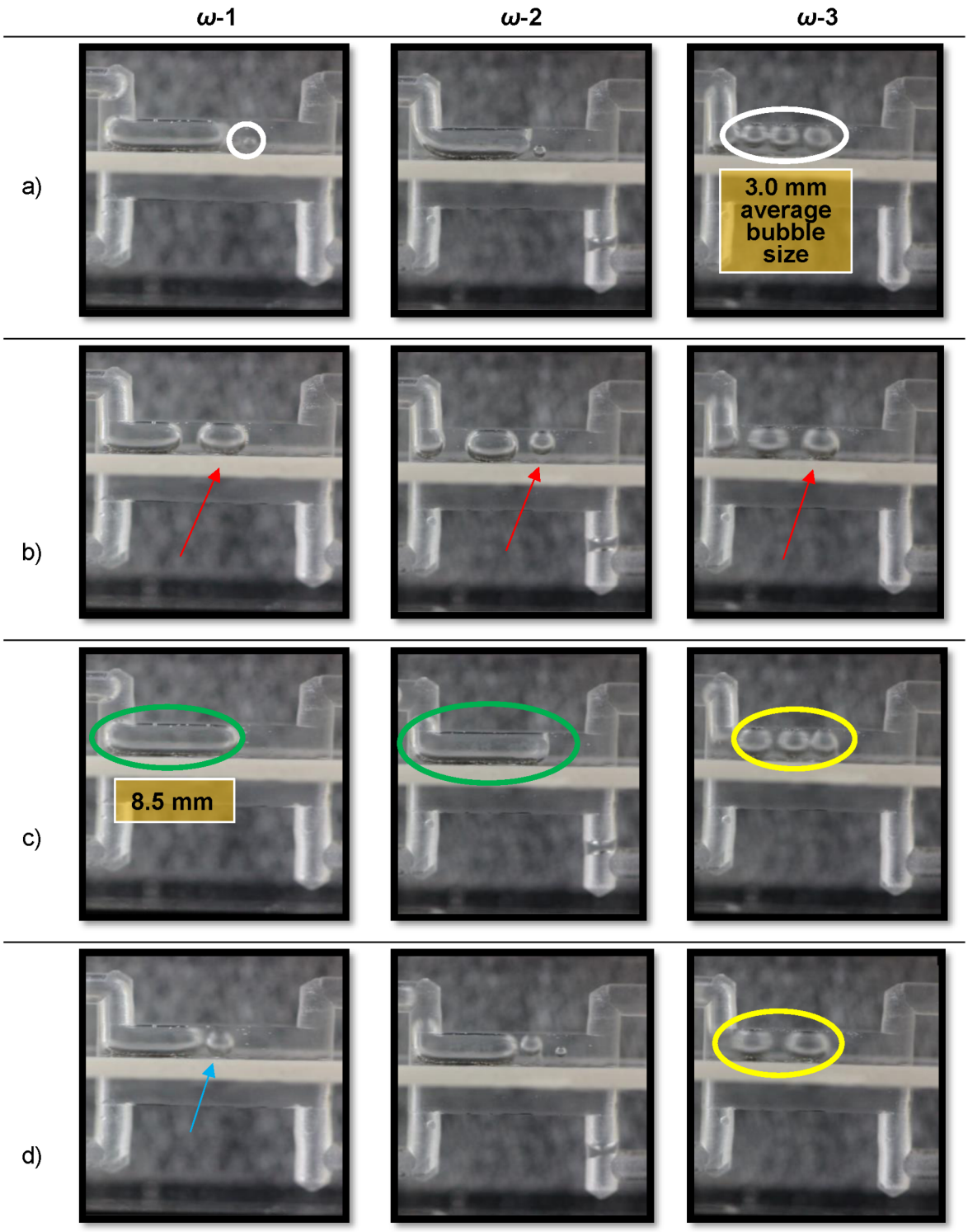

Figure 5-7: The release of bubbles into the water channel across the PTL captured at different stoichiometries (see Table 2-4) using a transparent flow cell. The PTL is sandwiched between the two channels: water channel (top) and air channel (bottom).

5.2 Electrochemical cells

Using PEMWE cells with neutron imaging, can provide more realistic insights in to the dependency of phase distributions on the structure or, possibly, on flow conditions. For this reason, some of the results from the collaborative neutron imaging experiments of electrochemical cells, planned and designed by M.Sc. Tamara Miličić (Ph.D. candidate at the Max Planck Institute for Dynamics of Complex Technical Systems, Magdeburg), are analyzed here. The images presented in this section are adapted from the master's thesis[127] of B.Sc. Ece Cakmak (OVGU Magdeburg), primarily supervised by M.Sc. Tamara Miličić and co-supervised by the author of this work.

Figure 5-8 shows the saturation profiles of PTLs in PEMWE-1 and PEMWE-2 across the thickness of each PTL. The solid lines are for an inlet water flow rate of 3.25 ml·min^{-1} in and the dashed lines (only in Figure 5-8b) represent an inlet flow rate of 10.0 ml·min^{-1}. It can be observed that, regardless of the current density, the water saturation profiles in PTL do not change significantly with a change in current density for both cells. This is something that was also anticipated by the non-electrochemical experiments shown in Section 5.1.2 and by other studies in the literature[84–88]. It further confirms the strong dependency of PTL saturation on its structure and not on the current density. Another notable difference observed between the two PEMWE cells compared in Figure 5-8 is that PEMWE-1 has higher water saturations because of higher PTL porosity (Table 2-5) for a flow rate of 3.25 ml·min^{-1} (solid lines).

These experiments also showed that PEMWE-1 exhibited better electrochemical performance than PEMWE-2 at an anode inlet flow rate of 3.25 ml·min^{-1}, although there was no significant difference in mass transport losses between the two cells. This could be attributed to the higher water saturation observed in PEMWE-1 with a higher porosity PTL (Figure 5-8). This is interesting because, normally, higher porosity PTLs could potentially also lead to poor interfacial contact with CCMs and a loss in performance[156]. A detailed electrochemical analysis of the cells will be presented in the Ph.D. thesis of M.Sc. Tamara Miličić.

Additionally, Figure 5-8b shows that water saturation in the PTL is primarily influenced by the inlet water flow rate rather than the current density, contrary to common assumptions in the literature[82]. As the anode inlet flow rate increased from 3.25 ml·min^{-1} to 10.0 ml·min^{-1} the overall water saturation rose from approximately 0.55 to 0.75.

This is a notable finding, as it indicates that PTL saturation is not solely governed by its structure, but also by the applied inlet flow rate. Based on the results presented in Section 5.1.3, the consistent break-through locations of air bubbles into the water channel were initially attributed to pressure gradients in the channel and/or PTL structure. However, the role of the inlet flow rate remained unclear, as the through-plane images obtained during the non-electrochemical experiments did not allow direct observation of saturation within the PTL. In practice, it is highly likely

that the PTL saturation depends on a combination of factors: the PTL structure, the inlet water flow rate, and the pressure distribution across the channel/PTL interface. Once steady-state is reached, the saturation then remains constant across different current densities.

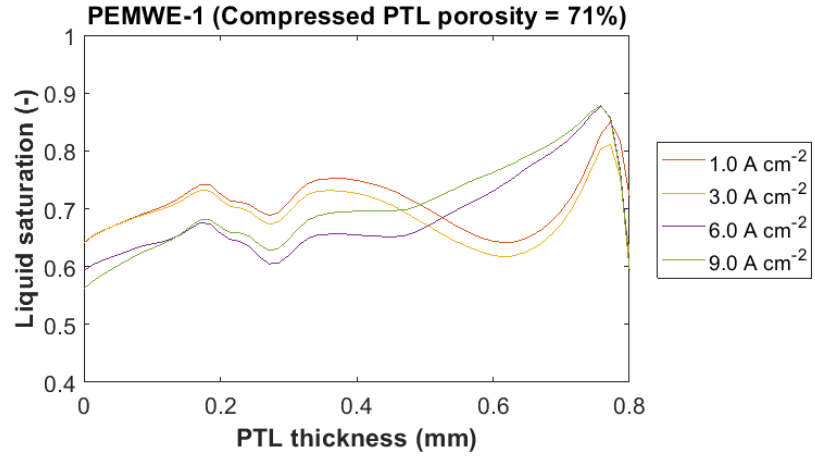

a)

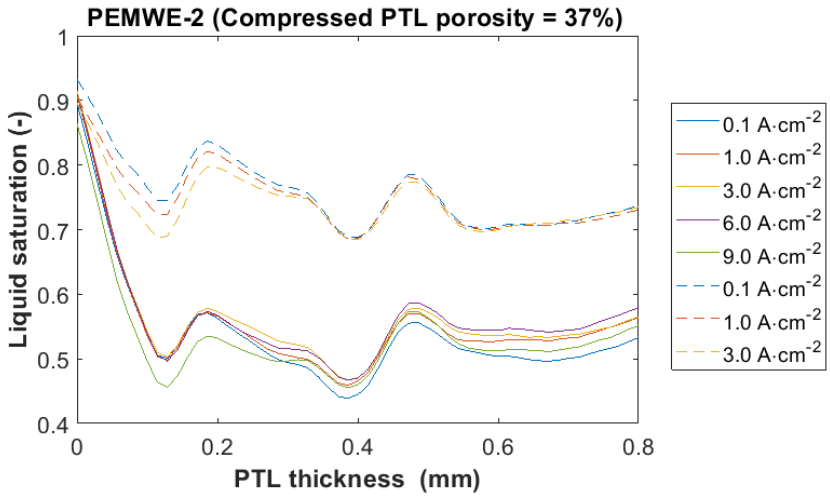

b)

Figure 5-8: Saturation profiles of PTLs in electrochemical cells. a) PEMWE-1 saturation profile at different current densities at an inlet flow rate of 3.25 ml·min^{-1}; b) PEMWE-2 saturation profiles at different current densities and two different flow rates for anode inlet; 3.25 ml·min^{-1} (solid lines) and 10.0 ml·min^{-1} (dashed lines). Images adapted from the work of Cakmak[127], a master's thesis completed at OVGU, supervised by M.Sc. Tamara Miličić and co-supervised by the author of this work.

In Section 5.1.3., for non-electrochemical cells, single break-through points were found by observing the minima on the water thickness plots and, as well as, the color grading of the raw images. In the case of electrochemical cells, water saturation profiles do not show a single distinct minimum that could be referred to as the break-through point. In fact, various minima can be observed (PEMWE-1 in Figure 5-9 and PEMWE-2 in Figure 5-10). Although, for a current density of 1.0 A·cm^{-2} and 3.0 A·cm^{-2} for PEMWE-1 and all current densities for PEMWE-2, it can be seen that the saturation profiles have several minima, showing the same break-through-points which can also be the preferential pathways of drainage. The observed minima remain unaffected by the current densities, as evident from the

color-graded PTL images, which appear identical across the mentioned current density ranges. The images also suggest multiple break-through points, with several regions of low water saturation at the interface between PTL and water channel.

In comparison to the non-electrochemical cells, it can be said that a single break-through point was not observed but rather multiple ones. Although, both cells suggest the existence of preferential pathways during operation as also assumed by the PNM. It must also be clearly stated here that the break-through points were analyzed using through-plane images in non-electrochemical cells and in-plane images in electrochemical cells. The observed discrepancy could also just be due to the difference in the observation perspective.

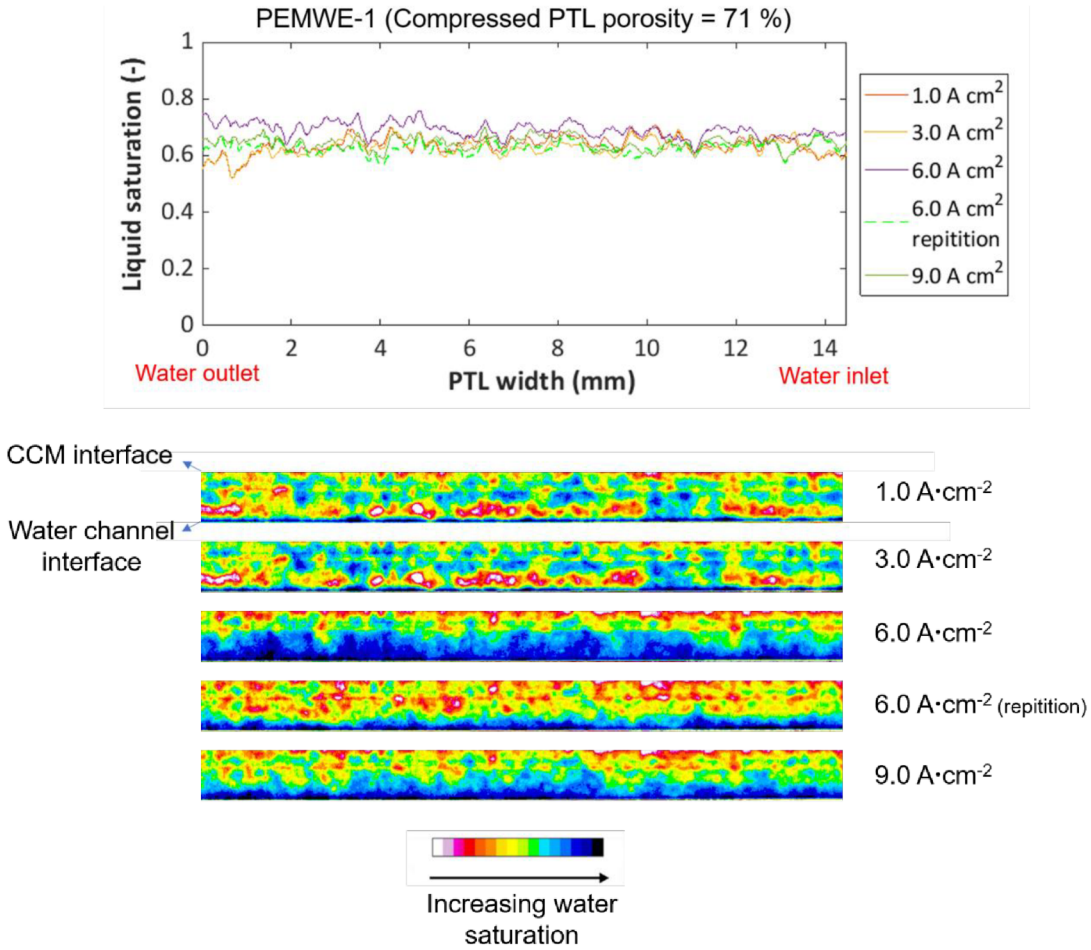

Figure 5-9: Water saturation profile across the PTL width along with the radiography results at different current densities. Images adapted from the work of Cakmak[127], a master's thesis completed at OVGU, supervised by M.Sc. Tamara Miličić and co-supervised by the author of this work.

In the case of PEMWE-1, a change in water distribution can be seen at 6.0 A·cm^{-2} (Figure 5-9). This change resulted because the cell was at open circuit voltage before this measurement, and that is why more water can be seen. Once the steady-state is achieved again, the new image at 6.0 A·cm^{-2} shows water distribution as similar to what is observed at other current densities in Figure 5-9. Although it can be seen that the average saturation increases only slightly

(approximately from 0.65 to 0.70) during this disruption at 6.0 A·cm^{-2}, highlighting that the gas/liquid distributions in the PTL can be disrupted and reset during start up and shut down. However, once the steady-state is achieved (shown by 6.0 A·cm^{-2} repetition), the produced gas reduced the overall water saturation to about 0.65 again.

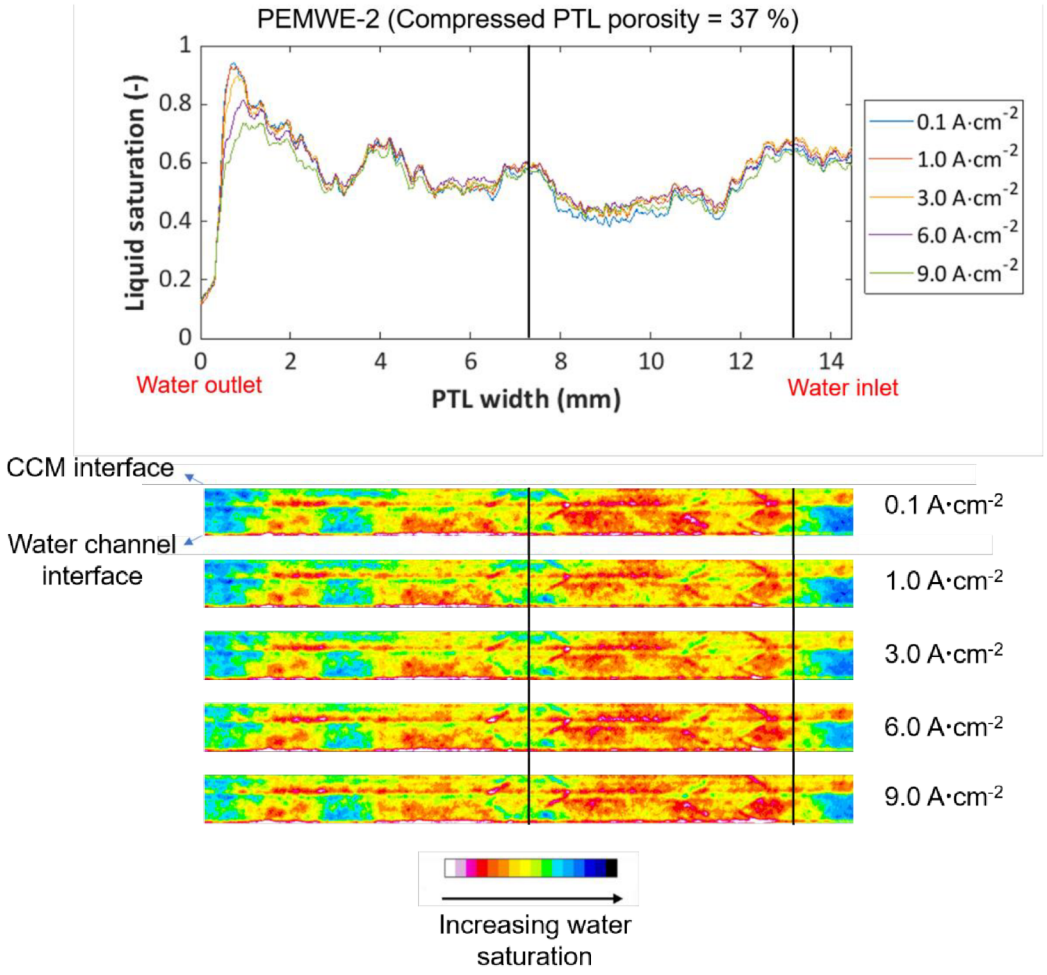

a)

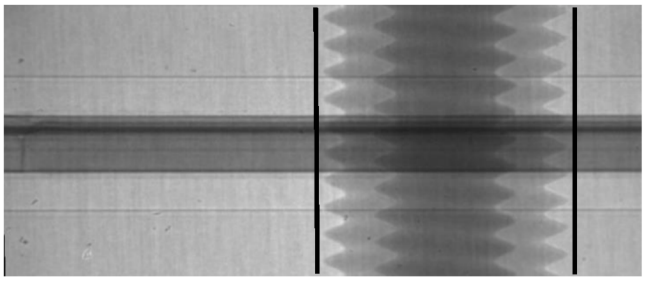

b)

Figure 5-10: a) Water saturation profile across the PTL width along with the radiography results at different current densities. The region marked with black lines is disregarded due to the presence of a screw in the filed of view; b) raw image of the screw in front of the PTL which was used to provide compression to the cell. Images adapted from the work of Cakmak[127], a master's thesis completed at OVGU, supervised by M.Sc. Tamara Miličić and co-supervised by the author of this work.

Comparing the saturation profiles of the two PTLs with different porosities (71 % in Figure 5-9; 37 % in Figure 5-10), it can be seen that the high-porosity PTL has a more uniform saturation (between 0.60 and 0.65) in comparison to the low-porosity PTL. In the low-porosity PTL, there are also regions (3 mm and 5 mm to 7 mm) with a saturation of approximately 0.5 and a maximum up to 0.9 at a distance of 1 mm. The regions at a distance of more than 7 mm are disregarded during analysis for this cell as a screw was in the filed of view. This screw had to be added to adjust the cell tightness and avoid leakages. The images in Figure 5-9 also reveal that the bottom regions (blue areas) of high-porosity samples retain more water. In contrast, the low-porosity PTLs show no such water-rich zones; instead, they exhibit significantly drier areas (red and yellow) near the bottom (in Figure 5-10). This difference could be due to the effects of lower porosity, which may have contributed to the reduced performance of PEMWE-2 compared to PEMWE-1 observed from the electrochemical results (to be published in the thesis of M.Sc. Tamara Miličić).

From these experiments, it can be concluded that the water thickness in the PTL does not strongly depend on the current density. The PTL saturation is found to be highly influenced by the inlet water flow rate, with higher flow rates leading to a significant increase in water saturation which remains unchanged at different current densities. Higher flow rates have also been recommended by a few other studies[85,86]. However, these recommendations are primarily aimed at enhancing bubble removal from the channel, ensuring an unobstructed inlet water flow.

While PNM simulations rely on the assumption that increasing gas pressure (due to higher oxygen production rate at higher current densities) can lead to progressive invasion and ultimately reach residual saturation, this assumption does not hold up when compared to the experimental observations in this work. In neutron imaging experiments, no systematic decrease in water thickness within the PTL was observed with increasing current density. This strongly suggests that, once a gas pathway is established (i.e., at break-through along with the existing gas islands due to incomplete wetting), further increases in current density do not open additional pathways or reduce saturation meaningfully. Instead, it could be that the gas release rate increases, but it occurs through the same already-invaded channels.

The increased mass transport losses at higher current densities, as commonly reported in the literature, may not stem from further gas invasion that empties the PTL. Rather, they could result from water scarcity due to increased water consumption in at the CL and insufficient replenishment, especially under low stoichiometry or flow rate conditions, amplifying transport limitations. Other contributing factors may include bubble accumulation at the water inlet, clogging at the interface between PTL and the channel, localized drying of thin CL, or non-uniform wetting, all of which can increase resistance and hinder reactant transport without requiring a significant change in bulk PTL saturation. Furthermore, increased operating temperature at high current densities can accelerate water evaporation, reducing liquid saturation within the PTL and contributing to mass transport limitations These mechanisms provide a more physically grounded and

experimentally consistent explanation for the observed performance losses at high current densities. If, however, the increased mass transport losses reported in the literature do stem from gas blocking water transport, it is likely confined to the microscale, occurring in isolated pores at the interface between PTL and CL, and thus remains unresolved in neutron imaging experiments.

Therefore, based on the results of these experiments, the assumption in PNM that saturation continues to decrease with increasing gas pressure, ultimately approaching a residual saturation, does not appear realistic for high-porosity fiber-PTLs under steady-state PEMWE conditions. It is more likely that the structure determines the degree of PTL wetting and break-through path, which remain stable over a wide range of operating currents. As such, the residual saturation predicted by PNM may be more representative of a theoretical drainage limit rather than an experimentally observable or practically relevant state during operation.

In this context, experimental results provide a more accurate picture, indicating that inlet water flow rate, rather than current density, governs the local saturation in the PTL. The PNM models remain useful for capturing structural limits (e.g., the invasion and break-through patterns), but their assumption of progressive drainage beyond break-through may overestimate the role of electrochemically generated gas in displacing water under various operating conditions.

Chapter 6
Conclusion

In this work, a comprehensive investigation of PTLs for PEMWE was presented. The thesis primarily explored the applicability of PNM in studying mass transport in PTLs. This was done by employing extracted PNs and idealized PNs. The extracted PNs were obtained with the help of micro-CT imaging of commercial fiber-PTLs. Such high-porosity commercial PTLs with different properties were studied and compared for the first time in this work. The idealized PNs were used to simulate and study different types of PTLs from the literature, as well as arbitrarily graded structures in PTLs. Besides modeling, neutron imaging experiments were employed to investigate and visualize the two-phase flow within the commercial fiber-PTLs.

6.1 Summary

At the start of the thesis, in Chapter 1, a detailed literature review was provided. The purpose of this overview was twofold: One was to provide an overview of the existing materials and methods used in the literature, and the second was to identify gaps in the existing studies. It was highlighted that there is a lack of studies focusing on the interconnection between the transport in PTLs and their structure. Moreover, it was observed that there is a distinct scarcity of studies based on commercial fiber-PTLs used in PEMWE stacks. Besides, the transport parameters, e.g. permeability and thermal conductivity, are also rarely found in literature for such PTLs. These parameters are crucial, not only for material characterization and comparison between different structures but also for parameterizing CMs. Based on these findings, the scope of the thesis was defined.

The introduction was followed by the description of PNM and neutron imaging experiments in Chapter 2. At first, the model extraction methodology was described in detail consisting of the image processing steps along with the drainage model and its assumptions. In this chapter, it was also shown that an over-segmentation issue exists when using OpenPNM[78] for high-porosity PTLs, and the MorphLibJ[104] plugin in ImageJ proved to be a much better option for the image segmentation. Furthermore, this chapter presented the extraction of transport parameters, including permeability, capillary pressure curves, and thermal conductivity. Additionally, neutron imaging experiments for analyzing two-phase flow in PTLs were discussed. The experimental setups, materials used and post-processing steps for acquired image data were explained in detail in this chapter. The experiments were performed using non-electrochemical cells with three different PTLs and, as well as, with electrochemical cells with two different PTLs.

In Chapter 3, the applicability of PMNs for simulating the drainage of water from PTLs and parameter extraction was explored. At first, it was demonstrated that the PMN is capable of accurately predicting the invasion patterns observed in a 2D microfluidic device and in LBM and CFD simulations. In terms of computational time, the differences were substantial; for example, PNM simulation took less than a second, while, for the same domain, CFD and LBM simulations required 4 h and

90 h, respectively. It was argued that the PNM suffices the need for studying the invasion patterns and saturations and provides a good compromise between the accuracy and computational cost. On the other hand, if the goal is to study the pore-scale physics then direct numerical simulations are a much better option.

This was followed by PNM simulations using extracted PNs from micro-CT images in Section 3.2. PNs were generated from 3D images to derive correlations for permeability and capillary pressure. The permeability values were compared to experiment-based models (TSM and JJM, for all PTLs), and GeoDict (only for PTL-1). It was observed that TSM and JJM yield similar values of absolute permeability for the studied ranges of porosity and fiber diameter. However, these values were lower than those predicted by the PNM, for all three PTLs. The PNM predicted similar values for all PTLs, with PTL-1 being slightly more permeable than the other two PTLs. This was probably due to the graded structure of PTL-1 with relatively large pores on one side. The intrinsic permeability value predicted by GeoDict ($1.1 \cdot 10^{-10}$ m^2) was found to be very similar to the value predicted by PNM for PTL-1 ($1.5 \cdot 10^{-10}$ m^2). This further highlighted the balance between computational cost and accuracy provided by PNM. For a domain size of 5.40 × 5.10 × 0.53 mm used in this work, PNM can estimate permeability within a few seconds, whereas for the same domain size GeoDict simulation would have required several hours on an eight-core workstation. Additionally, it was observed that the fiber diameter has a great impact on the predicted permeability values from literature correlations (TSM and JJM). A good agreement with PNM was found for PTL-1 only, when averaging the permeability values at d_f = 25 µm and d_f = 40 µm, which are the two fiber sizes used to produce PTL-1. PTL-2 and PTL-3 had a fiber diameter of 20 µm. From this, it was deduced that the TSM and JJM are expected to more accurately predict permeability of PTLs with larger fiber diameters. With respect to porosity, the permeabilities varied linearly in the studied range with $\Delta K/\Delta\varepsilon = 4.5 \cdot 10^{-10}$ m^2.

Furthermore, in Chapter 3, the capillary pressure curves obtained from drainage simulations were compared to empirical correlations, namely LE and BCE. A sensitivity analysis was performed by varying the independent variables (e.g. θ, r_{max}, λ, K, etc.) in LE and BCE. The goal was to observe the limitations of these correlations and see under which conditions they agree with or deviate from PNM predicted curves. The parameters resulting in best-fit curves for LE and BCE on the PNM were also identified for each PTL. Both models showed good agreement at intermediate liquid saturation levels (~ 0.5). However, while LE failed to accurately predict capillary pressure at both high and low saturation levels, BCE provided a better fit to the PNM curves, particularly at low saturations (s_l < 0.2). Nevertheless, such low saturation values are not reached in drainage simulations due to the presence of isolated liquid clusters. Notably, the graded PTL-1 exhibited a transitional behavior between PTL-2, which has generally larger pores, and PTL-3, which consists of smaller pores. Consequently, it could be said that LE and BCE should not be used for high-porosity PTLs when compared to PNM as they are

largely empirical in nature, whereas, PNM can provide much better predictions by considering the role of local pore connectivity.

In terms of relative permeability plots, PTL-1 exhibited high liquid and gas permeabilities at high liquid saturations, in comparison to PTL-2. This serves the purpose of a PTL best by providing efficient oxygen removal and, as well as, efficient water transport. Such behavior can be attributed to the graded structure of PTL-1, resulting in less lateral invasions and more connected pathways for fluid transport. For PTL-3, due to a thicker structure with no gradient resulting in more lateral invasions, high relative gas permeability values were observed at low liquid saturation and relative liquid permeabilities. This might aid in efficient gas removal but, if the PTL is not imbibed again and again by water effectively, it could lead to water starvation issues. Direct evidence, however, for periodic imbibition and drainage during steady-state PEMWE operation is missing. Unchanged gas/liquid distributions in a PTL even at varying current densities are more commonly reported[85–87]. Based on these results, PTL-1 is recommended as a promising candidate for PEMWEs. Such a PTL, with smaller pore sizes on the CL side, also offers the advantage of potentially smaller interfacial contact resistance (PTL-CCM interface). This aspect was not explored in this work, but the literature highlights it as an important PTL functionality as well[42–44].

In addition to PNM, thermal conductivity of the PTLs was analyzed using VNs and extracted PNs. Conductivity values for both dry and wet PTLs were estimated using VNs. The dry conductivity values were also obtained by using Hot Disk experiments. The experimental values reported were: 0.34 $W \cdot m^{-1} \cdot K^{-1}$ (PTL-1); 0.21 $W \cdot m^{-1} \cdot K^{-1}$ (PTL-2); 0.20 $W \cdot m^{-1} \cdot K^{-1}$ (PTL-3). For PTL-1, the weighting parameter f was fitted to 0.81, indicating that the series conductivity model dominates due to the layered structure and high porosity, which increases the thermal resistance. For PTL-2 and PTL-3, even the lower bound of thermal conductivity at $f = 1$ exceeded the experimental values, likely due to model simplifications. Since direct fitting was not possible, $f = 1$ was used to have better agreement with the experimental results, yielding conductivities of 0.26 $W \cdot m^{-1} \cdot K^{-1}$ for PTL-2 and 0.28 $W \cdot m^{-1} \cdot K^{-1}$ for PTL-3. The measured values for PTL-1 were slightly higher, which could be attributed to potential variations in the graded structure, fiber diameter distribution, or the sintering process of this particular PTL (manufactured by a different producer than the other two PTLs). Additionally, thermal conductivity was evaluated at the residual saturation (s_r) using the PNM-derived phase distributions. PTL-3 had the lowest value (1.28 $W \cdot m^{-1} \cdot K^{-1}$) due to minimal residual liquid saturation (0.19). PTL-1 and PTL-2 had similar saturation levels (~0.65), but PTL-1 showed 1.8 times higher conductivity, possibly due to large liquid-filled pores on the water channel side.

The thermal conductivity values for dry PTLs were also calculated using structural models from literature (ME models[117,118], EMT[120], and exponential relation[119]) in Section 3.2.2. However, none of these models closely matched the values obtained from Hot Disk experiments for all PTLs. A similar observation was made by Wang et al.[119] in a study on GDLs, where they suggested modifying structural models for

specific materials. It could be concluded that using VNs and Fourier's law captures the effects of pore connectivity and localized conduction bottlenecks, while models like ME and EMT assume more uniform phase distribution, leading to higher predicted conductivities. In fiber-PTLs, actual heat transfer is limited by fiber connectivity, which these literature models do not fully account for. Incorporating more complex mechanisms, such as the heat pipe effect[109], would improve the model and better capture the heat transfer processes in a PTL of an operating PEMWE. However, there is still limited understanding of the microscale dynamics of water within PTLs.

A generalized relationship between saturation and thermal conductivity for high-porosity fiber-based PTLs was developed using randomized pore-throat saturation states. While more rigorous correlations would ideally rely on saturation profiles from a very large and diverse simulation-dataset, rather than just three PTLs exhibiting three different distinct saturation profiles only, covering only a certain range of saturation. The randomized method provides a practical alternative, enabling trend analysis across the full saturation range without being tied to a specific structure or invasion pattern. This offers a useful approximation for modeling purposes and helps guide future studies on multiphase transport in fiber-PTLs. Despite the limited dataset and simplified modeling approach, the results remain significant, as this work presents the first saturation-based correlation for thermal conductivity that can be integrated into CMs to predict temperature profiles within a PEMWE.

In the last part of Chapter 3 (Section 3.3), extracted and idealized PNs were compared. It was argued that the idealized PNs have further reduced computational requirements with the absence of image processing steps used for the extraction of structure. The permeabilities and saturation profiles were compared using an idealized PN and an extracted PN, with same number of pores. The permeabilities of the two PNs were found to be in a very good agreement. In terms of saturation profiles, the absolute values of the saturation across the network height differed as the geometry and coordination number of the two networks differ notably, but the trends observed in the saturation were found to be in good agreement. In addition to that, the overall liquid saturation of both PNs was found fairly similar too, with a difference of only 7 %. This highlighted the applicability of idealized PNs for studying invasion patterns, as well as for extracting saturations and permeabilities for various PTLs, whether from literature or those generated in order to study the influence of various graded structures.

The idealized PN simulations were then shown in Chapter 4. In the first part (Section 4.1), the influence of PTL structure on the invasion process was investigated using different types of PTLs with different properties. Idealized 3D simulations were used to study ten different PTLs from literature. The findings aligned with theoretical investigations based on invasion probability[157]. Similar to the findings from extracted PNs, it was observed that thicker PTLs, due to more lateral invasion, exhibited lower relative liquid permeabilities. This demonstrated

that the phenomena observed in extracted PNs (in Section 3.2.2) can also be replicated in idealized PNs. The permeability values were also calculated for the PTLs from literature and compared with literature-provided values. It was argued why, in some cases, the comparison may not work, because the PNM provides intrinsic permeability values, whereas the literature values found were mostly non-intrinsic, obtained from fluid flow simulations or experiments.

In the second part of Chapter 4 (Section 4.2), it was shown using PN simulations how gradients in pore/throat sizes can impact the invasion of gas into a liquid saturated porous medium. Mainly five different cases were studied. It was shown, that the final saturation of the gas phase decisively depends on the direction of the gradient and, as well as, on the design of the gradient, as the PN with dual porosity revealed a different invasion behavior than the LTH network. Lower overall gas saturations at break-through of the gas phase were obtained in the case of PNs with LTH gradient, in both, 2D and 3D simulations. Only when an increase in gas pressure was simulated to invade beyond the break-through point, the formation of new gas fingers resulted in a higher gas saturation in the LTH-case. Interestingly, the obtained saturation profiles for LTH and HTL were not opposed when the break-through point was considered. The HTL gradient revealed a significantly lower liquid saturation at the top side (CL side) than obtained for the LTH case because of more lateral invasions based on the invasion probability rules favoring the larger pores present at the top of a PN. In the DP case also, a high liquid saturation was observed at the low-porosity side (CL side). However, inside the high-porosity region of the DP network, gas invasion resulted in the formation of more isolated liquid clusters and thus, resulted in a lower overall liquid permeability than in the LTH network, leaving some open questions for future work and the design of the PTLs. In the LTH and DP cases, it was observed that the top side of a PTL consistently had higher liquid saturations, which could be beneficial for high current density operations where membrane dehydration is a risk.

In summary, optimizing phase transport is a trade-off, as higher gas permeability typically reduces liquid permeability. This is especially problematic if the liquid phase is split up into a large number of isolated liquid clusters that hinder the transport of liquid and gas as well. This was mainly observed in the simulations without pore/throat size gradient and in simulations with HTL networks. However, the simulation results indicated that the best scenario is obtained for LTH, followed by the DP case, as the distinct gas fingers provide pathways for the gas phase while maintaining high liquid permeabilities. This was similar to what was observed for PTL-1, using the extracted PNs, which has a graded structure too.

In Chapter 5, the results from the neutron imaging experiments were shown. From the tomography of imbibition and drainage of PTL-2 and PTL-3, water scarcity was documented using non-electrochemical cells. More dry regions were identified for thicker PTL (PTL-3). Even after repetition of several imbibition/drainage cycles, these regions remained dry throughout the thickness of the PTL and not just in a few pockets. Such dry regions are expected to enhance the gas removal, if they

form an interconnected path between the top and bottom interface. At the same time, such dry regions also hint towards water scarcity in the PTL, thus impeding the water transport.

The most important takeaway from the non-electrochemical cell experiments was that the break-through of gas through each PTL occurred at a constant location, independent of the flow setting (current density) applied. These experiments also showed repetitive pressure build-up cycles with frequencies depending on the PTL structure and the flow rates. However, the frequencies of pressure build-up cycles for PTL-1 (the graded PTL) were the highest. This certainly shows the importance of the microstructure and the PSD. The impact of graded PTL structure was once again highlighted and proved to be better than non-graded PTLs, as also shown using the extracted and idealized PNs in Chapter 3 and Chapter 4, respectively. The bubble release period between these gas and liquid pressure build-up cycles presented a more realistic scenario of transport through PTLs at steady-state in a PEMWE, as shown by Selamet et al.[86] as well. In this period, bubbles are continuously released through the PTL into the channel, while simultaneously water is transported through the already developed pathways, with no new pathways being formed for either liquid or gas. These findings hint towards the PTL architecture to be enhanced using novel techniques, such as 3D printing, vacuum plasma spraying, etc. The tuning of the PTL microstructure could also be done by using fibers of different wettability. The work of Shojaei et al.[158] suggests that a mixed wettability fibrous structure gives rise to minimal surfaces , which are interfaces that minimize surface energy and curvature, and can enhance fluid transport through porous materials.

From the results of non-electrochemical cell experiments, it was concluded that imbibition must be incorporated in the PNM and the simulation must start with an imbibition cycle, thereby realizing an initial situation where not all pores are saturated at the start. Imbibition could also be used to simulate the effect of start-up and shut-down of a PEMWE on the PTL saturation. Moreover, the PTL seems to never be completely saturated or re-saturated during steady-state operation. This is an important fact that needs to be considered while modeling PTLs. For this purpose, the average water saturation of a PTL during operation should be determined (by simulations, validated by ex-situ experiments). And, the fact that the PTLs might have a constant average saturation during operation, must be considered for determination of transport properties.

In Section 5.1.4, the results from the transparent non-electrochemical cell experiments were used to visualize the bubble release patterns at three different stoichiometries. It was seen, in these experiments too, that the bubbles emerge always at the same location in the channel, as concluded from the neutron imaging experiments. Additionally, it was seen that the bubbles occupy the water channel completely at lower water flow rates (lower stoichiometries), whereas higher water flow rates improve the removal of gas bubbles. This means that if the bubbles are not carried away efficiently by water, the blockage in the channel can hinder the

water transport towards the CL, especially at high current densities. This has also been highlighted in literature[85,86].

The neutron imaging experiments performed using electrochemical cells showed that PTL saturation is independent of the operating current density (regardless of the inlet flow rate). This further highlights the importance of the PTL microstructure. These experiments were performed using two PEMWE cells with non-graded PTLs with two different porosities (71 % and 37 %). Moreover, only in-plane images were analyzed for these experiments and, for this reason, it was hard to clearly identify the break-through points. This is because the in-plane images contain a lot of cumulated information. From the images, one could only say that there is a possibility of multiple break-through points, unlike one break-through in non-electrochemical cells. From the steady-state images and saturation profiles, it was observed that the phase distribution did not change in the PTLs with changing current density and it can be said that preferential pathways do exist, as argued using the PNM simulations and non-electrochemical cell experiments.

Using the electrochemical cells with low-porosity PTL (PEMWE-2), the impact of inlet water flow rate at the anode was studied too. Interestingly, it was observed that for a higher inlet flow rate, the PTL saturation increased and then remained unchanged with changing current density. This suggests that saturation within the PTL is influenced by the inlet flow rate, highlighting that PTL wetting is governed by an interplay between structural characteristics and water supply conditions. The influence of inlet flow rate not anticipated in the non-electrochemical cells could be due to the through-plane setup, making it impossible to analyze PTL saturation alone, and/or due to the influence of pressure distribution in the water channel. The mass transport overpotentials were also observed to be marginally lower than at higher flow rates for PEMWE-2 (electrochemical results from this collaborative study will be provided in the Ph.D. thesis of M.Sc. Tamara Miličić, a Ph.D. candidate at the Max Planck Institute for Dynamics of Complex Technical Systems, Magdeburg). This improvement was likely associated with the increased water saturation and more efficient water delivery to the CL. In addition to that, it can be due to the bubble coverage phenomena observed by the transparent non-electrochemical cell in Section 5.1.4. At higher flow rates, probably the bubbles did not coalesce, preventing blockages of water flow in the channel, which could have led to better water transport and, consequently, lower mass transport overpotential. This finding, highlighted by Selamet et al.[86] as well, must be considered when designing strategies to improve mass transport in PEMWE.

The experimental results challenge a key assumption in PNM that increasing current density (and thus oxygen production) leads to progressive gas invasion and eventually residual saturation within the PTL. Neutron imaging revealed no significant decrease in water thickness with increasing current density, indicating that once a breakthrough pathway is formed, additional pathways are not activated (at least not on a scale that could be visualized). This suggests that structural characteristics along with the inlet flow rate determine the degree of initial PTL

wetting and breakthrough behavior, which remain stable across a wide range of current densities. Consequently, increased mass transport losses at high current densities are more plausibly attributed to water scarcity at the CL, caused by increased consumption and insufficient replenishment under low stoichiometries, rather than to additional gas invasions causing water scarcity. Other factors such as bubble accumulation at the channel inlet, local drying, non-uniform wetting, and evaporation at elevated temperatures may further hinder transport without significantly altering bulk PTL saturation. Therefore, the residual saturation predicted by PNM likely represents a theoretical drainage limit rather than a physically realized state under steady-state PEMWE operation.

6.2 Key highlights and findings

The main highlights and their implications are outlined below:

- For the first time, commercial high-porosity fiber-PTLs were used to investigate the invasion behavior in PTLs by means of extracted PNs from micro-CT imaging.

- PNM was demonstrated to be a viable tool for analyzing and comparing PTLs, as well as for extracting key transport parameters, offering a feasible alternative to empirical correlations commonly found in the literature.

- Graded PTL, PTL-1, was observed to be the best candidate in terms of providing a balance between liquid and gas transport.

- For the first time, a correlation for thermal conductivity and saturation was provided for PTLs which highlights the importance of PTL saturation on thermal conductivity.

- PTLs with LTH gradient were suggested to enhance the water imbibition due to higher liquid permeability and better gas drainage based on invasion probability.

- For the first time, neutron imaging tomography was used to compare water distribution in different PTLs. It was shown that a thicker PTL can have much more unsaturated regions compared to a thinner PTL.

- Additionally, using tomography, water scarcity was observed even in high-porosity PTLs.

- Similarly, for the first time, radiography data from neutron imaging experiments were used to compare different fiber-PTLs and the impact of their structure on the transport behavior.

- Using a non-electrochemical and transparent flow cell, it was understood that bubble transport through the PTL and into the channel could be influenced by the pressure distribution and flow conditions within the channel. The impact of stoichiometry on bubble growth in the channel was also highlighted, as it can lead to localized variations in PTL wetting.

- Most interestingly, neutron imaging experiments demonstrated that two-phase transport through the PTL is largely independent of current density, and is instead governed by the microstructure of the PTL, the applied inlet water flow rate, and the pressure distribution in the channel.

6.3 Outlook

Building on the findings of this work, several key areas for improvement can be identified to enhance the understanding and optimization of transport in PTLs. While the PNM has proven effective in predicting drainage profiles, adding imbibition processes to the PNM and coupling it with CMs would allow for a more detailed analysis of PTL wetting under different dynamic conditions. This would be especially relevant in PEMWEs powered by intermittent energy sources like solar and wind, where load fluctuations occur. It would help in simulating the fluctuations in a PEMWE for such applications and, generally, for understanding the impact of start-up and shut-down operations.

Although extracted PNs have demonstrated their effectiveness, certain simplifications, particularly in pore-throat geometry, introduce uncertainties. A potential improvement involves incorporating a shape factor to refine the representation of complex geometries. The Mayer & Stowe and Princen (MS-P) method, as suggested by Huang et al.[97], could enhance the accuracy of capillary pressure calculations for fibrous structures. Similarly, Dong et al.[159] highlighted the significance of shape factors in defining intricate geometries. However, calculating shape factors is computationally demanding, requiring precise perimeter measurements from 3D images. While this refinement would be valuable when studying microscale invasion physics, it may not be necessary for computationally efficient transport parameter extraction, as demonstrated in this work.

Additionally, water management remains a crucial issue, as understood by the neutron imaging experiments and prior studies[84,88]. However, the lack of significant observable changes in the bulk PTL under varying current densities suggests that key transport limitations could originate at the microscale, particularly at the PTL-CL interface, where localized evaporation, thin liquid films, or phase changes could play a significant role at high current densities. Understanding these phenomena requires more targeted investigations using operando high-resolution imaging at a pore-scale level or advanced pore-scale multiphase modeling that incorporates e.g., evaporation and condensation effects. Gaining such insights could clarify the true limiting mechanisms beyond what bulk measurements reveal. In parallel, advanced manufacturing techniques, such as 3D printing or vacuum plasma spraying, could provide greater flexibility to design and test graded or hybrid PTL structures that promote more effective water uptake and retention. Such engineered architectures could expand the operational window of PEMWEs by ensuring reliable water delivery to the CL, enhancing heat removal, and supporting stable membrane hydration across a range of dynamic conditions.

While transport properties have been a major focus, electrical resistivity and mechanical stability of PTLs must also be considered. Future studies should include fatigue testing (e.g., compressive cycling) to evaluate long-term mechanical robustness of different PTL types and structures. Additionally, electrical resistance measurements should be conducted to determine how different PTL structures impact overall cell performance. Another key aspect to consider is the surface

topography of PTLs, which significantly influences contact resistance at the PTL-CCM interface. Detailed microscopic analyses of different fiber- and particle-based PTLs could provide valuable insights into how surface roughness and material composition affect interfacial resistances, and, consequently, PEMWE efficiency.

Furthermore, while this work has primarily focused on fiber-based PTLs, particle-based PTLs offer an alternative approach that warrants further investigation. Although widely discussed in the literature, particle-PTLs have not been thoroughly analyzed or compared to understand how different structures influence transport properties and PEMWE performance. A comparative analysis of particle-PTLs and fiber-PTLs, in terms of transport properties, mechanical stability, and conductivity, could uncover potential advantages. Additionally, exploring different particle sizes, morphologies, or hybrid materials may lead to optimized PTL designs for improved performance. In the author's view, based on the materials available on the market, a high-porosity fiber-PTL (ε = 60 % to 80 %) combined with a particle-based MPL (ε = 30 % to 40 %) could present an optimal design, balancing both efficient water transport and reduced interfacial contact resistance at the PTL-CCM interface. The high porosity of the fiber-PTL would enhance liquid permeability, ensuring sufficient water supply to the CL, while the particle-based MPL could improve interfacial contact, reducing resistive losses and enhancing overall performance. This combination may offer a promising pathway for improving both mass transport and electrical conductivity in PEMWEs.

Thermal conductivity also remains a crucial parameter influencing temperature distribution within the PEMWE. Future experimental efforts should focus on measuring PTL thermal conductivity under dynamic conditions. Conducting in-operando conductivity measurements would provide real-time insights into temperature variations during operation. This could potentially be achieved through in-situ methods, using embedded microsensors, infrared thermography, or operando thermal impedance spectroscopy, providing insights into how water saturation, gas evolution, and compression influence thermal transport in real time. These experiments would help develop and refine models by incorporating localized temperature effects and saturation-dependent conductivity for more accurate predictions.

While this work has laid a strong foundation for understanding and modeling transport in PTLs, several key areas remain open for further exploration. These include enhancing modeling accuracy, studying dynamic transport behavior, and integrating experimental validation. Moreover, since commercial PEMWEs operate as stacks (series of individual cells) rather than single cells, future research should increasingly focus on stack-level studies. The performance and dynamics in a stack can differ significantly due to their design, and factors such as the mechanical behavior of components and contact pressure distribution play a critical role too. Addressing these topics and challenges will support the development of more efficient, durable, and scalable PEMWE systems for sustainable hydrogen production.

Bibliography

1. Intergovernmental Panel on Climate Change (IPCC). Climate change 2021: The physical science basis. *Cambridge University Press* 2023. DOI: 10.1017/9781009157896.
2. Filkov, A. I.; Ngo, T.; Matthews, S.; Telfer, S.; Penman, T. D. Impact of Australia's catastrophic 2019/20 bushfire season on communities and environment. Retrospective analysis and current trends. *Journal of Safety Science and Resilience* 2020, *1* (1), 44–56. DOI: 10.1016/j.jnlssr.2020.06.009.
3. Lombe, P.; Carvalho, E.; Rosa-Santos, P. Drought dynamics in sub-Saharan Africa: Impacts and adaptation strategies. *Sustainability* 2024, *16* (22), 9902. DOI: 10.3390/su16229902.
4. Our World in Data. Global Direct Primary Energy Consumption. https://ourworldindata.org/grapher/global-primary-energy (accessed 04.08.2024).
5. Ramasubramanian, B.; Ling, J.; Jose, R.; Ramakrishna, S. Ten major challenges for sustainable lithium-ion batteries. *Cell Reports Physical Science* 2024, *5* (6), 102032. DOI: 10.1016/j.xcrp.2024.102032.
6. Hassan, Q.; Algburi, S.; Sameen, A. Z.; Salman, H. M.; Jaszczur, M. Green hydrogen: A pathway to a sustainable energy future. *International Journal of Hydrogen Energy* 2024, *50*, 310–333. DOI: 10.1016/j.ijhydene.2023.08.321.
7. Haoran, C.; Xia, Y.; Wei, W.; Yongzhi, Z.; Bo, Z.; Leiqi, Z. Safety and efficiency problems of hydrogen production from alkaline water electrolyzers driven by renewable energy sources. *International Journal of Hydrogen Energy* 2024, *54*, 700–712. DOI: 10.1016/j.ijhydene.2023.08.324.
8. Kim-Lohsoontorn, P.; Prasopchokkul, P.; Wongmaek, A.; Temluxame, P.; Visvanichkul, R.; Bairak, S.; Nuengjumnong, N. Durability and degradation issues in solid oxide electrolysis cells. In *High Temperature Electrolysis*; Laguna-Bercero, M. A., Ed.; Lecture Notes in Energy; Springer International Publishing 2023, 277–312. DOI: 10.1007/978-3-031-22508-6_10.
9. Sebbahi, S.; Nabil, N.; Alaoui-Belghiti, A.; Laasri, S.; Rachidi, S.; Hajjaji, A. Assessment of the three most developed water electrolysis technologies: Alkaline water electrolysis, proton exchange membrane and solid-oxide electrolysis. *Materials Today: Proceedings* 2022, *66*, 140–145. DOI: 10.1016/j.matpr.2022.04.264.
10. Guo, Y.; Li, G.; Zhou, J.; Liu, Y. Comparison between hydrogen production by alkaline water electrolysis and hydrogen production by PEM electrolysis. *IOP Conference Series: Earth and Environmental Science* 2019, *371* (4), 42022. DOI: 10.1088/1755-1315/371/4/042022.
11. Zeng, K.; Zhang, D. Recent progress in alkaline water electrolysis for hydrogen production and applications. *Progress in Energy and Combustion Science* 2010, *36* (3), 307–326. DOI: 10.1016/j.pecs.2009.11.002.
12. Xiang, C.; Papadantonakis, K. M.; Lewis, N. S. Principles and implementations of electrolysis systems for water splitting. *Materials Horizons* 2016, *3* (3), 169–173. DOI: 10.1039/c6mh00016a.
13. Motealleh, B.; Liu, Z.; Masel, R. I.; Sculley, J. P.; Richard Ni, Z.; Meroueh, L. Next-generation anion exchange membrane water electrolyzers operating for commercially relevant lifetimes. *International Journal of Hydrogen Energy* 2021, *46* (5), 3379–3386. DOI: 10.1016/j.ijhydene.2020.10.244.
14. Turner, J. A. A realizable renewable energy future. *Science* 1999, *285* (5428), 687–689. DOI: 10.1126/science.285.5428.687.

15. Esposito, D. V. Membraneless electrolyzers for low-cost hydrogen production in a renewable energy future. *Joule* 2017, *1* (4), 651–658. DOI: 10.1016/j.joule.2017.07.003.

16. Lettenmeier, P.; Wang, R.; Abouatallah, R.; Helmly, S.; Morawietz, T.; Hiesgen, R.; Kolb, S.; Burggraf, F.; Kallo, J.; Gago, A. S.; Friedrich, K. A. Durable membrane electrode assemblies for proton exchange membrane electrolyzer systems operating at high current densities. *Electrochimica Acta* 2016, *210*, 502–511. DOI: 10.1016/j.electacta.2016.04.164.

17. Sauermoser, M.; Kizilova, N.; Pollet, B. G.; Kjelstrup, S. Flow field patterns for proton exchange membrane fuel cells. *Front. Energy Res.* 2020, *8. DOI:* 10.3389/fenrg.2020.00013.

18. Carmo, M.; Fritz, D. L.; Mergel, J.; Stolten, D. A comprehensive review on PEM water electrolysis. *International Journal of Hydrogen Energy* 2013, *38* (12), 4901–4934. DOI: 10.1016/j.ijhydene.2013.01.151.

19. Shiva Kumar, S.; Himabindu, V. Hydrogen production by PEM water electrolysis: A review. *Materials Science for Energy Technologies* 2019, *2* (3), 442–454. DOI: 10.1016/j.mset.2019.03.002.

20. Zhang, H.; Sarker, M.; Rahman, M. A.; Zhan, Z.; Sui, P.-C.; Chuang, P.-Y. A. Numerical investigation and experimental validation of water condensation in the gas diffusion layer with different properties. *Journal of Cleaner Production* 2023, *402*, 136792. DOI: 10.1016/j.jclepro.2023.136792.

21. Park, S.; Lee, J.-W.; Popov, B. N. A review of gas diffusion layer in PEM fuel cells: Materials and designs. *International Journal of Hydrogen Energy* 2012, *37* (7), 5850–5865. DOI: 10.1016/j.ijhydene.2011.12.148.

22. Samu, A. A.; Szenti, I.; Kukovecz, Á.; Endrődi, B.; Janáky, C. Systematic screening of gas diffusion layers for high performance CO2 electrolysis. *Communications Chemistry* 2023, *6* (1), 41. DOI: 10.1038/s42004-023-00836-2.

23. Babic, U.; Suermann, M.; Büchi, F. N.; Gubler, L.; Schmidt, T. J. Critical Review: Identifying critical gaps for polymer electrolyte water electrolysis development. *Journal of Electrochemical Society* 2017, *164* (4), F387-F399. DOI: 10.1149/2.1441704jes.

24. Ayers, K. E.; Anderson, E. B.; Capuano, C.; Carter, B.; Dalton, L.; Hanlon, G.; Manco, J.; Niedzwiecki, M. Research advances towards low cost, high efficiency PEM electrolysis. *ECS Transactions* 2010, *33* (1), 3–15. DOI: 10.1149/1.3484496.

25. Schalenbach, M.; Carmo, M.; Fritz, D. L.; Mergel, J.; Stolten, D. Pressurized PEM water electrolysis: Efficiency and gas crossover. *International Journal of Hydrogen Energy* 2013, *38* (35), 14921–14933. DOI: 10.1016/j.ijhydene.2013.09.013.

26. Lewinski, K. A.; van der Vliet, D.; Luopa, S. M. NSTF advances for PEM electrolysis: The effect of alloying on activity of nstf electrolyzer catalysts and performance of NSTF based PEM electrolyzers. *ECS Transactions* 2015, *69* (17), 893–917. DOI: 10.1149/06917.0893ecst.

27. Lickert, T.; Kiermaier, M. L.; Bromberger, K.; Ghinaiya, J.; Metz, S.; Fallisch, A.; Smolinka, T. On the influence of the anodic porous transport layer on PEM electrolysis performance at high current densities. *International Journal of Hydrogen Energy* 2020, *45* (11), 6047–6058. DOI: 10.1016/j.ijhydene.2019.12.204.

28. Suermann, M.; Schmidt, T. J.; Büchi, F. N. Investigation of mass transport losses in polymer electrolyte electrolysis cells. *ECS Transactions* 2015, *69* (17), 1141–1148. DOI: 10.1149/06917.1141ecst.

29. Suermann, M.; Schmidt, T. J.; Büchi, F. N. Cell performance determining parameters in high pressure water electrolysis. *Electrochimica Acta* 2016, *211*, 989–997. DOI: 10.1016/j.electacta.2016.06.120.

30. Garcia-Navarro, J. C.; Schulze, M.; Friedrich, K. A. Measuring and modeling mass transport losses in proton exchange membrane water electrolyzers using electrochemical impedance

spectroscopy. *Journal of Power Sources* 2019, *431*, 189–204. DOI: 10.1016/j.jpowsour.2019.05.027.

31. Hussain, J.; Kim, D.-K.; Park, S.; Khalid, M.-W.; Hussain, S.-S.; Lee, B.; Song, M.; Kim, T.-S. Porous material (titanium gas diffusion layer) in proton exchange membrane fuel cell/electrolyzer: Fabrication methods & GeoDict: A critical review. *Materials* 2023, *16* (13). DOI: 10.3390/ma16134515.

32. Liu, C.; Carmo, M.; Bender, G.; Everwand, A.; Lickert, T.; Young, J. L.; Smolinka, T.; Stolten, D.; Lehnert, W. Performance enhancement of PEM electrolyzers through iridium-coated titanium porous transport layers. *Electrochemistry Communications* 2018, *97*, 96–99. DOI: 10.1016/j.elecom.2018.10.021.

33. Liu, C.; Shviro, M.; Bender, G.; Gago, A. S.; Morawietz, T.; Dzara, M. J.; Biswas, I.; Gazdzicki, P.; Kang, Z.; Zaccarine, S. F.; Pylypenko, S.; Friedrich, K. A.; Carmo, M.; Lehnert, W. Degradation effects at the porous transport layer/catalyst layer interface in polymer electrolyte membrane water electrolyzer. *Journal of Electrochemical Society* 2023, *170* (3), 34508. DOI: 10.1149/1945-7111/acc1a5.

34. Doan, T. L.; Lee, H. E.; Shah, S. S. H.; Kim, M.; Kim, C.-H.; Cho, H.-S.; Kim, T. A review of the porous transport layer in polymer electrolyte membrane water electrolysis. *International Journal of Energy Research* 2021, *45* (10), 14207–14220. DOI: 10.1002/er.6739.

35. Schuler, T.; Bruycker, R. de; Schmidt, T. J.; Büchi, F. N. Polymer electrolyte water electrolysis: Correlating porous transport layer structural properties and performance, Part 1: Tomographic analysis of morphology and topology. *Journal of Electrochemical Society* 2019, *166* (4), F270-F281. DOI: 10.1149/2.0561904jes.

36. Suermann, M.; Takanohashi, K.; Lamibrac, A.; Schmidt, T. J.; Büchi, F. N. Influence of operating conditions and material properties on the mass transport losses of polymer electrolyte water electrolysis. *Journal of Electrochemical Society* 2017, *164* (9), F973-F980. DOI: 10.1149/2.13517109jes.

37. Grigoriev, S. A.; Millet, P.; Volobuev, S. A.; Fateev, V. N. Optimization of porous current collectors for PEM water electrolysers. *International Journal of Hydrogen Energy* 2009, *34* (11), 4968–4973. DOI: 10.1016/j.ijhydene.2008.11.056.

38. Borgardt, E.; Panchenko, O.; Hackemüller, F. J.; Giffin, J.; Bram, M.; Müller, M.; Lehnert, W.; Stolten, D. Mechanical characterization and durability of sintered porous transport layers for polymer electrolyte membrane electrolysis. *Journal of Power Sources* 2018, *374*, 84–91. DOI: 10.1016/j.jpowsour.2017.11.027.

39. Schuler, T.; Schmidt, T. J.; Büchi, F. N. Polymer electrolyte water electrolysis: Correlating performance and porous transport layer structure, Part 2: Electrochemical performance analysis. *Journal of Electrochemical Society* 2019, *166* (10), F555-F565. DOI: 10.1149/2.1241908jes.

40. Li, H.; Fujigaya, T.; Nakajima, H.; Inada, A.; Ito, K. Optimum structural properties for an anode current collector used in a polymer electrolyte membrane water electrolyzer operated at the boiling point of water. *Journal of Power Sources* 2016, *332*, 16–23. DOI: 10.1016/j.jpowsour.2016.09.086.

41. Steen, S. M.; Mo, J.; Kang, Z.; Yang, G.; Zhang, F.-Y. Investigation of titanium liquid/gas diffusion layers in proton exchange membrane electrolyzer cells. *International Journal of Green Energy* 2017, *14* (2), 162–170. DOI: 10.1080/15435075.2016.1253582.

42. Schuler, T.; Ciccone, J. M.; Krentscher, B.; Marone, F.; Peter, C.; Schmidt, T. J.; Büchi, F. N. Hierarchically structured porous transport layers for polymer electrolyte water electrolysis. *Advanced Energy Materials* 2020, *10* (2), 1903216. DOI: 10.1002/aenm.201903216.

43. Ernst, M. F.; Meier, V.; Kornherr, M.; Gasteiger, H. A. Developing microporous transport layers for polymer electrolyte membrane (PEM) water electrolyzer anodes. *ECS Meeting Abstracts* 2022, *MA2022-01* (39), 1750. DOI: 10.1149/MA2022-01391750mtgabs.

44. Immerz, C.; Paidar, M.; Papakonstantinou, G.; Bensmann, B.; Bystron, T.; Vidakovic-Koch, T.; Bouzek, K.; Sundmacher, K.; Hanke-Rauschenbach, R. Effect of the MEA design on the performance of PEMWE single cells with different sizes. *Journal of Applied Electrochemistry* 2018, *48* (6), 701–711. DOI: 10.1007/s10800-018-1178-2.

45. Liu, J.; Kerner, F.; Schlüter, N.; Schröder, D. Predicting the topological and transport properties in porous transport layers for water electrolyzers. *ACS Applied Materials & Interfaces* 2023, *15* (46), 54129–54142. DOI: 10.1021/acsami.3c12345.

46. Lettenmeier, P.; Kolb, S.; Burggraf, F.; Gago, A. S.; Friedrich, K. A. Towards developing a backing layer for proton exchange membrane electrolyzers. *Journal of Power Sources* 2016, *311*, 153–158. DOI: 10.1016/j.jpowsour.2016.01.100.

47. Lettenmeier, P.; Kolb, S.; Sata, N.; Fallisch, A.; Zielke, L.; Thiele, S.; Gago, A. S.; Friedrich, K. A. Comprehensive investigation of novel pore-graded gas diffusion layers for high-performance and cost-effective proton exchange membrane electrolyzers. *Energy and Environmental Science* 2017, *10* (12), 2521–2533. DOI: 10.1039/c7ee01240c.

48. Lee, J. K.; Lee, C.; Fahy, K. F.; Kim, P. J.; LaManna, J. M.; Baltic, E.; Jacobson, D. L.; Hussey, D. S.; Stiber, S.; Gago, A. S.; Friedrich, K. A.; Bazylak, A. Spatially graded porous transport layers for gas evolving electrochemical energy conversion: High performance polymer electrolyte membrane electrolyzers. *Energy Conversion and Management* 2020, *226*, 113545. DOI: 10.1016/j.enconman.2020.113545.

49. Mo, J.; Steen, S.; Han, B.; Kang, Z.; Terekhov, A.; Zhang, F.-Y.; Retterer, S. T.; Cullen, D. A. Investigation of titanium felt transport parameters for energy storage and hydrogen/oxygen production. In *13th International Energy Conversion Engineering Conference*; American Institute of Aeronautics and Astronautics: Reston, Virginia, 2015. DOI: 10.2514/6.2015-3914.

50. Ito, H.; Maeda, T.; Nakano, A.; Kato, A.; Yoshida, T. Influence of pore structural properties of current collectors on the performance of proton exchange membrane electrolyzer. *Electrochimica Acta* 2013, *100*, 242–248. DOI: 10.1016/j.electacta.2012.05.068.

51. Majasan, J. O.; Iacoviello, F.; Shearing, P. R.; Brett, D. J. L. Effect of microstructure of porous transport layer on performance in polymer electrolyte membrane water electrolyser. *Energy Procedia* 2018, *151*, 111–119. DOI: 10.1016/j.egypro.2018.09.035.

52. Marangio, F.; Santarelli, M.; Cali, M. Theoretical model and experimental analysis of a high-pressure PEM water electrolyser for hydrogen production. *International Journal of Hydrogen Energy* 2009, *34* (3), 1143–1158. DOI: 10.1016/j.ijhydene.2008.11.083.

53. Oliveira, L. F. L.; Jallut, C.; Franco, A. A. A multiscale physical model of a polymer electrolyte membrane water electrolyzer. *Electrochimica Acta* 2013, *110*, 363–374. DOI: 10.1016/j.electacta.2013.07.214.

54. Brooks, R. H.; Corey, A. T. Hydraulic properties of porous media and their relation to drainage design. *Transactions of the ASAE* 1964, *7* (1), 26–28. DOI: 10.13031/2013.40684.

55. Gostick, J. T. Versatile and efficient pore network extraction method using marker-based watershed segmentation. *Physical Review E* 2017, *96* (2-1), 23307. DOI: 10.1103/PhysRevE.96.023307.

56. Satjaritanun, P.; O'Brien, M.; Kulkarni, D.; Shimpalee, S.; Capuano, C.; Ayers, K. E.; Danilovic, N.; Parkinson, D. Y.; Zenyuk, I. V. Observation of preferential pathways for oxygen removal through porous transport layers of polymer electrolyte water electrolyzers. *iScience* 2020, *23* (12), 101783. DOI: 10.1016/j.isci.2020.101783.

57. Bhaskaran, S.; Pandey, D.; Surasani, V. K.; Tsotsas, E.; Vidakovic-Koch, T.; Vorhauer-Huget, N. LBM studies at pore scale for graded anodic porous transport layer (PTL) of PEM water electrolyzer. *International Journal of Hydrogen Energy* 2022, *47* (74), 31551–31565. DOI: 10.1016/j.ijhydene.2022.07.079.

58. Zhang, H.; Abderrahmane, H.; Al Kobaisi, M.; Sassi, M. Pore-scale characterization and PNM simulations of multiphase flow in carbonate rocks. *Energies* 2021, *14* (21), 6897. DOI: 10.3390/en14216897.

59. Lu, X.; Tsotsas, E.; Kharaghani, A. Drying of capillary porous media simulated by coupling of continuum-scale and micro-scale models. *International Journal of Multiphase Flow* 2021, *140*, 103654. DOI: 10.1016/j.ijmultiphaseflow.2021.103654.

60. Metzger, T.; Irawan, A.; Tsotsas, E. Influence of pore structure on drying kinetics: A pore network study. *AIChE Journal* 2007, *53* (12), 3029–3041. DOI: 10.1002/aic.11307.

61. Vorhauer, N., Metzger, T., Tsotsas, E., Eds. Extraction of effective parameters for continuous drying model from discrete pore network model. *Proceedings of the 17th International Drying Symposium* 2010, Magdeburg, Germany, 3 - 6 October 2010.

62. Agaesse, T.; Lamibrac, A.; Büchi, F. N.; Pauchet, J.; Prat, M. Validation of pore network simulations of ex-situ water distributions in a gas diffusion layer of proton exchange membrane fuel cells with X-ray tomographic images. *Journal of Power Sources* 2016, *331* (10), 462–474. DOI: 10.1016/j.jpowsour.2016.09.076.

63. Raeini, A. Q.; Yang, J.; Bondino, I.; Bultreys, T.; Blunt, M. J.; Bijeljic, B. Validating the generalized pore network model using micro-CT images of two-phase flow. *Transport in Porous Media* 2019, *130* (2), 405–424. DOI: 10.1007/s11242-019-01317-8.

64. Garfi, G.; John, C. M.; Rücker, M.; Lin, Q.; Spurin, C.; Berg, S.; Krevor, S. Determination of the spatial distribution of wetting in the pore networks of rocks. *Journal of Colloid and Interface Science* 2022, *613*, 786–795. DOI: 10.1016/j.jcis.2021.12.183.

65. Esteves, B. F.; Lage, P. L.; Couto, P.; Kovscek, A. R. Pore-network modeling of single-phase reactive transport and dissolution pattern evaluation. *Advances in Water Resources* 2020, *145*, 103741. DOI: 10.1016/j.advwatres.2020.103741.

66. Li, M.; Foroughi, S.; Zhao, J.; Bijeljic, B.; Blunt, M. J. Image-based pore-scale modelling of the effect of wettability on breakthrough capillary pressure in gas diffusion layers. *Journal of Power Sources* 2023, *584*, 233539. DOI: 10.1016/j.jpowsour.2023.233539.

67. Xiong, Q.; Baychev, T. G.; Jivkov, A. P. Review of pore network modelling of porous media: Experimental characterisations, network constructions and applications to reactive transport. *Journal of Contaminant Hydrology* 2016, *192*, 101–117. DOI: 10.1016/j.jconhyd.2016.07.002.

68. Lee, J. K.; Bazylak, A. Optimizing porous transport layer design parameters via stochastic pore network modelling: Reactant transport and interfacial contact considerations. *Journal of Electrochemical Society* 2020, *167* (1), 13541. DOI: 10.1149/1945-7111/ab6557.

69. Vorhauer-Huget, N.; Altaf, H.; Dürr, R.; Tsotsas, E.; Vidaković-Koch, T. Computational optimization of porous structures for electrochemical processes. *Processes* 2020, *8* (10), 1205. DOI: 10.3390/pr8101205.

70. Huang, X.; He, Y.; Zhou, W.; Deng, D.; Zhao, Y. Pore network modeling of fibrous porous media of uniform and gradient porosity. *Powder Technology* 2019, *343*, 350–361. DOI: 10.1016/j.powtec.2018.11.022.

71. Tranter, T. G.; Boillat, P.; Mularczyk, A.; Manzi-Orezzoli, V.; Shearing, P. R.; Brett, D. J. L.; Eller, J.; Gostick, J. T.; Forner-Cuenca, A. Pore network modelling of capillary transport and relative diffusivity in gas diffusion layers with patterned wettability. *Journal of Electrochemical Society* 2020, *167* (11), 114512. DOI: 10.1149/1945-7111/ab9d61.

72. Stiber, S.; Balzer, H.; Wierhake, A.; Wirkert, F. J.; Roth, J.; Rost, U.; Brodmann, M.; Lee, J. K.; Bazylak, A.; Waiblinger, W.; Gago, A. S.; Friedrich, K. A. Porous transport layers for proton exchange membrane electrolysis under extreme conditions of current density, temperature, and pressure. *Advanced Energy Materials* 2021, *11* (33), 2100630. DOI: 10.1002/aenm.202100630.

73. Lee, J. K.; Lee, C.; Bazylak, A. Pore network modelling to enhance liquid water transport through porous transport layers for polymer electrolyte membrane electrolyzers. *Journal of Power Sources* 2019, *437*, 226910. DOI: 10.1016/j.jpowsour.2019.226910.

74. Eghbalmanesh, A.; Fathiganjehlou, A.; Rieder, D. R.; Hoogendoorn, M.; Miloshevska, M.; Baltussen, M. W.; Peters, E.; Buist, K. A.; Kuipers, J. CFD-validated pore network modeling of packed beds of non-spherical particle. *Chemical Engineering Science* 2024, *283*, 119396. DOI: 10.1016/j.ces.2023.119396.

75. Sourya, D. P.; Gurugubelli, P. S.; Bhaskaran, S.; Vorhauer-Huget, N.; Tsotsas, E.; Surasani, V. K. A comparative study on the Lattice Boltzmann Method and the VoF-continuum method for oxygen transport in the anodic porous transport layer of an electrolyzer. *International Journal of Hydrogen Energy* 2024, *92*, 1091–1098. DOI: 10.1016/j.ijhydene.2024.10.340.

76. Dullien, F. A. L. Porous media: Fluid transport and pore structure, 2nd edition. *Elsevier Science: Burlington* 2012.

77. Gostick, J. T.; Ioannidis, M. A.; Fowler, M. W.; Pritzker, M. D. Pore network modeling of fibrous gas diffusion layers for polymer electrolyte membrane fuel cells. *Journal of Power Sources* 2007, *173* (1), 277–290. DOI: 10.1016/j.jpowsour.2007.04.059.

78. Gostick, J.; Aghighi, M.; Hinebaugh, J.; Tranter, T.; Hoeh, M. A.; Day, H.; Spellacy, B.; Sharqawy, M. H.; Bazylak, A.; Burns, A.; Lehnert, W.; Putz, A. OpenPNM: A pore network modeling package. *Computing in Science and Engineering* 2016, *18* (4), 60–74. DOI: 10.1109/MCSE.2016.49.

79. Blunt, M. J.; Jackson, M. D.; Piri, M.; Valvatne, P. H. Detailed physics, predictive capabilities and macroscopic consequences for pore-network models of multiphase flow. *Advances in Water Resources* 2002, *25* (8-12), 1069–1089. DOI: 10.1016/S0309-1708(02)00049-0.

80. Miličić, T.; Altaf, H.; Vorhauer-Huget, N.; Živković, L. A.; Tsotsas, E.; Vidaković-Koch, T. Modeling and analysis of mass transport losses of proton exchange membrane water electrolyzer. *Processes* 2022, *10* (11), 2417. DOI: 10.3390/pr10112417.

81. Ma, S.; Saitou, T.; Nakajima, H.; Ito, K. Effect of porous transport layers on the limiting current density of PEM electrolysis cells: Visualization and numerical analysis. *Journal of Power Sources* 2025, *632*, 236292. DOI: 10.1016/j.jpowsour.2025.236292.

82. Lee, J. K.; Lee, C.; Fahy, K. F.; Zhao, B.; LaManna, J. M.; Baltic, E.; Jacobson, D. L.; Hussey, D. S.; Bazylak, A. Critical current density as a performance indicator for gas-evolving electrochemical devices. *Cell Reports Physical Science* 2020, *1* (8), 100147. DOI: 10.1016/j.xcrp.2020.100147.

83. Seweryn, J.; Biesdorf, J.; Schmidt, T. J.; Boillat, P. Neutron radiography of the water/gas distribution in the porous layers of an operating electrolyser. *Journal of Electrochemical Society* 2016, *163* (11), F3009-F3011. DOI: 10.1149/2.0641607jes.

84. Panchenko, O.; Giesenberg, L.; Borgardt, E.; Zwaygardt, W.; Kardjilov, N.; Markötter, H.; Arlt, T.; Manke, I.; Müller, M.; Stolten, D.; Lehnert, W. Influence of stoichiometry on the two-phase flow behavior of proton exchange membrane electrolyzers. *Energies* 2019, *12* (3), 350. DOI: 10.3390/en12030350.

85. Maier, M.; Dodwell, J.; Ziesche, R.; Tan, C.; Heenan, T.; Majasan, J.; Kardjilov, N.; Markötter, H.; Manke, I.; Castanheira, L.; Hinds, G.; Shearing, P. R.; Brett, D. Mass transport in polymer electrolyte membrane water electrolyser liquid-gas diffusion layers: A combined neutron imaging and X-ray computed tomography study. *Journal of Power Sources* 2020, *455*, 227968. DOI: 10.1016/j.jpowsour.2020.227968.

86. Selamet, O. F.; Pasaogullari, U.; Spernjak, D.; Hussey, D. S.; Jacobson, D. L.; Mat, M. D. Two-phase flow in a proton exchange membrane electrolyzer visualized in situ by simultaneous neutron radiography and optical imaging. *International Journal of Hydrogen Energy* 2013, *38* (14), 5823–5835. DOI: 10.1016/j.ijhydene.2013.02.087.

87. Zlobinski, M.; Schuler, T.; Büchi, F. N.; Schmidt, T. J.; Boillat, P. Transient and steady state two-phase flow in anodic porous transport layer of proton exchange membrane water

electrolyzer. *Journal of Electrochemical Society* 2020, *167* (8), 84509. DOI: 10.1149/1945-7111/ab8c89.

88. Panchenko, O.; Borgardt, E.; Zwaygardt, W.; Hackemüller, F. J.; Bram, M.; Kardjilov, N.; Arlt, T.; Manke, I.; Müller, M.; Stolten, D.; Lehnert, W. In-situ two-phase flow investigation of different porous transport layer for a polymer electrolyte membrane (PEM) electrolyzer with neutron spectroscopy. *Journal of Power Sources* 2018, *390*, 108–115. DOI: 10.1016/j.jpowsour.2018.04.044.

89. Lee, C.; Lee, J. K.; Zhao, B.; Fahy, K. F.; Bazylak, A. Transient gas distribution in porous transport layers of polymer electrolyte membrane electrolyzers. *Journal of Electrochemical Society* 2020, *167* (2), 24508. DOI: 10.1149/1945-7111/ab68c8.

90. Joekar-Niasar, V.; Hassanizadeh, S. M. Analysis of fundamentals of two-phase flow in porousmedia using dynamic pore-network models: A review. *Critical Reviews in Environmental Science and Technology* 2012, *42* (18), 1895–1976. DOI: 10.1080/10643389.2011.574101.

91. Lee, K.-J.; Nam, J. H.; Kim, C.-J. Pore-network analysis of two-phase water transport in gas diffusion layers of polymer electrolyte membrane fuel cells. *Electrochimica Acta* 2009, *54* (4), 1166–1176. DOI: 10.1016/j.electacta.2008.08.068.

92. Sinha, P. K.; Wang, C.-Y. Pore-network modeling of liquid water transport in gas diffusion layer of a polymer electrolyte fuel cell. *Electrochimica Acta* 2007, *52* (28), 7936–7945. DOI: 10.1016/j.electacta.2007.06.061.

93. Lenormand, R. Liquids in porous media. *Journal of Physics: Condensed Matter* 1990, *2* (S), SA79-SA88. DOI: 10.1088/0953-8984/2/S/008.

94. Zhang, C.; Oostrom, M.; Wietsma, T. W.; Grate, J. W.; Warner, M. G. Influence of viscous and capillary forces on immiscible fluid displacement: Pore-scale experimental study in a water-wet micromodel demonstrating viscous and capillary fingering. *Energy Fuels* 2011, *25* (8), 3493–3505. DOI: 10.1021/ef101732k.

95. Vorhauer, N.; Tran, Q. T.; Metzger, T.; Tsotsas, E.; Prat, M. Experimental investigation of drying in a model porous medium: influence of thermal gradients. *Drying Technology* 2013, *31* (8), 920–929. DOI: 10.1080/07373937.2012.724750.

96. Wang, F.; Schiller, U. D. Computational characterization of nonwoven fibrous media, Part 1: Pore-network extraction and morphological analysis. *Physical Review Materials* 2020, *4* (8), 227. DOI: 10.1103/PhysRevMaterials.4.083803.

97. Huang, X.; Zhou, W.; Deng, D. Validation of pore network modeling for determination of two-phase transport in fibrous porous media. *Scientific Reports* 2020, *10* (1), 20852. DOI: 10.1038/s41598-020-74581-0.

98. Altaf, H.; Vorhauer, N.; Tsotsas, E.; Vidaković-Koch, T. Steady-state water drainage by oxygen in anodic porous transport layer of electrolyzers: A 2D pore network study. *Processes* 2020, *8* (3), 362. DOI: 10.3390/pr8030362.

99. Vorhauer, N.; Altaf, H.; Tsotsas, E.; Vidakovic-Koch, T. Pore network simulation of gas-liquid distribution in porous transport layers. *Processes* 2019, *7* (9), 558. DOI: 10.3390/pr7090558.

100. Hubbell, J. H.; Seltzer, S. X-ray mass attenuation coefficients. *NIST standard reference database 126*. DOI: 10.18434/T4D01F. (Accessed on 03.04.2022).

101. Altaf, H.; Miličic, T.; Faber, F.; Vidaković-Koch, T.; Tsotsas, E.; Vorhauer-Huget, N. Use of reconstructed pore networks for determination of effective transport parameters of commercial Ti-felt PTLs. *Processes* 2025, *13* (4), 943. DOI: 10.3390/pr13040943.

102. Thomik, M.; Gruber, S.; Foerst, P.; Tsotsas, E.; Vorhauer-Huget, N. Determination of 3D pore network structure of freeze-dried maltodextrin. *Drying Technology* 2022, *40* (4), 748–766. DOI: 10.1080/07373937.2021.1966030.

103. Makki, I.; Younes, R.; Francis, C.; Bianchi, T.; Zucchetti, M. A survey of landmine detection using hyperspectral imaging. *ISPRS Journal of Photogrammetry and Remote Sensing* 2017, *124*, 40–53. DOI: 10.1016/j.isprsjprs.2016.12.009.

104. Legland, D.; Arganda-Carreras, I.; Andrey, P. MorphoLibJ: Integrated library and plugins for mathematical morphology with ImageJ. *Bioinformatics* 2016, *32* (22), 3532–3534. DOI: 10.1093/bioinformatics/btw413.

105. Silin, D.; Patzek, T. Pore space morphology analysis using maximal inscribed spheres. *Physica A: Statistical Mechanics and its Applications* 2006, *371* (2), 336–360. DOI: 10.1016/j.physa.2006.04.048.

106. Hoshen, J. On the application of the enhanced Hoshen–Kopelman algorithm for image analysis. *Pattern Recognition Letters* 1998, *19* (7), 575–584. DOI: 10.1016/S0167-8655(98)00018-X.

107. Vorhauer, N. Experiment based development of a non-isothermal pore network model with secondary capillary invasion (*Ph.D. dissertation*). Chair of Thermal Process Engineering, Otto-von-Guericke-University Magdeburg, Germany; 2019.

108. Xu, K.; Wei, W.; Chen, Y.; Tian, H.; Xu, S.; Cai, J. A pore network approach to study throat size effect on the permeability of reconstructed porous media. *Water* 2022, *14* (1), 77. DOI: 10.3390/w14010077.

109. Tsotsas, E.; Kwapinska, M.; Saage, G. Modeling of contact dryers. *Drying Technology* 2007, *25* (7-8), 1377–1391. DOI: 10.1080/07373930701439079.

110. Schlünder, E.-U.;Tsotsas, E. Wärmeübertragung n Festbetten, druchmischten Schüttgütern und Wirbelschichten. *Georg Thieme Verlag, Stuttgart – New York* 1988. ISBN: 3137130018

111. Le, K. H.; Kharaghani, A.; Kirsch, C.; Tsotsas, E. Pore network simulations of heat and mass transfer inside an unsaturated capillary porous wick in the dry-out regime. *Transport in Porous Media* 2016, *114* (3), 623–648. DOI: 10.1007/s11242-016-0737-4.

112. Ren, C. Parametric effects on heat transfer in loop heat pipe's wick. *International Journal of Heat and Mass Transfer* 2011, *54* (17-18), 3987–3999. DOI: 10.1016/j.ijheatmasstransfer.2011.04.026.

113. Le, K. H.; Kharaghani, A.; Kirsch, C.; Tsotsas, E. Discrete pore network modeling of superheated steam drying. *Drying Technology* 2017, *35* (13), 1584–1601. DOI: 10.1080/07373937.2016.1264414.

114. Konduru, V.; Allen, J. S. Material and morphological heat transfer properties of fuel cell porous transport layers. *Journal of Electrochemical Society* 2017, *164* (13), F1316-F1322. DOI: 10.1149/2.0341713jes.

115. Bauer, T. H. A general analytical approach toward the thermal conductivity of porous media. *International Journal of Heat and Mass Transfer* 1993, *36* (17), 4181–4191. DOI: 10.1016/0017-9310(93)90080-P.

116. Gonzo, E. E. Estimating correlations for the effective thermal conductivity of granular materials. *Chemical Engineering Journal* 2002, *90* (3), 299–302. DOI: 10.1016/S1385-8947(02)00121-3.

117. Rocha, R. P. A.; Cruz, M. A. E. Computation of the effective conductivity of unidirectional fibrous composites with an interfacial thermal resistance. *Numerical Heat Transfer, Part A: Applications* 2001, *39* (2), 179–203. DOI: 10.1080/104077801300004267.

118. Carotenuto, G. B. A. The effective thermal conductivity of packed beds of spheres for a finite contact area. *Numerical Heat Transfer, Part A: Applications* 2000, *37* (4), 343–357. DOI: 10.1080/104077800274217.

119. Wang, J.; Carson, J. K.; North, M. F.; Cleland, D. J. A new approach to modelling the effective thermal conductivity of heterogeneous materials. *International Journal of Heat and Mass Transfer* 2006, *49* (17-18), 3075–3083. DOI: 10.1016/j.ijheatmasstransfer.2006.02.007.

120. Sundén, B.; Yuan, J. Evaluation of models of the effective thermal conductivity of porous materials relevant to fuel cell electrodes. *International Journal of CMEM* 2013, *1* (4), 440–455. DOI: 10.2495/CMEM-V1-N4-440-455.

121. Sauerhering, J.; Angel, S.; Fend, T.; Brendelberger, S.; Smirnova, E.; Pitz-Paal, R. Characterisation of flow and heat transfer in sintered metal foams. In *ASME 2008 6th International Conference on Nanochannels, Microchannels, and Minichannels*; ASMEDC, 2008, pp 121–127. DOI: 10.1115/ICNMM2008-62311.

122. Gustavsson, M.; Karawacki, E.; Gustafsson, S. E. Thermal conductivity, thermal diffusivity, and specific heat of thin samples from transient measurements with hot disk sensors. *Review of Scientific Instruments* 1994, *65* (12), 3856–3859. DOI: 10.1063/1.1145178.

123. Gustafsson, S. E. Transient plane source techniques for thermal conductivity and thermal diffusivity measurements of solid materials. *Review of Scientific Instruments* 1991, *62* (3), 797–804. DOI: 10.1063/1.1142087.

124. Tengattini, A.; Lenoir, N.; Andò, E.; Giroud, B.; Atkins, D.; Beaucour, J.; Viggiani, G. NeXT-Grenoble, the neutron and X-ray tomograph in Grenoble. *Nuclear Instruments and Methods in Physics Research Section A: Accelerators, Spectrometers, Detectors and Associated Equipment* 2020, *968*, 163939. DOI: 10.1016/j.nima.2020.163939.

125. Altaf, H.; Miličić, T.; Vidakovic-Koch, T.; Tsotsas, E.; Arlt, T.; Kardjilov, N.; Manke, I.; Vorhauer-Huget, N. Neutron imaging experiments to study mass transport in commercial titanium felt porous transport layers. *Journal of Electrochemical Society* 2023, *170* (064507). DOI: 10.1149/1945-7111/acd7a8.

126. Tekseth, K. R.; Mirzaei, F.; Lukic, B.; Chattopadhyay, B.; Breiby, D. W. Multiscale drainage dynamics with Haines jumps monitored by stroboscopic 4D X-ray microscopy. *Proceedings of the National Academy of Sciences of the United States of America* 2024, *121* (1), e2305890120. DOI: 10.1073/pnas.2305890120.

127. Cakmak, E. Investigation of two-phase transport in the porous transport layer of proton exchange membrane water electrolyzer (*master's dissertation*). Chair of Thermal Process Engineering, Otto-von-Guericke-University Magdeburg, Germany; 2024.

128. Arbabi, F.; Kalantarian, A.; Abouatallah, R.; Wang, R.; Wallace, J.; Bazylak, A. Visualizing bubble flows in electrolyzer GDLs using microfluidic platforms. *ECS Transactions* 2013, *58* (1), 907–918. DOI: 10.1149/05801.0907ecst.

129. Jinadath, A. K. A. CFD simulation of oxygen drainage in anodic porous transport layer in PEM electrolyzers (*master's dissertation*). Chair of Thermal Process Engineering, Otto-von Guericke-University Magdeburg, Germany; 2021.

130. Thomson, P.-R.; Aituar-Zhakupova, A.; Hier-Majumder, S. Image segmentation and analysis of pore network geometry in two natural sandstones. *Frontiers in Earth Science* 2018, *6. DOI:* 10.3389/feart.2018.00058.

131. Domander, R.; Felder, A. A.; Doube, M. BoneJ2: Refactoring established research software. *Wellcome Open Research* 2021, *6*, 37. DOI: 10.12688/wellcomeopenres.16619.2.

132. Faber, F.; Vorhauer-Huget, N.; Thomik, M.; Gruber, S.; Först, P.; Tsotsas, E. Pore-scale study of coupled heat and mass transfer during primary freeze-drying using an irregular pore network model. *Drying Technology* 2024, 1–21. DOI: 10.1080/07373937.2024.2407062.

133. Arbabi, F.; Kalantarian, A.; Abouatallah, R.; Wang, R.; Wallace, J. S.; Bazylak, A. Feasibility study of using microfluidic platforms for visualizing bubble flows in electrolyzer gas diffusion layers. *Journal of Power Sources* 2014, *258*, 142–149. DOI: 10.1016/j.jpowsour.2014.02.042.

134. Holzer, L.; Pecho, O.; Schumacher, J.; Marmet, P.; Büchi, F. N.; Lamibrac, A.; Münch, B. Microstructure-property relationships in a gas diffusion layer (GDL) for polymer electrolyte fuel cells, Part II: Pressure-induced water injection and liquid permeability. *Electrochimica Acta* 2017, *241*, 414–432. DOI: 10.1016/j.electacta.2017.04.141.

135. Vorhauer, N.; Tsotsas, E.; Prat, M. Temperature gradient induced double stabilization of the evaporation front within a drying porous medium. *Physical Review Fluids* 2018, *3* (11). DOI: 10.1103/PhysRevFluids.3.114201.

136. Hoseini Larimi, S. Z.; Ramiar, A.; Shafaghat, R.; Esmaili, Q. The effect of geometric parameters of PTL on oxygen transport in PEM electrolysis cell. *Proceedings of the Institution of Mechanical Engineers, Part C: Journal of Mechanical Engineering Science* 2021, *235* (24), 7484–7495. DOI: 10.1177/09544062211038025.

137. Jackson, G. W.; James, D. F. The permeability of fibrous porous media. *Canadian Journal of Chemical Engineering* 1986, *64* (3), 364–374. DOI: 10.1002/cjce.5450640302.

138. Tomadakis, M. M.; Robertson, T. J. Viscous permeability of random fiber structures: Comparison of electrical and diffusional estimates with experimental and analytical results. *Journal of Composite Materials* 2005, *39* (2), 163–188. DOI: 10.1177/0021998305046438.

139. Tomadakis, M. M.; Sotirchos, S. V. Ordinary and transition regime diffusion in random fiber structures. *AIChE Journal* 1993, *39* (3), 397–412. DOI: 10.1002/aic.690390304.

140. Bhaskaran, S.; Miličić, T.; Vidaković-Koch, T.; Kumar Surasani, V.; Tsotsas, E.; Vorhauer-Huget, N. Model PEM water electrolyzer cell for studies of periodically alternating drainage/imbibition cycles. *International Journal of Hydrogen Energy* 2024, *77*, 1432–1442. DOI: 10.1016/j.ijhydene.2024.06.268.

141. Rajora, A.; Haverkort, J. W. An Analytical Model for Liquid and Gas Diffusion Layers in Electrolyzers and Fuel Cells. *Journal of Electrochemical Society* 2021, *168* (3), 34506. DOI: 10.1149/1945-7111/abe087.

142. Han, B.; Mo, J.; Kang, Z.; Yang, G.; Barnhill, W.; Zhang, F.-Y. Modeling of two-phase transport in proton exchange membrane electrolyzer cells for hydrogen energy. *International Journal of Hydrogen Energy* 2017, *42* (7), 4478–4489. DOI: 10.1016/j.ijhydene.2016.12.103.

143. Grigoriev, S. A.; Kalinnikov, A. A.; Millet, P.; Porembsky, V. I.; Fateev, V. N. Mathematical modeling of high-pressure PEM water electrolysis. *Journal of Applied Electrochemistry* 2010, *40* (5), 921–932. DOI: 10.1007/s10800-009-0031-z.

144. Surasani, V. K.; Metzger, T.; Tsotsas, E. Consideration of heat transfer in pore network modelling of convective drying. *International Journal of Heat and Mass Transfer* 2008, *51* (9-10), 2506–2518. DOI: 10.1016/j.ijheatmasstransfer.2007.07.033.

145. Liu, H. L.; Hwang, W. R. Permeability prediction of fibrous porous media with complex 3D architectures. *Composites Part A: Applied Science and Manufacturing* 2012, *43* (11), 2030–2038. DOI: 10.1016/j.compositesa.2012.07.024.

146. Gamero, R.; Martínez, J. The use of drying experiments in the study of the effective thermal conductivity in a solid containing a multicomponent liquid mixture. *Chemical Engineering Research and Design* 2012, *90* (11), 1765–1778. DOI: 10.1016/j.cherd.2012.04.003.

147. Tsotsas, E.; Schlünder, E. Contact drying of mechanically agitated particulate material in the presence of inert gas. *Chemical Engineering and Processing: Process Intensification* 1986, *20* (5), 277–285. DOI: 10.1016/0255-2701(86)80021-6.

148. Ghafourian, M. Unteruschungen zur Struktur von Porösen Transportschichten in Polymer-Elektrolyt-Membran-Wasserelektrolyseuren (*master's dissertation*). Chair of Thermal Process Engineering, Otto-von-Guericke-University Magdeburg, Germany; 2022.

149. Majasan, J. O.; Iacoviello, F.; Cho, J. I.; Maier, M.; Lu, X.; Neville, T. P.; Dedigama, I.; Shearing, P. R.; Brett, D. J. Correlative study of microstructure and performance for porous transport layers in polymer electrolyte membrane water electrolysers by X-ray computed tomography and electrochemical characterization. *International Journal of Hydrogen Energy* 2019, *44* (36), 19519–19532. DOI: 10.1016/j.ijhydene.2019.05.222.

150. Hwang, C. M.; Ishida, M.; Ito, H.; Maeda, T.; Nakano, A.; Hasegawa, Y.; Yokoi, N.; Kato, A.; Yoshida, T. Influence of properties of gas diffusion layers on the performance of polymer

electrolyte-based unitized reversible fuel cells. *International Journal of Hydrogen Energy* 2011, *36* (2), 1740–1753. DOI: 10.1016/j.ijhydene.2010.10.091.

151. Zielke, L.; Fallisch, A.; Paust, N.; Zengerle, R.; Thiele, S. Tomography based screening of flow field/current collector combinations for PEM water electrolysis. *RSC Advances* 2014, *4* (102), 58888–58894. DOI: 10.1039/C4RA12402B.

152. Liu, S.; Xi, Z.; Tang, H.; Yang, X.; Zhang, Z.; Liu, Q. Sintering behavior of porous titanium fiber materials. *Journal of Iron and Steel Research International* 2014, *21* (9), 849–854. DOI: 10.1016/S1006-706X(14)60152-7.

153. Li-Yin, G.; Hao-Kun, Y.; Xuan, C.; Wei-Dong, T.; Xing-Ming, H.; Zhi-Quan, L. The development of porous metallic materials: A short review of fabrication, characteristics, and applications. *Physica Scripta* 2023, *98* (12), 122001. DOI: 10.1088/1402-4896/ad086c.

154. Lee, C.; Zhao, B.; Abouatallah, R.; Wang, R.; Bazylak, A. Compressible-gas invasion into liquid-saturated porous media: Application to polymer-electrolyte-membrane electrolyzers. *Physical Review Applied* 2019, *11* (5). DOI: 10.1103/PhysRevApplied.11.054029.

155. Mularczyk, A.; Lin, Q.; Blunt, M. J.; Lamibrac, A.; Marone, F.; Schmidt, T. J.; Büchi, F. N.; Eller, J. Droplet and percolation network interactions in a fuel cell gas diffusion layer. *Journal of Electrochemical Society* 2020, *167* (8), 84506. DOI: 10.1149/1945-7111/ab8c85.

156. Lee, J. K.; Anderson, G.; Tricker, A. W.; Babbe, F.; Madan, A.; Cullen, D. A.; Arregui-Mena, J. D.; Danilovic, N.; Mukundan, R.; Weber, A. Z.; Peng, X. Ionomer-free and recyclable porous-transport electrode for high-performing proton-exchange-membrane water electrolysis. *Nature Communications* 2023, *14* (1), 4592. DOI: 10.1038/s41467-023-40375-x.

157. Wilkinson, D.; Willemsen, J. F. Invasion percolation: A new form of percolation theory. *Journal of Physics A: Mathematical and General* 1983, *16* (14), 3365–3376. DOI: 10.1088/0305-4470/16/14/028.

158. Shojaei, M. J.; Bijeljic, B.; Zhang, Y.; Blunt, M. J. Minimal surfaces in porous materials: X-ray image-based measurement of the contact angle and curvature in gas diffusion layers to design optimal performance of fuel cells. *ACS Applied Energy Materials* 2022, *5* (4), 4613–4621. DOI: 10.1021/acsaem.2c00023.

159. Dong, H.; Blunt, M. J. Pore-network extraction from micro-computerized-tomography images. *Physical Review E* 2009, *80* (3 Pt 2), 36307. DOI: 10.1103/PhysRevE.80.036307.

Appendix

A.1 Calculation of V_{rev}° and V_{tn}°

The values of V_{rev}° and V_{tn}° provided in Eq. 1-4 and Eq. 1-5 are calculated at standard conditions (1 atm and 25 °C) using

$$V_{rev}^{\circ} = \frac{\Delta G^{\circ}}{nF} = \frac{237000\,\mathrm{J\cdot mol^{-1}}}{2\times 96485\,\mathrm{C\cdot mol^{-1}}} = 1.23\ \mathrm{V} \qquad \text{(A-1)}$$

and

$$V_{tn}^{\circ} = \frac{\Delta H^{\circ}}{nF} = \frac{286000\,\mathrm{J\cdot mol^{-1}}}{2\times 96485\,\mathrm{C\cdot mol^{-1}}} = 1.48\ \mathrm{V}, \qquad \text{(A-2)}$$

respectively. In these calculations, standard Gibbs free energy change for water splitting ($\Delta G^{\circ} \approx 237$ kJ·mol^{-1}) represents the minimum energy required to drive the reaction spontaneously under standard conditions. The standard enthalpy change ($\Delta H^{\circ} \approx 285$ kJ·mol^{-1}) is the total heat absorbed during the process, $n = 2$ is the number of electrons transferred per mole of water split, and $F = 96485$ C·mol^{-1} is the Faraday constant, representing the charge of one mole of electrons.

A.2 Pumps used in non-electrochemical experiments

Table A-1: Syringe pump specifications.

Name	AL-4000 Double Syringe Pump
Manufacturer	World Precision Instruments, Friedberg, Germany
Type	Infusion/Withdrawal
Channels	2
Flow rate range	0.001 µL/hr (0.5 µL syringe) to 7515 mL/hr (60 mL syringe)
Dispensing accuracy	±1%
Syringe size	60 ml each

To control the pumps (Table A-1) remotely from a workstation during the experiments, the software *SyringPumpPro* was used.

A.3 Dimensions of the non-electrochemical cell prototype

Before the non-electrochemical cells used in the experiments were built, a prototype cell was built. This was based on the design of Panchnko et al.[84]. This prototype cell was also used to capture the bubble release through the PTL into the channel using a Canon EOS 550D camera (results discussed in Section 5.1.4). Figure A-1 shows the dimensions of this cell.

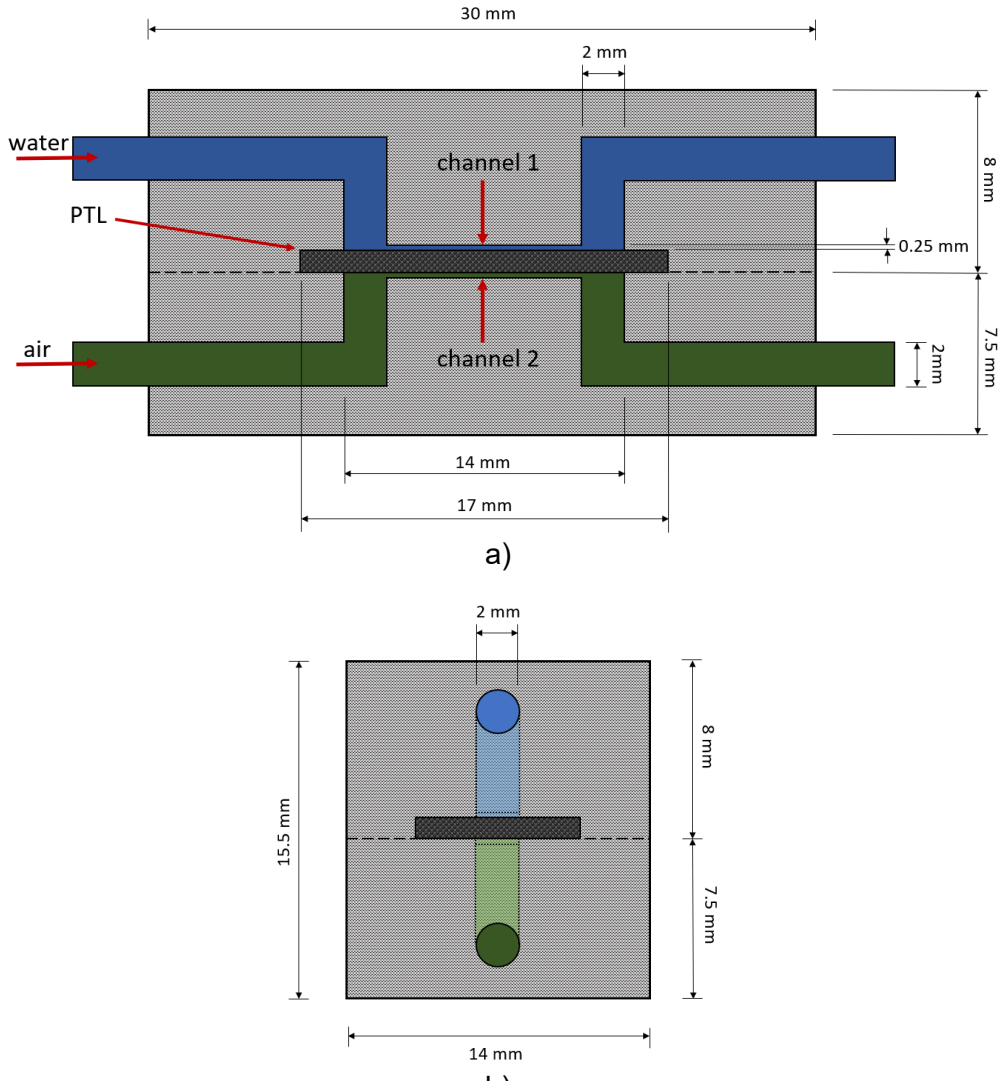

Figure A-1: a) A cross-section of the prototype non-electrochemical cell; b) side view of the non-electrochemical cell, showing the water and air inlets.

A.4 Micro-CT scanning of PTLs

The micro-CT scans were performed using CT-Alpha from ProCon X-ray GmbH, Sarstedt, Germany. The parameters used for these scans are summarized in Table A-2. The reconstruction of the image was done in Volex software by Fraunhofer IIs, Fürth, Germany. The image processing (cropping, segmentation, etc.) was done in ImageJ 2.1051. Table A-3 shows the scans obtained after cropping the edges to obtained a straightened 3D image stack with the dimensions.

Table A-2: The parameters used during the micro-CT scanning of PTLs.

Acceleration voltage	50 kV
Current	160 µA
Energy	5.8 W
Exposure time	2000 ms
Number of projecitons	1200
Measurement time	2.4 h

Table A-3: The micro-CT scans of all PTLs along with their respective thickness. These domains were used in the extracted PNs.

Scanned image	**PTL**	**Thickness** (mm)
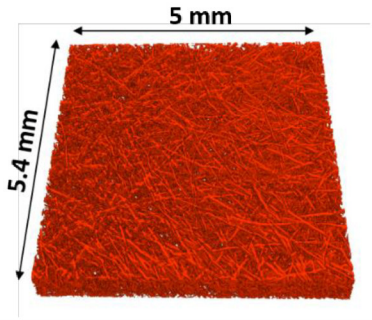	1	0.53
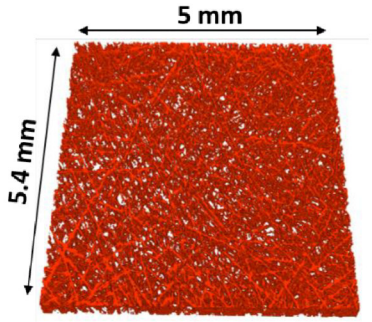	2	0.34
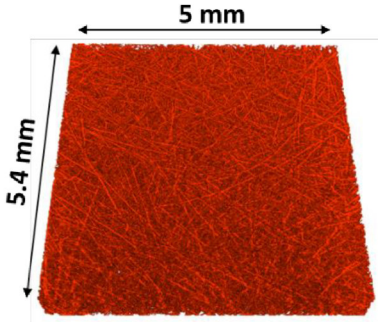	3	0.78

A.5 GeoDict simulations

To calculate the porosity and permeability of PTL-1 using GeoDict, the domain shown in Figure A-2 was used. The details of the simulations are provided in Table A-4.

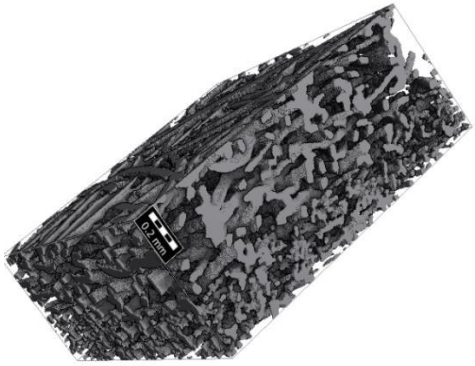

Figure A-2: Micro-CT scan of the domain used for porosity and permeability calculations.

Table A-4: The domain, modules and resulting values from the GeoDict simulations.

PTL	PTL-1 (Bekaert)
Domain size (voxels)	500 × 500 × 205
Voxel length (µm)	3.9
Domain size (mm^3)	1.95 × 1.95 × 0.80
Porosity module	PoroDict
Porosity solver	OpenAndClosedPorosity
Open porosity	74 %
Closed porosity	74 %
Permeability module	FlowDict
Permeability solver	SolveEJStokes
Permeability value	$1.1 \cdot 10^{-10}\ m^2$

To verify the porosity value, the *OpenAndClosedPorosity* solver was also used on a relatively larger domain of 1181 × 894 × 205 voxels (Figure A-3). The same values for open and closed porosity were found as in the smaller domain (74 % for both).

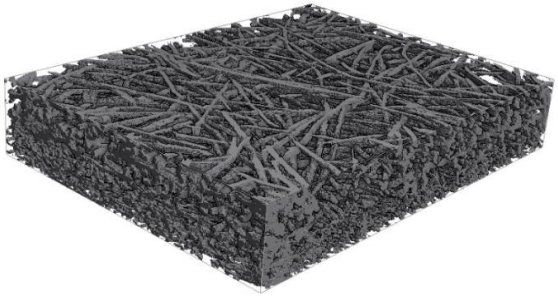

Figure A-3: A relatively larger domain, than the one shown in Figure A-2, used to verify the porosity value obtained.

A.6 Sensitivity analysis of LE and BCE

LE depends on K, ε, and θ, whereas BCE depends on r_{max}, λ, and θ. To assess the sensitivity of these correlations to their respective parameters and to determine the conditions under which PNM, LE, and BCE yield similar results, each parameter was varied within a defined range. While one parameter is varied, the rest are kept constant at values provided in Table A-5.

Table A-5: Values of the fixed parameters in the sensitivity analysis.

	PTL-1	**PTL-2**	**PTL-3**
$\boldsymbol{\varepsilon}$ (%)	74	73	72
$\boldsymbol{K}$ (m^2)	$1.5 \cdot 10^{-10}$	$1.4 \cdot 10^{-10}$	$1.1 \cdot 10^{-10}$
$\boldsymbol{\theta}$ (°)	60°	60°	60°
$\boldsymbol{\lambda}$ (-)	4	4	4
$\boldsymbol{r_{max}}$ (µm)	128	106	81

Figure A-4 shows variation of θ which influences both LE and BCE. Figure A-5 and Figure A-6 show variations in ε and K, respectively. These variables impact the LE only. Figure A-7 and Figure A-8 show variations in λ and r_{max}, respectively. These variables impact the BCE only. These figures are used to find the best-fit curves provided in Section 3.2.2 (Figure 3-13).

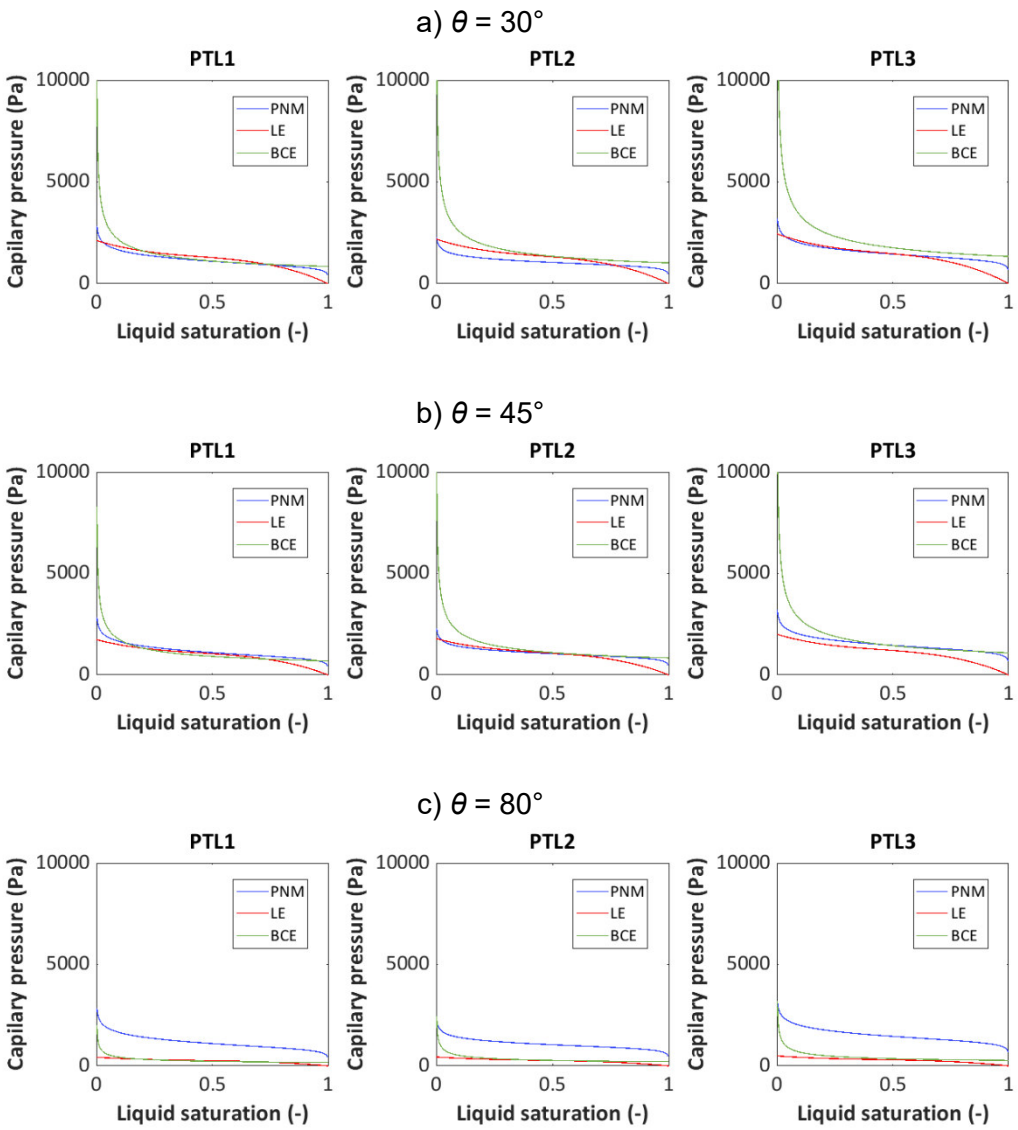

Figure A-4: Comparison of capillary pressure curves at different values of θ, increasing from a) to c).

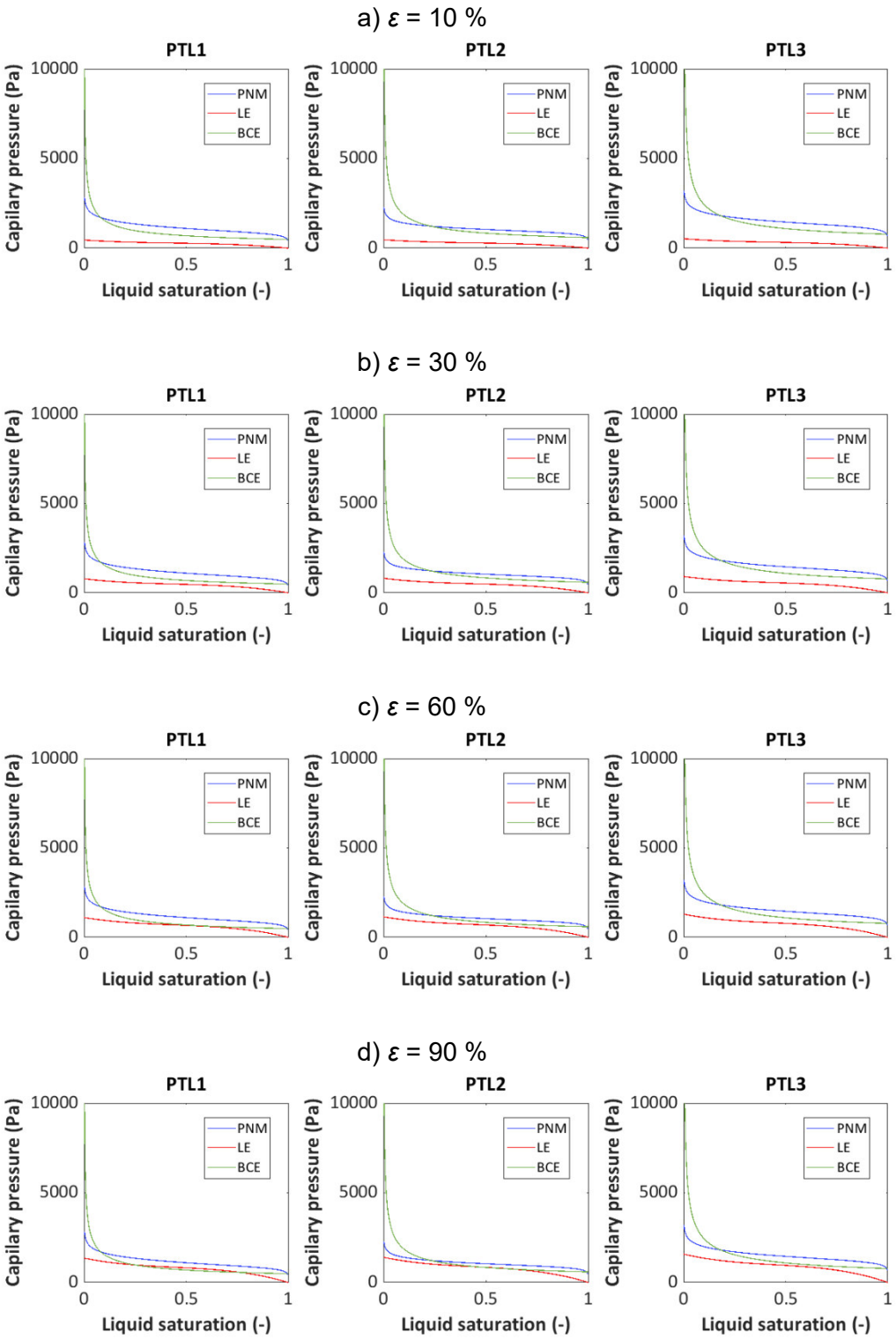

Figure A-5: Comparison of capillary pressure curves at different values of ε, increasing from a) to d).

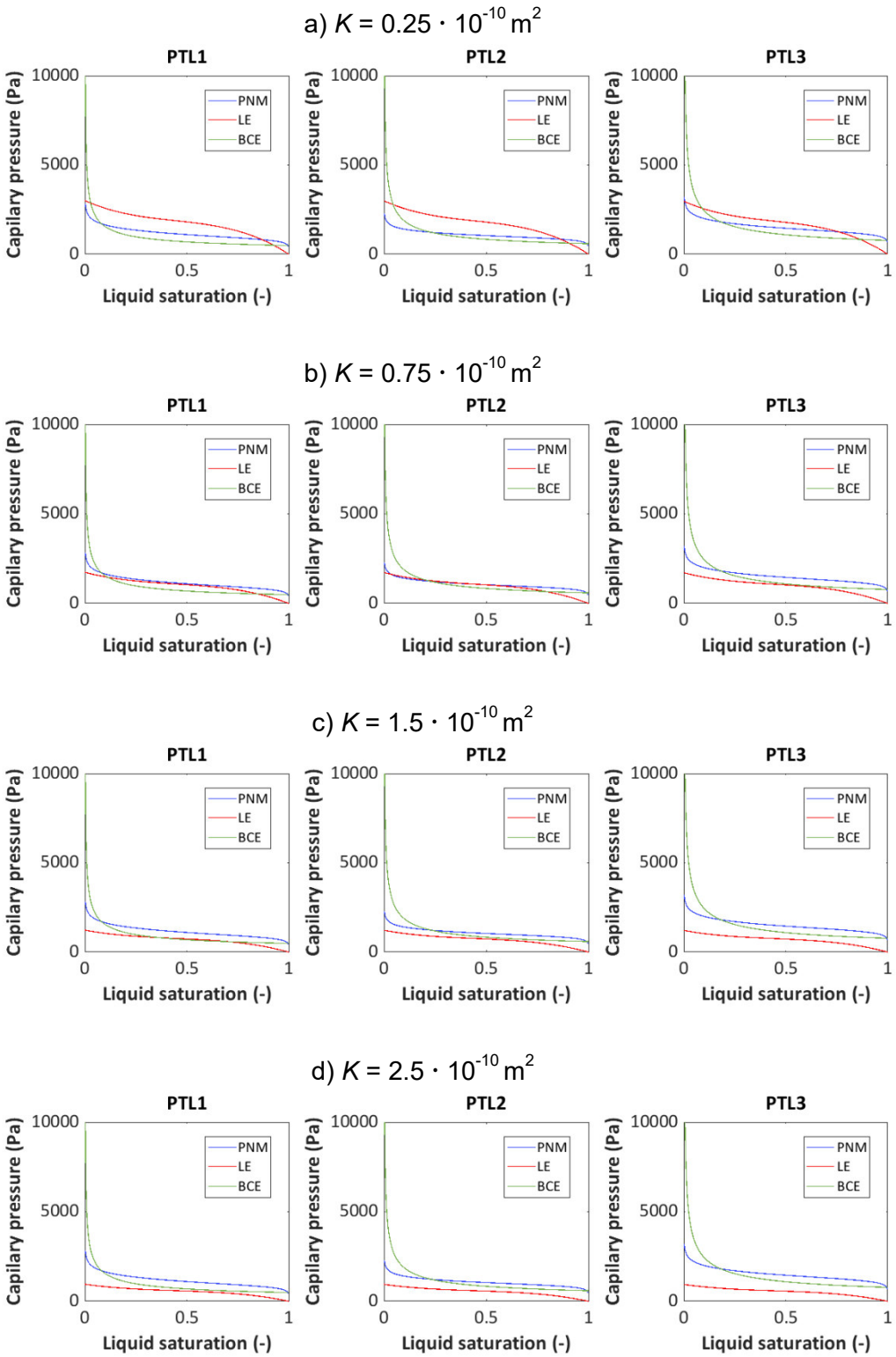

Figure A-6: Comparison of capillary pressure curves at different values of K, increasing from a) to d).

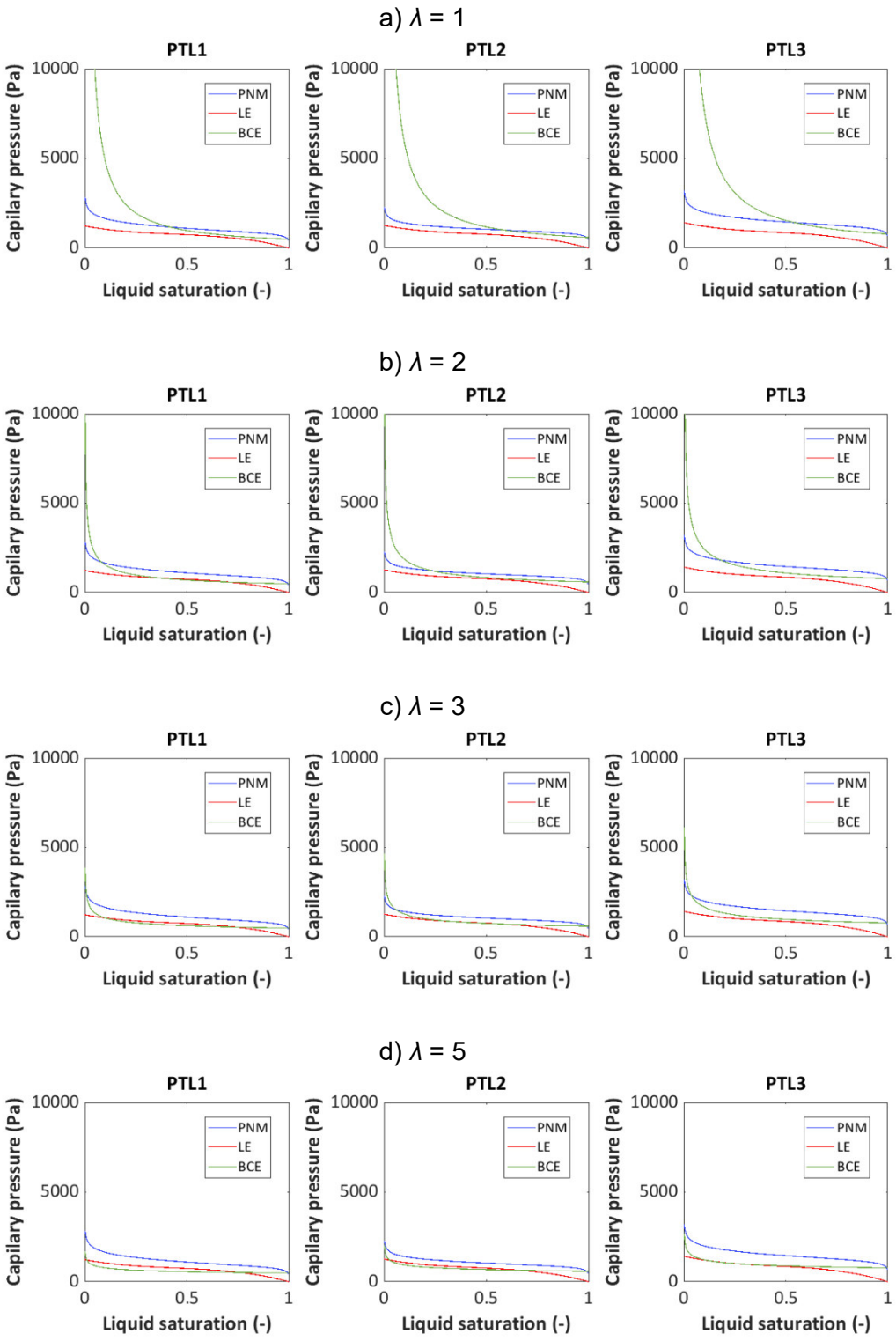

Figure A-7: Comparison of capillary pressure curves at different values of λ, increasing from a) to d).

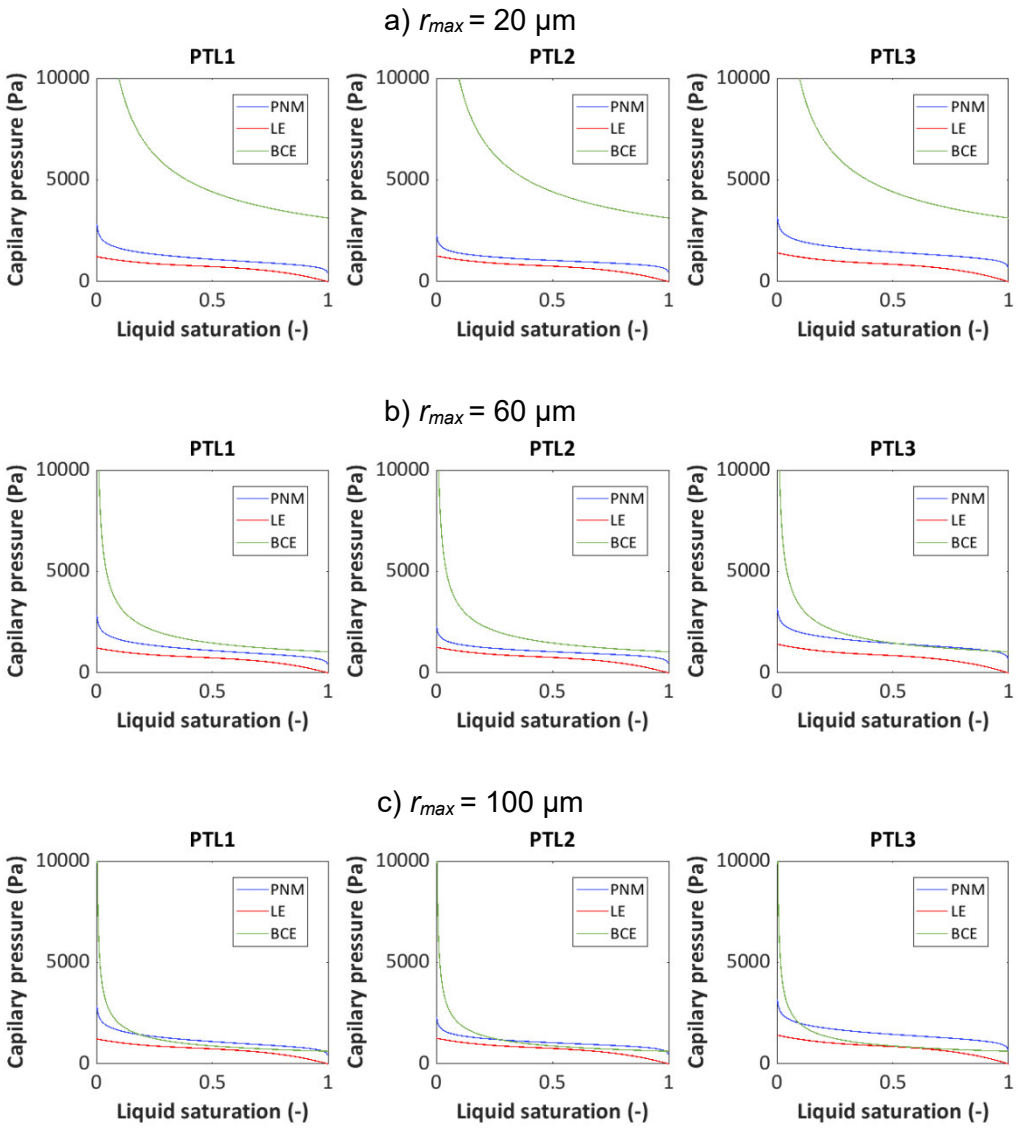

Figure A-8: Comparison of capillary pressure curves at different values of r_{max}, increasing from a) to c).

A.7 CFD simulation of a channel in non-electrochemical cell

To estimate the pressure-drop within the channels of non-electrochemical cells, a half-cell geometry is used to simulate water and air flow through the channel. Figure A-9 shows the geometry used. The flow settings used in experiments (Section 2.3.1) are also applied in the simulations. These simulations only provide an estimate, as the geometry does not include an actual PTL next to the channel. However, the estimates are sufficient to assess whether the pressure drops in the channel could influence the break-through locations observed.

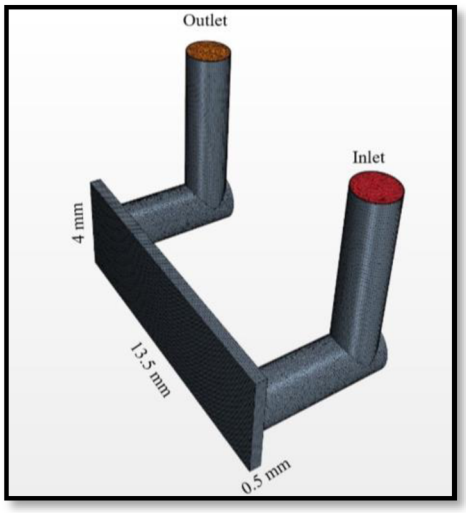

Figure A-9: The geometry used to run the flow simulations.

It is seen in Table A-6 that only minor pressure drops occur within the air channel (~ 0.3 Pa to 1.5 Pa), whereas in the water channel the pressure drops can be higher (up to 17 Pa). Regardless of the values, it can be anticipated that these pressure-drop values may influence the break-through regions/locations through the PTL into the channel. As an example, the pressure-drop within the water channel for Setting-3 is also shown in Figure A-10 using a contour plot.

Table A-6: The results of the simulated pressure drop within the channel for water and air at each setting used in non-electrochemical cell experiments.

Setting	**Phase**	**Flow rate** ($ml \cdot min^{-1}$)	**Inlet velocity** ($m \cdot s^{-1}$)	**Inlet pressure** (Pa)	**Outlet pressure** (Pa)	**ΔP** (Pa)
1	Water	0.582	0.003	2.580	0.259	2.321
2	Water	2.183	0.011	10.315	1.147	9.168
3	Water	3.056	0.016	14.926	1.759	13.167
4	Water	3.929	0.020	19.838	2.478	17.36
1	Air	3.950	0.020	0.358	0.0352	0.322
2	Air	9.874	0.052	0.910	0.0912	0.818
3	Air	13.823	0.073	1.285	0.130	1.115
4	Air	17.773	0.094	1.669	0.171	1.498

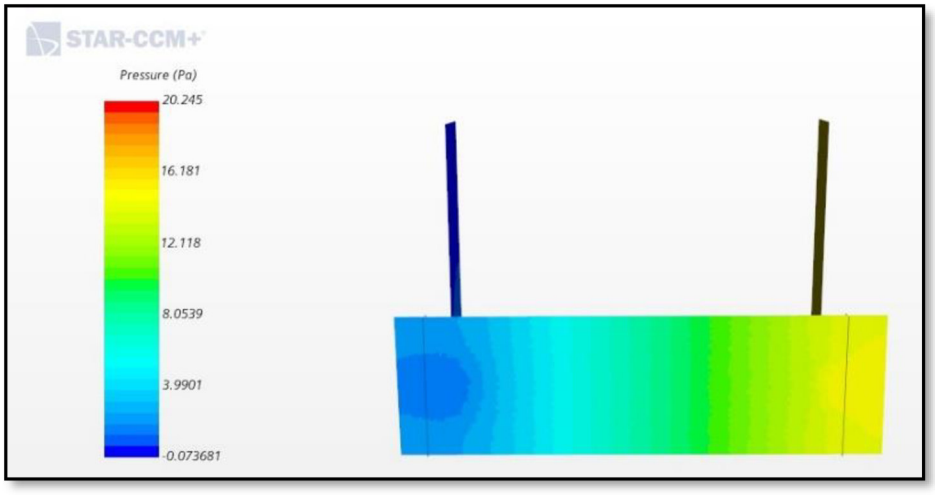

Figure A-10: The contour plot of pressure distribution within the channel. The right side (yellow in color) corresponds to the inlet water side.

Declaration

I hereby declare that I produced this thesis without prohibited external assistance and that none other than the listed references and tools have been used.

In the case of co-authorship, especially in the context of a cumulative dissertation, the own contribution is correctly and completely stated. I did not make use of any commercial consultant concerning graduation. A third party did not receive any nonmonetary perquisites neither directly nor indirectly for activities which are connected with the contents of the presented thesis. All sources of information are clearly marked, including my own publications.

In particular I have not consciously:

- Fabricated data or rejected undesired results,
- Misused statistical methods with the aim of drawing other conclusions than those warranted by the available data,
- Plagiarized data or publications, Presented the results of other researchers in a distorted way.

During the writing process, Generative AI (ChatGPT 4) was utilized to enhance the language in certain sections of the manuscript. After using this tool, the text was always reviewed and edited if necessary, with full responsibility taken for the content of the publication.

I do know that violations of copyright may lead to injunction and damage claims of the author and also to prosecution by the law enforcement authorities.

I hereby agree hat the thesis may need to be reviewed with an electronic data processing for plagiarism.

This work hat not yet been submitted as a doctoral thesis in the same or a similar form in Germany or in any other country. It has not yet been published as a whole.

Hamburg, 14.01.2026

Haashir Altaf

Journal publications and conferences

Journal publications

1. Vorhauer, N.; Altaf, H.; Tsotsas, E.; Vidakovic-Koch, T. Pore network simulation of gas-liquid distribution in porous transport layers. *Processes* 2019, *7* (9), 558. DOI: 10.3390/pr7090558.

2. Altaf, H.; Vorhauer, N.; Tsotsas, E.; Vidaković-Koch, T. steady-state water drainage by oxygen in anodic porous transport layer of electrolyzers: A 2D pore network study. *Processes* 2020, *8* (3), 362. DOI: 10.3390/pr8030362.

3. Vorhauer-Huget, N.; Altaf, H.; Dürr, R.; Tsotsas, E.; Vidaković-Koch, T. Computational optimization of porous structures for electrochemical processes. *Processes* 2020, *8* (10), 1205. DOI: 10.3390/pr8101205.

4. Miličić, T.; Altaf, H.; Vorhauer-Huget, N.; Živković, L. A.; Tsotsas, E.; Vidaković-Koch, T. Modeling and analysis of mass transport losses of proton exchange membrane water electrolyzer. *Processes* 2022, *10* (11), 2417. DOI: 10.3390/pr10112417.

5. Altaf, H.; Miličić, T.; Vidakovic-Koch, T.; Tsotsas, E.; Arlt, T.; Kardjilov, N.; Manke, I.; Vorhauer-Huget, N. Neutron imaging experiments to study mass transport in commercial titanium felt porous transport layers. *Journal of Electrochemical Society* 2023. DOI: 10.1149/1945-7111/acd7a8.

6. Altaf, H.; Miličić, T.; Faber, F.; Vidaković-Koch, T.; Tsotsas, E.; Vorhauer-Huget, N., Use of reconstructed pore networks for determination of effective transport parameters of commercial Ti-felt PTLs*, Processes* 2025, *13*(4), 943. DOI: 10.3390/pr13040943.

Oral presentations

1. Pore network modeling of oxygen invasion in porous transport layer of electrolyzers for H_2 production; *13th European Congress of Chemical Engineering and 6th European Congress of Applied Biotechnology* (virtual), Germany. Sep 20 - 23, 2021.

2. Pore graded anodic transport layers in PEM electrolyzers: A pore network study; *InterPore 2021, 13th Annual Meeting* (virtual), Germany. May 31 - Jun 4, 2021.

3. Pore network modeling of anodic porous transport layer in electrolyzers; *17th Symposium on Modeling and Experimental Validation of Fuel Cells, Electrolyzers and Batteries* (virtual), Germany. Apr 20 - 22, 2021.

4. In-situ neutron imaging and pore network modeling of counter-current mass transfer inside porous transport layers used for PEMWE; *241st ECS Meeting of the Electrochemical Society*, Vancouver, Canada. May 29 - June 2, 2022.

5. Investigating the mass transport in porous transport layers of PEMWE using neutron imaging; *GDE Symposium Magdeburg*, Germany. Sep 5 - 7, 2022.

Poster presentations

1. 3D pore network simulation of anode gas diffusion layer (GDL) of electrolyzers and their permeability analysis at high current densities; *YCOPE 2019 - 1st International Young Professionals Conference on Process Engineering*, Magdeburg, Germany. Mar 18 - 20, 2019.

2. Pore network modeling of invasion processes in electrochemistry; *71st Annual Meeting of the International Society of Electrochemistry "Electrochemistry towards Excellence"*, Belgrade Online, Germany. Aug 31 - Sep 1, 2020.

3. Micro-CT imaging of electrolyzer gas diffusion layers to extract pore space information for pore network modeling; *Symposium on Insights into Gas Diffusion Electrodes: From Fundamentals to Industrial Applications*, Magdeburg, Germany. Sep 23 - 25, 2019.

Summer school attended

Joint European Summer School 2022: Low temperature fuel cells and electrolyzers, Athens, Greece. Sep 11 - 17, 2022.

Student thesis

Cakmak, E. Investigation of two-phase transport in the porous transport layer of proton exchange membrane water electrolyzer (Master's thesis). *Max Planck Institute for Dynamics of Complex Technical Systems*, 2024.